Investigation of Chalcogenide Absorber Materials for Photovoltaic Applications

Colombara, Diego

Award date:
2012

Awarding institution:
University of Bath

Investigation of Chalcogenide Absorber Materials for Photovoltaic Applications

Diego Colombara

A thesis submitted for the degree of Doctor of Philosophy

University of Bath

Department of Chemistry

Bath, June 2012

Table of contents

Acknowledgements 5

Work done in conjunction with others 6

Foreword 7

Abstract 8

1. Introduction 9

1.1 Current scenario of photovoltaics 9

1.2 Semiconductors as photovoltaic components 13

1.3 Photoelectrochemistry of semiconductors 21

1.4 Project outline and aim of this work 24

Part A

Introduction to part A: major debates on absorber layer formation 31

2. Formation of $CuSbS_2$ and $CuSbSe_2$ thin films 37

2.1 $CuSb(S,Se)_2$ thin film precursor deposition 39

2.1.1 Evaporation of Sb, Cu, Sb/Cu and $CuSbS_2$ thin films 39

2.1.2 Sb-Cu co-electrodeposition 39

2.2 Chalcogenization of $CuSb(S,Se)_2$ precursors 47

2.3 Morphology and composition of $CuSb(S,Se)_2$ thin films 49

2.4 Structural characterization of $CuSbS_2$ thin films 53

2.5 Photoelectrochemistry of $CuSb(S,Se)_2$ thin films 56

2.6 Experimental details 61

3. Formation of Cu_3BiS_3 and $CuBiS_2$ thin films 65

3.1 Cu_3BiS_3 and $CuBiS_2$ thin film precursor deposition 68

3.1.1 Evaporation and RF co-sputtering of Bi and Cu-Bi thin films 68

3.1.2 Sequential electrodeposition of Cu/Bi/Cu thin films 68

3.1.3 Co-electrodeposition of Cu-Bi thin films 68

3.2 Sulfurization of Cu-Bi metal precursors 73

3.2.1 Sulfurization via Rapid Thermal Processing 73

3.2.2 Sulfurization with H_2S and S in a conventional tube furnace 78

3.3 Morphology and composition of Cu-Bi-S thin films 80

3.3.1 Co-electroplated Cu-Bi films 80

3.3.2 Cu-Bi films sulfurized with elemental sulfur (RTP) 81

3.3.3 Cu-Bi films sulfurized with hydrogen sulfide or sulfur 86

3.4 Structural characterization of Cu-Bi(S) thin films 88

3.4.1 Structural properties of annealed electroplated Cu-Bi films 88

3.4.2 Structural properties of sulfurized evaporated Bi films 89

3.4.3 Structural properties of sulfurized electroplated Cu-Bi films 91

3.5 Photoelectrochemistry of sulfurized Cu:Bi 3:1 films 93

3.6 Experimental details 96

4. Study of the chalcogenization reaction ____ *99*

4.1 Following compound formation via structural analysis ____ **101**

4.2 Morphological implications of the reaction sequence ____ **111**

4.3 The role of the sulfurizing conditions in phase evolution ____ **119**

4.4 Elemental losses during the thermal treatments of chalcogenide layers ____ **131**

Concluding remarks for part A ____ *143*

Part B

Introduction to part B: fundamental debates on CZTS ____ *151*

5. Thermodynamics of the Cu-Zn-Sn-S-I system ____ *159*

5.1 Computational procedure ____ **162**

5.2 Unary components: S and I ____ **164**

5.3 Binary components: Cu-S, Cu-I, Sn-S, Sn-I, Zn-S, Zn-I ____ **168**

5.4 Ternary systems: Cu-S-I, Sn-S-I, Zn-S-I ____ **172**

5.5 Quaternary system: Cu-Sn-S-I ____ **177**

5.6 Pentenary system: Cu-Zn-Sn-S-I ____ **180**

6. Chemical vapour transport growth of CZTS with I_2 ____ *185*

6.1 Experimental details of crystal growth ____ **187**

6.2 Compositional and structural characterization ____ **191**

6.3 Results of Chemical Vapour Transport Experiments ____ **192**

6.3.1 Summary of experimental results ____ 192

6.3.2 Experiment No. 9: growth with iodine load of $9 \cdot 10^{-4}$ gcm^{-3} ____ 194

6.3.3 Experiment No. 3: growth with iodine load of $5 \cdot 10^{-3}$ gcm^{-3} ____ 197

6.4 Discussion of preferential crystallization ____ **200**

7. Cu_2ZnSnS_4: Kesterite or Stannite? ____ *211*

7.1 X-ray and neutron scattering analyses of CZTS crystals ____ **212**

7.2 Raman spectroscopy analysis of CZTS crystals ____ **217**

7.3 Photoluminescence spectroscopy analyses ____ **221**

Concluding remarks for part B ____ *225*

Appendices ____ *229*

(1) Derivation of detailed balance efficiency limit ____ **229**

(2) Diagrams of I-42m and I-4 space groups ____ **233**

(3) Thermochemical functions ____ **236**

(4) Cu-S phase equilibria ____ **238**

(5) Sn-S phase equilibria ____ **239**

(6) Zn-S phase equilibria ____ **240**

(7) Convective share of transport ____ **241**

Bibliographic references ____ *243*

Acknowledgements

I would like to thank my supervisor Prof. Laurence Peter for his great help, inspiration and motivation during the course of the PhD. His supportive and enthusiastic attitude allowed me to conduct research in freedom and always comforted me whenever I needed guidance. During these years he also gave me the opportunity to attend many conferences, meetings and schools around Europe, which helped me establishing valuable collaborations worldwide. I thank him for all this.

I am grateful to my second supervisor Prof. Frank Marken, for his kind support and precious advice. His help was always much appreciated.

Many people at the University, past and present, are very much thanked for support of science and spirit: Dr. Charlie Cummings, Dr. John Scragg, Dr. Claire Thompson, Jesse Dufton, Prof. Saiful Islam, Anna Sudlow, Prof. Kieran Molloy, Dr. Mary Mahon, Dr. Aron Walsh, Lee Burton, Dr. Pooja Panchmatia, Dr. Alberto Fattori, Prof. Chick Wilson, Dr. Lynne Thomas, Lauren Hatcher, Dr. Ibrahim Hassan, Andreas Løken, Dr. Halina Dunn, Dr. Hongxia Wang, Dr. Anne Vuorema, Dr. Sara Dale, Phil Jones, Tom Risbridger, Katryn Wills, Dr. Petra Cameron, Dr. Daniel Wolverson, Dr. Jon Mitchels, Dr. Anne O'Reilly, Dr. Hugh Perrott, Dr. Andrea Marini, Dr. Francesco Ciampa, Fulvio Pinto and Dr. Ettore Barbieri.

Prof. Gabriella Borzone and Dr. Simona Delsante (Università di Genova) are thanked for providing help and phase diagram information. Dr. Scilla Roncallo, Dr. Jonathan Painter, Prof. Keith Rogers and Kyle Hutchings (Cranfield University) are thanked for XRD and SEM. Dr. Maxim Ganchev, Prof. Enn Mellikov, Julia Iljina (TUT Tallinn), Dr. Edgardo Saucedo (IREC Barcelona), Dr. Phillip Dale (UniLu), Prof. Matsumura and Wilman Septina (Osaka University) are thanked for their hospitality and advice. Dr. Konstantin Mariolacos (Goettingen University) is greatly thanked for finding and sharing his original thermochemical calculations [1] that served as inspiration for part of the present study. Alan Dinsdale is acknowledged for the adapted Cu-Bi phase diagram [2, 3]. Funding was provided by EPSRC (Supergen: Photovoltaic Materials for the 21st Century EP/F029624/1). The whole PV21 group is thanked for the fruitful discussions during the 6 month meetings.

I wish to thank all my friends in Bath and my family and friends back in Arquata. Very special thanks go to Bilge: teşekkürler!

Work done in conjunction with others

(1) The Cu_3BiS_3 unit cell picture shown in chapter 3 was constructed by Jesse Dufton (University of Bath, Chemistry Department) using the software VESTA [4].

(2) The Mo-coated substrates employed for the work in chapters 2 and 3 were provided either by Dr. Guillaume Zoppi and Pietro Maiello (Northumbria University) or by Dr. Stefan Schäfer (Enthone GmbH).

(3) The co-sputtered and stacked electroplated Cu-Bi metal precursors employed for the works in sections 3.1.1 and 3.1.2 were provided by Dr. Ian Forbes (Northumbria University) and Dr. Stefan Schäfer (Enthone GmbH) respectively.

(4) The evaporated $CuSbS_2$ films employed for the work in section 2.3 were provided by Prof. Mounir Kanzari, Dr. Bahri Rezig and Adel Rabhi (ENI Tunis).

(5) The XRD measurements employed for chapters 2, 3 and 4 were made either by Dr. Scilla Roncallo, Kyle Hutchings or Prof. Keith Rogers (Cranfield University).

(6) The Sb-S and Bi-S pressure equilibria reported in section 4.4 were computed on the MATLAB software with the help of Fulvio Pinto, Francesco Ciampa (University of Bath, Mech. Eng. Department) and Dr. Ettore Barbieri (University of Oxford).

(7) The Gauss-Jordan matrix reductions in chapter 5 were possible thanks to the advice offered by Dr. Andrea Marini (Max Planck Institute) and Francesco Ciampa.

(8) The TEM analyses shown in sections 6.3.2 and 6.3.3 were performed respectively by Dr. Budhika Mendis (University of Durham) and Dr. John Mitchels (University of Bath, Physics Department).

(9) The SEM-EDS analyses of Fig.6.3.2d-g were made by Dr. Simona Delsante and Prof. Gabriella Borzone (Università degli Studi di Genova).

(10) The XRD single crystal analyses in sections 6.3.1 and 7.1 were performed by either Prof. Kieran Molloy and Dr. Mary Mahon (Experiment No. 9) or Dr. Lynne Thomas (Experiment No. 3). The XRD powder analyses were done with the help of Gabriele Kociok-Kohn (University of Bath, Chemistry Department).

(11) The neutron diffraction analysis reported in section 7.1 and corresponding data reduction was performed by Marie-Hélène Lemée-Cailleau (ILL Grenoble), space group refinement was made by Dr. Lynne Thomas.

(12) The mechanical etching employed for the work in section 7.2 was performed with the aid of Charlie Cummings (University of Bath, Chemistry Department).

(13) The Raman analyses in section 7.2 were performed by Dr. Victor Izquierdo-Roca and Prof. Alejandro Perez-Rodriguez (IREC Barcelona).

(14) The PL analyses in section 7.3 were performed by Rabie Djemour and Dr. Levent Gütay (Luxembourg University).

Foreword

The structure of this thesis is designed as to strongly reflect the different studies carried out during the course of the PhD. As the reader will soon realise, this is the most convenient way of rationalise the work, since it gives the proper weight into the two main research areas investigated, each of which is given a distinct part: A and B.

A general, concise, introductory section is given to initiate the reader to the world of photovoltaics with an easy and updated literature review of the current scenario of this technology in the global context. Section 1.2 of the introduction will give the essential information concerning the role of semiconductors in solar cell devices, with focus on thin-film PV, while section 1.3 is devoted to the Photoelectrochemistry of semiconductors. A brief outline of the work and aims is given in section 1.4, which also acts as a junction between parts A and B of the thesis.

1.1	Current scenario of photovoltaics	9
1.2	Semiconductors as photovoltaic components	13
1.3	Photoelectrochemistry of semiconductors	21
1.4	Project outline and aim of this investigation	24

The choice has been made to write an additional introductory chapter for each of the two research aspects dealt within this thesis. These chapters have been placed at the beginning of the two main parts devoted to the experimental work and discussion (A and B). The aim of these two chapters is to give the reader a more detailed description of the two distinct but linked research topics.

Introduction to part A: major debates on the absorber layer formation 31

Introduction to part B: fundamental matters seeking solutions 151

Each part ends with a concluding section where summaries of the lessons learned during the PhD, and outlines of recommendation for future work are given.

Concluding remarks for part A 143

Concluding remarks for part B 225

Abstract

The synthesis of morphologically good thin chalcogenide films via the two-stage route is a chemical challenge. The reactivity towards the chalcogen-bearing reactants of the different metals within the precursor film is a trade-off between thermodynamic driving force and kinetics of binary sulfide formation.

In this work, $CuSbS_2$ and Cu_3BiS_3 thin films were produced by conversion of stacked and co-electroplated metal precursor layers in the presence of elemental sulfur vapour. Ex-situ XRD and SEM/EDS analyses of RTP treated samples were employed to study the reaction sequence and create ‘‘Time-Temperature-Reaction’’ diagrams for the description of the reaction kinetics. Modified Pilling–Bedworth coefficients were introduced for the interpretation of the experimental results.

The chalcogenizing conditions have a strong influence on the following aspects:
(1) Extent of intermediate phase segregation and/or crystallite size
(2) Thermodynamic (de)stabilization at low temperature
(3) Thermodynamic (de)stabilization at high temperature
The design of a successful synthetic route needs consideration of all these points, so that tailored choices of precursor film configuration and profiles of temperature and reactant partial pressure are made.

The synthesis of single crystals of the system Cu-Zn-Sn-S via the Chemical Vapour Transport (CVT) with iodine was investigated. Current knowledge of CVT in multinary systems is limited. A computation of the thermochemistry of the system was performed with the intent to estimate the risk for compositionally incongruent mass transport.

Experimental studies reveal no meaningful effect of the iodine pressure employed on the composition of the CZTS products. However, samples obtained under different I_2 pressure showed different morphology and had slightly different unit cell sizes.

Longitudinally isothermal treatments were carried out with the intent to form large size crystals. Under the investigated conditions, the experiments resulted in the formation of crystals with 2D predominance. A possible explanation for this phenomenon is proposed, based on considerations of the vessel’s thermal conductivity and decomposition/crystallization rate at the steady-state equilibrium.

1. Introduction

1.1 Current scenario of photovoltaics

The economic recovery of the OECD countries from the 2008-2010 recession has, so far, been slower than from previous global downturns [5]. Nevertheless, for many emerging countries such as China, India and Brazil the growth rates are expected to remain very high [6]. The U.S. Energy Information Administration has translated these figures into an increase of the global primary power demand from the current 17 to nearly 26 TW by 2035 [7]. Currently, the main part of this energy demand ~83% is supplied by fossil fuels, with a share of ~34% from oil, ~26% from coal and ~21% from natural gas, while approximately 6% is provided by nuclear plants [7]. The geopolitical and environmental issues associated to such provision in the long term are apparent [8-10].

Humankind is ethically committed to find sustainable solutions to ensure that future growth will occur in equity and wealth. Every sector of society should contribute in order to meet this noble objective. The scientific community cannot feel exempted from undertaking all the efforts aimed at discovering and understanding Nature. The word Physics comes from the Ancient Greek φύσις for Nature. Nature is the best place where solutions can be found and the Physical Sciences give us the tools to uncover them. Our duty is to use these tools, so that we can make the most intelligent use of the resources that Nature has set aside for us.

Alexandre-Edmond Bequerel is often referred to as the father of solar cells. His experiments published in 1839 [11] are the first documented evidence of the interaction between semiconductors and solar radiation. Although indirectly, his works constitute the basis for the discovery of the photovoltaic (PV) effect, the principle upon which the PV technology is based. In a solar cell device, the energy of sunlight is directly converted into electricity due to absorption of photons by semiconductors. Electrons are excited in the semiconductor and promoted to higher energy states. The subsequent charge separation allows the formation of a voltage, and a power can be extracted by letting electrical current pass through external circuits (ref. section 1.2).

Solar photovoltaics (PV) is currently the world's fastest growing power-generation technology [12], although it provides the smallest contribution (after biofuels) to the primary energy production (0.2%) [13].

From the PhotoVoltaic Geographical Information System database [14] it can be estimated that the land area required to satisfy the global primary energy demand with hypothetical solar modules of 14% efficiency installed in remote locations, like deserts, where the solar irradiance is higher than 2200 kWh/m^{2}y, corresponds to a square of ~ 660 km on each side. Fig. 1 shows how the Earth's surface would look with a hypothetical distribution of solar plants.

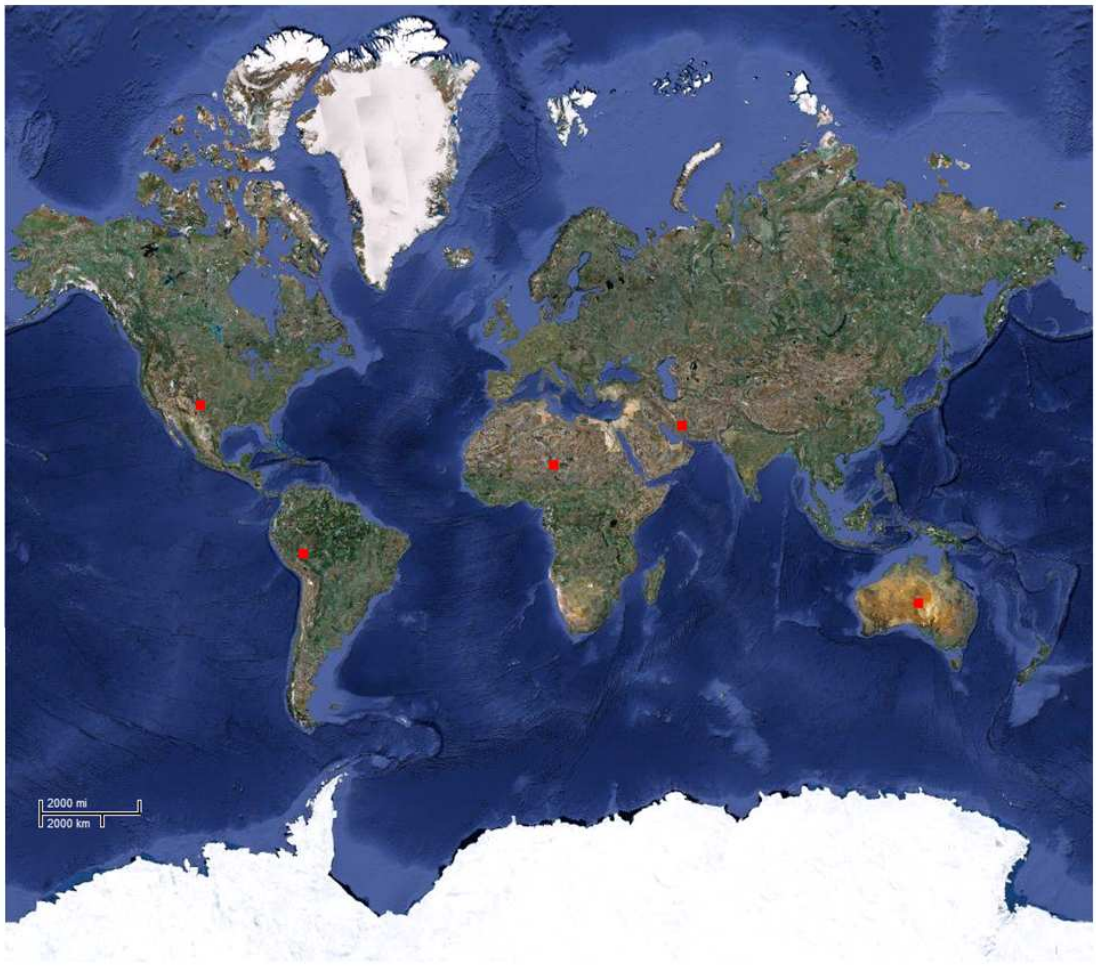

Fig. 1.1.1 Hypothetical distribution on the Earth's surface of 14% efficient solar modules that would be required to supply the current global primary energy demand.

Although projects involving huge remote solar power stations are being considered seriously [15], the technological and geopolitical issues that they would create are remarkable. With the current systems of electricity distribution, a more scattered location of the plants seems more plausible.

It must be highlighted that, in order to ensure continuity of power from an irregular source of energy, the given figure is an underestimate, unless storage technology makes substantial progress in the future [16].

The general consensus on PV in 2005 can be summarised by this sentence. “The major challenge in PV technology is to strongly reduce the cost/watt of delivered solar electricity by a factor of 5-10 to compete with fossil electricity and by a factor of 25-50 to compete with primary fossil energy” [17, 18]. There are several different PV technologies, but for a detailed treatment the interested reader is referred to more comprehensive sources [19].Currently, the PV market is dominated by silicon-based technologies, but due to their high purification costs and high material utilization, it seems likely that alternative technologies based on so-called “thin films” will receive increasing attention in the near future. The chief target of this alternative technology, often referred to as II generation, is to reduce the costs by replacing the thick silicon wafers with thinner inorganic compound semiconductors that can be deposited using less energy-intensive techniques. Progress in this field is bringing down the costs considerably, with a steady increase of the module efficiency and improvements of the fabrication routes. However, due to the scale effect, the generational overtake will be possible only if the efforts directed towards the thin film technology will not be dwarfed by those absorbed by silicon.

We can now define a number that estimates the sustainability for any PV system; the most important is called energy payback time (EPBT). EPBT is given by the total energy required for fabrication, deployment and recycling of a photovoltaic system divided by the yearly primary energy that is saved using the system. In some cases EPBT is now set below one year [20, 21]. Nevertheless, it soon becomes clear that this scenario still presents real challenges for humankind.

The two main light-harvesting materials currently employed in thin-film solar cells are: $CuIn_xGa_{1-x}Se_2$ and CdTe [22]. Unfortunately there are serious availability and/or toxicity issues related to the extensive use of elements such as In, Ga, Se, Cd and Te [23-26]. For example, from a quick calculation it can be demonstrated that if the whole economically exploitable world reserves of Te were to be employed for the fabrication of 20% efficient CdTe modules (to be placed in locations such as the south of Spain where the yearly average insolation is about 2000 kWh m^{-2} y^{-2}), the so obtained energy production would be below 1% of the current primary energy demand. Furthermore, at the current rate of Te extraction ($5 \cdot 10^2$ $t \cdot y^{-1}$), it would take about 6500 years for this figure to be reached. It must be highlighted that these considerations are based on the world resources reported by the U.S. Geological Survey [23]. As such, the potential contributions of urban mining (especially for the

case of indium) and other sources currently unexplored (for which data are not available) are ignored.

Clearly, the limitations arising from the scarcity of these resources necessitate a careful selection of candidate replacement materials. This selection should be based on the principle of sustainability [27]. Such aspects constitute the aim of this work and are treated in more detail in section 1.3.

1.2 Semiconductors as photovoltaic components

Semiconductors suitable for utilisation as absorber layers in inorganic thin-film solar cells are the subject of this research project. As mentioned in section 1.1, the main advantage of the second generation PV technology is that, compared to silicon, about 100 times less material is required to completely absorb the sunlight. This is possible because of a substantial difference in the electronic structure of silicon and the competitor inorganic compounds, that brings about an evolution with light trapping. The electronic properties of non-molecular solid materials are well described by the *band theory*. Let us consider the formation of lattices of solids starting from isolated atoms in vacuum; when these atoms come close, their atomic orbitals start to interact in a similar way as in the *Linear Combination of Atomic Orbitals*, the model that is used explain the formation and stability of molecules. The only difference is in the number of these interactions. Due to the formation of a semi-infinite three-dimensional arrays of atoms, a huge number of interactions take place and consequently the electronic states in the new "lattice orbitals" are no longer separated by energy gaps, as in the molecular orbitals but form a continuum of energy [28]. Filled bonding orbitals form *valence bands* while empty antibonding orbitals form *conduction bands*. These bands are energetically separated by a region of forbidden states called the energy band-gap with magnitude *Eg*. Silicon is a so-called *indirect* band-gap material; electrons can be excited from its valence band to its conduction band only if absorption of a suitable photon is accompanied by the absorption of a phonon. In *direct* band-gap semiconductors there is no such requirement, and absorption of photons with energy exceeding the band-gap results in the excitation of electrons. In these materials the oscillator strength of the optical transition is much higher. For example the absorption coefficients of Si (indirect band-gap) and CdTe/CIGS (direct band-gaps) are approximately 10^2 and 10^4 cm^{-1} near the respective band edges. This translates into a much different thickness required for harvesting e.g. 90% of the radiation in the two cases: ~ 230 μm for Si and 2.3 μm for CdTe and CIGS, respectively.

Electrons in the CB and holes in the VB can also be introduced artificially by doping the semiconductor respectively with *donors* or *acceptors*. In intrinsic semiconductors, like pure silicon, positive-type (*p*-type) character can be obtained by replacing some of the group IV atoms with atoms of the group III, while negative-

type (*n*-type) are obtained with atoms of the group V instead. However, compounds semiconductors such as CdS, CdTe and $CuIn_xGa_{1-x}Se_2$ exhibit naturally occurring extrinsic properties, i.e. there are defects such as vacancies, interstitials and/or antisites that correspond to the formation of donors or acceptors. Acceptors in the lattice of an intrinsic semiconductor create isolated empty energy states just above the valence band maximum (VBM); electrons from the VB are thermally excited to these states and immobilized, leaving behind an equal number of mobile electron vacancies (holes) in the VB. In a similar way, donors create isolated filled energy states just below the conduction band minimum (CBM); these electrons are thermally excited to the CB, leaving behind them an equal number of ionized donors.

Electrons are *fermions*, i.e. particles with a non-integral spin quantum number that follow the *Fermi-Dirac* statistics. The occupation of the states satisfies the *Pauli exclusion principle* for which only one particle can occupy the same quantum state. The *Fermi-Dirac distribution* (*F(E)*) that minimizes the free energy of the system is a function of the absolute temperature *T* and of the band-gap energy (Eq. 1.2.1).

Eq. 1.2.1 $f_e(\varepsilon_e) = 1/(\exp((\varepsilon_e-\varepsilon_f)/k_BT)+1)$

where k_B is the Boltzmann constant, ε_e is the electron energy and ε_f is the *Fermi energy*, defined as the energy at which the probability to find an electron is 50%.

The density of free electrons in *n*-type, and of free holes in *p*-type semiconductors $n_{e,h}$ is given by Eq. 1.2.2.

Eq. 1.2.2 $n_{e,h} = N_{C,V} \cdot f_e(\varepsilon_e)$

where $N_{C,V}$ are constants called effective densities of states in conduction and valence bands. According to Eq. 1.2.2, the electron and hole densities vary exponentially with the position of the Fermi level in the band-gap. The position of the Fermi level depends on the doping density and for a *p*-type semiconductor with shallow acceptors is given by Eq. 1.2.3.

Eq. 1.2.3 $\varepsilon_f \sim \varepsilon_V - k_BT \cdot \ln(N_V/n_h)$

where ε_V is the energy level of the valence band maximum.

Holes in *p*-type and electrons in *n*-type semiconductors are called majority carriers, because they are free to move due to the fact that they lie in energetic bands with continuum of energy, where free energy states are available.

The energy distribution of electrons and holes in a semiconductor can always be expressed by two separate functions. The concept of quasi-Fermi energy is particularly convenient for the description of the semiconductors physics under illumination. Upon irradiation, carrier densities are greater than in the dark. Therefore, the Fermi energies of electrons (ε_{fC}) and holes (ε_{fV}) diverge and are closer respectively to the conduction (ε_C) and valence band (ε_V) than in the dark. This situation is exemplified considering the electron and hole density functions described by Eq. 1.2.4 and 1.2.5.

Eq. 1.2.4 $n_e = N_C \cdot \exp(-(\varepsilon_C - \varepsilon_{fC})/k_B T)$

Eq. 1.2.5 $n_e = N_V \cdot \exp(-(\varepsilon_{fV} - \varepsilon_V)/k_B T)$

As in any other system, the total energy of electrons (and holes) in a semiconductor can be expressed by a sum of terms. As far as we are concerned, this sum for electrons corresponds to the expression in Eq. 1.2.6.

Eq. 1.2.6 $E_e = TS_e - p_e V_e + \mu_e N_e + \varphi N_e = TS_e - p_e V_e + \eta_e N_e$

where E_e is the total energy of the electrons, TS_e is the entropic energy, $p_e V_e$ is the compressional energy, $\mu_e N_e$ is the chemical energy and φN_e is the electrical energy. The term η_e is also known as the electrochemical potential of the electrons. The same procedure (Eq. 1.2.6) can be applied to holes, with analogous results. For electrons and holes in electrochemical equilibrium, $\eta_{e,h}$ is uniform within the device. It can be demonstrated [29] that $\eta_e = \varepsilon_{fC}$ and $\eta_h = \varepsilon_{fV}$.

When *p* and *n*-type semiconductors are joined together a *p-n junction* is formed. This is the core of solar cells. At the interface between the two solids in the dark, the free electrons in the *n* side are tempted to diffuse towards the *p* side, in order to fill the holes in the VB, and by doing so they leave behind an equal number of fixed positive charges. Similarly the holes tend to flow from the *p* to the *n* side, leaving an equal number of fixed negative charges in the *p*-type semiconductor. This process terminates when equilibrium between the internal electric field and the chemical

potential of electrons and holes is reached, i.e. when the electrochemical potential of electrons and holes is uniform across the junction. In such conditions the gradient of the electrical energy is compensated by the gradient of the chemical energy. Therefore, the Fermi energy of electrons and holes is equal in the two sides of the junction, electrons and holes do not experience any forces and their random motion does not provide any net current flow. The creation of a space charge region results in the formation of a band bending, as illustrated by Fig. 1.2.1a.

Thin-film PV is based on *p-n heterojunctions*, where the *p* and the *n*-type materials are not based on the same (differently doped) semiconductor as in the Si based devices, but are distinct semiconductors, e.g. *p*-type CdTe and *n*-type CdS.

When light shines on a *p-n* junction, photons with energy higher than the band-gap energy of the semiconductors are absorbed and electron-hole pairs are generated on both sides of the junction. This creates a gradient of the quasi-Fermi levels of electrons and holes across the junction, as shown in Fig. 1.2.1b. The excited electrons from the *p* side and the holes from the *n* side diffuse towards the junction driven by the gradient of electrochemical potential. Under illumination, carriers with opposite charge are separated and a voltage is observed.

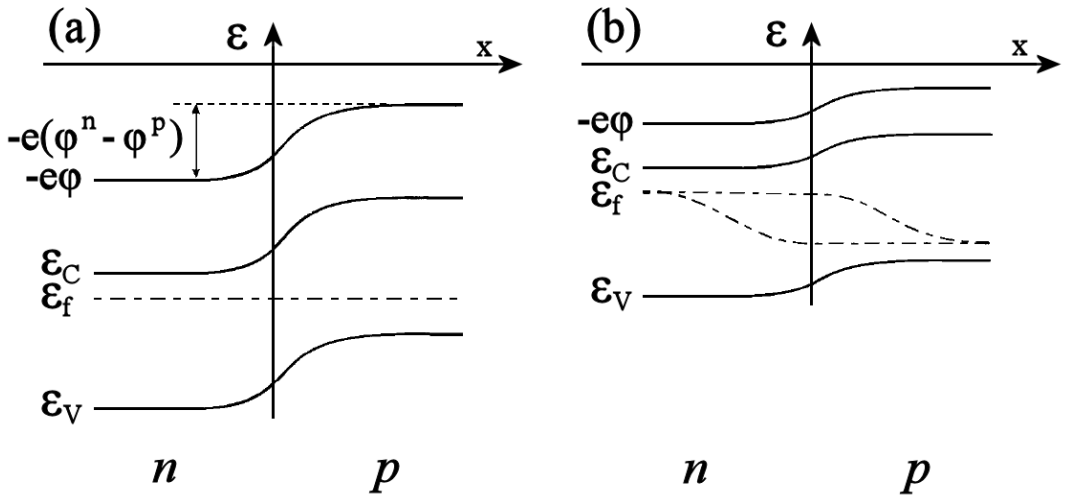

Fig. 1.2.1 *p-n* junction under dark (a) and under illumination (b) [29].

If the two sides of the junction are connected with an external circuit, an electrical current will flow (conventionally from the *n* to the *p* side). This current can deliver a free energy equal to the energy difference between the quasi-Fermi levels on the two sides of the junction per electron-hole pair.

Depending on the load applied to the circuit, the measured current will pass from a maximum (in closed circuit conditions) to zero. The so-called *JV curve* shown in Fig. 1.2.2, illustrates the electrical behaviour of an ideal *p-n* junction in the dark and under illumination.

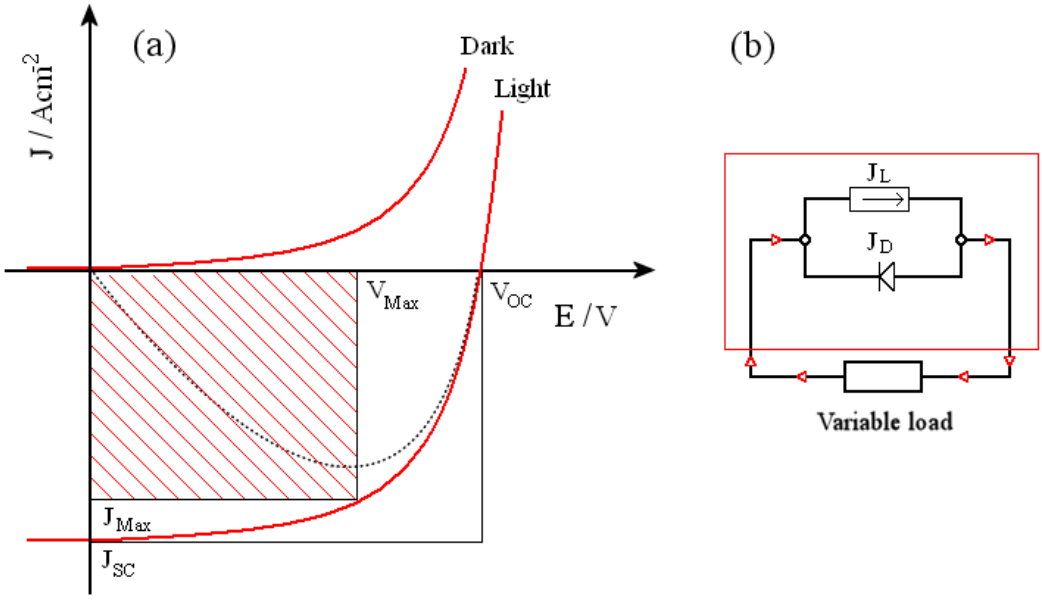

Fig. 1.2.2 J-V characteristics of an ideal p-n junction in the dark and under illumination. The dotted line represents the product J·V with its minimum corresponding to the maximum power (a). Equivalent electrical circuit (b).

In order to analyse the properties of a solar cell, an *equivalent circuit* made of standard electronic components can be drawn and used as a model (Fig. 1.2.2b) [30]. A range of fundamental properties of the solar cell can be obtained from the analysis of its JV curve. Let us have a look at the equivalent circuit. A simple current generator represents the photoactive material which provides the photocurrent density J_L, an ideal diode represents the rectifying junction, while an external load is added representing a generic power user. The output current density J is given by the difference between the photocurrent of the cell under illumination and in the dark, J_L and J_D. The dark current density flowing through a diode is given by Eq. 1.2.1.

Eq. 1.2.7 $J_D = J_0 [e^{qV/kT} - 1]$

where V is the voltage, q the electron charge, T the absolute temperature, k_B the Boltzmann constant and J_0 the diode saturation current. Eq. 1.2.7 shows that the

current flowing through a p-n junction is rectified on the forward bias direction. The photocurrent density J_L is given by Eq. 1.2.8.

Eq. 1.2.8 $J_L = Nq$

where N is the number of photogenerated electrons per unit of illuminated area and q is the electronic charge. The output current density is given by Eq. 1.2.9.

Eq. 1.2.9 $J = Nq - J_0 [e^{qV/nkT} - 1]$

At short circuit conditions the voltage is zero ($V_{SC} = 0$) and $J_{SC} = J_L$. The short-circuit current density is controlled only by the current generation and it is the highest obtainable from the device. At open circuit conditions (i.e. $R = \infty$) the output current density is zero ($J_{OC} = 0$); we can then calculate the voltage V_{OC} (Eq. 1.2.10).

Eq. 1.2.10 $V_{OC} = kT/q \ln(J_L/J_0 + 1)$

This is the highest voltage obtainable from the device. J_0 is proportional to the electron-hole recombination rate, thus V_{OC} is also a measure of the recombination of the device.

The power density produced by the device is given by the product JV. This product is zero both in short and open circuits conditions (dotted line in Fig. 1.2.2a). The maximum electrical power produced by a solar cell occurs when the absolute product J·V is maximised (Fig. 1.2.2a). We can now introduce a parameter called *Fill Factor*, defined as the ratio between the areas depicted in Fig. 1.2.2a (Eq. 1.2.11).

Eq. 1.2.11 $ff = J_{Max} V_{Max} / J_{SC} V_{OC}$

where J_{Max} and V_{Max} are the current density and voltage values at the maximum power point, so that $P_{Max} = ff \cdot J_{SC} V_{OC}$.

The efficiency η of a solar cell is defined as the ratio between the maximum output power of the cell (under AM1.5 radiation at 25 °C, see Appendix 1) and the power of the incident radiation (Eq. 1.2.12).

Eq. 1.2.12 $\eta\% = 100 \cdot (P_{Max}/P) = 100 \cdot (ff \cdot J_{SC} V_{OC}/P)$

In single-junction solar cells, electrons excited by photons with energy greater than Eg rapidly lose the excess energy by thermalization (phonon emission). Furthermore, photons with energy smaller than the band-gap will not be capable of generating any photocurrent, due to the absence of energetic states within the band-gap region. The balance of these two aspects is included in treatments reported by Loferski [31] and Shockley and Queisser [32], and it is shown in Fig. 1.2.3.

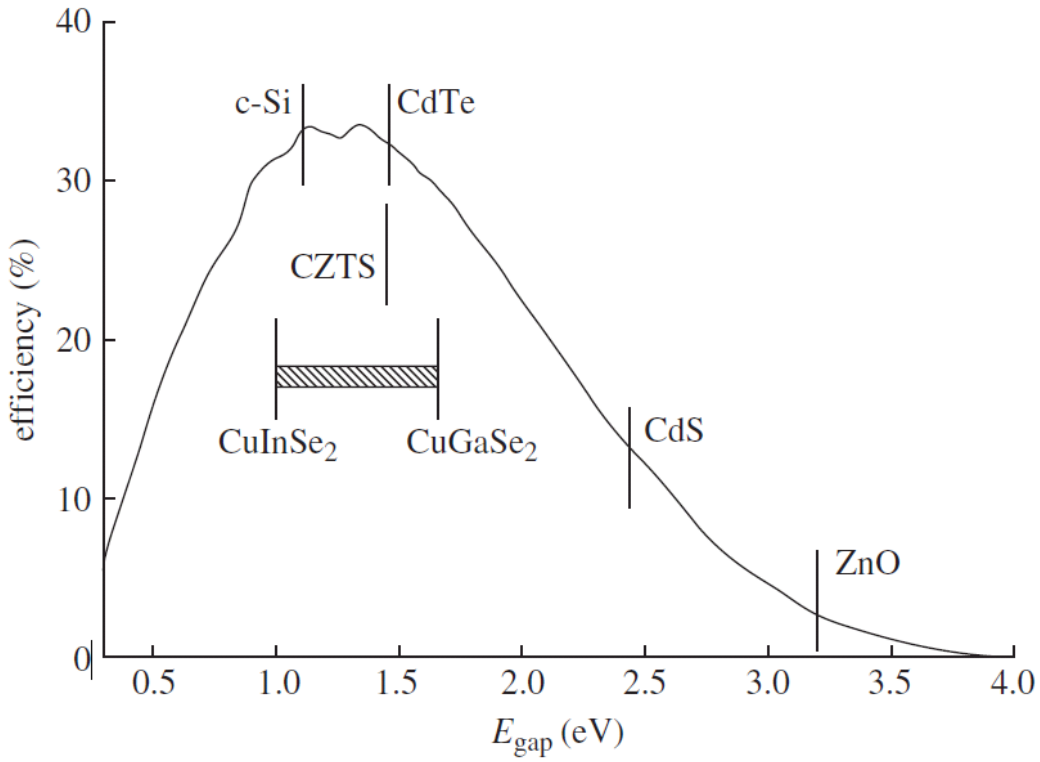

Fig. 1.2.3 Detailed balance efficiency limit for a single-junction solar cell with reported band-gaps of c-Si, CdTe, $CuInSe_2$-$CuGaSe_2$, CZTS, CdS and ZnO [27]. (N.B. there is no relationship between the y-axis and the band-gap values of the semiconductors reported).

The detailed balance limit in Fig. 1.2.3 was calculated for single-junction solar cells based on the AM1.5 solar radiation (the solar radiation attenuated by the Earth's atmosphere corresponding to the solar zenith angle of 48.2 °, 1.5 times the thickness of the Earth's atmosphere normally to the Sun). Details on how this calculation is performed are given in Appendix 1.

Multijunction solar cells are able to exceed the limit in Fig. 1.2.3 by converting different regions of the solar spectrum with a junction tuned to that region.

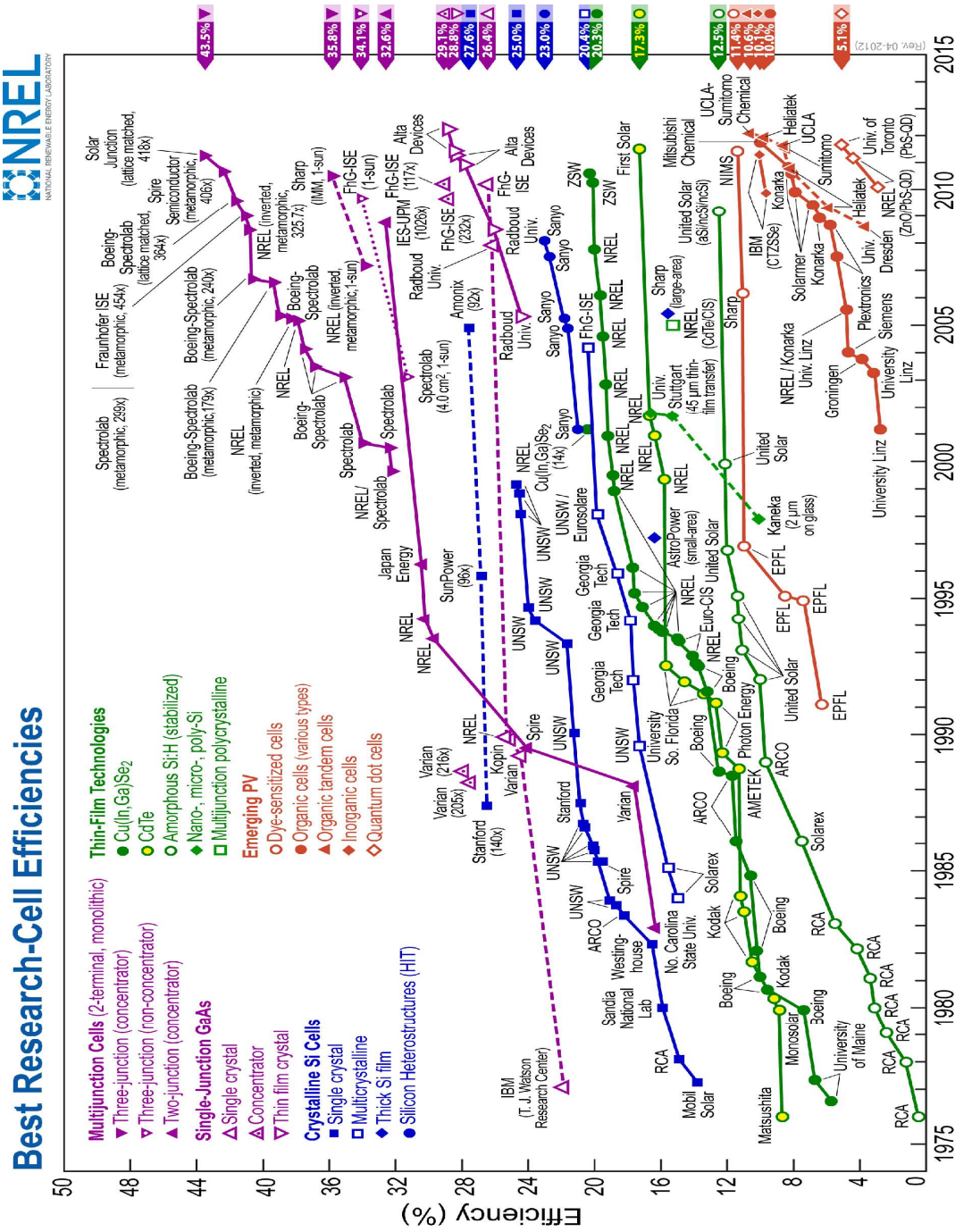

Fig. 1.2.4 History of the worldwide best research solar cell conversion efficiencies for various photovoltaic technologies [18, 33].

Research is also progressing to overcome the efficiency limits imposed by thermalization. The so-called *third generation* solar cells are based on principles such as: intermediate-band structures, thermo-photovoltaic conversion, conversion with hot carriers and multiple electron-hole pair generation. The interested reader is referred to the extensive literature [16, 29].

1.3 Photoelectrochemistry of semiconductors

Redox couples dissolved in liquid solutions are able to create rectifying junctions with semiconductors by creation of semiconductor-electrolyte contacts, similarly to solid state *p-n* junctions.

The electrochemical reduction potential E of electrons in a redox electrolyte is given by the Nernst equation (Eq. 1.3.1).

Eq. 1.3.1 $$E = E° + RT/nF \cdot ln(a_{ox}/a_{red})$$

where $E°$ is the standard half-cell reduction potential, n the number of electrons exchanged in the redox reaction, F is the Faraday constant (~96485 $C \cdot mol^{-1}$) and $a_{ox,red}$ are the activities of oxidised and reduced species of the redox couple in the electrolyte solution.

The standard hydrogen electron scale (SHE) is conventionally employed in electrochemistry to measure and compare the relative reduction potentials of redox couples in aqueous solutions. In order to relate electron energy levels in solids and electrolytes on a common basis, the potential of SHE was estimated on the absolute vacuum scale (Fig. 1.3.1c) [34]. This allows the Fermi levels of redox species to be defined on the same scale as the Fermi levels in semiconductors.

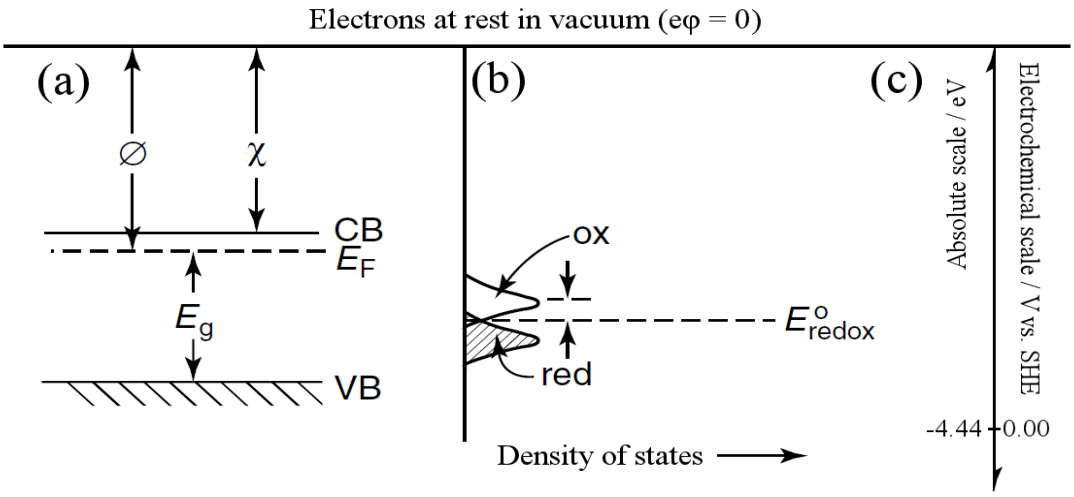

Fig. 1.3.1 Energy levels in a semiconductor (a) and a redox electrolyte (b) (modified from [35]) shown on a common vacuum / standard reduction potential scale (c) (arrows pointing to more positive values) [34]. Ø and χ are the semiconductor work function and electron affinity, respectively.

When semiconductors are immersed in electrolyte solutions (Fig. 1.3.2a), electron transfer takes place at the junction until equilibration of the Fermi levels is achieved. Similarly to the *p*-*n* junction, band bending occurs within the semiconductor phase (Fig. 1.3.2b); while a corresponding Helmholtz layer is produced on the electrolyte side of the junction.

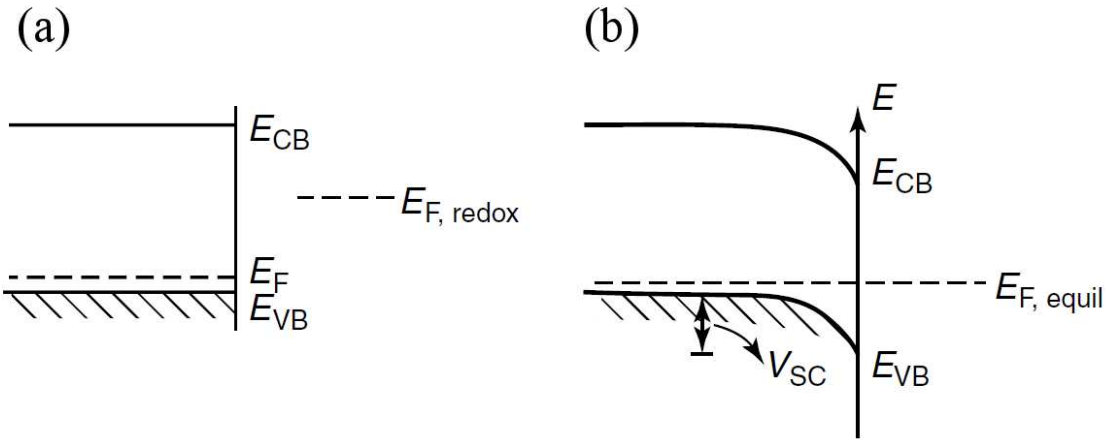

Fig. 1.3.2 Semiconductor-redox electrolyte energy levels before (a) and after (b) formation of the junction by immersion [35].

Provided that no electrochemical reactions involving the semiconductor occur, the extent of the band bending is controlled by the potential applied to the semiconductor electrode. When the band bending exceeds k_BT, the width W of the space charge region is given by Eq. 1.3.2 [36].

Eq. 1.3.2 $$W = [2\varepsilon\varepsilon_0(E_{FB}-E)/(eN_{a,d})]^{1/2}$$

where E is the applied potential, E_{FB} is the flat-band potential (i.e. the potential at which the semiconductor energy bands are not bent), ε is the relative permittivity of the material, ε_0 is the vacuum permittivity, e is the elementary charge and $N_{a,d}$ is the acceptor or donor (doping) density for *p* and *n*-type semiconductors respectively.

In the absence of recombination in the space charge region or at the semiconductor / electrolyte interface, the external photocurrent quantum efficiency Φ (EQE), also known as the incident photon to current efficiency (IPCE) is given by the Gärtner equation (Eq. 1.3.3) [37, 38].

Eq. 1.3.3 $$\Phi = 1- [\exp(-\alpha W) / (1 + \alpha L_{e,h})]$$

where α is the optical absorption coefficient of the material, W is the width of the space charge region and $L_{e,h}$ is the minority carrier diffusion length (electrons for p and holes for n-type semiconductors).

When defects act as recombination centres by trapping minority and majority carriers, the EQE is lower than predicted by Eq. 1.3.3. Under such circumstances, the minority carrier diffusion length, $L_{e,h}$, is negligibly small (i.e. $\alpha L_{e,h} << 1$) and Eq. 1.3.3 reduces to Eq. 1.3.4 [39].

Eq. 1.3.4 $\Phi = 1 - \exp(-\alpha W)$

The dependence of the absorption coefficient of semiconductors on the photon energy and band-gap value is given by Eq. 1.3.5 [40].

Eq. 1.3.5 $\alpha \cdot h\upsilon = A(E-Eg)^n$

where n is an integer number that depends on the nature of band-gap and optical transition: respectively 1/2, 3/2, 2 and 3 for direct, direct forbidden, indirect and indirect forbidden.

The band-gap values of semiconductors may be conveniently estimated from the EQE data measured near the onset region of absorption [38]. By combination of Eqs. 1.3.4 and 1.3.5, plots of $[h\upsilon \cdot \ln(1-\Phi)]^{1/n}$ versus the incident photon energy $h\upsilon$ should give straight lines which intercepts on the x-axis are the band-gap values (Eq. 1.3.6).

Eq. 1.3.6 $[-h\upsilon \cdot \ln(1-\Phi)/(WA)]^{1/n} = E-Eg$

Similarly to the band-gap, the doping density of semiconductors can be extracted from the EQE data. Combination of Eqs. 1.3.2 and 1.3.4 gives Eq. 1.3.7 [41].

Eq. 1.3.7 $[\ln(1-\Phi)]^2 = 2\alpha^2 \varepsilon\varepsilon_0(E_{FB}-E)/(eN_{a,d})$

The acceptor or donor density of the semiconductor can be extracted from the slope of the lines if the values of the flat-band potential E_{FB}, the relative permittivity ε and the optical absorption coefficient of the semiconductor are known.

1.4 Project outline and aim of this work

Section 1.1 showed that the current thin-film solar cells have achieved very good results in terms of efficiencies [42], energy pay-back time and cost/watt, such that we can expect a market overtake over the silicon technology in the foreseeable future. However, it was also highlighted that, due to the scarcity of appropriate minerals, these technologies will only give a very limited contribution to the primary energy demand. Therefore, the need of finding sustainable candidate materials to replace CI(G)S and CdTe is urgent [27].

The current availability and cost of some of the elements relevant to this research, as reported by the U.S. Geological survey, are shown in Fig. 1.4.1.

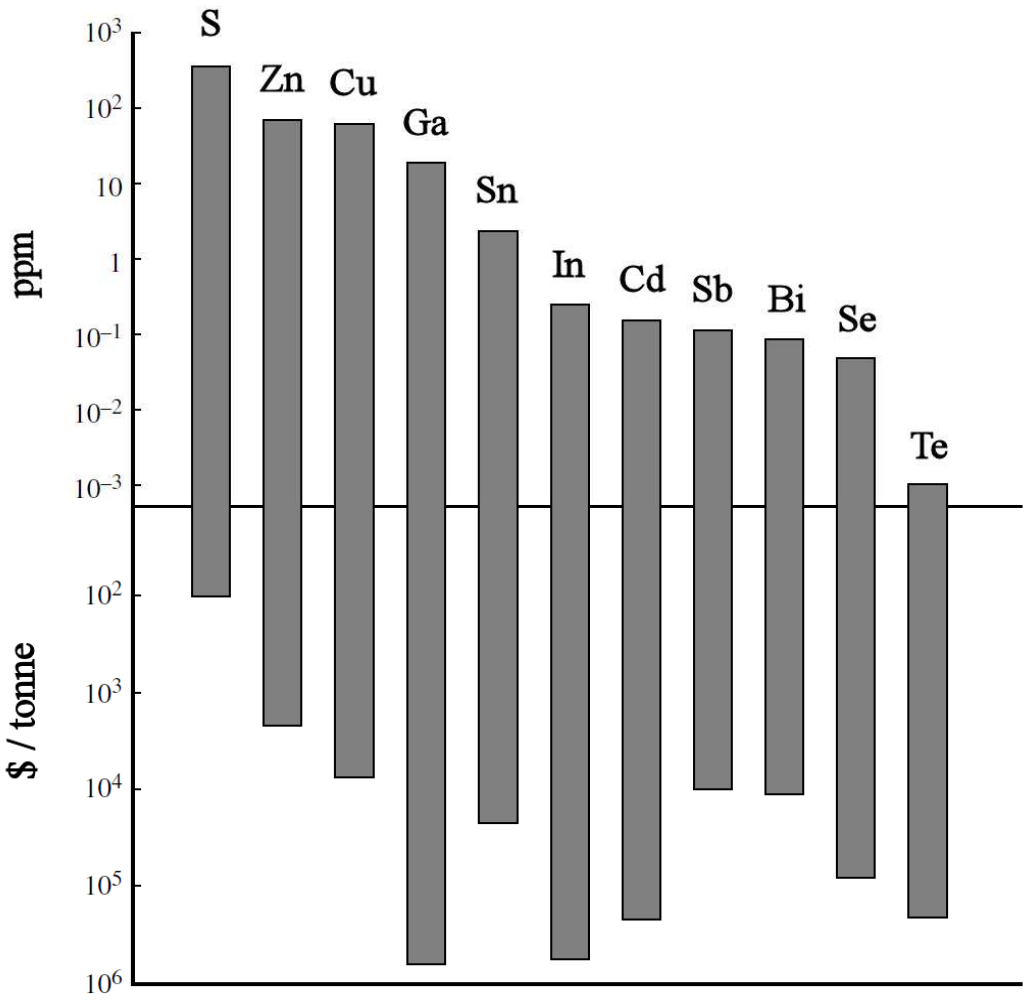

Fig. 1.4.1 Availability on the upper continental Earth's crust and costs of some elements relevant to this research on a double logarithmic scale [23, 27, 43].

An approach that is often followed when it comes to finding alternative materials is the principle of *isoelectronic* or *cross substitution* [44]. Application of this approach to the diamond structure of silicon gives rise to the so-called adamantine family of compounds [45]. Let us show an example of genealogy: starting with silicon as the "ancestor" (group IV), we pass through GaAs (III-V) and CdTe (II-VI), to $CuInSe_2$ (I-III-VI_2) up to Cu_2ZnSnS_4 (I_2-II-IV-VI_4) with virtually no change in the average outer shell electron density. It is not by chance that the first two "descendents" of silicon show semiconductor properties that are suitable for photovoltaic applications. The hope is that the third "progeny" of silicon, i.e. Cu_2ZnSnS_4 (CZTS) or a sulfoselenide solid solution of it, will also show properties that will make it a viable candidate to replace CIGS in thin-film solar cells. In fact, CZTS contains mainly Earth-abundant (Fig. 1.4.1) and environmentally benign elements, and its potential application in this field would be of great benefit [38]. A recent review of the progress on research into CZTS as a PV absorber has been reported by Wang [46].

The suitable properties of CZTS as a potential absorber material for heterojunction thin-film solar cells were first reported by Ito et al. in 1988 [47]. CZTS has *p*-type character, a high absorption coefficient and a band-gap energy of about 1.5 eV that fulfils the requirements for the efficient harvesting of solar radiation (Fig. 1.2.3) [32]. Ito's work was continued a decade later by Nakayama et al. [48], Katagiri et al. [49] and Friedlmeier et al. [50], when the first devices with a maximum measured efficiency of 2.3% were reported. Since then, there has been a steady improvement of the cell efficiencies, resulting from research into a wide range of deposition techniques and conditions [51-57]. The current world record is 10.1%, for a cell with a mixed sulfoselenide obtained via a hydrazine-based solution process [58]. This result highlights the great potential of CZTS(Se) as an alternative material for thin-film technology.

CZTS occurs in nature as the mineral *Kesterite* [59]. Although most of the research on this material is focused on its thin-film properties, there are fundamental aspects that can better be assessed using bulk material or single crystals. These fundamental properties include: crystal [59-71], electronic and defect structures [72-74], phonon frequencies and line widths of Raman active modes [75], extension of the compositional homogeneity range [76].

Synthesis of single crystalline CZTS samples was one of the aims of this research, and the method employed was the Chemical Vapour Transport (CVT) with iodine.

Compositional, structural and electronic analyses of the synthesized CZTS samples were performed, with the intent to uncovering some of the key fundamental properties that still need to be fully understood. Results are reported in part B of this thesis.

There is another class of compounds known as *chalcosalts*, with general formula $A_xB_yC_z$ (where A=Cu, Pb, Ag, Fe, Hg, Zn, V; B=As, Sb, Bi, Ge, Sn V; C=S, Se, Te). An extensive review by Moëlo et al. [77] of the sulfur members of this complex family of inorganic compounds has identified approximately 260 known formulae, most of which occur as natural minerals. Among these minerals, in this thesis attention was placed on the Cu-Sb-S and Cu-Bi-S systems. Fig. 1.4.2 shows the ternary plots of these two systems and the composition of the known binary and ternary compounds.

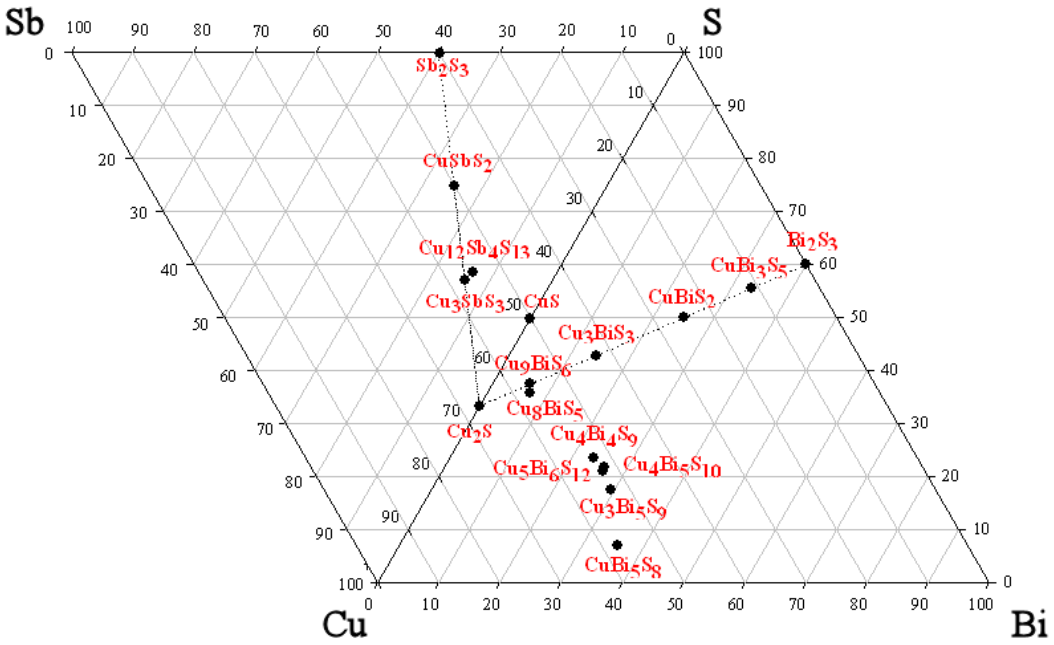

Fig. 1.4.2 Ternary plots reporting the family of known binary and ternary compounds shown by the Cu-Sb-S and Cu-Bi-S systems [78].

The chalcosalts that were chosen for investigation are: *Wittichenite* Cu_3BiS_3 [79], *Emplectite* $CuBiS_2$ [80], *Chalcostibite* $CuSbS_2$ [81] and the isostructural selenide $CuSbSe_2$ [82]. The thin-film literature of these compounds is relatively limited. Nonetheless, their reported semiconductivity and suitable band-gaps are evidence of their promising properties for PV applications [83, 84].

In this work, thin-film syntheses of these compounds with a range of metal precursor deposition techniques followed by chalcogenization were performed, with the aim of assessing their properties for potential applications in PV devices.

Fig. 1.4.1 shows that Sb and Bi, despite having availability similar to In, are almost two orders of magnitude more abundant than Te, besides being much cheaper than both In and Te. The lower cost of Sb and Bi compared to In is a consequence of two different aspects. The world demand for In has risen considerably in the last decade, due to its extensive use in the production of indium tin oxide (ITO) conductive coatings, that find application in flat screens of many consumer products. Secondly, In is obtained mostly as a by-product of Zn refinery in sphalerite ores, and according to the U.S. Geological Survey [23], its current production rate is about 10 and 200 times lower than those of Bi and Sb, respectively. These figures suggest that these two elements have at least a 10-fold higher commercially exploitation potential than In. Therefore, their successful use in PV devices could become of market-driven industrial importance, as it is currently the case for Te in CdTe devices. Considering hypothetical modules with equivalent efficiency, the estimated potential contribution to the primary energy demand would be about 10 times that of CdTe [26]. Due to the availability constraints of Bi and Sb, this would correspond to about 10% of current energy requirements.

Chemical elements of strategic importance have been recently considered by the British Geological Survey [24] for the creation of a “risk list” in which, besides availability, other factors such as location of current production and reserves, and the political stability of those locations, are weighed as to provide an index that highlights the potential supply disruption. According to this list, Sb and Bi are marked at high risk and considered to be even more critical than In, which could call the practical importance of this research into question. Nevertheless, it is hoped that the scientific significance and consequences of this work will still find some useful applications in the research and development of other material systems.

Part A

Quelli che s'innamoran di pratica sanza scienzia
son come 'l nocchier ch'entra in navilio senza timone o bussola,
che mai ha certezza dove si vada.

Leonardo da Vinci

Introduction to part A: major debates on absorber layer formation

This section introduces the experimental work carried out on $CuSbS(Se)_2$ and Cu_3BiS_3 and, more generally, it highlights the major challenges associated with the thin-film synthesis via the two-step route that has been followed in this research. This route dates back to the 1980s [85-87] and is based on the deposition of either a homogeneous or a stacked metal thin-film containing the elements of interest, followed by a thermal treatment performed in a reactive atmosphere of chalcogen or chalcogen precursor. Ideally, the thin-film metal precursor incorporates the chalcogen during the thermal treatment, and a uniform crystalline film of the desired chalcogenide compound is formed. The annealing temperature employed, typically ranging between 400 and 600 °C, plays a crucial role in the process. Due to the thermal energy made available, activation barriers to diffusion are overcome, and the most stable compounds are likely to emerge from the mixtures of possible products.

The challenging philosophy of the two-step process is to match the good results typical of the vacuum-based processes, with lower production costs. This aspect becomes very interesting if the precursor deposition is performed with high throughput and highly scalable techniques such as electrodeposition [88] or screen printing [89]. Electroplating of metal films is a well established industry, thus making this procedure a good candidate for large area mass production, although the subsequent annealing step required for the semiconductor formation presents some technological challenges. In the recent past, successful electroplating routes have been reported for CdTe [90, 91] and CIS thin-film PV devices with efficiencies up to 13.4% [92, 93].

Having seen the high efficiency and reliability of CIGS solar cells [42, 94-96] and the structural similarity of this compound to CZTS [67], the general attitude in the literature has so far tried to achieve the same results by transferring the expertise from the former to the latter. Let us first compare the two cases and see what makes CIGS such a good-performing semiconductor for thin-film solar cells.

The relative success of the two-step route for the synthesis of device quality CIGS is demonstrated by literature efficiencies up to 16% [97-101].

It is known that the best grain size qualities are attained with Cu-rich precursors [102-106], possibly due to a liquid phase assisted growth mechanism, and a similar

behaviour was also reported for CZTSe [107]. To date, Cu-poor $Cu(In,Ga)Se_2$ (22-24 at% Cu) has been the key for high CIGSSe device efficiency [108], while Cu-rich precursors are preferred for $Cu(In,Ga)S_2$ [52]. Recent findings [109, 110] indicate that, due to a widening of the Fermi level splitting, CIS grown under Cu-rich conditions shows promise for higher open circuit voltage, but this potential is hindered by increased recombination losses at the CdS/CIS interface. Due to Cu_xSe phase separation [111], it is known that the highest achievable Cu/(III) ratio corresponds to the stoichiometric composition ($CuInSe_2$), even under Cu-rich growth conditions, while deviation up to a few percent towards the In-rich side is tolerated. It is common practice to remove the excess Cu_xSe and Cu_xS phases that segregate at the surface of the CIGS films via selective KCN etching [112, 113]. Cu-poor conditions are also preferred for the growth of CZTS [114].

The different behaviour of these compounds as a function of the off-stoichiometry can be explained on the basis of the intrinsic defects within the bulk of the materials. Computational studies are a valuable tool to investigate the defect physics that is the source of *p*-type conductivity and composition-dependent performance variation. Density functional theory calculations by Zhang et al. [115] explained the *p*-type conductivity of $CuInSe_2$ on the basis of a shallow acceptor energy level attributed to copper vacancy formation. Furthermore, it was shown that partial passivation of defects by the formation of ordered defect clusters (ODC) has a benign effect on the electrical properties of CIS, because it results in a surface layer with wider band-gap that enhances electron-hole separation [116, 117].

Similar DFT calculations have been performed on CZTS by Chen et al. [118]. Their work points towards Cu_{Zn} antisite defects as the source of *p*-type conductivity, while ODCs have less beneficial effects on charge separation than for CIS. However, in agreement with experimental evidence [114], the growth from Cu-poor and Zn-rich compositions give the optimal CZTS device performance. The reasons for the better performance of selenides compared to the sulfides [119] may be partially attributed to effective charge carrier masses smaller in CZTSe and CISe compared to CZTS and CIS, according to Persson [120, 121], and to the resulting higher mobility.

CIGS presents an exceptional tolerance to defects arising from grain boundaries [122], surfaces [123] and impurities [124]. Furthermore, conversely to Cu_2S solar cells [125], Cu ionic mobility represents an advantage rather than a drawback, due to its self-healing quality [126].

The preparation of a compact single-phase thin-film compound containing four/five elements (Cu, In, Ga, S and Se or Cu, Zn, Sn and S/Se) is unquestionably a chemical challenge [127]. However, the role of secondary phase formation during re-crystallization of CISe electrodeposited films has been reported to be beneficial for the enhancement of the crystalline properties [128]. Conversely, the detrimental effect of secondary phases in the formation of a compact single-phase CZTS is a well known issue [52, 129-132]. In addition, the homogeneity range of CZTS is narrower compared to CIS [133, 134], and therefore secondary phase formation is harder to avoid. This problem is exacerbated by the two-stage synthesis route, because the fourth/fifth element (S, Se) is introduced at a second stage from the gaseous phase. As a consequence, the morphology of the CZTS layer depends strongly on the order of deposition of the three metal precursor layers and this, in turn, affects the device performance as first reported by Araki et al. [135]. Recent findings suggest that grain boundaries have the same enhancing effects on the minority carrier collection in CZTS and CIGS [136]. Nevertheless, the record efficiency for a CZTS device obtained by the electrodeposition sulfurization route is currently 7.3 % [137], which is around half of the best values reported for $Cu(In,Ga)(S,Se)_2$ [113, 138, 139].

Given the 30+ years of R&D in CIGS, the "copy and paste" exercise transferred to CZTS has been of great help at the early stages of CZTS development. However, it is becoming increasingly clear that this approach lacks a thorough chemical basis. Indeed, a careful examination of the thermodynamic and kinetic aspects of chalcogenization is required to successfully adapt its application to CZTS.

The potential effects of secondary phases on the properties of solar cells are briefly highlighted here. Fig. 1A.1 shows a representation of a thin film device in the so-called *substrate configuration*, in which the presence of secondary phases in four different locations and their effect on the device performance are illustrated schematically. An equivalent electric circuit that models the effects of some defects is also shown (cfr. section 1.2). Depending on where the secondary phase segregates and on its electrical properties, a range of detrimental effects can be expected. In case (a) the phase is located between the columnar grains of the absorber material, and, if conductive, it decreases the parallel resistance of the equivalent circuit, leading to *shunting*, i.e. to parasitic current paths. An example of this behaviour is given by $Cu_{2-x}Se$ and other nanoscopic phases in CIGS devices [140, 141]. In case (b) the phase is located at the back contact. If it is insulating it acts as a series resistance in the device, as is probably the case for MoS_2 at the CZTS/Mo interface [142]. In case

(c) the phase is located between the absorber and the window layer, where the heterojunction is formed. This is the heart of the solar cell, and a decrease of the open circuit voltage and short circuit current are likely to occur due to formation of barriers for the charge carriers, as it was shown for ZnS in CZTS devices [143]. In case (d) the phase is located in the bulk of the absorber layer. It is possible that these defects could act as recombination centres, leading to a decrease of the short circuit current density and open circuit voltage [56].

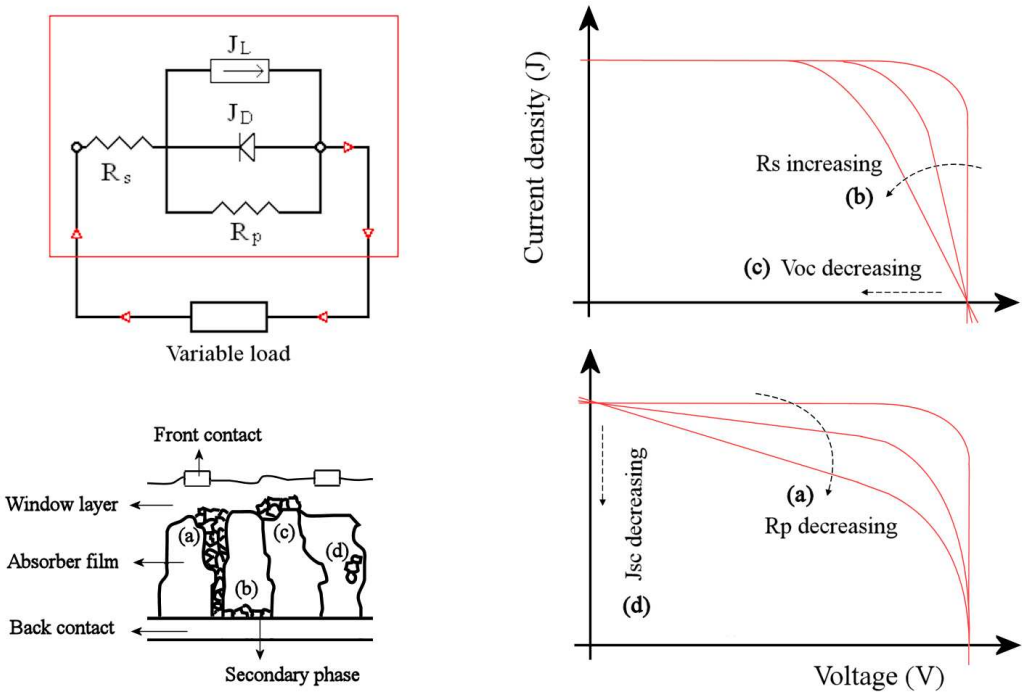

Fig. 1.A.1 Schematic representation of four possible secondary phase segregations and their effects on the thin-film device performance. Equivalent electric circuit employed to model the defects (cfr. section 1.2). Modified from [144, 145].

As far as the device efficiency is concerned, the ratio R_s/R_p needs to be minimised. This can only be achieved if segregation of the detrimental secondary phases is reduced [64-67].

Secondary phase formation is often unavoidable even in simpler systems such as Cu-Sb-S(Se) and Cu-Bi-S, especially if the chalcogen is introduced at a second stage. Issues concerning the formation of compact layer morphologies in these two cases have been reported [41, 146-148] and are included in chapter 2 and 3. In general the sulfurization conditions need to be carefully designed so as to suit the

thermodynamic requirements and the kinetics of the elemental systems that concern the compound of interest. This lesson constitutes the basis of section 4.3.

A detailed investigation of the effects of annealing temperature on the crystalline properties of $CuIn(S,Se)_2$ thin-films obtained by an electrodeposition/ sulfurization route has been reported by Izquierdo-Roca et al. [149]. With increasing temperature, they observed sharpening of the Raman spectra that they attributed to the decreasing density of crystalline defects. This behaviour was not detectable with conventional XRD structural investigation, because of the superior sensitivity of Raman spectroscopy to the local ordering in crystal lattices [150]. The achievement of single-phase absorber layers with supposedly good crystalline quality is necessary, but it may not be enough for high performance devices. These defects act as recombination centres in the space charge region of the devices, and are the cause of reported reductions of the open circuit voltage [151]. The effect of the sulfurization temperature on CIS device performance relates very well to the microcrystalline features assessed through Raman scattering [151]. This highlights the second, very important effect of the thermal treatment, besides the chalcogen incorporation. Device quality semiconductor properties can only be attained if such *Raman-visible* defects are reduced.

Thermal energy is required to decrease the level of defects arising from the chemistry of growth and improve the bulk properties of the absorber layers obtained after cooling. At high temperatures, thermodynamic effects dominate, meaning that the most stable phases are likely to form, compositional uniformity is achieved, and any structural tensions are relieved. As a rule of thumb, the higher the temperature the more effective the annealing treatment is. However, limits are imposed by the possible occurrence of decomposition reactions and the potentially irreversible formation of defects such as chalcogen vacancies [126, 152, 153]. The first of these two aspects is of particular interest, because it relates to the partial or complete destruction of the absorber compound involving the formation of secondary phases that may remain and harm the device properties. Several examples of chalcogenide decomposition during synthetic thermal treatments are reported in the literature. The most recent has been for the Sn losses in CZTS [154], but similar issues have been reported earlier for Sb and Bi during formation of $CuSbS_2$ and Cu_3BiS_3 respectively [146, 155]. An educational review of the key principles that need to be borne in mind when annealing multinary compounds has been reported recently [156].

As we will see in section 4.4, knowledge of the potential decomposition reactions via thermochemical assessment is a valuable basis for designing the control of the annealing processes [157]. The equilibrium thermochemical approach applicable to the bulk studies can only be partially transferred to the thin film scenario, where the thickness scale is much smaller. In fact, critical thicknesses of the developing precursor phases need to be reached before a fourth phase can start growing [158]. Furthermore, it is no surprise to find thin-film compounds that would be unstable in the bulk form, simply because of the kinetic stabilization gained by the non-equilibrium deposition processes employed [159]. Nevertheless, knowledge of the thermodynamics of the system is important, because it gives a measure of the inherent (in)stability of the compound under study.

2. Formation of $CuSbS_2$ and $CuSbSe_2$ thin films

In this research work the potential of $CuSbS_2$ and $CuSbSe_2$ as thin-film alternative absorber materials to replace CdTe and $CuIn(Ga)(S,Se)_2$ –based photovoltaic devices has been assessed. $CuSbS_2$, also known as the mineral *Chalcostibite*, and its isostructural selenide $CuSbSe_2$ belong to the space group 62 (*Pnma*) and have orthorhombic unit cells containing four formula units [160]. Despite the formula analogy, the structural parallelism of *Chalcopyrite* with *Chalcostibite* is not as strong as with *Kesterite*. In fact, although it has been highlighted that Sb and In have almost the same ionic radius [161], $CuSb(S,Se)_2$ and $CuInS_2$ have markedly different crystal structures, as can be seen from a comparison of the coordination polyhedra [67, 162]. In $CuSb(S,Se)_2$ antimony is coordinated by 5 chalcogen atoms forming square pyramidal $Sb(S,Se)_5$ units, while copper shows a classical tetrahedral coordination (Fig. 2.0).

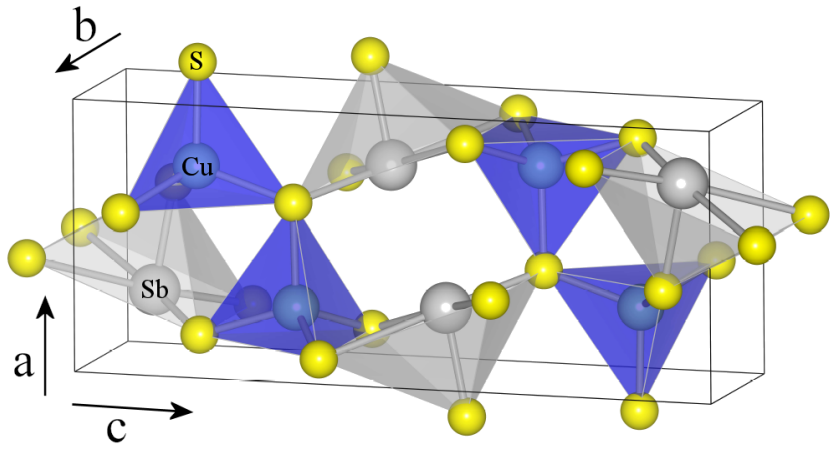

Fig. 2.0 Representation of the unit cell of $CuSbS_2$ showing the coordination polyhedra of Cu and Sb. Drawing produced using VESTA [4].

$CuSbS_2$ appears to be a direct band-gap semiconductor [161]. The band-gap energy of $CuSbS_2$ is reported to be between 1.38 eV [160] and 1.5 eV [83], which is close to the optimum value required for terrestrial solar energy conversion (1.4 eV) [29, 32]. The defect chemistry of $CuSbS_2$ has been explored theoretically by Perniu et al. [163] using lattice reactions combined with electroneutrality conditions and equilibrium constants for each intrinsic defect formation mechanism. Their study suggests that, depending on the defect formation mechanism ionic conduction dominates in the case of deviation from molecularity (incorporation of Cu_2S or

Sb_2S_3), while mixed electronic-ionic conduction is observed if $CuSbS_2$ deviates from stoichiometry. $CuSb(S,Se)_2$ compounds have only partially been explored in the literature [82, 85]. At the start of this PhD, very limited information was available on $CuSbSe_2$. Zhou et al. [160] estimated the band-gap energy of $CuSbSe_2$ crystals obtained from a solvothermal route as 1.05 eV from optical absorption measurements. This figure is in accordance with the decreasing trend of band-gap energy that is generally expected when one or more elements of a compound are replaced with heavier ones [164] (e.g. chalcogen in a generic chalcogenide being replaced by an atom further down the group VI). Soliman et al. [82] studied the temperature dependence of the *p*-type electrical conductivity for thin films of both $CuSbS_2$ and $CuSbSe_2$, but the range investigated (80-500 K) was too low to draw any conclusions concerning the band-gap energies. It is only very recently that an optical measurement of this parameter has been reported for thin-films of $CuSbSe_2$ [165], and the value of 1.10 eV is in agreement with that reported earlier for the bulk [160].

In the literature, thin-films of $CuSbS_2$ have been deposited using a range of techniques such as spray pyrolysis [166], direct evaporation [82, 167], and chemical bath deposition followed by interdiffusion annealing treatment [83, 168]. However, formation of $CuSb(S,Se)_2$ via a simple two-stage process [87], as described in the introduction to part A, has never been attempted. Conversion of co-deposited and stacked electroplated metal precursors followed by conversion into the chalcogenide has proved to give promising results on laboratory scale Cu_2ZnSnS_4 (CZTS)-based devices [55, 56]. Therefore, in this work, a similar procedure was tested for the synthesis of $CuSb(S,Se)_2$ thin-films.

Section 2.1 describes the deposition of Sb/Cu metal precursors both as a homogeneous electroplated alloy mixture and as a sequence of stacked evaporated layers. A different approach also consisted in the conversion of evaporated $CuSbS_2$ films into the corresponding selenide Section 2.2 deals with the heat treatment performed in the presence of the chalcogen vapour, employed to convert the metals or sulfide into polycrystalline thin films of $CuSb(S,Se)_2$. The morphological, compositional and structural properties of the films have been analysed, and the results are reported in sections 2.3 and 2.4. Section 2.5 is dedicated to the photoelectrochemical characterization employed to establish the photoactive properties of the absorber layer materials. The essential experimental details are reported in section 2.6. Part of this chapter is based on published results [146].

2.1 $CuSb(S,Se)_2$ thin film precursor deposition

2.1.1 Evaporation of Sb, Cu, Sb/Cu and $CuSbS_2$ thin films

A conventional evaporator was employed to carry out sequential evaporation of metallic Sb and Cu layers in a stacked configuration, as well as films of plain Sb and plain Cu. The substrates employed were either transparent electrically conductive fluorine-doped SnO_2-coated glass (TEC-8 by Libbey Owens Ford) or soda lime glass microscope slides. The stoichiometric Cu:Sb thickness ratio in the stacked configuration was ensured by loading calibrated amounts of the metals into the crucible. The details are reported in section 2.6.

Films of the plain elements were deposited with the intent to determine the phase evolution of the elemental films separately. This was done in order to discriminate the effect of the Sb/Cu interface in the formation of the desired compounds in precursor films containing both elements. The absolute amount of precursors was adjusted to a thickness of about 1 μm as to allow the growth of 2 μm thick chalcogenide layers after conversion completion.

Thin films of amorphous $CuSbS_2$ were also provided by our colleagues Adel Rabhi and Mounir Kanzari from the Ecole Nationale d'Ingénieurs de Tunis. The deposition procedure consisted of the thermal evaporation of $CuSbS_2$ powder synthesized from the elements in a sealed quartz ampoule, as described elsewhere [161]. The evaporation was carried out onto Mo-coated soda lime glass substrates kept at room temperature. These films served as the precursors for the chalcogen substitution treatment, i.e. the formation of $CuSbSe_2$ or sulfoselenide films via selenization of the sulfide. Their Cu:Sb compositional ratio was estimated at the SEM/EDS as ~ 0.5, in agreement with previous works [167] and with the reported separation of Sb_2S_3 from the films after annealing up to 200 °C [161].

2.1.2 Sb-Cu co-electrodeposition

Thin-metal films containing both Sb and Cu were obtained by co-electrodeposition from aqueous solutions. The substrate employed was radio-frequency (RF) sputtered molybdenum coated soda lime glass prepared by our colleague Guillaume Zoppi

from Northumbria University [169]. The electrolytic cell was in the typical three electrode configuration. The substrate was held as the working electrode (W.E.) in a vertical geometry, the reference electrode (R.E.) employed was Hg/HgO/NaOH 1 M, and Pt foil was used as the counter electrode (C.E.).

Appropriate electrochemical conditions for the 1:1 Cu:Sb "alloy" formation were obtained by systematically studying the effect of consecutive Cu^{2+} or Sb^{3+} salt additions on the composition of the electroplated films. The Cu-Sb phase diagram is rather complex with up to 8 between known phases and intermetallic compounds. Different phase notations can be found in the literature, and their homogeneity compositional ranges are still debated [170-175]. Fig. 2.1.1shows the Cu-Sb phase diagram, as reported by Massalski et al. [176].

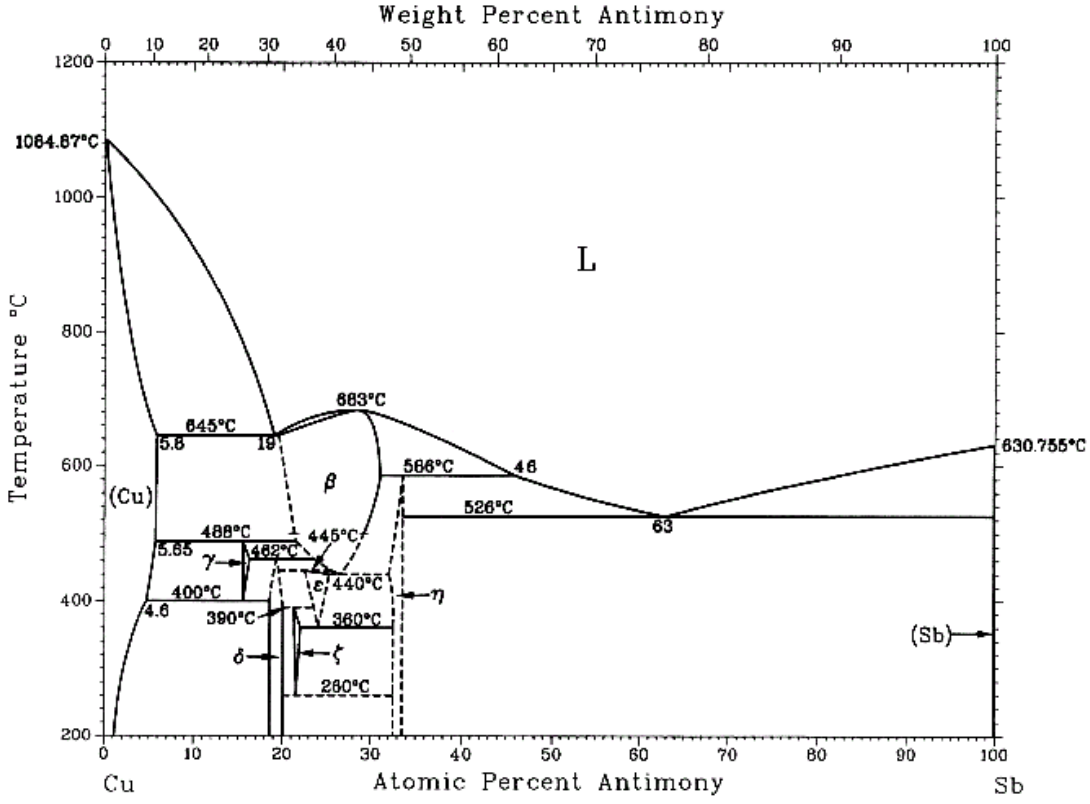

Fig. 2.1.1 Cu-Sb phase diagram as reported by Massalski et al. [176]. (η ~Cu_2Sb).

It is obvious from Fig. 2.1.1 that the formation of an alloy with composition Cu:Sb = 1:1 is impossible under equilibrium conditions. However, it is known that electrodeposition allows the formation of metastable structures that may be considerably different from those obtained by metallurgical processing [177, 178].

Sometimes large deviations from the equilibrium solubility ranges are achievable, allowing plating of amorphous films of the desired composition [179].

The theory and status of cathodic electrodeposition of binary alloys and compounds have been described by Kröger [180] and Lincot [181] to whom we refer for accurate treatments. Brenner [182] has reviewed the work of Raub [183] on the co-electrodeposition of Cu-Sb alloys from ammoniacal and cyanide baths. It was found that with the cyanide, the whole compositional range from 0 to 100% Cu could be obtained by variation of the Cu concentration in the bath, while almost no variation was observed with the ammoniacal bath (Cu being far nobler than Sb in such conditions).

In order to avoid the use of cyanide salts, electrodeposition from a friendlier complexing agent such as D-sorbitol ($C_6H_8(OH)_6$) was developed in this work. The procedure is based on an adaptation of the alkaline electrolyte reported by Barbosa et al. [184], which was successfully employed by Scragg et al. [38] for the Cu deposition of CZTS precursors. In strongly alkaline solutions, D-sorbitol loses two protons and forms complexes with the Cu^{2+} cation, stabilising it and preventing the precipitation of cupric oxide CuO. Sb^{3+} is unstable in water, where it forms the trioxide Sb_2O_3 that slowly dissolves in alkaline solutions to form antimonite SbO_2^-. Figs. 2.1.2 and 2.1.3 show the electrochemical equilibrium diagrams respectively of Cu and Sb in water at 25 °C, as taken from Pourbaix [185].

Voltammetry was performed using solutions of Cu, Sb salts and mixtures of the two, in order to investigate deposition at the surface of a polished Mo wire working electrode. 3 M NaOH and 0.2 M D-sorbitol were employed in all cases. Fig. 2.1.4 shows the linear sweep voltammetry of a 0.1M $CuSO_4$ (a) and cyclic voltammograms of a 0.1M $SbCl_3$ solution (b) and of an equimolar solution of Cu and Sb salts (c).

By comparison of the Pourbaix diagram of Cu in Fig. 2.1.2 with the corresponding onset of cathodic deposition (Fig. 2.1.4 (a)), it can be noticed that the reduction of Cu^{2+} is shifted towards more negative potentials (i.e. the metal becomes less noble). This is due to the complexation of the Cu^{2+} by the anions of D-sorbitol. On the other hand, the reduction of SbO_2^- (b) occurs in accordance to the Pourbaix diagram in Fig. 2.1.3, and the plating efficiency is very high. Overall, the two reductions occur roughly at the same potential.

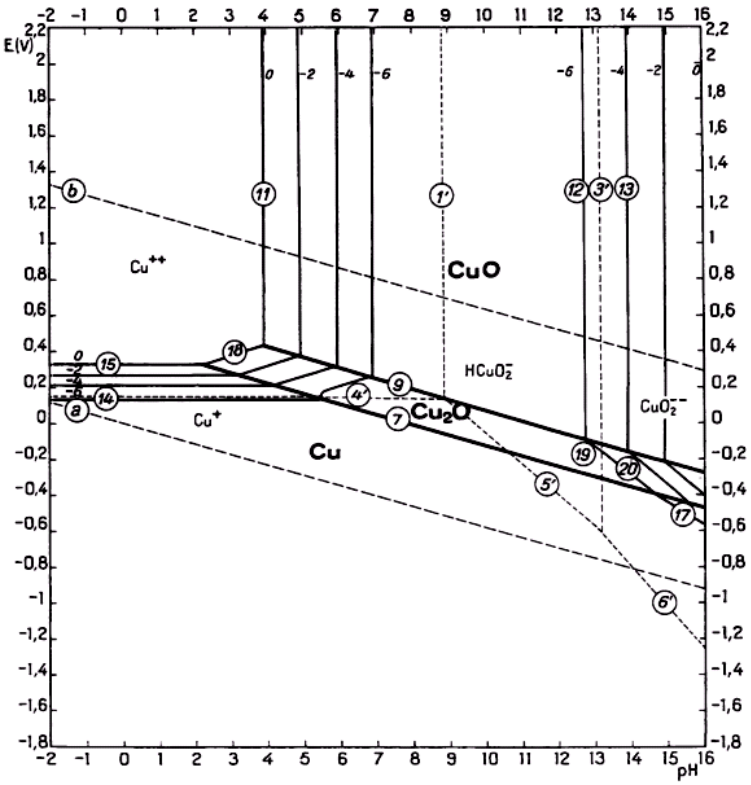

Fig. 2.1.2 Potential-pH equilibrium diagram for the system Cu-H_2O [185]

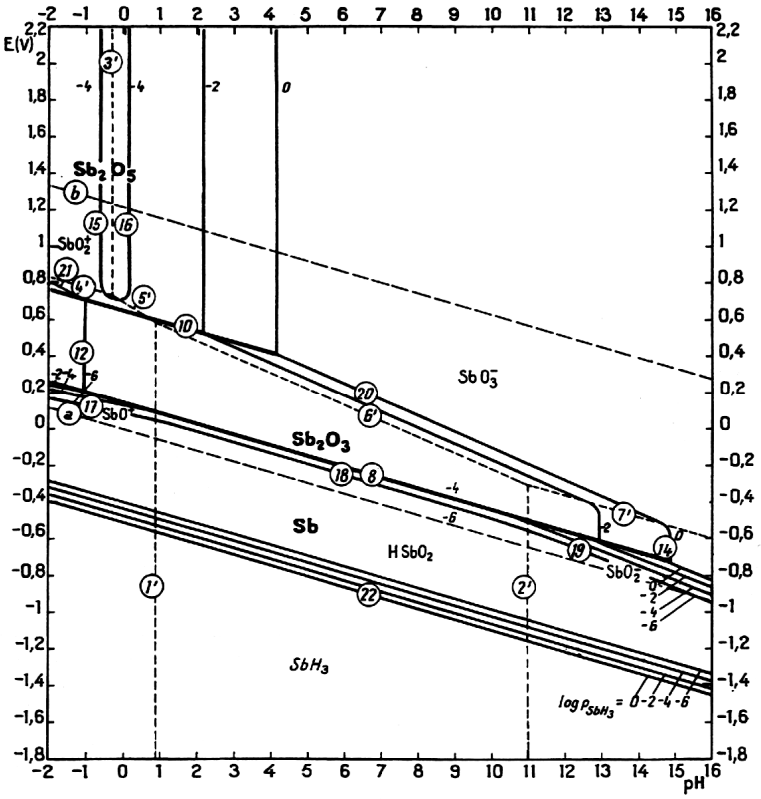

Fig. 2.1.3 Potential-pH equilibrium diagram for the system Sb-H_2O [185]

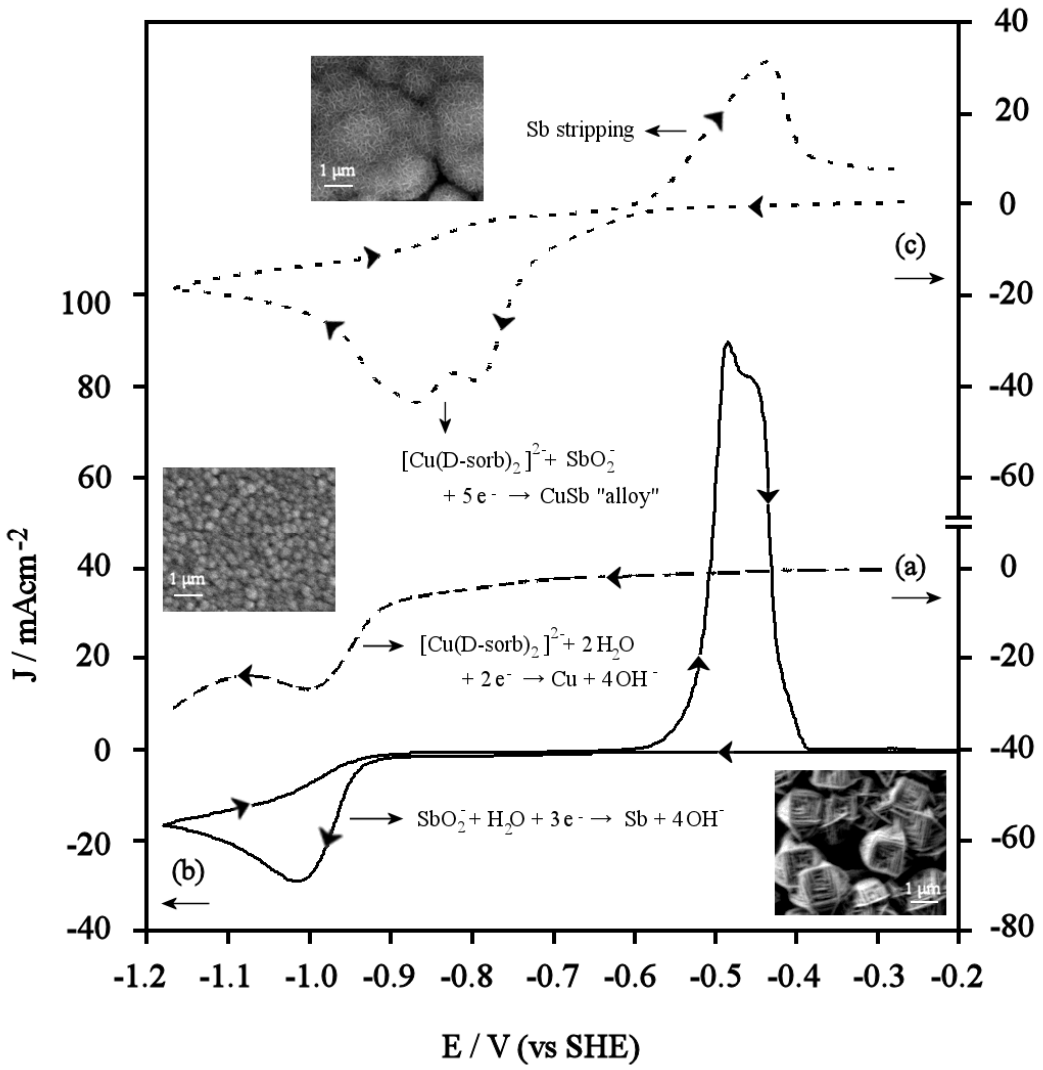

Fig. 2.1.4 Voltammetric analyses in unstirred solutions of 0.1M Cu^{2+} (a), 0.1M SbO_2^- (b) and an equimolar solution of Cu and Sb salts (c) in 3M NaOH and 0.2M D-sorbitol on a polished Mo wire working electrode (sweep rate 50 mVs^{-1}). The figure shows also the corresponding morphologies of the electroplated layers onto Mo-coated glass obtained at (a) -0.80, (b) -0.95 and (c) -0.95 V vs SHE with a cut-off of -0.47 Ccm^{-2} on the stirred solutions.

However, solutions containing both Cu and Sb salts show a cathodic onset at significantly more positive potentials compared to the two cations taken separately, Fig. 2.1.4 (c). This is a hint that an "alloy" or a disordered structure containing both Cu and Sb is being deposited, and the shift of the cathodic process may be associated to the free energy gain of "alloy" formation. Integration of the stripping peak in (c) up to -0.3 V vs SHE gives about 40% of the charge involved in the cathodic process. Sb is oxidised at a potential close to that observed for pure Sb (b). However, it is not sure whether the whole Sb is oxidised up to -0.3 V vs SHE or traces are left in the Cu-rich matrix.

Fig. 2.1.5 shows a series of cyclic voltammograms with different cathodic limits, carried out with the intent of deconvoluting the cathodic current.

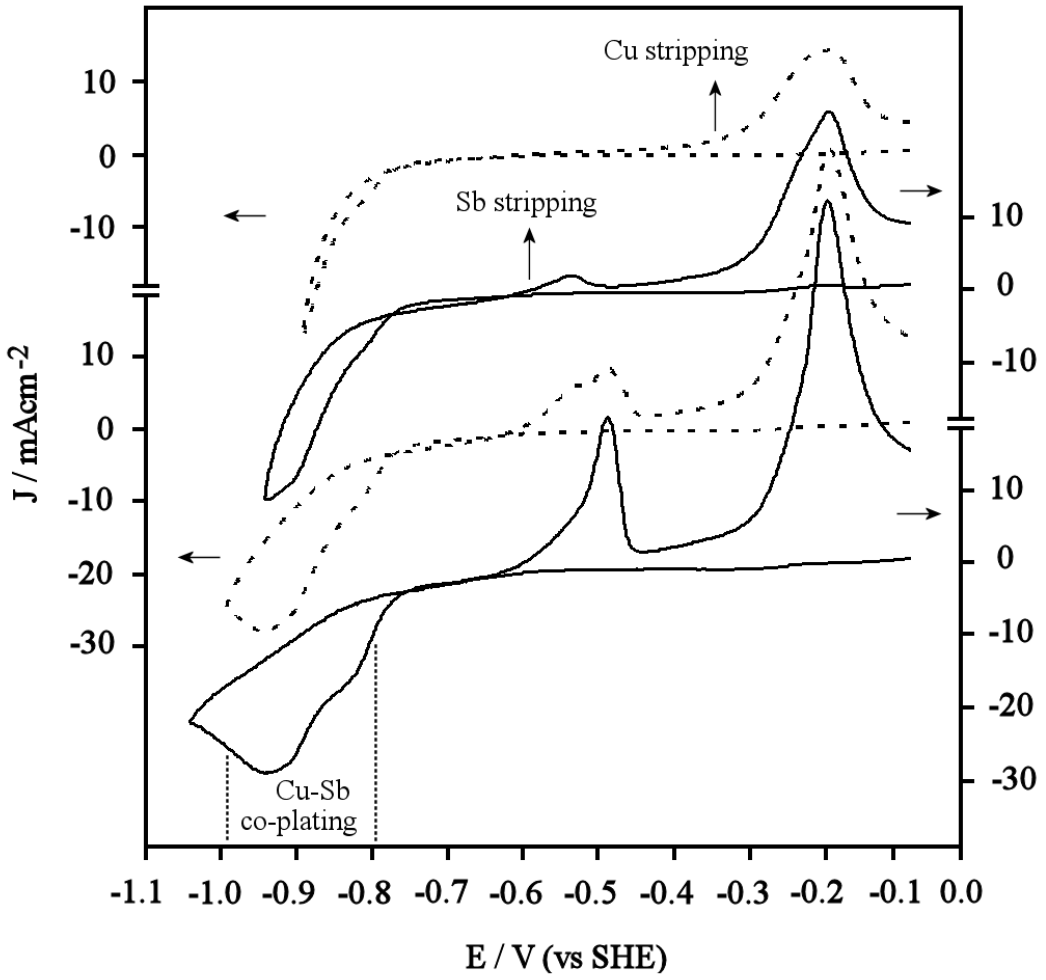

Fig. 2.1.5 Voltammetric analysis of an unstirred equimolar solution of Cu^{2+} and SbO_2^- with sequential reversing of the potential. The area of investigated co-deposition is also marked.

Integration of the anodic peaks of Cu and Sb in Fig. 2.1.5 gives a charge ratio of ~5:1. However, the elemental ratio determined in cyclic voltammetry is generally not the same as that of potentiostatic deposition. Furthermore, it must be highlighted that the anodic peak of Cu partially overlaps with that of Mo from the electrode [185].

With the vertical geometry employed in this study (section 2.6), the mass flux is only ensured by stirring (and not artificially induced, e.g. with a Rotating Disc Electrode RDE). The optimum conditions for the deposition of a Cu:Sb 1:1 "alloy" were found with a trial and error approach, by varying the relative concentration of the Cu and Sb salts. The results of EDS elemental analyses performed on

electroplated films obtained potentiostatically between -0.8 and -1.0 V vs SHE are shown in Fig. 2.1.6.

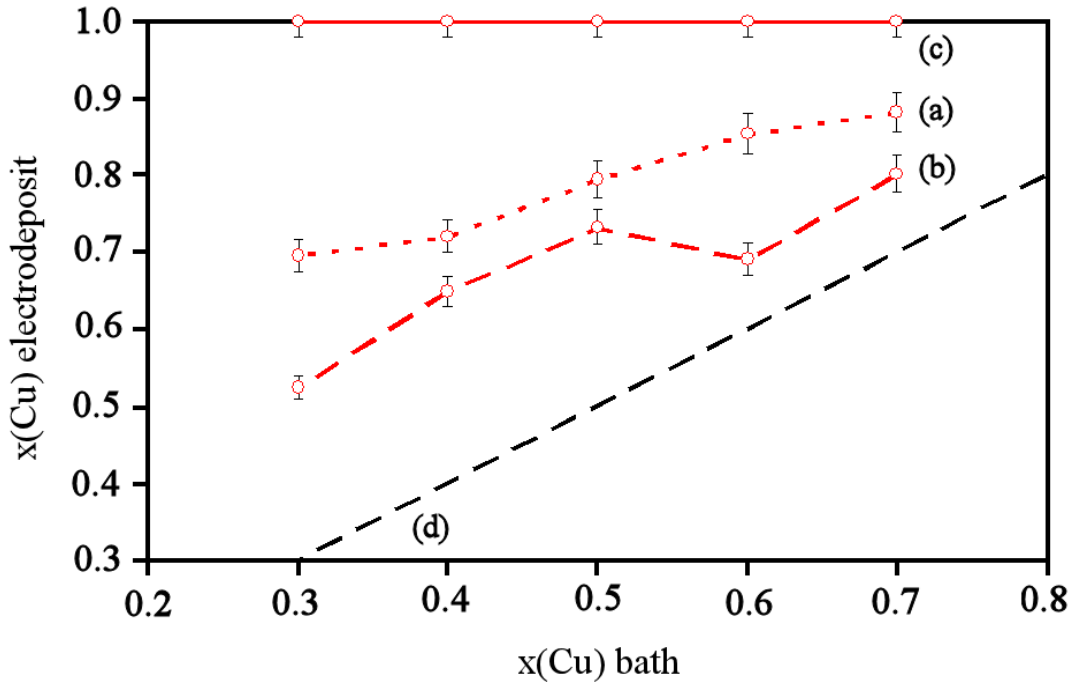

Fig. 2.1.6 Molar fraction of Cu in the electrodeposited films as a function of the composition of the electrolytic bath. Films were deposited potentiostatically at -0.8 (a), -0.9 (b) and -1.0 V vs SHE (c). The isopleth line (d) is indicated for reference.

The concentration of Cu in the electrodeposits decreases with the increase of the molar fraction of Sb salt in the electrolytic solution. However, in all cases it lies above the isopleth line corresponding to the points where the molar fractions of bath and plated film are equal. This might suggest that the deposition of Sb is slower than that of Cu, possibly due to a limitation imposed by the kinetics of charge transfer. Also it is not clear why the concentration of Cu in the electrodeposits decreases between -0.8 and -0.9 and then it rises again at -1.0V vs SHE. This phenomenon might be associated with the release of $SbH_{3\,(g)}$.

The optimum conditions for the deposition of a Cu:Sb 1:1 "alloy" were as follows. The solution composition was: 3 M NaOH, 0.2 M D-sorbitol, 0.10 M $CuSO_4$ and 0.15 M $SbCl_3$. Potentiostatic depositions were performed at -1.0 V vs SHE with a charge cut-off of 0.471 C in the stirred solution. This charge corresponds to the amount required for a 2 μm thick film of $CuSbS_2$ to be obtained after complete sulfurization of the Sb-Cu alloy deposited onto 0.25 cm^2 substrates (i.e. 5 electrons per $CuSbS_2$ formula unit), assuming a 100% electroplating efficiency.

Nucleation and growth of electrodeposits depend on the charge transfer process occurring at the surface of the working electrode. Therefore, it is obvious that the nature of the surface has a strong influence on the morphology and adhesion of the film being plated.

The poor properties that Mo offers as a substrate for electroplating are a well known issue [186]. The presence of a surface oxide decreases the "wetting" of the electrodeposit (i.e. the contact angle) and prevents direct metal-metal interaction. MoO_3 is soluble in alkaline solutions, and a treatment in concentrated ammonia solution has been suggested for its removal from Mo-coated substrates [187]. However, in our case, even the deposition in a highly alkaline solution did not ensure a perfect coverage of the alloy with possible preferential 3D as opposed to a 2D nucleation. This could be caused by an atomic oxide layer that may remain on the Mo surface due the high oxygen affinity of Mo [188]. This issue was overcome with the deposition of a very thin Cu layer with the method of Barbosa et al. [184] prior to the actual alloy electrodeposition, as reported e.g. for CZTS metal precursor electrodeposition [130].

2.2 Chalcogenization of $CuSb(S,Se)_2$ precursors

Several different procedures have been followed in this research to convert metal and metal sulfide precursors into the chalcogenide film of interest. They can be divided into two main categories: based either on a conventional resistive heating or on the Rapid Thermal Processing (RTP).

Only conventional heating was employed for the formation of $CuSb(S,Se)_2$. This choice was made in order to avoid potential contamination of the RTP system by Sb, as it will be clear in chapter 4. A wire-wound quartz tubular furnace (Thermo Scientific), was adapted for this purpose. The procedure for the conversion of the $CuSb(S,Se)_2$ precursors consisted of a heat treatment performed in the presence of an excess of elemental sulfur vapour (equivalent to 45 mbar in the tube furnace assuming S_2 at 298 K) or selenium vapour (equivalent to 2.8 mbar in the tube furnace assuming Se_2 calculated at 298K, similarly to Cummings et al. [189]).

The precursors - either co-electroplated or evaporated metals or evaporated $CuSbS_2$ films - were loaded in a loose-lid graphite box, together with the chalcogen. The box was introduced in the quartz tube of the furnace, the ceramic plugs were inserted and the whole system was evacuated and purged several times with nitrogen (Fig. 2.2.1).

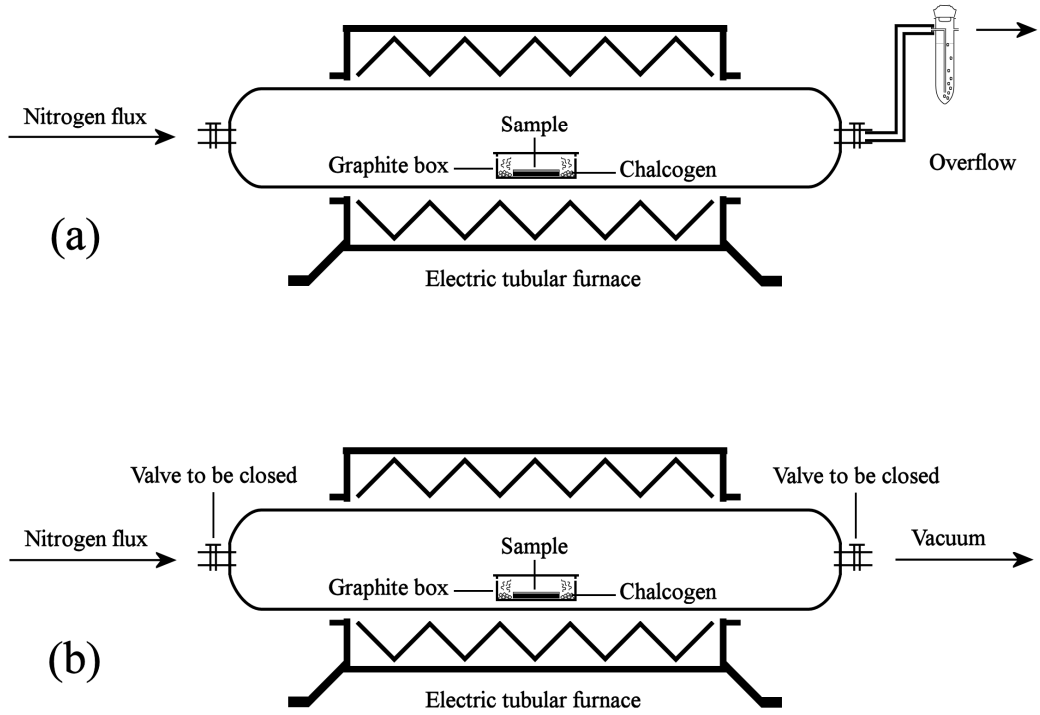

Fig. 2.2.1 Representation of the apparatus employed for the chalcogenization with a conventional tubular furnace under N_2 flux (a) and under vacuum (b). The built-in thermocouple is located outside the quartz tube at the centre.

The heating rate employed was 10 °Cmin^{-1}, and the samples were left at the maximum temperature for up to 1 hour, after which they were allowed to cool down naturally to room temperature (estimated cooling rate 2 °Cmin^{-1}).

The Cu-Sb metal films were chalcogenized at 200, 250, 300, 350 and 400 °C, under a 10 ml·min^{-1} flux of nitrogen at atmospheric pressure, with the intent to avoid oxygen contamination during the process (Fig. 2.2.1 a). However, the consequent chalcogen pressure decrease was not taken into account. The same treatments were also adopted for the evaporated films of plain Cu and Sb on soda lime glass.

The substitution of sulfur with selenium from the $CuSbS_2$ evaporated films was investigated at 300, 400 and 500 °C (Fig. 2.2.1 b) under moderate static vacuum (10^{-3} bar). The films were also annealed at the same set of temperatures under similar conditions but in the absence of chalcogen, in order to differentiate the effect of the thermal treatment itself from the effect of chalcogen substitution.

2.3 Morphology and composition of $CuSb(S,Se)_2$ thin films

The appearance of the samples after the chalcogenization treatments was as follows. Both the stacked (on FTO substrates) and the co-electroplated films (on Mo substrates) were dark blue if treated between 200 and 300 °C and grey if treated at 350 and 400 °C. They were smooth and adherent to the Mo and FTO-coated glass substrates. The sulfurized films of evaporated plain Cu (on soda-lime glass) were blue-green in colour and adhered poorly to SLG substrates. The sulfurized films of plain Sb were grey, smooth and adherent; however, the samples treated at 350 °C or at higher temperature revealed some losses (i.e. they became semi-transparent). The samples of evaporated $CuSbS_2$ after the selenization treatments looked dull and of a light grey colour, while those annealed in absence of chalcogen at 400 and 500 °C were darker.

The samples were analysed morphologically and compositionally. This was achieved at a microscopic level with a Jeol 6480LV Scanning Electron Microscope operated with an accelerating voltage of 20 KV. The same instrument was connected to an INCA x-act Energy Dispersive Spectroscopy microprobe that was employed to estimate the Cu:Sb ratio of the metallic precursors and annealed films after calibration with a Cu-Sb standard of known composition (produced by melting together known amounts of solid Cu and Sb). Fig. 2.3.1 shows the secondary electron micrographs of the metal precursor and of the chalcogenised films.

The cracks and pinholes that can be observed on the electroplated precursor film (Fig. 2.3.1a,b) reveal that the adhesion to the underlying Mo substrate is not optimal. As discussed in section 2.1, improved adhesion was obtained with the deposition of a 50 nm thin Cu layer prior to the Cu-Sb alloy.

The Cu:Sb elemental ratio of the precursor film determined by EDS is 1.3 and, although slightly high, it is thought to be suitable for the conversion to $CuSb(S,Se)_2$. The samples sulfurized below 350 °C (Fig. 2.3.1c) show a characteristic surface covered by idiomorphic crystals that the EDS microprobe identified as stoichiometric CuS. Only traces of Sb signal were detected in the EDS spectrum (c). This is attributed to the characteristic morphology of the films with the voluminous CuS crystals on the surface. These may act as a physical hindrance to the electron beam that does not penetrate enough to interact with the lower part of the film.

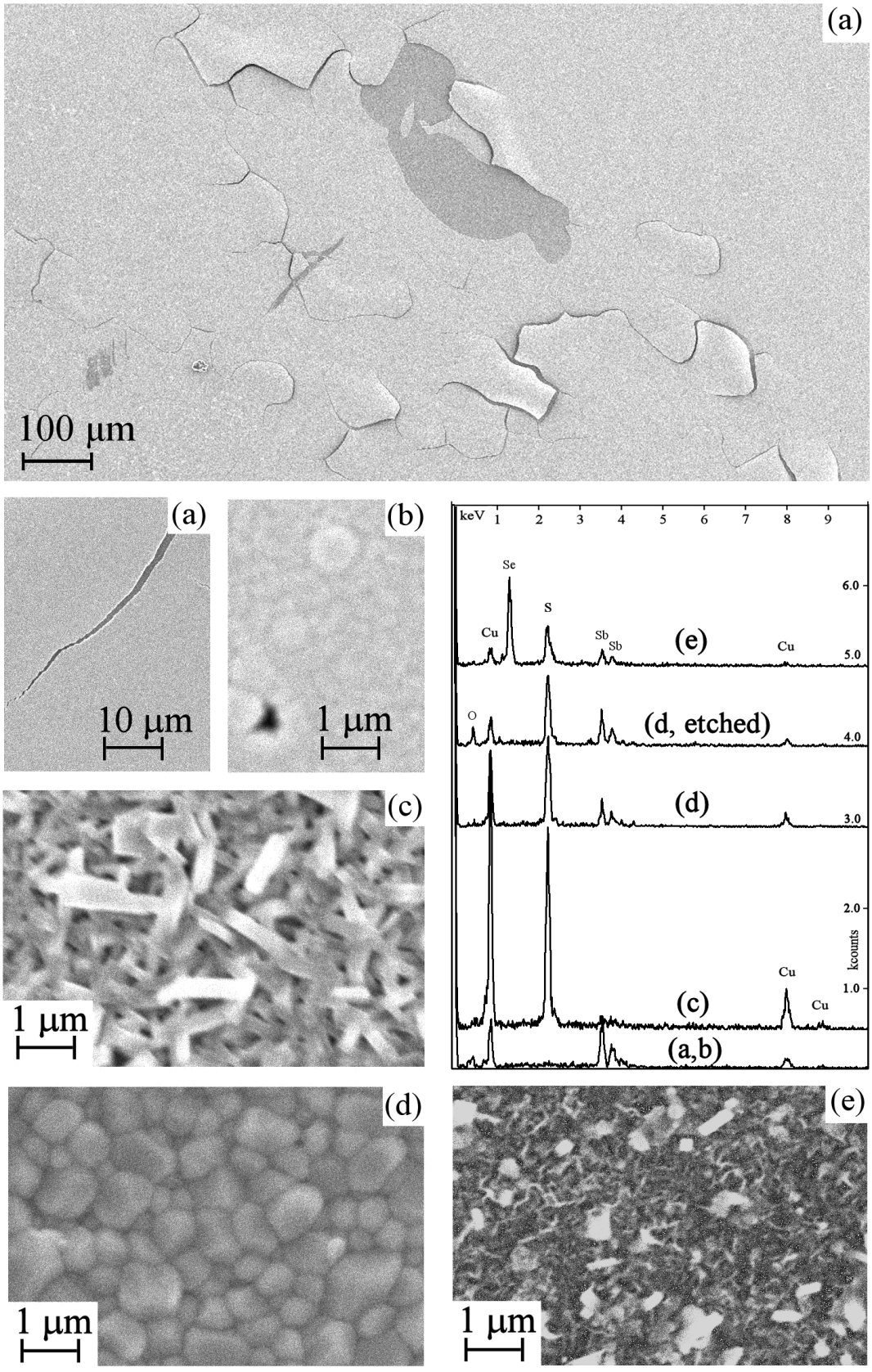

Fig. 2.3.1 Secondary electron images of the electrodeposited Sb-Cu alloy precursor untreated (a, b) and after sulfurization at 300 (c) and 400 °C (d) and selenization at 400 °C (e). The corresponding EDS spectra are also shown.

The samples sulfurized at 350 and 400 °C (Fig. 2.3.1d) show a nice compact film, with grain size of the order of 1 μm, and a Cu:Sb ratio of 2.6 (d), as determined via EDS. This ratio decreased substantially to 0.96 after the samples were etched in a KCN solution, which is known to selectively remove Cu-S phases (the reason for such a treatment is explained in section 2.5).

Fig. 2.3.1e shows the morphology of a sample selenized at 400 °C and its EDS spectrum, from which a composition consistent with $CuSbSe_2$ can be estimated.

The SEM/EDS analyses of the evaporated $CuSbS_2$ films after either selenization or annealing in absence of chalcogen are shown in Figs. 2.3.2a-c and 2.3.2d-f, respectively. The grain size of the films increases with the increase of the selenization temperature from 300 (a) to 400 °C (b). The EDS spectra of the samples selenized at 300 (a) and 400 °C (b) show that the films do not possess a stoichiometric composition, i.e. they are most likely formed by mixture of phases. At 300 °C, CuSe seems to be formed first and segregate at the surface, while at 400 °C the films show predominantly Sb_2Se_3 rich surfaces (Cu is almost not detected). The treatment at 500 °C results in a smoother and more compact film (c) with composition much poorer in Sb, approximately consistent with a copper antimony sulfoselenide of formula $CuSbS_{0.3}Se_{0.7}$.

Annealing of the evaporated $CuSbS_2$ precursors in the absence of chalcogen causes a detrimental effect on the morphology of the films (Fig. 2.3.2d-f). The samples annealed at 300 °C show the appearance of abundant holes (d), but the composition is still consistent with that of the amorphous precursor film (i.e. Cu:Sb = 0.5). In the samples annealed at 400 and 500 °C, the film structure is completely destroyed, and only isolated crystals with euhedral shape and average size of 3 (e) and 10 μm (f) can be observed. Their Sb concentration is reduced, and for the sample annealed at 500 °C the Cu:Sb ratio is consistent with the formula Cu_3SbS_3, revealing Sb losses.

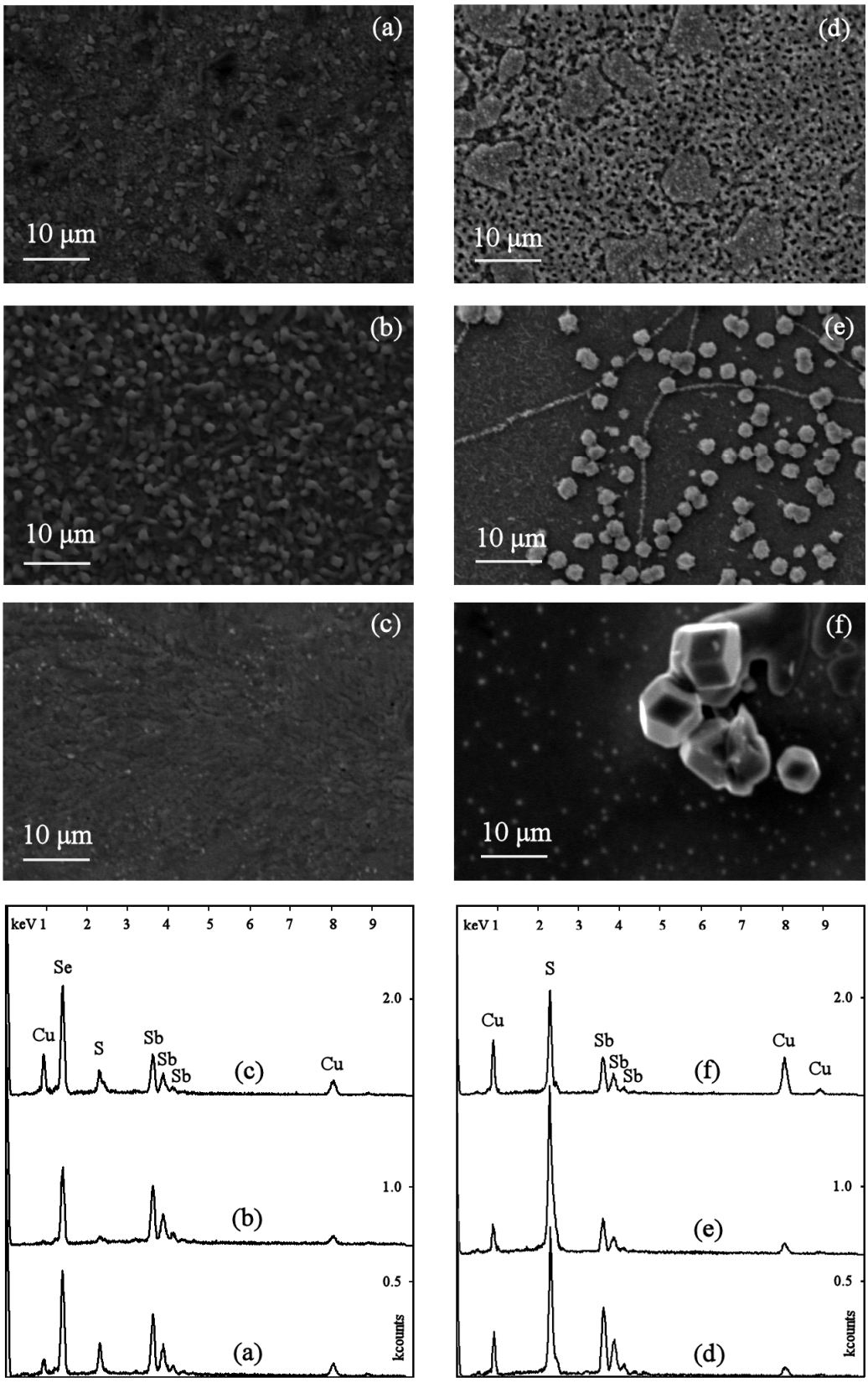

Fig. 2.3.2 Secondary electron images of the evaporated $CuSbS_2$ films after selenization at 300 (a), 400 (b) and 500 °C (c), and after annealing in absence of chalcogen at 300 (d), 400 (e) and 500 °C (f) and corresponding EDS spectra.

2.4 Structural characterization of $CuSbS_2$ thin films

The structural characterization of the thin films in this thesis was carried out by means of XRD with conventional Bragg-Brentano geometry. More specifically, the samples obtained via sulfurization of the evaporated and co-electroplated Cu-Sb metal precursors and via the selenization of the evaporated $CuSbS_2$ films were analysed with a Panalytical X'pert X-ray powder diffractometer. Films of the sulfurized plain elements were also analysed, with the intent to determine the phase evolution of the elemental films separately and investigate the effect of the Sb/Cu interface in the formation of the desired compounds (see chapter 4). Fig. 2.4.1 shows the XRD spectra of the films of plain Cu, plain Sb and Cu-Sb of the two configurations (stacked evaporated and co-electroplated) after sulfurization with elemental sulfur in the conventional furnace in the temperature range 200-400 °C.

The phase composition of the films sulfurized between 200 and 400 °C is also summarised in Table 2.4.2 where the Powder Diffraction File (PDF) card number for each phase is reported.

	Evaporated Cu	**Evaporated Sb**	**Evaporated Sb/Cu**	**Co-electroplated Sb-Cu**
200 °C	CuS, PDF № 65-3561	Sb, PDF № 35-732	CuS, PDF № 65-3561 Sb, PDF № 35-732	CuS, PDF № 65-3561
250 °C	CuS, PDF № 65-3561	Sb, PDF № 35-732 Sb_2S_3, PDF № 42-1393	CuS, PDF № 65-3561 Sb, PDF № 35-732	CuS, PDF № 65-3561
300 °C	CuS, PDF № 65-3561	Sb, PDF № 35-732 Sb_2S_3, PDF № 42-1393	CuS, PDF № 65-3561 Sb, PDF № 35-732 Sb_2S_3, PDF № 42-1393	CuS, PDF № 65-3561 Sb, PDF № 35-732 Sb_2S_3, PDF № 42-1393
350 °C	CuS, PDF № 75-2236 (unindexed peaks at 2θ= 28.9° and 33.1°)	Sb_2S_3, PDF № 42-1393	$CuSbS_2$, PDF № 65-2416	$CuSbS_2$, PDF № 65-2416
400 °C	CuS, PDF № 75-2236 (unindexed peaks at 2θ= 28.9° and 33.1°)	Sb_2S_3, PDF № 42-1393	$CuSbS_2$, PDF № 65-2416	$CuSbS_2$, PDF № 65-2416

Table 2.4.2 Phase composition of evaporated Sb, Cu, Sb/Cu stacked and co-electroplated Sb-Cu precursor films after sulfurization treatments at 200, 250, 300, 350 and 400 °C.

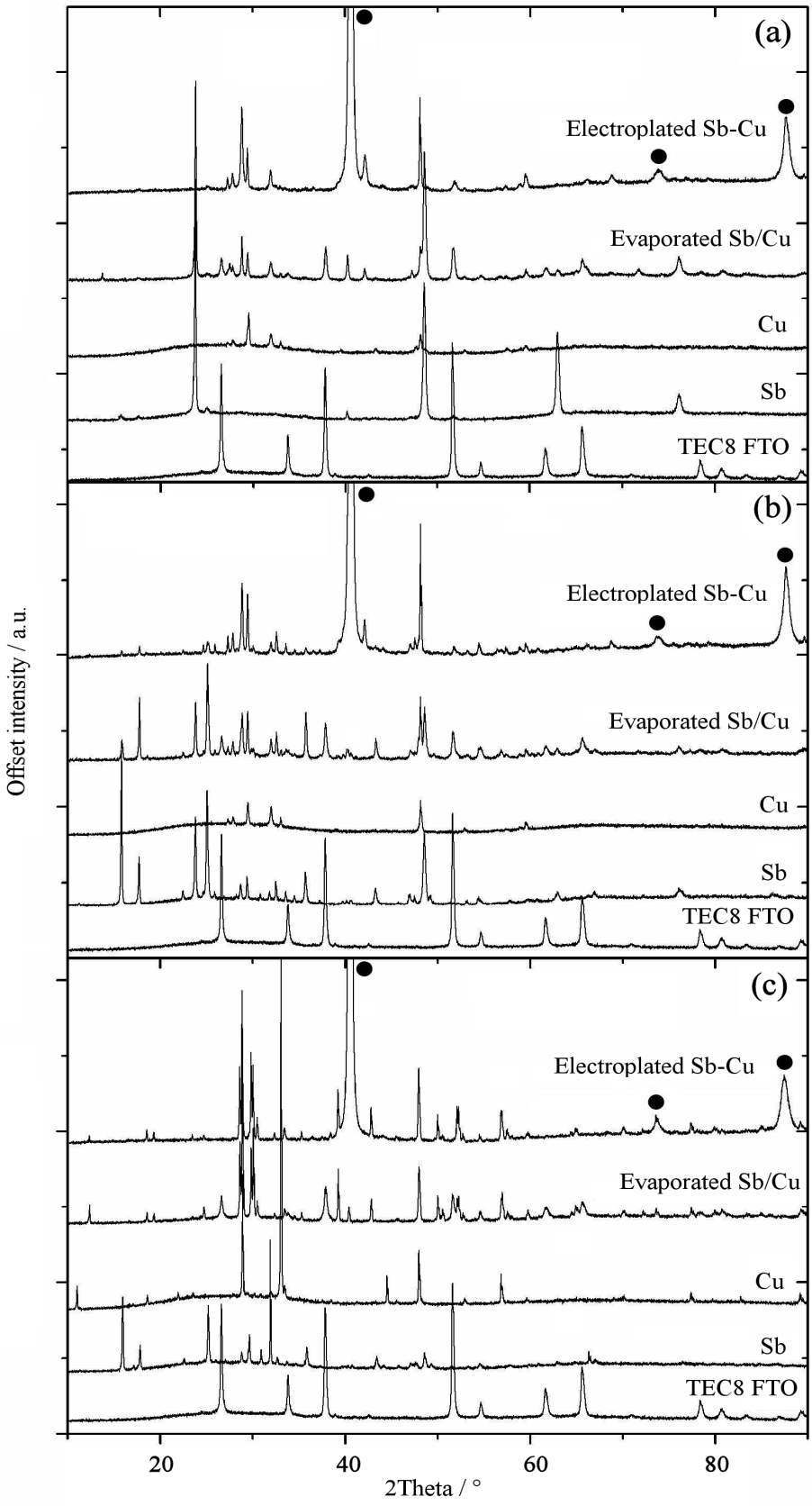

Fig. 2.4.1 XRD spectra of evaporated Sb, Cu, Sb/Cu stacked and co-electroplated Sb-Cu alloy films sulfurized at 200 (a), 300 (b) and 400 °C (c) for 30 minutes. (To assist the reader, the XRD spectrum of the TEC8 FTO substrate is also reported; ● labels refer to the peaks of the Mo substrate).

The phase composition, as obtained from the XRD analysis, points towards equivalence between the co-electroplated/sulfurized samples and the evaporated/sulfurized ones. This is also consistent with the visual appearance of the samples, as discussed in section 2.3. The main appreciable difference is due to the metal precursor employed. The co-electroplated Cu-Sb precursor does not show any peak corresponding to antimony below 300 °C, as opposed to the evaporated stacked Cu/Sb precursor that shows this phase even at lower temperature, this might be due to the presence of a Cu-Sb alloy with poor scattering properties.

The diffractogram of the evaporated Cu films is a good match to the pattern of hexagonal CuS (*Covellite*), even at sulfurization temperatures as low as 200 °C. This suggests that the formation of such a phase is highly favoured under the conditions investigated. For treatments at 350 °C or higher temperature, other diffraction peaks emerge, revealing some thermally-induced modification (attribution to CuS PDF no. 75-2236 is an option for a close match, but additional $Cu_{1.8}S$ as *low* and *high Digenite* may be present [190, 191]). It is worth noticing that no Cu_2S was detected.

The evaporated Sb film sulfurized at 200 °C does not show the presence of the corresponding sulfide peaks within the detection limit of the instrument, and it possesses highly (*00l*) preferred orientation, similar to the as-deposited Sb. A systematic shift of the diffraction maxima towards higher 2θ relative to the literature pattern of Sb is observed. This indicates the presence of uniform compression strains of the unit cell along [*00l*]. Such distortion becomes less significant at higher temperatures as the lattice relaxes and leads to a pattern which is close to the standard powder pattern of Sb, for thermal treatment of 300 °C. The conversion of Sb to Sb_2S_3 is incomplete below 350 °C (mixtures of the two phases are detected), indicating that this element has apparently a lower tendency to form its sulfide, compared to Cu. However, the diffraction peaks of the sulfide phase are a good match to orthorhombic Sb_2S_3 (*Stibnite*).

Between 200 and 300 °C the X-ray patterns of the Sb/Cu stacked samples are the superimposition of the elemental Sb and Cu diffractograms. The ternary phase, orthorhombic $CuSbS_2$ (*Chalcostibite*), starts to appear at 350 °C, and at 400 °C the conversion into this stoichiometry is fully attained. A sharp variation of the colour of the films was observed from the blue films up to 300 °C to the grey films at 350 and 400 °C. This observation is consistent with the structural findings.

No traces of MoS_2 were detected by XRD.

2.5 Photoelectrochemistry of $CuSb(S,Se)_2$ thin films

The conductivity type and photoactivity of the converted samples were assessed with photoelectrochemical techniques using an electrolyte contact. For this purpose, a standard three electrode cell was employed with Ag/AgCl reference and a Pt wire counter electrodes, as described by Scragg et al. [39]. The electrolyte solution contained 0.2 M Eu^{3+} (pH ~ 3) which acts as a scavenger of photogenerated electrons. Photovoltammograms and chronoamperometric measurements were carried out under the pulsed illumination from a white LED, while the potential was applied and the current recorded by a μ Autolab type III potentiostat.

External quantum efficiency (EQE) spectra were acquired by illuminating the samples with monochromatic light of variable wavelength optically chopped at 27 Hz. The photocurrent was measured with a lock-in amplifier (Stanford Research Systems). The system was calibrated using a calibrated silicon photodiode traceable to NBS standards. The EQE setup is schematically depicted in Fig. 2.5.1.

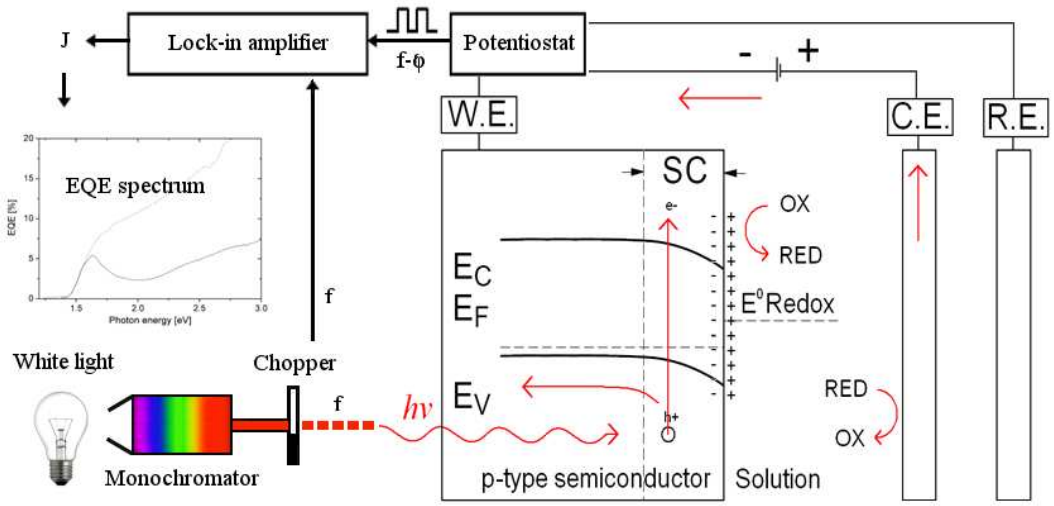

Fig. 2.5.1 Representation of the electrochemical photocurrent spectroscopy setup employed for the estimation of the EQE spectra of the converted films.

Cu-Sb samples that were chalcogenized up to 300 °C did not show any photoresponse. Those annealed at 350 °C and 400 °C were slightly photoactive showing *p*-type conductivity, as noticeable from the negative photocurrent response. The photoactive samples were then etched in a 5 % weight KCN aqueous solution in order to remove the presence on the surface of Cu-S and Cu-Se phases. This is a

generally accepted practice for removal of those phases from CIGSSe [112, 113] and CZTSSe materials [55, 192, 193]. Chronoamperometric analyses under pulsed white light performed on samples etched for increasing time periods revealed that the treatment increased considerably the magnitude of the photocurrent. The results are shown in Fig. 2.5.2 for measurements performed at -0.5 V vs Ag/AgCl, where the photocurrent was maximum.

If the photoactive samples were left in the KCN solution for 60 seconds or more, the improvement of the photoresponse allowed the External Quantum Efficiency (EQE) spectra to be acquired. Fig. 2.5.3 shows the EQE of the chalcogenide films obtained from co-electroplated and evaporated metal precursors.

The EQE of the films is low, reaching maxima of just ~8 % and ~20 % at 3 eV for the evaporated and for the electroplated sulfurized samples respectively. The unusual shape of the IPCE spectrum of the evaporated/sulfurized sample, with the presence of a maximum at the photon energy of ~1.65 eV, is likely caused by the presence of other phases at the surface of the film. Such phases may absorb the incident light with energy higher than ~1.65 eV without contributing to the photocurrent , as was also observed by Bryant et al. [194]. Possible secondary phases are Sb_2S_3 (*Stibnite*) [117, 118] and $Cu_{31}S_{16}$ (*Djurleite*) [194], which have band-gaps of about 1.6 and 1.8 eV respectively.

The EQE of the selenized sample is very low, with maxima of just 2.5 %, consistent with the high recombination rate seen in the photocurrent transients (Fig. 2.5.2). Fig. 2.5.4 shows the plots generated to estimate the direct band-gap energy values for both the evaporated and the electroplated samples chalcogenized at 400 °C (see section 1.4 for derivation of such plots).

Reasonably sharp edges in the range 1.47-1.53 eV are observed for the sulfurized samples, while broad edges in the range 1.2-1.3 eV are seen for the selenized ones. The result for the sulfide is in good agreement with Rodríguez-Lazcano et al. [83] who reported a band-gap energy of 1.52 eV for the $CuSbS_2$ film. Both these values fulfil the Shockley-Queisser requirements for efficient harvesting of the solar radiation [32].

Due to the relatively poor quantum efficiencies it was decided not to incorporate these absorber layers into complete devices, because the process of device completion required substantial efforts. Efforts were directed to address more fundamental questions concerning the chalcogenization process, aimed at understanding how to improve the absorber film morphology and performance.

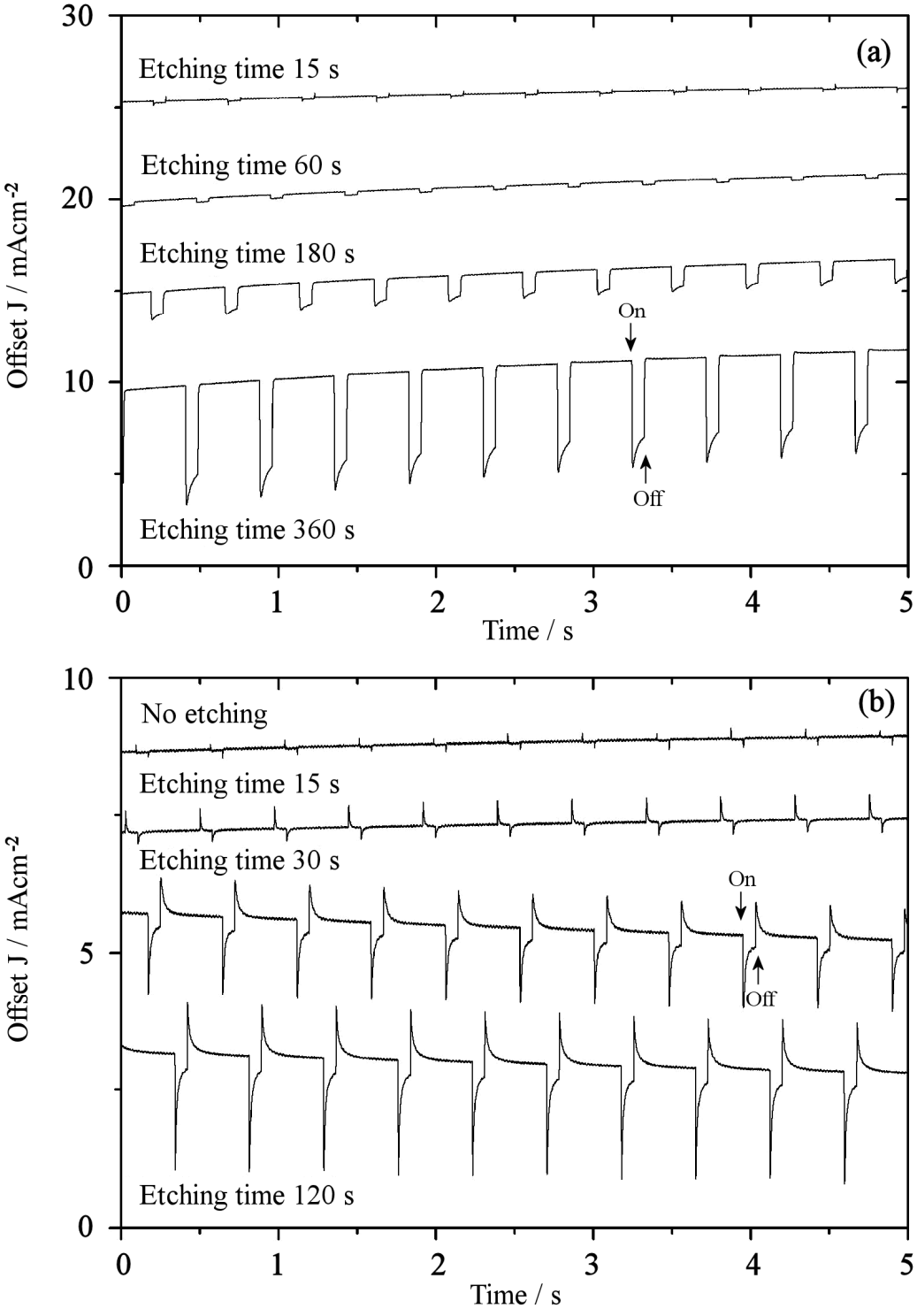

Fig. 2.5.2 Chronoamperometric tests in a 0.2 M Eu^{3+} solution at -0.5 V vs Ag/AgCl after KCN etch of increasing time periods under pulsed illumination of a white LED of electroplated samples after (a) sulfurization and (b) selenization at 400 °C. The negative sign of the photocurrent shows *p*-type conductivity. The plots are shifted on the y axis for graphical purposes.

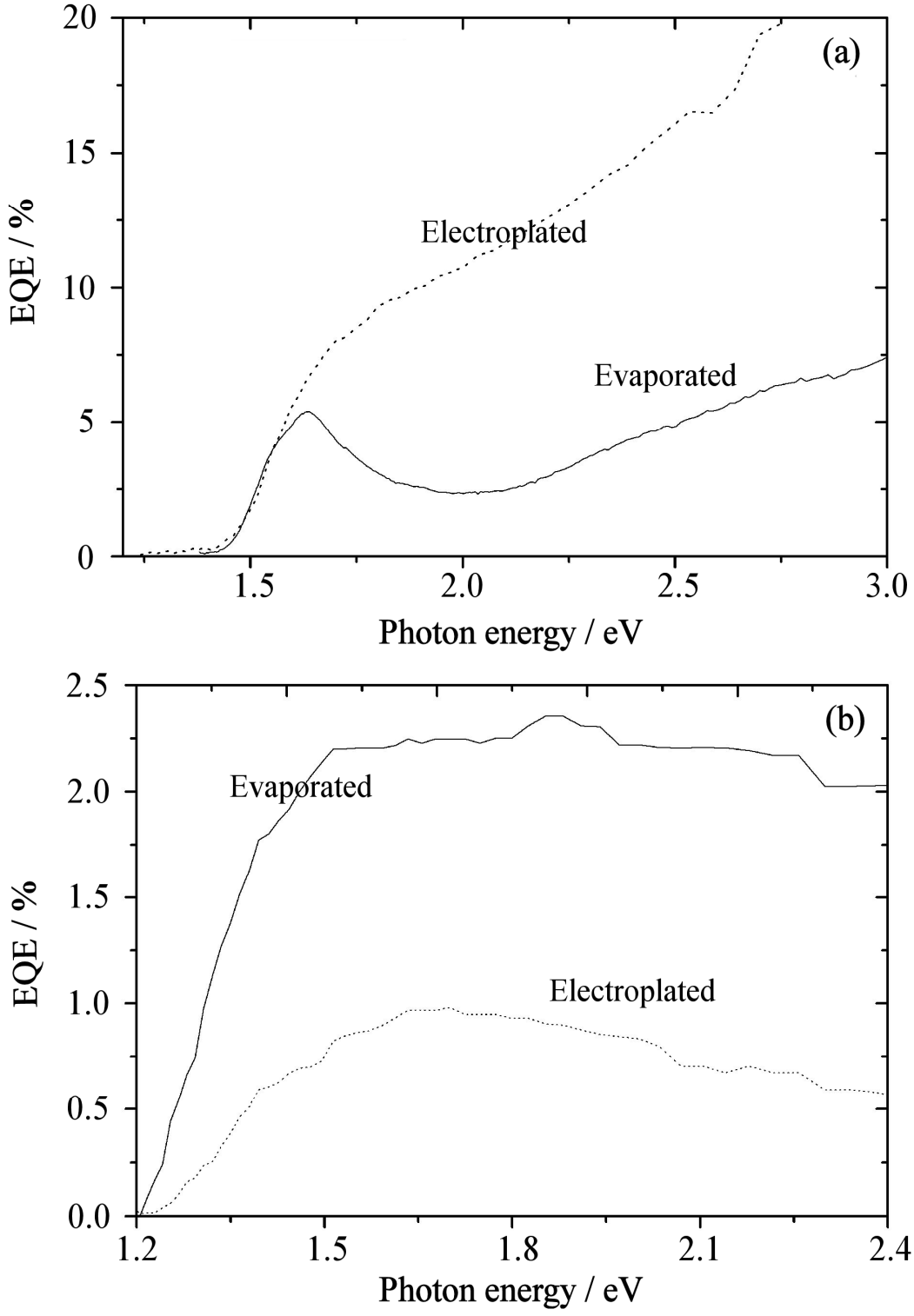

Fig. 2.5.3 EQE spectra of the evaporated Sb/Cu stacked and of the Sb-Cu "alloy" electroplated precursors sulfurized (the electroplated/annealed sample was analysed after 360 s of KCN etching) (a), and selenized (b) at 400 °C. The spectra were acquired in a 0.2 M Eu^{3+} solution with the samples held at -0.5 V vs Ag/AgCl and a light chopping frequency of 27 Hz.

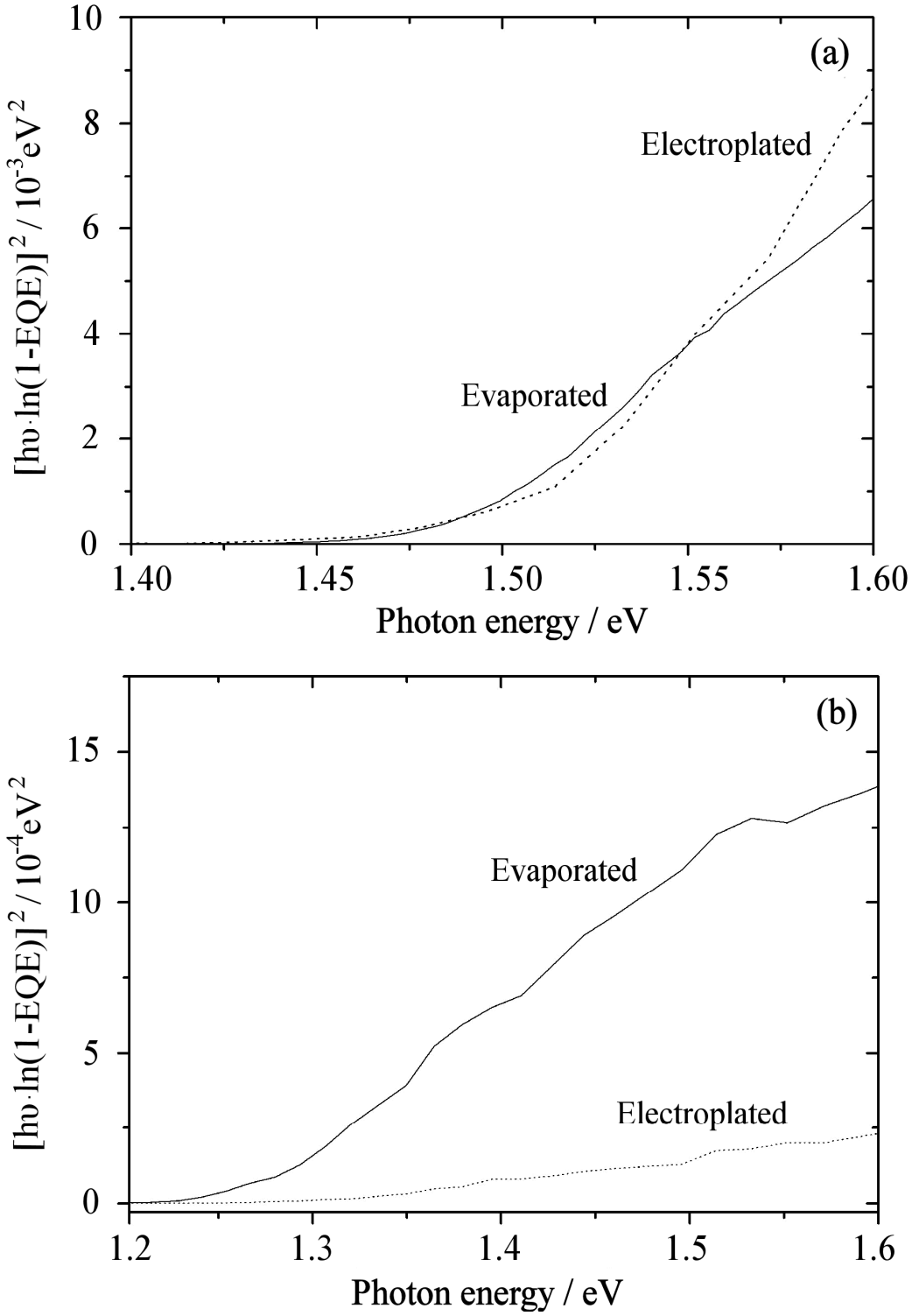

Fig. 2.5.4 Plots of $[h\upsilon \cdot \ln(1\text{-EQE})]^2$ generated to estimate the band-gap energies for stacked evaporated Sb/Cu and alloy electroplated Sb-Cu precursors sulfurized (a) and selenized (b) at 400 °C. The analysis assumes that the electronic structure of both compounds have direct band-gaps.

2.6 Experimental details

The co-electrodeposition of Cu-Sb thin film metal precursors was carried out in an electrolytic cell with the capacity of 150 ml with a vertical geometry and a three electrodes configuration, as shown in Fig. 2.6.1a. The Mo coated substrate held as the working electrode (W.E.) was provided by Northumbria University [169] (RF sputtered on microscope slides glass). The reference electrode (R.E.) employed was Hg/HgO/NaOH 1 M (Radiometer Analytical). The counter electrode (C.E.) was a house-built Pt foil (1 cm^2).

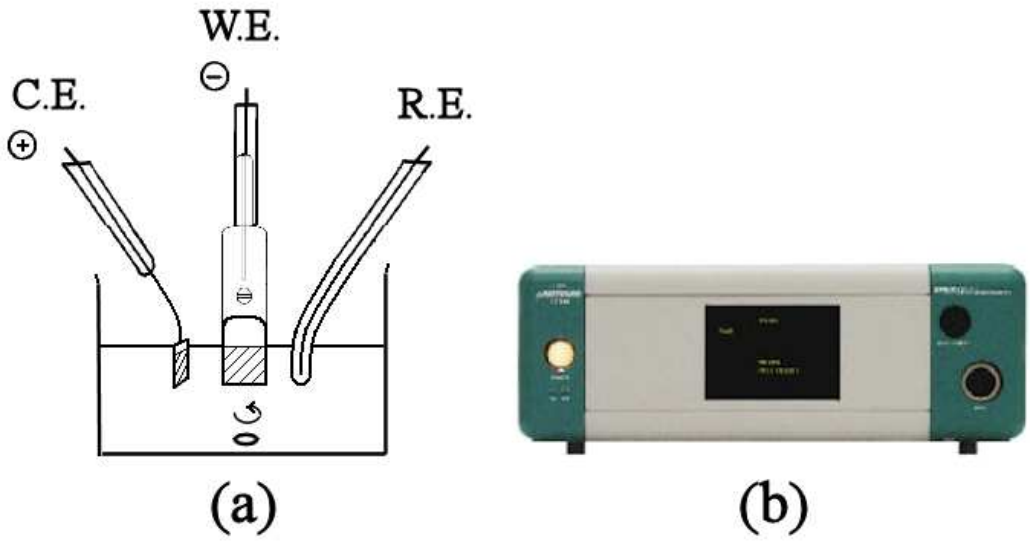

Fig. 2.6.1 Electrolytic cell with vertical geometry and three electrodes configuration employed for the co-electrodeposition of Cu-Sb thin film metal precursors (a). μ Autolab type III potentiostat employed for the electrodepositions (b).

The solution composition was: 3 M NaOH, 0.2 M D-sorbitol, 0.10 M $CuSO_4$ and 0.15 M $SbCl_3$ (Sigma Aldrich). Potentiostatic depositions were performed at -1.0 V vs SHE with a charge cut-off of 0.471 C in the stirred solution (400 rpm). The Mo coated substrates were connected to the W.E. with a crocodile clip and the deposition area (0.25 cm^2) was delimited using PTFE tape. The potential was applied with a μ Autolab type III potentiostat (Fig. 2.6.1b). The substrates were ultrasonically cleaned in 5% Decon 90 solution (Decon Laboratories Ltd.) for 15 minutes followed by the same treatments first with deionised water and finally with ethanol.

The evaporation of Cu and Sb to produce stacked and plain thin metal precursor films was carried out with a conventional Edwards evaporator. The substrates employed were either transparent electrically conductive fluorine-doped SnO_2-coated glass (TEC-8 by Libbey Owens Ford) or soda lime glass microscope slides, cleaned as described earlier. The stoichiometric Cu:Sb thickness ratio in the stacked configuration was ensured by loading calibrated amounts of the metals into the crucible, as per Fig. 2.6.2.

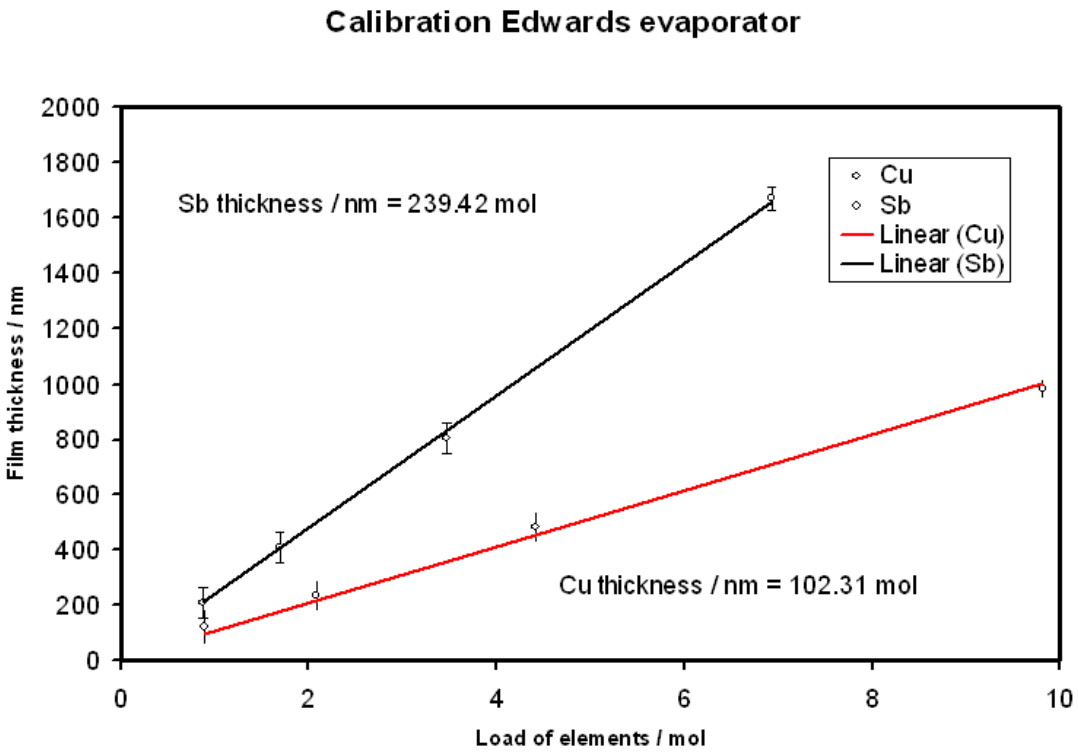

Fig. 2.6.2 Calibration of the Cu and Sb films thickness as functions of the respective loads in the tungsten crucible of the evaporator employed in this work. The thickness was measured with a Dektak 6M stylus surface profilometer.

Details of the heat treatment experiments performed to study the reaction conversions of the Cu-Sb-S-Se precursor films into the chalcogenide layers of interest are found in Table 2.6.1. For all experiments in chapter 2 the treatments were performed in a wire-wound quartz tubular surface (Thermo Scientific) employing a heating rate of 10 °C·min^{-1} and an uncontrolled cooling step (approximately 2 °C·min^{-1}).

Precursor type(s)	Max. temperature	Dwell time	Chalcogen pressure	N_2 flux
evaporated Cu, Sb, Cu-Sb and co-electroplated Cu-Sb	200 °C	30 min	45 mbar S_2 calculated at 298K	10 °C·min^{-1}
evaporated Cu, Sb, Cu-Sb and co-electroplated Cu-Sb	250 °C	30 min	45 mbar S_2 calculated at 298K	10 °C·min^{-1}
evaporated Cu, Sb, Cu-Sb and co-electroplated Cu-Sb	300 °C	30 min	45 mbar S_2 calculated at 298K	10 °C·min^{-1}
evaporated Cu, Sb, Cu-Sb and co-electroplated Cu-Sb	350 °C	30 min	45 mbar S_2 calculated at 298K	10 °C·min^{-1}
evaporated Cu, Sb, Cu-Sb and co-electroplated Cu-Sb	400 °C	30 min	45 mbar S_2 calculated at 298K	10 °C·min^{-1}
co-electroplated Cu-Sb	200 °C	30 min	2.8 mbar Se_2 calculated at 298K	10 °C·min^{-1}
co-electroplated Cu-Sb	300 °C	30 min	2.8 mbar Se_2 calculated at 298K	10 °C·min^{-1}
co-electroplated Cu-Sb	400 °C	30 min	2.8 mbar Se_2 calculated at 298K	10 °C·min^{-1}
evaporated $CuSbS_2$	300 °C	60 min	2.8 mbar Se_2 calculated at 298K	no flux
evaporated $CuSbS_2$	400 °C	60 min	2.8 mbar Se_2 calculated at 298K	no flux
evaporated $CuSbS_2$	500 °C	60 min	2.8 mbar Se_2 calculated at 298K	no flux
evaporated $CuSbS_2$	300 °C	60 min	10^{-3} mbar vacuum (no chalcogen)	no flux
evaporated $CuSbS_2$	400 °C	60 min	10^{-3} mbar vacuum (no chalcogen)	no flux
evaporated $CuSbS_2$	500 °C	60 min	10^{-3} mbar vacuum (no chalcogen)	no flux

Table 2.6.1 Details of the heating treatments employed for the study of the Cu-Sb-S-Se chalcogenide layers in chapter 2.

3. Formation of Cu_3BiS_3 and $CuBiS_2$ thin films

As indicated in section 1.3, the Earth's crust contains much more economically exploitable bismuth than indium. The U.S. Geological Survey assessed the 2010 annual world mine production of Bi as 7600 t, with estimated world reserves of 320000 t. As a comparison, the annual world production of In relies almost entirely on zinc refining and amounts to 574 t, while no estimation of the world reserves is yet reported [23]. During 2010, the price for Bi was below 20 U.S. \$ kg^{-1}, while In had an average price over 500 U.S. \$ kg^{-1}. Owing to its low toxicity [195] as well as relatively low cost, Bi has been considered in the framework of the COST Action 531 as a potential candidate for the development of lead-free soldering alloys [196-199], and some of its compounds are employed in a range of pharmaceutical and cosmetic products.

Similarly to $CuSb(S,Se)_2$, deposition of Cu_3BiS_3 and $CuBiS_2$ thin films has been investigated with the intent to test if their properties make them suitable to replace CdTe and $CuIn(Ga)(S,Se)_2$ in photovoltaic devices. As for the Cu-Sb case, the films were obtained by sulfurization of the metal precursor. Comparison of the sulfurization reactions in the two cases allowed us to draw some important conclusions that are presented in chapter 4.

$CuBiS_2$, also known as the mineral *Emplectite*, is isostructural with $CuSbS_2$. Formation of a complete solid solution between *Emplectite* and *Chalcostibite* has been reported [200]. Therefore, the same structural considerations presented in section 2 apply also for $CuBiS_2$ [80, 162]. To the best of our knowledge, $CuBiS_2$ thin films have only been deposited via spray pyrolysis [201] and chemical bath deposition [121, 122]. Potential application of this compound in PV devices was suggested by Sonawane et al. [202], although the semiconductor was reported to possess *n*-type conductivity. When compared to $CuSbS_2$ and other related ternary chalcogenides, this latter feature is thought to be peculiar enough to deserve further attention from a computational perspective [203], although no indication of intrinsic ionic defects has been reported to date.

Cu_3BiS_3 is a naturally occurring sulfosalt named *Wittichenite*. It crystallises in a orthorhombic unit cell (a = 7.723 Å, b = 10.395 Å, c = 6.715 Å) [79, 204] containing 4 formula units (Fig. 3(I)). Its low temperature polymorph belongs to a low symmetry space group (19, $P2_12_12_1$). This makes its structure even more different

than those of *Chalcostibite* and *Emplectite* from the adamantine family of compounds that form the basis of most current solar cell technologies. The coordination of the Cu atoms is nearly trigonal planar (Fig. 3(II)), while Bi shows a particularly unusual trigonal pyramidal geometry with the three closest sulfur atoms, as shown in Fig. 3.0(III).

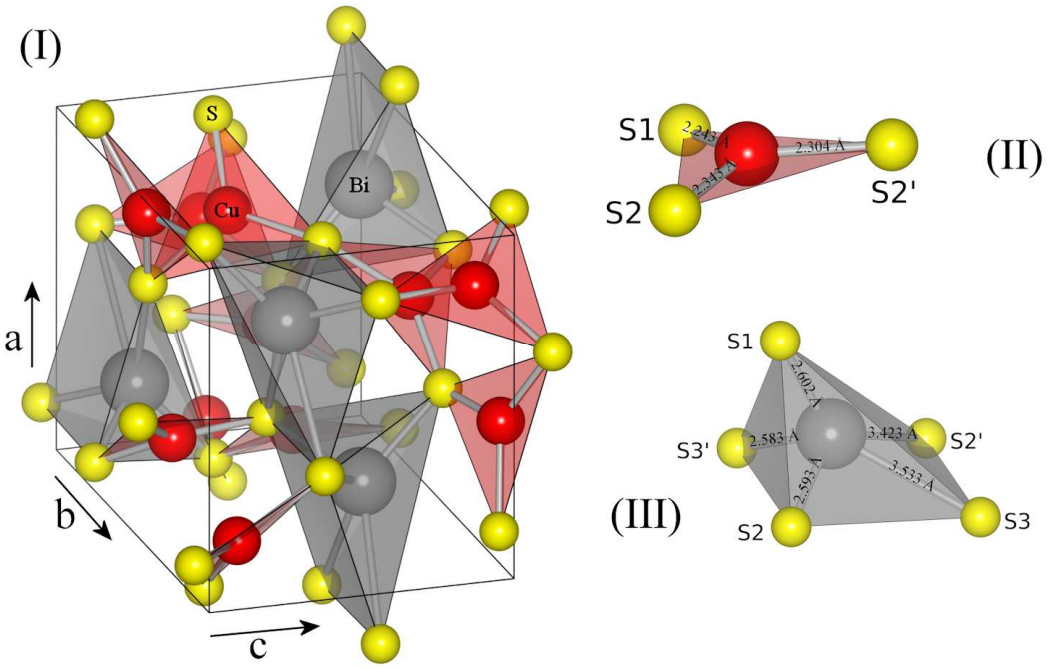

Fig. 3.0 (I) Orthorombic unit cell of Cu_3BiS_3, with highlighted coordinations of Cu forming trigonal planar CuS_3 (II) and distorted square pyramidal BiS_5 units (III) by the S atoms (yellow). These structures were reproduced using VESTA software [4].

Makovicky et al. [205] found that Cu_3BiS_3 undergoes a series of phase transitions, starting from 118.5°C, that involve reorganization of the Cu distribution with their conversion from a stationary to a mobile state, turning the compound into a solid electrolyte at relatively low temperatures. This may be a problem for application in pure photovoltaic devices. Application in combined PV-thermal solar devices may be necessary to keep the operating temperature low [206]. Its *p*-type conductivity was first considered by Nair et al. [84] as a quality for potential applications in single heterojunction thin film solar cells. The optical and electrical properties recently reported by Mesa et al. [207] seem to confirm this potential. The material has a direct forbidden band gap of 1.4 eV [208] that matches the Shockley-Queisser requirements [32]. Nevertheless, the structural peculiarity of Cu_3BiS_3 makes its adaptation to well-established solar cell technologies a scientific challenge.

Thin films of crystallographically pure Cu_3BiS_3 have been synthesized by annealing diffusion couples of chemical bath deposited Bi_2S_3 and CuS layers [84] as well as chemical bath deposited CuS and thermally evaporated Bi layers [209]. A one-step reactive sputter deposition route was developed by Haber et al. [208] for the production of Cu_3BiS_3 films with optical, electrical and morphological properties that are ideal for incorporation into devices. A combinatorial strategy for rapid device screening was reported to be in progress [76, 136], but no results have been published yet. Previous work by the same group [147] on a two-step synthesis process using metal and metal sulfide precursors demonstrated complete conversion into the phase pure ternary chalcogenide under H_2S, but the morphology of the films was found to be unsuitable for use in photovoltaics. Best results were achieved with co-sputtered precursors at processing temperatures as low as 270 °C, but with very long heating times (> 16 h). According to this [147] and to a previous report [155], the useful range of processing conditions for the formation of the ternary chalcogenide is limited by the volatility of Bi above 300 °C, since treatments at higher temperatures resulted in Bi depletetion.

Following the approach taken previously on the study of the $CuSb(S,Se)_2$ system (chapter 2), the present chapter describes the deposition of Cu-Bi metal precursors (section 3.1) and their subsequent conversion into Cu_3BiS_3 (section 3.2.1) and $CuBiS_2$ (section 3.2.2) thin films. The morphological, compositional (section 3.3), structural (section 3.4) and photoelectrochemical (section 3.5) assessments are also reported. The essential experimental details are reported in section 3.6.

Part of this chapter is based on published results [41].

3.1 Cu_3BiS_3 and $CuBiS_2$ thin film precursor deposition

3.1.1 Evaporation and RF co-sputtering of Bi and Cu-Bi thin films

Films of metallic Bi were vacuum-evaporated onto soda lime glass substrates, similarly to the Sb case (section 2.1.1), in order to study the kinetics of phase formation during sulfurization. Thin film metal precursors with Cu:Bi elemental ratio 1:1 were provided by our colleagues Ian Forbes and Pietro Maiello from Northumbria University. They were deposited on Mo-coated glass substrates at room temperature by RF magnetron sputtering with 5N purity Cu and Bi targets in the presence of high purity Ar plasma. Cu and Bi were co-sputtered with the intent to produce a thin film precursor for the conversion to a 2 μm thick $CuBiS_2$.

3.1.2 Sequential electrodeposition of Cu/Bi/Cu thin films

Sequential electrodeposition of Cu/Bi/Cu layers with an overall Cu:Bi ratio of 3:1 was carried out by Stefan Schäfer from Enthone GmbH R&D laboratories. The commercially available electroplating solutions employed were Cupralyte 1525 and adapted Stannostar® SnBi for Cu and Bi respectively. The charge cut-off was adjusted as to obtain a precursor thickness of about 1 μm (0.13 μm Cu / 0.26 μm Bi / 0.13 μm Cu), which after conversion to Cu_3BiS_3 should correspond to 2 μm.

3.1.3 Co-electrodeposition of Cu-Bi thin films

Thin films containing both elemental Cu and Bi were also produced via co-electrodeposition from aqueous solutions, similarly to the Cu-Sb case (section 2.1). The substrate employed was RF-sputtered molybdenum-coated soda lime glass provided by Stefan Schäfer from Enthone GmbH R&D laboratories. As for the Cu-Sb co-electrodeposition, a three electrode configuration was employed, but the substrate was held at a rotating disc working electrode (RDE) in order to induce a more uniform mass flux (section 3.6). The reference electrode employed was a

saturated calomel electrode (SCE), while a large Pt foil facing the rotating substrate was used as the counter electrode.

As seen in Fig. 3.1.1, the Cu-Bi phase diagram shows almost complete immiscibility of the two elements in the whole compositional range.

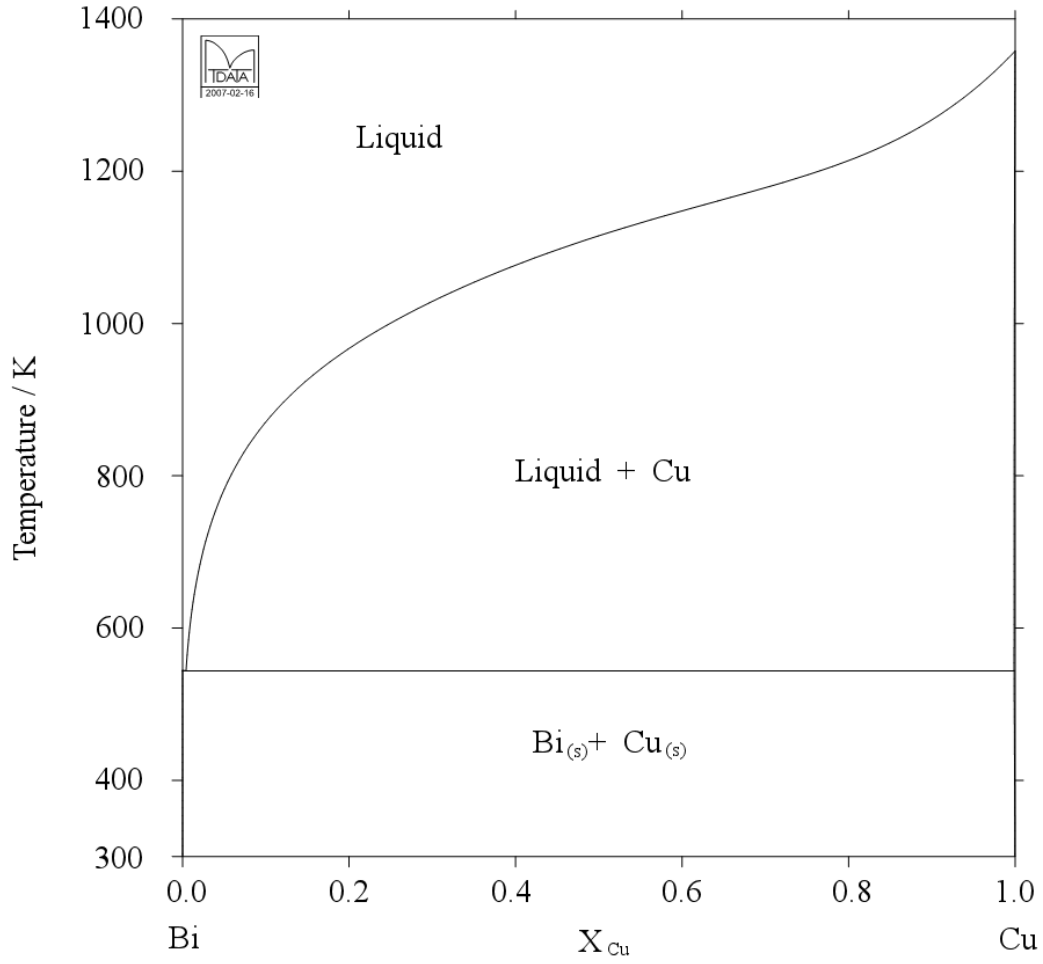

Fig. 3.1.1 Adapted Bi-Cu equilibrium phase diagram calculated using MTDATA, software from the National Physical Laboratory for the calculation of phase equilibria from thermodynamic data [2] (original data taken from [3]).

Nevertheless, co-deposition of these two elements in a disordered or highly intermixed eutectic-like structure is possible in principle [177].

An alkaline electrolytic solution based on the same procedure employed for the Cu-Sb films [184] was employed. Like Sb^{3+}, Bi^{3+} is unstable in water, where it forms the hydroxide $Bi(OH)_3$. However, this white precipitate was found to slowly dissolve in the alkaline solution.

Figs. 3.1.2 shows the electrochemical equilibrium diagram of Bi in water at 25 °C, as taken from Pourbaix [185].

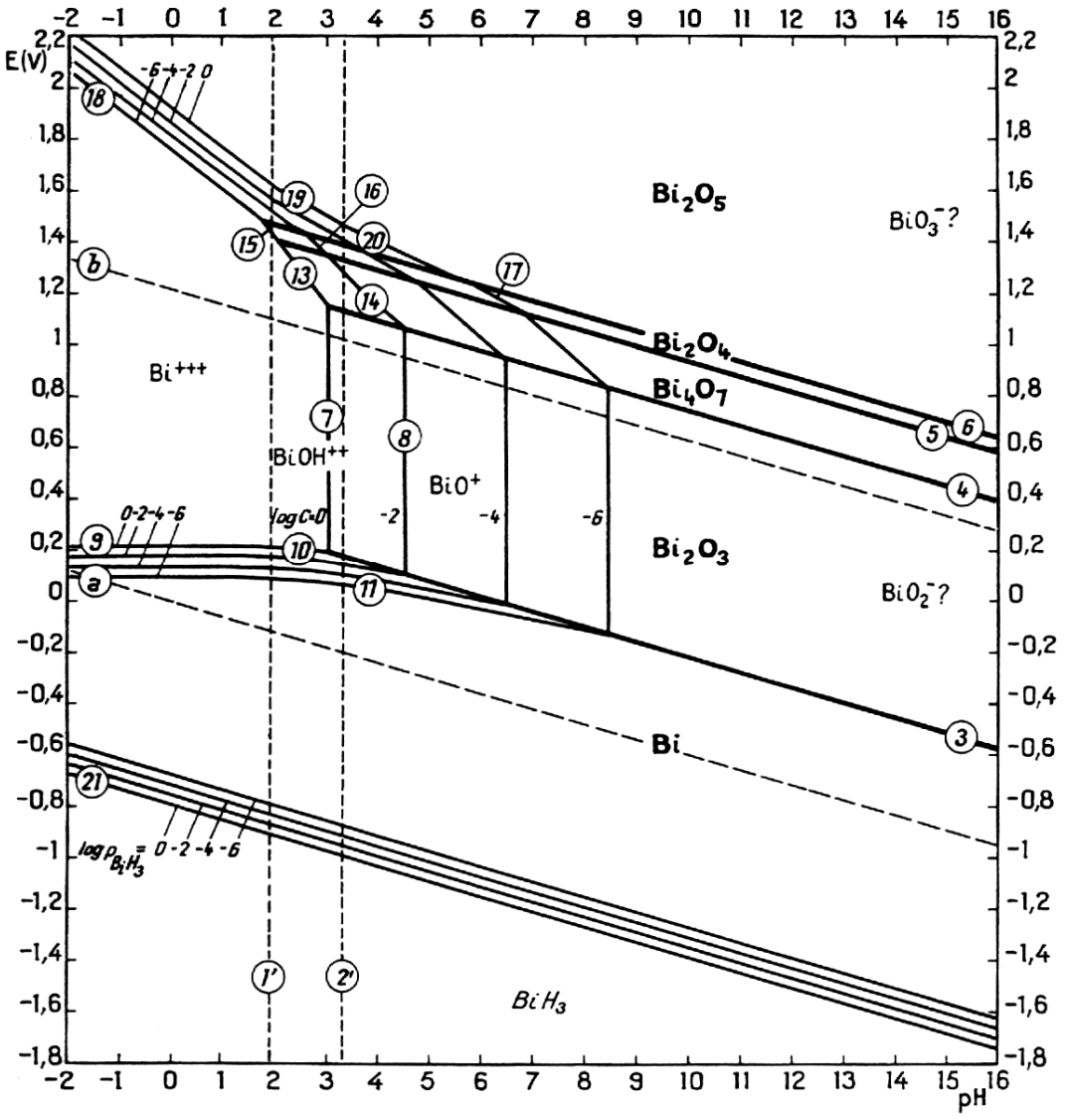

Fig. 3.1.2 Potential-pH equilibrium diagram for the system Bi-H_2O [185]

The composition of the solution employed was: 0.030 M $CuSO_4$, 0.010 M $Bi(NO_3)_3$, 2 M NaOH and 0.1 M D-sorbitol. The electrochemistry of the system was investigated with voltammetric measurements performed using the 4 cm^2 Mo coated glass substrates (Fig. 3.1.3). The substrates were connected to the head of the RDE through Cu wires and masked off with polyimide tape.

Fig. 3.1.3 shows the analyses of 0.010 M $Bi(NO_3)_3$ (a), 0.030 M $CuSO_4$ (b) and of both salts (c) in 2 M NaOH and 0.1 M D-sorbitol aqueous solutions. In agreement with the Pourbaix diagram (Fig. 3.1.2), the reduction of BiO_2^- alone (Fig. 3.1.3a) occurs at about -0.5 V vs SHE, a nobler potential compared to SbO_2^-. The reduction

of the solution containing both Bi and Cu salts (Fig. 3.1.3c) starts at about -0.3 V vs SHE, and saturates roughly at about -0.6 V vs SHE.

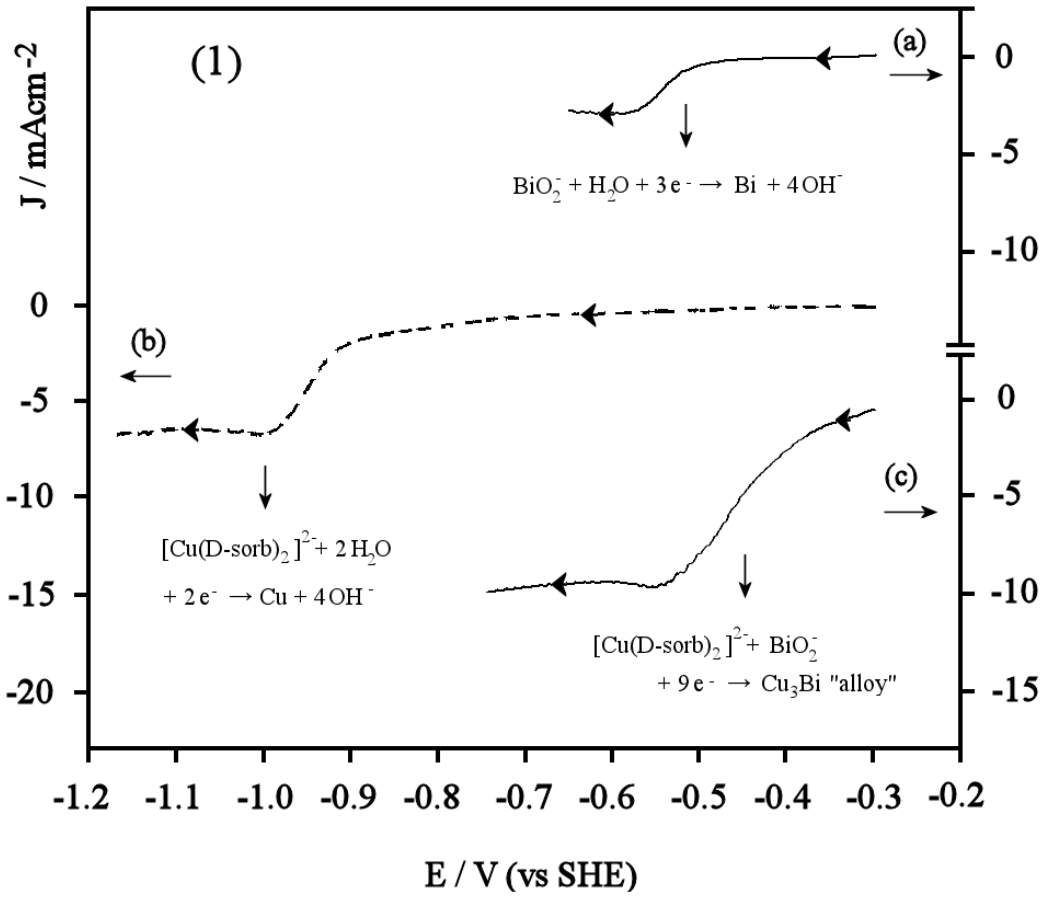

Fig. 3.1.3 Voltammetric measurements at the Mo working electrode of the RDE of 0.010 M $Bi(NO_3)_3$ (a), 0.030 M $CuSO_4$ (b) and both salts (c) in 2 M NaOH and 0.1 M D-sorbitol aqueous solutions. The measurements were performed with a rotation speed of 300 rpm.

The cathodic onset in Fig. 3.1.3c suggests that some uncomplexed Cu^{2+} is being electrodeposited, consistently with the Pourbaix diagram in Fig.2.1.2. Indeed, the potential for Cu^{2+} electrodeposition in the absence of D-sorbitol is very close to the electrodeposition potential of BiO_2^-. No under potential deposition (UPD) is observed. This suggests that Cu and Bi co-deposit without releasing free energy.

The conditions for the formation of a 3:1 Cu:Bi "alloy" film with suitable morphology were found by adjusting the deposition potential maintaining the RDE at 300 rotations per minute. Fig. 3.1.4 shows composition and morphology of Cu-Bi films electrodeposited potentiostatically in the range -0.4 to -0.7 V vs SHE.

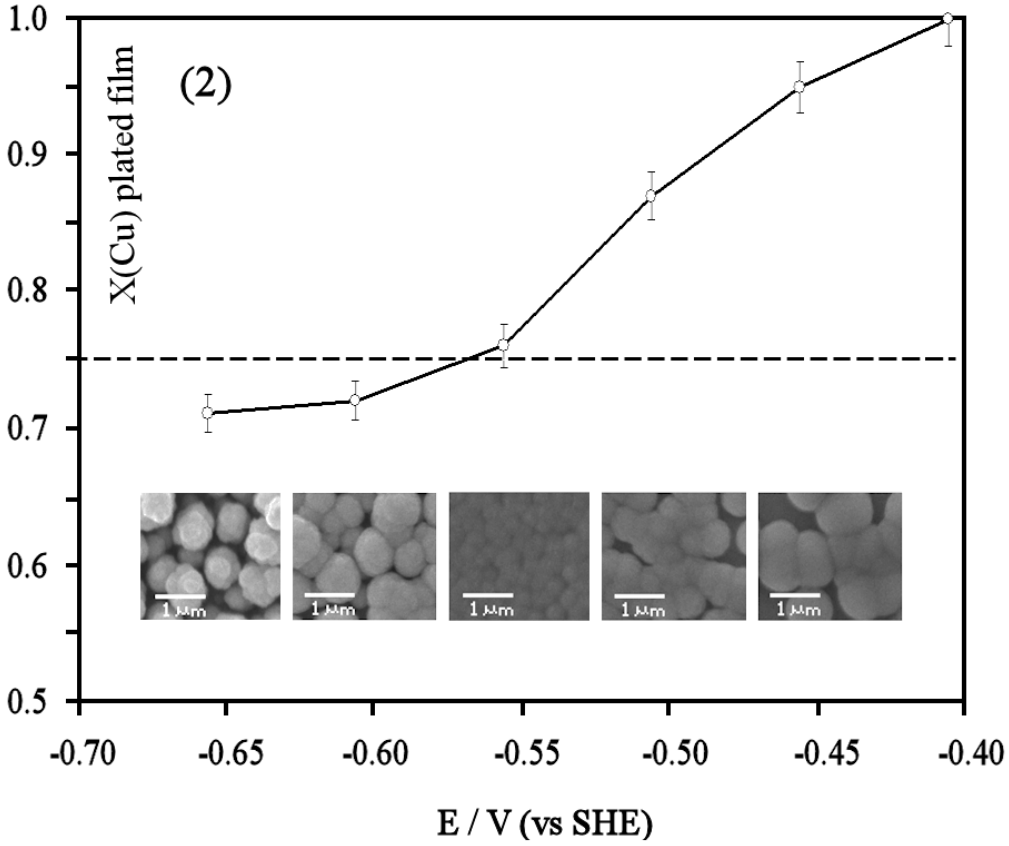

Fig. 3.1.4 Composition dependence of co-electroplated Cu-Bi films obtained potentiostatically in the range -0.4 to -0.7 V vs SHE with corresponding SEM morphologies.

Plating at -0.57 V vs SHE gave films with suitable composition and morphology. The charge cut-off was set to 2.1 Ccm^{-2} in order to attain precursors that can be converted – after complete sulfurization – into 2 µm thick films of Cu_3BiS_3 (i.e. 9 electrons per Cu_3BiS_3 formula unit). Measurement of the thickness of the converted films revealed that this assumption is reasonable (section 3.3).

3.2 Sulfurization of Cu-Bi metal precursors

The conversion of the Cu-Bi metal precursors into Cu_3BiS_3 and $CuBiS_2$ thin films has been performed with two distinct approaches.

3.2.1 Sulfurization via Rapid Thermal Processing

An AS-Micro Rapid Thermal Processor (AnnealSys) (RTP) furnace was employed to study the sulfurization reaction of the Cu-Bi precursors for the synthesis of Cu_3BiS_3, in the presence of elemental sulfur vapour. The system is depicted in Fig. 3.2.1.

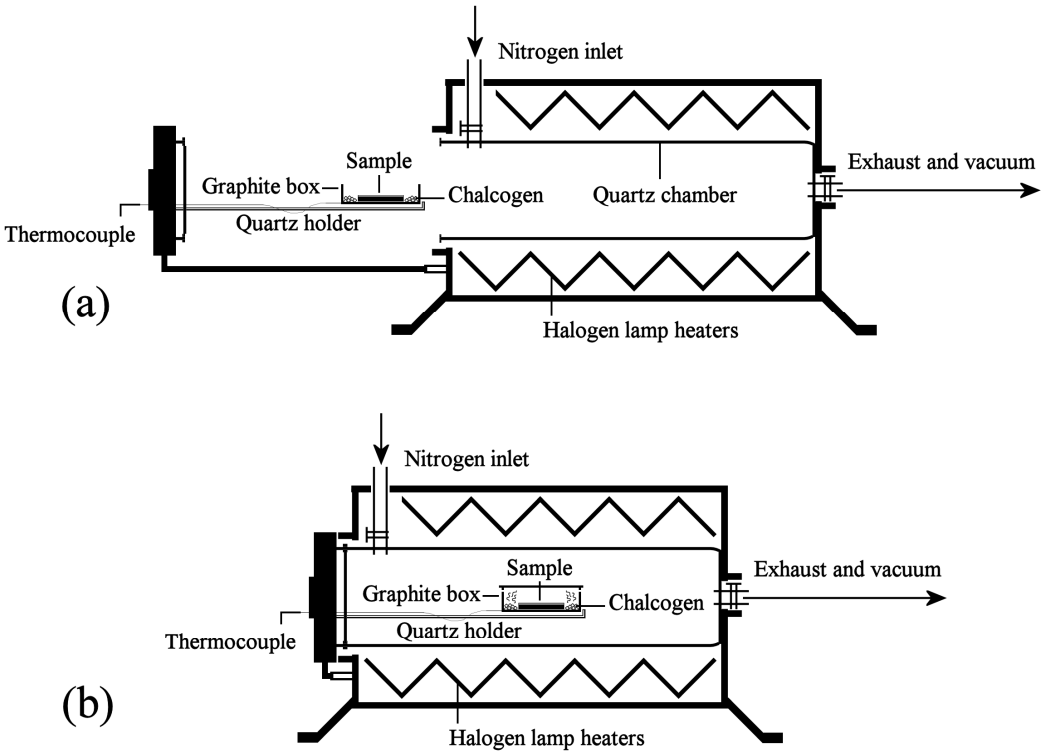

Fig. 3.2.1 Representation of the RTP apparatus employed for the study of Cu_3BiS_3 formation via sulfurization of Cu-Bi metal precursor films. Sample loading (a) and processing (b). (N.B. the exhaust valve is kept closed during processing).

The furnace is composed of a quartz cylindrical chamber (capacity of 1500 cm^3) that can be opened at one end, allowing the loading of sample and chalcogen into a graphite box held on a quartz holder. The heating is performed with powerful halogen lamps that surround the quartz chamber. A thermocouple connected to the

graphite box records the temperature and, according to the latter, the PC-run software adjusts automatically the power of the halogen lamps. The high power infrared source allows to achieve extremely high heating rates (up to 1200 °C·min^{-1}). A forced liquid cooling makes it possible to "quench" the samples with rates up to 600 °C·min^{-1} at the first cooling stages [210]. These are the key features of the RTP system. As we see in chapter 4, such features enable the investigation of the sulfurization kinetics if we assume that samples being quenched at a given temperature after a given dwell time are "frozen", i.e. they preserve the phase composition shown at the quenching temperature.

The system is attached to an Edwards XDS5 oil-free dry scroll pump designed to isolate the vacuum environment from all forms of lubricant and to a N_2 cylinder, so that consecutive vacuum and purge steps can be performed before the treatment in order to minimise the presence of oxygen. This makes it possible to perform the treatments under vacuum (up to 10^{-2} mbar) or in the presence of a N_2 background pressure (up to 1 atm). A detailed modelling of the effect of background pressure on the partial pressure of sulfur within the graphite box has been performed by Scragg [130].

The sulfur partial pressure within the box is not constant during the treatment. This is due to the fact that solid sulfur is loaded in the graphite box with a loose lid (along with the thin film precursors). Upon heating, the sulfur evaporates and, if its quantity is such that the pressure inside the box exceeds the pressure exerted by the lid and by the surrounding atmosphere, the lid lifts and pressure equilibration occurs.
The fraction (F_{eqm}) of sulfur molecules that remains inside the box after equilibration is given by equation 3.2.1 [130].

Eq. 3.2.1 $$F_{eqm} = [p(N_2) + p(S_2)\cdot Vb/Vt] / [p(N_2) + p(S_2)]$$

where $p(S_2)$ is the pressure of $S_{2\,(g)}$ that would be reached within the susceptor if this was kept sealed, $p(N_2)$ is the initial background pressure of nitrogen, V_b is the volume of the susceptor and V_t is the total volume of the system. It is clear that in such conditions the sulfur partial pressure inside the box in lower than it might be expected based solely on the amount of loaded sulfur [211]. More precisely, the pressure is a function of the background pressure inside the chamber.

The modelled partial pressure of sulfur within the graphite susceptor after pressure equilibration reported by Scragg [130] is given by Eq. 3.2.2, Fig. 3.2.2.

Eq. 3.2.2 $p(S_2)_{eqm} = p(S_2) \cdot F_{eqm} = p(S_2) \cdot [p(N_2) + p(S_2) \cdot V_b/V_t] / [p(N_2) + p(S_2)]$

Two limiting cases were identified.

When $p(N_2) << p(S_2)$, the partial pressure of $S_{2(g)}$ is given by Eq. 3.2.3.

Eq. 3.2.3 $p(S_2)_{eqm} = p(S_2) \cdot V_b/V_t = n_S RT/Vt$

where n_S is the number of moles of sulfur loaded in the susceptor, R is the ideal gas constant and T is the absolute temperature.

Figs. 3.2.2a,b show the effect of the background pressure of nitrogen introduced at the beginning of the treatment on the percentage of sulfur that remains in the box (Eq. 3.2.2) after equilibration and on its partial pressure (Eq. 3.2.3), calculated for a typical processing temperature of 500 °C.

Contrary to the conclusions of Scragg [130], in such conditions the pressure of sulfur within the susceptor after equilibration is independent of the susceptor size and depends solely on the initial sulfur load, although it is apparent that the sulfur pressure gets smaller as the volume of the reactor chamber gets larger. However, as the background pressure of inert gas is increased, the smaller the susceptor, the higher the inner $S_{2\,(g)}$ partial pressure after equilibration (Fig. 3.2.2).

The other limit case is when $p(N_2) >> p(S_2)$ (Eq. 3.2.4).

Eq. 3.2.4 $p(S_2)_{\,eqm} = p(S_2) = n_S RT/V_b$

In such conditions the fraction of moles escaping from the box tends to zero, so that the partial pressure of $S_{2\,(g)}$ within the susceptor after equilibration tends to $p(S_2)$ (equivalent to the sulfur pressure that would be reached if the box was kept sealed). This case can be achieved realistically only if the RTP setup is designed to operate at high pressure. Since the maximum operating pressure of the RTP chamber is approximately 1 bar, this limiting case is not relevant. In fact, with a susceptor size of 20 cm^3, $p(S_2)$ would exceed 2.6 bar with just 0.05 g of sulfur load.

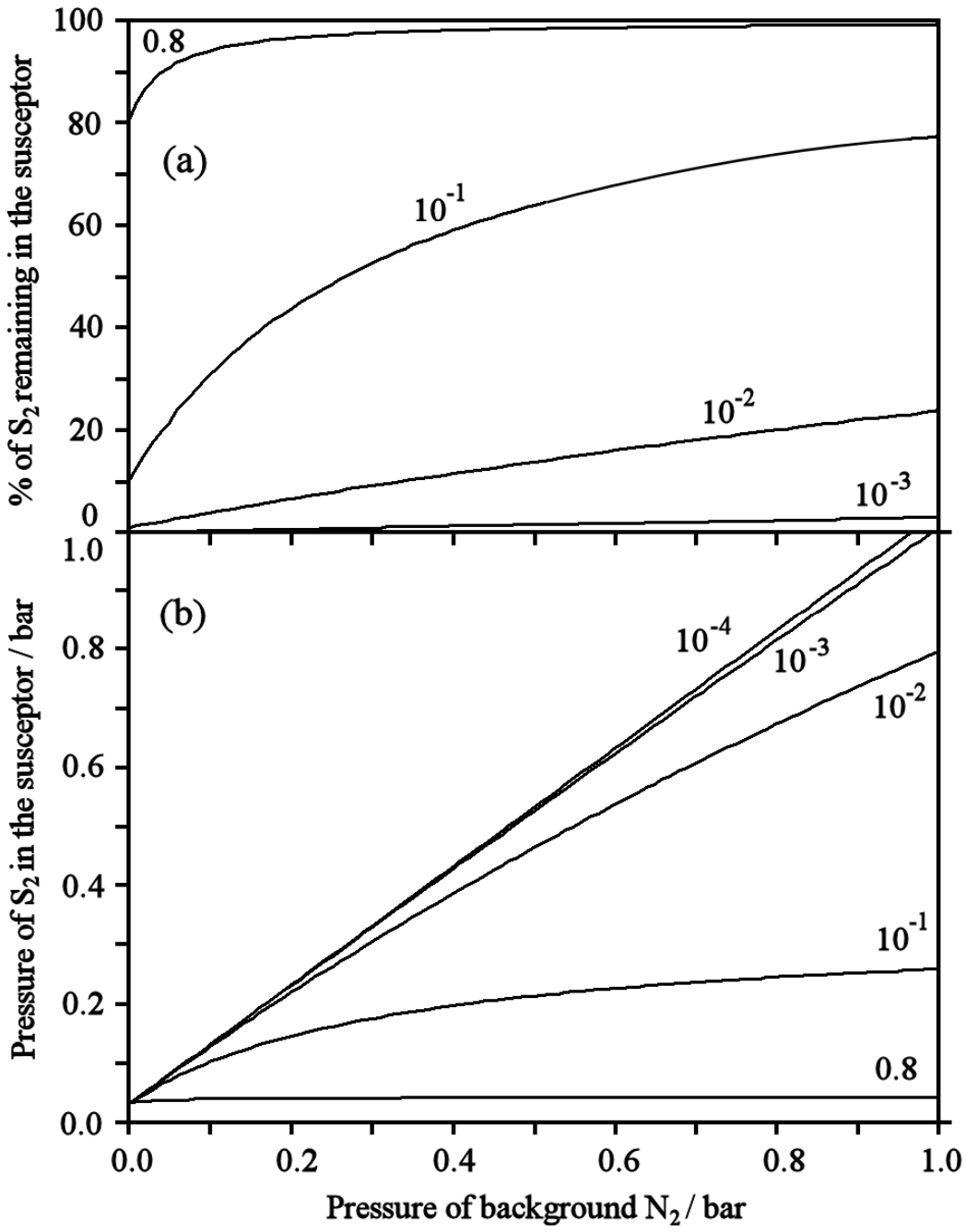

Fig. 3.2.2 Effect of the initial background pressure of nitrogen ($p(N_2)$) on the fraction of $S_{2\,(g)}$ molecules remaining inside the graphite box (a) and on the sulfur pressure ($p(S_2)_{eqm}$) (b) after pressure equilibration, calculated for different susceptor sizes (expressed as V_b/V_t ratoios) at 500 °C.

The variation of the partial pressure of $S_{2\,(g)}$ within the susceptor as a function of the initial N_2 background pressure for a sulfur load of 0.050 g is shown in Fig. 3.2.3 for the susceptor geometry employed in this work.

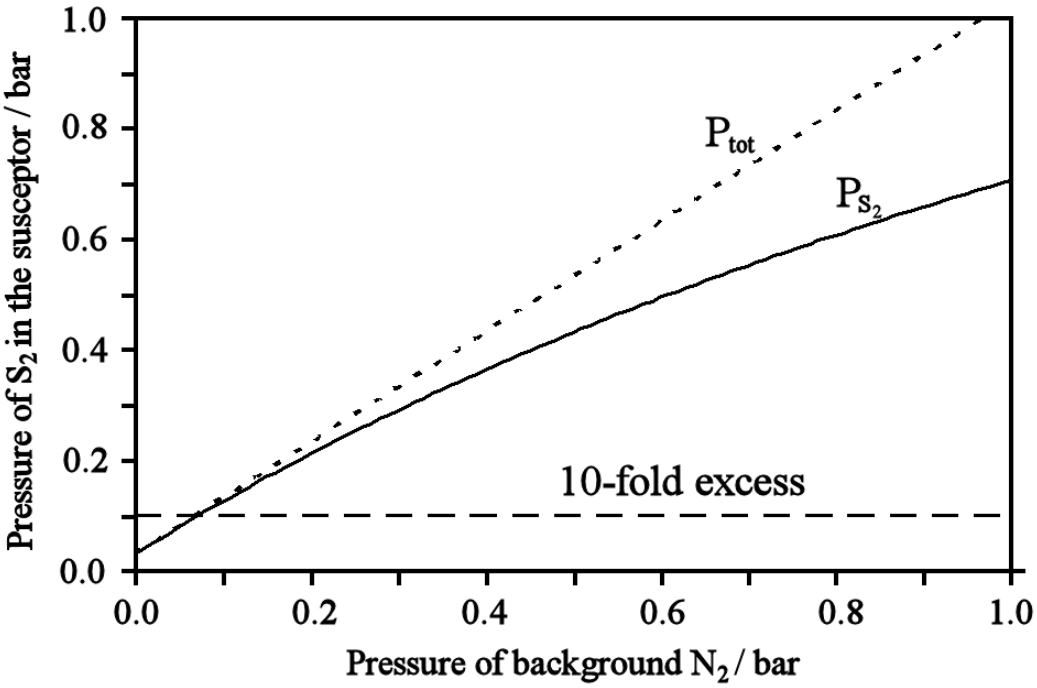

Fig. 3.2.3 $p(S_2)_{eqm}$ as a function of the $p(N_2)$ for a susceptor of 20 cm^3 capacity and with an initial load of 0.050 g of sulfur at 500 °C, as per the experimental conditions employed. The total pressure and a 10-fold sulfur excess pressure are also indicated.

The dashed line in Fig. 3.2.3 represents the $S_{2\,(g)}$ pressure corresponding to a 10-fold sulfur excess per cm^2 of Cu-Bi metal precursor for the production of 2μm thick Cu_3BiS_3 films. Fig. 3.2.3 highlights that the practical range of the starting background pressure of N_2 is ~70÷970 mbar. Sulfurization treatments performed with pressures lower than ~70 mbar might produce sulfur-poor films, while initial pressures higher than ~970 mbar will cause the pressure inside the reactor chamber to exceed 1 bar. Therefore, the investigation of the sulfur pressure effect on the synthesis of the chalcogenide is inherently limited to the range ~100÷690 mbar of $S_{2(g)}$. Wider ranges can only be investigated with RTP systems that support higher pressures.

The treatments were performed in the range 270 to 550 °C with dwell periods in the range 5 - 960 minutes and heating rates between 5 and 600 °C·min^{-1}. A static background pressure of 700 mbar of nitrogen was maintained during annealing, accounting for a nominal pressure of 500 mbar of $S_{2\,(g)}$ within the susceptor at the early stages of sulfurization (Fig. 3.2.3), slowly decreasing to 33 mbar, once the diffusion outside the box is complete. The treatments were adopted also for the evaporated films of plain Bi on soda lime glass, similarly to the Sb case (section 2.1).

3.2.2 Sulfurization with H_2S and S in a conventional tube furnace

Conventional resistive heating with the same wire-wound quartz tubular furnace employed for the synthesis of the Cu-Sb chalcogenides, was adapted to produce $CuBiS_2$ in the presence of either elemental sulfur vapour or H_2S. The treatment was performed in a different graphite box, in order to prevent potential Sb contamination from the previous experiments. The procedure employed is very similar to the one described in section 2.2, but the treatments were performed in moderate vacuum (10^{-3} bar), and no nitrogen flux was used. Fig. 3.2.4 shows a schematic representation of the sulfurization procedure.

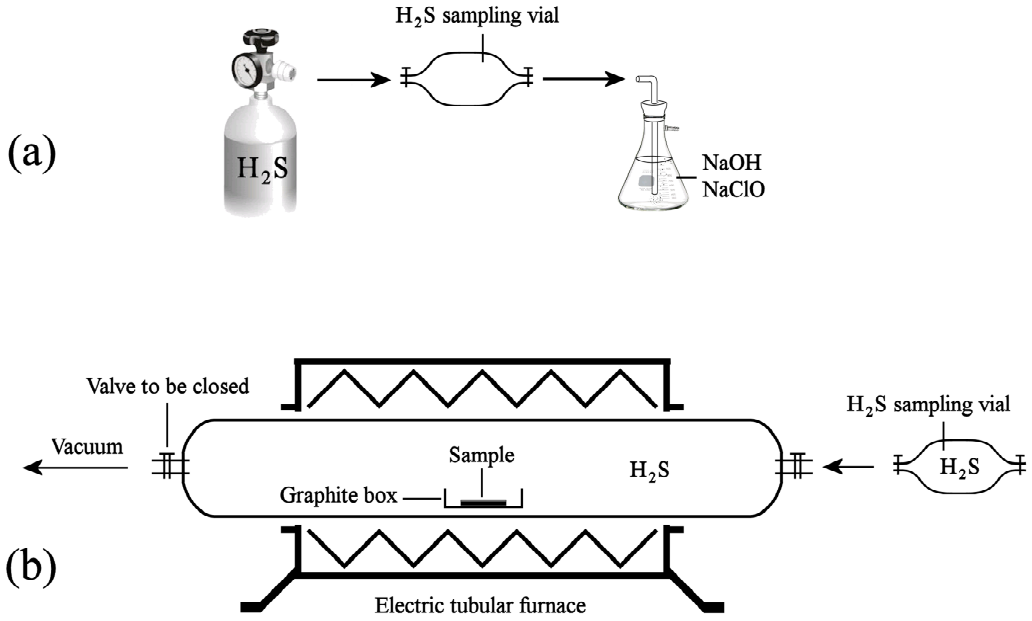

Fig. 3.2.4 Representation of the setup for H_2S sampling (a) and for the sulfurization with H_2S in the tubular furnace under moderate vacuum (b). The built-in thermocouple is located outside the quartz tube at the centre.

H_2S was sampled from a lecture bottle into vials of various capacities, allowing a minimum overflow through a gas scrubber immersed into a 1:4 solution of NaOH plus NaClO (pH > 12) to ensure complete reaction avoiding any hazardous release (Fig. 3.2.4a) [212]. The H_2S sample was then transferred into the quartz tubular furnace where a vacuum of about 10^{-3} mbar was previously established (after several vacuum / N_2 purge steps and after insertion of the precursor film) (Fig. 3.2.4b). After closing the valve, the system was ready for the H_2S treatment.

A heating rate of 10 °Cmin^{-1} was employed for these treatments, and samples were left at the maximum temperature between 5 and 180 minutes, after which they were allowed to cool down naturally to room temperature (with no control). The effect of the partial pressure of H_2S on the phase evolution was examined by sampling the gas with vials of either 94 or 9.8 cm^3 capacity. These correspond to partial pressures of 116 or 13.5 mbar respectively within the tube furnace (calculated at 298 K).

The same treatments were also performed with elemental sulfur under virtually the same conditions (Fig. 3.2.4b), in order to compare the different behaviour of these two sulfurizing reagents for the conversion of the precursor films. The sulfurization temperatures investigated were: 300, 400 and 500 °C.

3.3 Morphology and composition of Cu-Bi-S thin films

The morphological and compositional analyses of the Cu-Bi-S films were performed with a Jeol 6480LV SEM connected to an INCA x-act EDS microprobe. The Cu:Bi elemental ratios of the metallic precursors and sulfurized samples were estimated with acquisition of the X-Ray spectra obtained with an accelerating voltage of 20 kV. The M_α line of Bi and L_α line of Mo are just 0.13 keV apart, but the resolution of the microprobe is enough for the two contributions to be discerned quite well with the software deconvolutions. Localised EDS analyses averaged over several points across the film surface were found to be reasonably consistent (± 2% at. for Bi) with those obtained by Flame atomization Atomic Absorption Spectroscopy (FAAS AAnalyst 100 – Perkin Elmer) on samples dissolved in concentrated HNO_3:HCl 1:1 solution. Therefore, the EDS method was mainly employed for practical reasons. It was not possible to discriminate the contributions of Mo and S from the EDS spectra obtained from plane view interrogation, because the energy difference between the M_α line of Mo and the K_α line of S is too small (0.015 keV). Discrimination was only possible by matching the compositional line scan performed on the cross section of the films and the micrograph. The cross sectional preparation was performed embedding the samples in carbon-loaded resin with a Bühler moulding unit and polishing up to a 0.1 μm alumina finish (Streuers) with a Metaserv rotary polishing machine.

3.3.1 Co-electroplated Cu-Bi films

Cu-Bi co-electroplated metal precursor layers with a thickness up to 2 μm could be easily deposited, as shown in Fig. 3.3.1. The grains have an even size distribution and show a reasonably uniform composition which is slightly Cu poor (Cu:Bi molar ratio 2.6±0.2). From the charge cut-off and the thickness of the films, it was inferred that the co-deposited films are around 60% less dense than bulk Cu and Bi, suggesting the presence of porosity at a nanoscale level that is not detectable with the SEM. Such a porosity may arise from H_2 evolution during the electroplating step. Morphological and compositional uniformity are suitable for the subsequent sulfurization treatments.

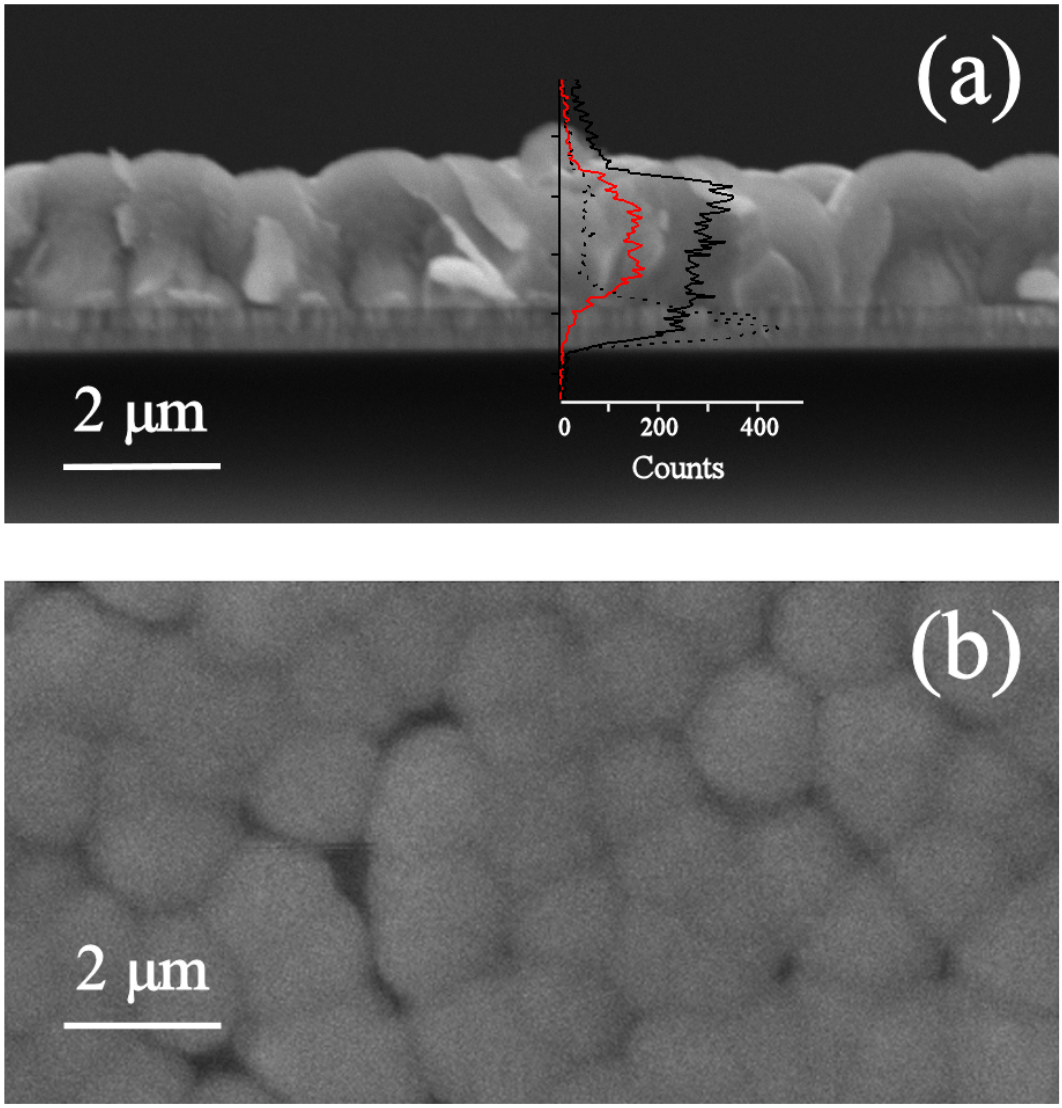

Fig. 3.3.1 SEM cross section (a) and top view (b) of a (Cu_3Bi) precursor as-deposited at -0.57 V vs SHE with a charge cut-off of -2.1 Ccm^{-2}. The inset shows the EDS compositional profile corresponding to Cu K_α (red), Bi M_α (black) and Mo L_α (dotted), performed on the same sample embedded in carbon loaded resin [41].

3.3.2 Cu-Bi films sulfurized with elemental sulfur (RTP)

The co-electroplated and stacked films of Cu-Bi had the same colour after sulfurization for 5 minutes with elemental sulfur vapour. The specimens were dark blue up to 450 °C and dark/light grey after treatments at 500 and 550 °C respectively. However, it was noticed that if the heating rate employed was high (600 $°Cmin^{-1}$), the films obtained from the co-electroplated precursors suffered from poor uniformity and adhesion.

Fig. 3.3.2 shows the SEM/EDS analyses of the Cu-Bi precursor films sulfurized with the RTP. Fig 3.3.2a-d and 3.3.2e-h correspond to stacked and co-electroplated

precursors respectively. These samples were sulfurized with a heating rate of 600 °Cmin^{-1} at 270 (a,e), 350 (b,f), 450 (c,g) and 500 °C (d,h) for 5 minutes (except sample f, that was sulfurized for 30 minutes).

Regardless of the precursor type, samples sulfurized at 270 °C (a,e) show a very similar surface morphology comprised evenly of crystals with euhedral features identified by the EDS microprobe as CuS (Fig. 3.3.2). This situation resembles closely what was found in the Cu-Sb system (section 2.3).

The morphology of the stacked Cu-Bi precursors sulfurized between 270 and 500 °C (Fig. 3.3.2b-d) changes gradually, the surface crystals get slightly smaller and they assume a rounder shape. The EDS spectrum of sample (d) sulfurized at 500 °C shows the presence of Cu and Bi in the ratio 3:1. On the other hand, the co-electroplated Cu-Bi films sulfurized with high heating rate at temperature higher than 270 °C (Fig. 3.3.2f-h) show a sharp variation of the morphology. The films are no longer microscopically uniform, and the underlying substrate is uncovered over a large fraction of the sample area (Fig. 3.3.3). Nevertheless, the average EDS spectrum of the grains of sample (h) sulfurized at 500 °C is consistent with the composition of the analogous sample obtained from the stacked precursor film (d), i.e. Cu:Bi = 2.6±0.2.

By lowering the heating rate to 5 °Cmin^{-1} and extending the dwell time to 30 minutes the morphology of the resulting films was greatly improved (Fig. 3.3.2i,l), and also the co-electroplated precursors were converted into uniform sulfide films with average grain size of ~1 μm. The composition of such films is very similar to that of other films sulfurized at the same temperature but with high heating rate.

Fig. 3.3.4 shows the cross sectional SEM views of a stacked Cu:Bi 3:1 precursor sulfurized at 270 °C (a) and of the co-electroplated film after sulfurization at 500 °C with 600 °Cmin^{-1} (b) and 5 °Cmin^{-1} heating rates (c).

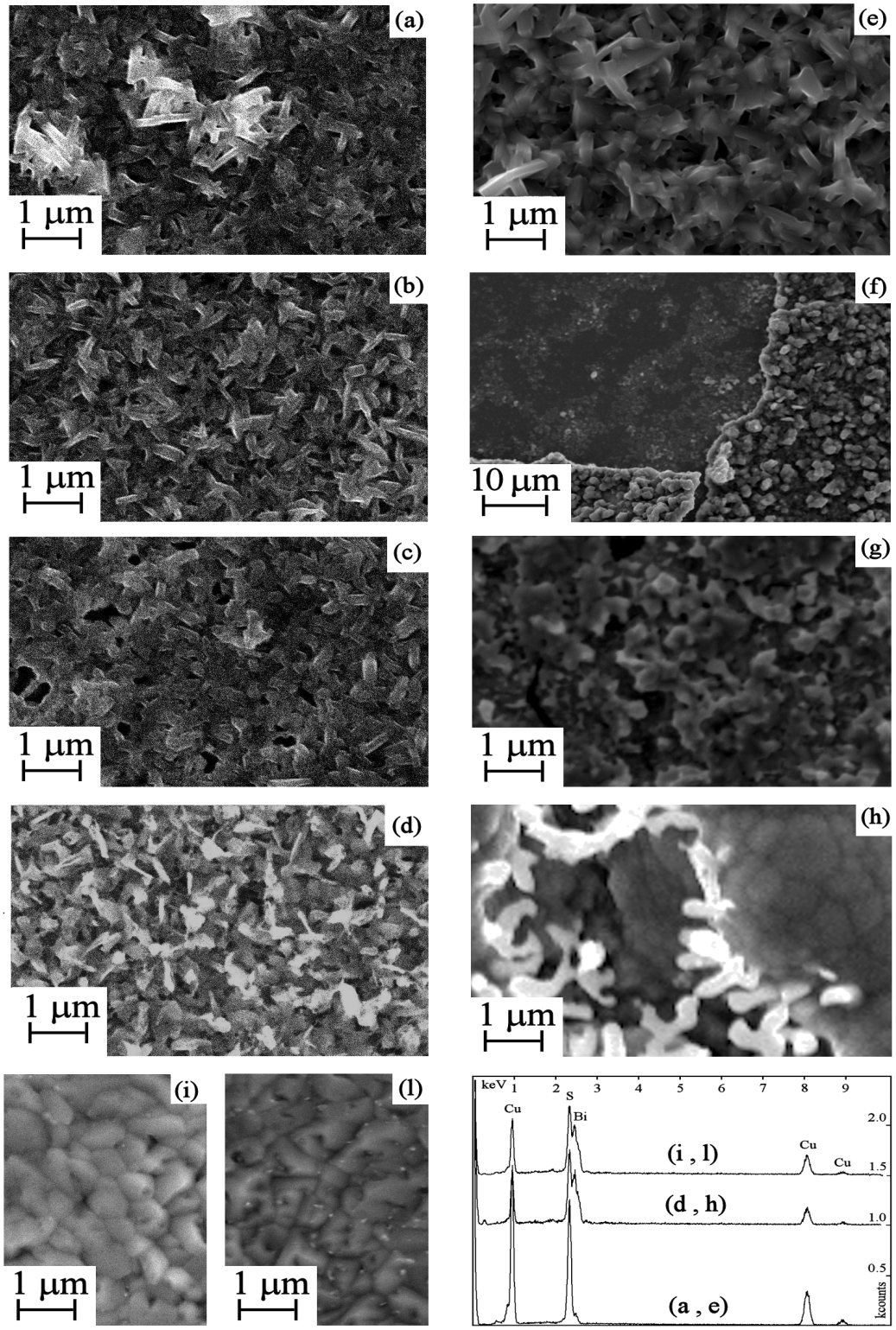

Fig. 3.3.2 SEM analyses of the Cu-Bi stacked (a-d) and co-electroplated (-0.57 V vs SHE with a charge cut-off of -2.1 Ccm^{-2}) (e-h) precursor films sulfurized with heating rate of 600 °$Cmin^{-1}$ at 270 (a,e), 350 (b,f), 450 (c,g) and 500 °C (d,h) for 5 minutes (30 minutes for sample f). Morphology of the stacked (i) and co-electroplated films (l) sulfurized at 500 °C at a rate of 5 °$Cmin^{-1}$ with 30 minutes plateau. The EDS spectra of samples (a,e), (d,h) and (i,l) are also shown.

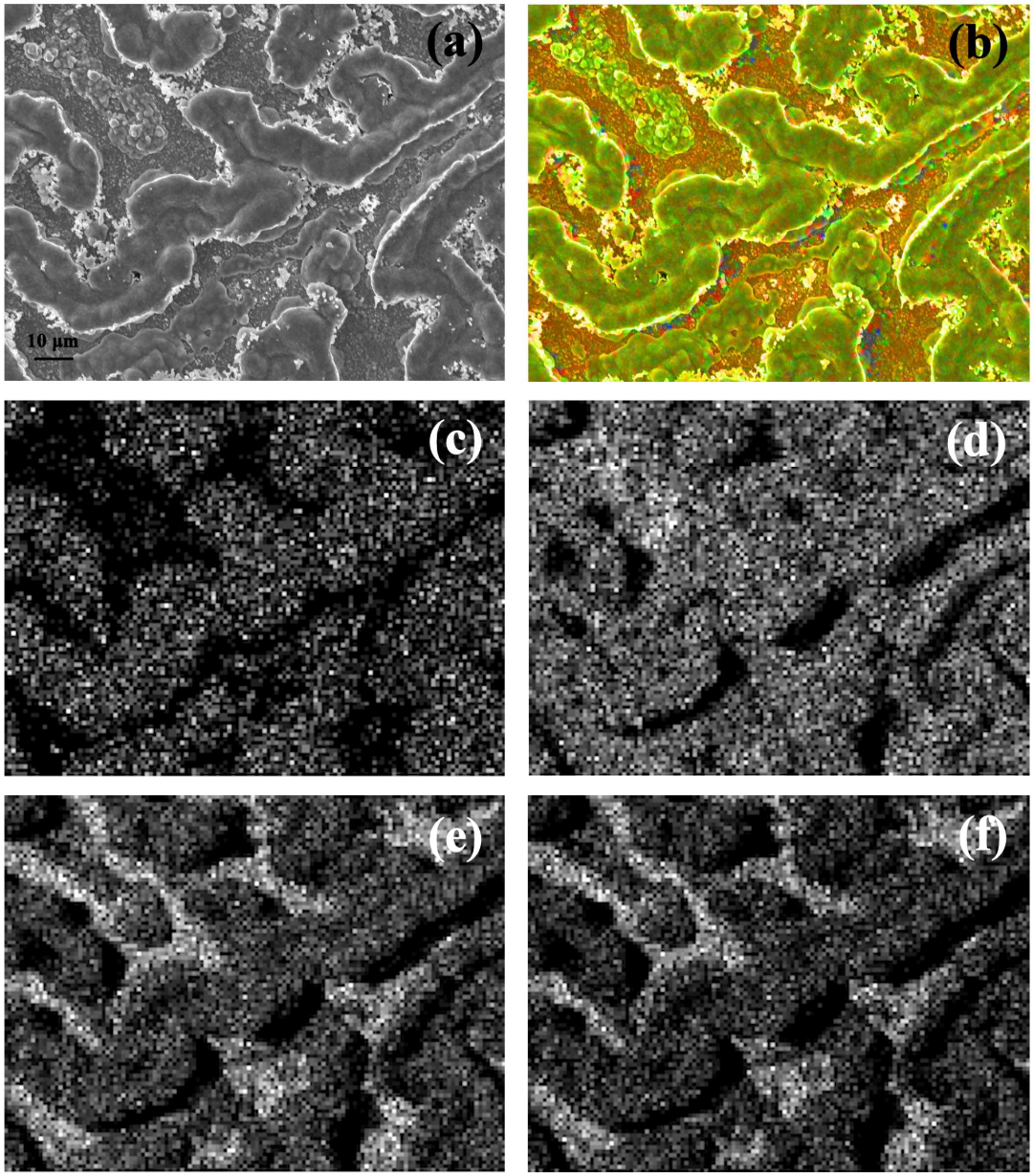

Fig. 3.3.3 (a) Secondary electron micrograph of a co-electroplated Cu:Bi 3:1 precursor sample (plated at -0.57 V vs SHE with a charge cut-off of -2.1 Ccm^{-2}) sulfurized at 500 °C for 5 minutes (heating rate: 600 $°Cmin^{-1}$); (b) overlaying of (a) with X-ray signals chromatically depicted in the range 2.2÷3.0 keV including L_α, K_α and M_α lines of Mo, S and Bi respectively. EDS maps of (a) relative to: K_α line of Cu (c), M_α line of Bi (d), K_α line of S (e) and L_α line of Mo (f) [157].

As seen from the top view images, cross sections of the films sulfurized up to 270 °C reveal a relatively homogeneous structure, while the co-electroplated films sulfurized rapidly at 500 °C have a very uneven morphology, with thickness ranging from ~ 5 to 0 µm. However, Fig. 3.3.4c shows that the sulfurization at 500 °C with heating rate of 5 $°Cmin^{-1}$ lead to compact films with homogeneous lateral compositional profiles (as assessed with EDS line scan).

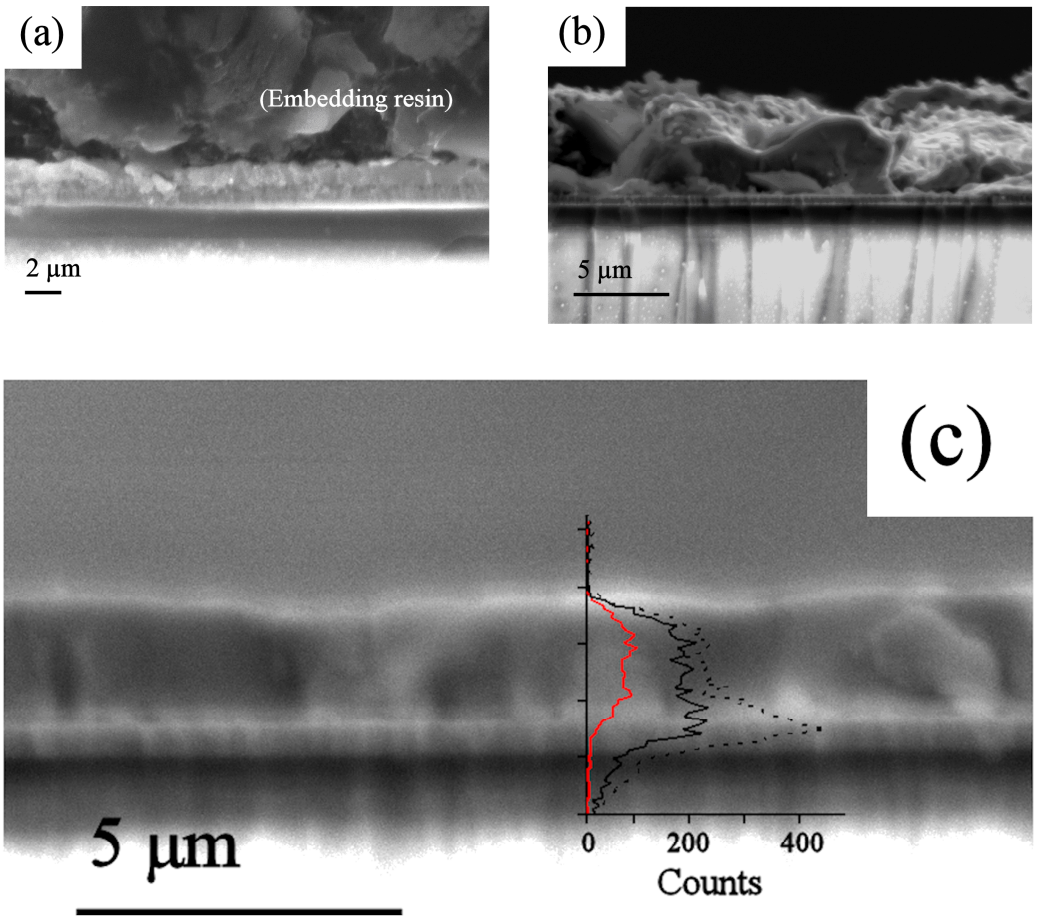

Fig. 3.3.4 Cross sectional views of the Cu/Bi/Cu stacked precursor sulfurized at 270 °C for 5 minutes with heating rate of 600 °Cmin^{-1} (a) and of the co-electroplated film (at -0.57 V vs SHE with a charge cut-off of -2.1 Ccm^{-2}) sulfurized at 500 °C for 5 minutes with heating rate of 600 °Cmin^{-1} (b) and for 30 minutes with heating rate of 5 °Cmin^{-1} (c). The EDS compositional profile in (c) shows the signals of Cu K_α (red), Bi M_α (black) and Mo L_α + S K_α (dotted) [41].

The thickness of the film in Fig. 3.3.4c is ~1.8 µm, revealing that the precursor did not undergo appreciable volume expansion during the slow conversion to the chalcogenide. A volume expansion of ~94% would be expected, based on the density difference between the bulk metals and the ternary chalcogenide. Nevertheless the thickness of the converted film is in agreement with the charge cut-off that was set during the electrodeposition of the metal precursor. Most probably, this discrepancy arises from the low density of the co-electrodeposited film employed as the precursor (which was found to be about 60% less dense than a stoichiometric mixture of bulk Cu and Bi metals, Fig. 3.3.1).

The preparation of nanoporous metal films can follow different routes, such as template-assisted [213] and dealloying methods [214-216]. In the present work a porous film was obtained serendipitly by co-electrodeposition of Cu and Bi.

At the time when this work was conducted, the use of porous metal precursor for conversion into sulfide films was a novel approach. At the time of writing this thesis, the relevant work by Ribeaucourt et al. [217] on the use of dendritic Cu-In-Ga metal precursors for the formation of CIGSe solar cells was available in the literature.

The fact that limited or no apparent volume expansion occurs during the process of porous precursors seems to present some morphological advantages. Furthermore, the high surface area may have a positive impact on both the gas-solid and solid-solid state reactions involved in the formation of a multinary sulfide. Such aspects are worth of notice and they clearly deserve further studies.

3.3.3 Cu-Bi films sulfurized with hydrogen sulfide or sulfur

Morphological and compositional analyses of the thin film samples obtained via sulfurization of the Cu:Bi 1:1 sputtered metal precursors with either elemental sulfur vapour or hydrogen sulfide are reported in Fig. 3.3.5. Figs. 3.3.5a-c show the morphology of the films sulfurized at 400 °C. Sulfurization with elemental sulfur vapour gave rise to a film with moderate uniformity and prominent roughness (a), while hydrogen sulfide at the same pressure produced films with reduced grain size but improved morphology (b). The treatment with reduced pressure of H_2S lead to a discontinuous film with islands of good morphology and uncovered areas where the Mo substrate can be seen (c). The EDS analysis shows a CuS rich surface for (a), while the compositions of (b) and (c) are very similar and consistent with a Cu:Bi ratio of approximately 1:1, after deconvolution of the Mo and S contriburions. Figs. 3.3.5d-f correspond to the equivalent treatments at 500 °C. The morphology is worse for all cases, compared to the 400 °C treatments, as one may foresee from phase separation subsequent to the eutectoid decomposition of $CuBiS_2$ into Cu_3BiS_3 + $Cu_3Bi_5S_9$ occurring at 475 °C [218]. No phase separation was detected on the cooled samples, but the poor morphology may be a consequence of the eutectoid reaction.

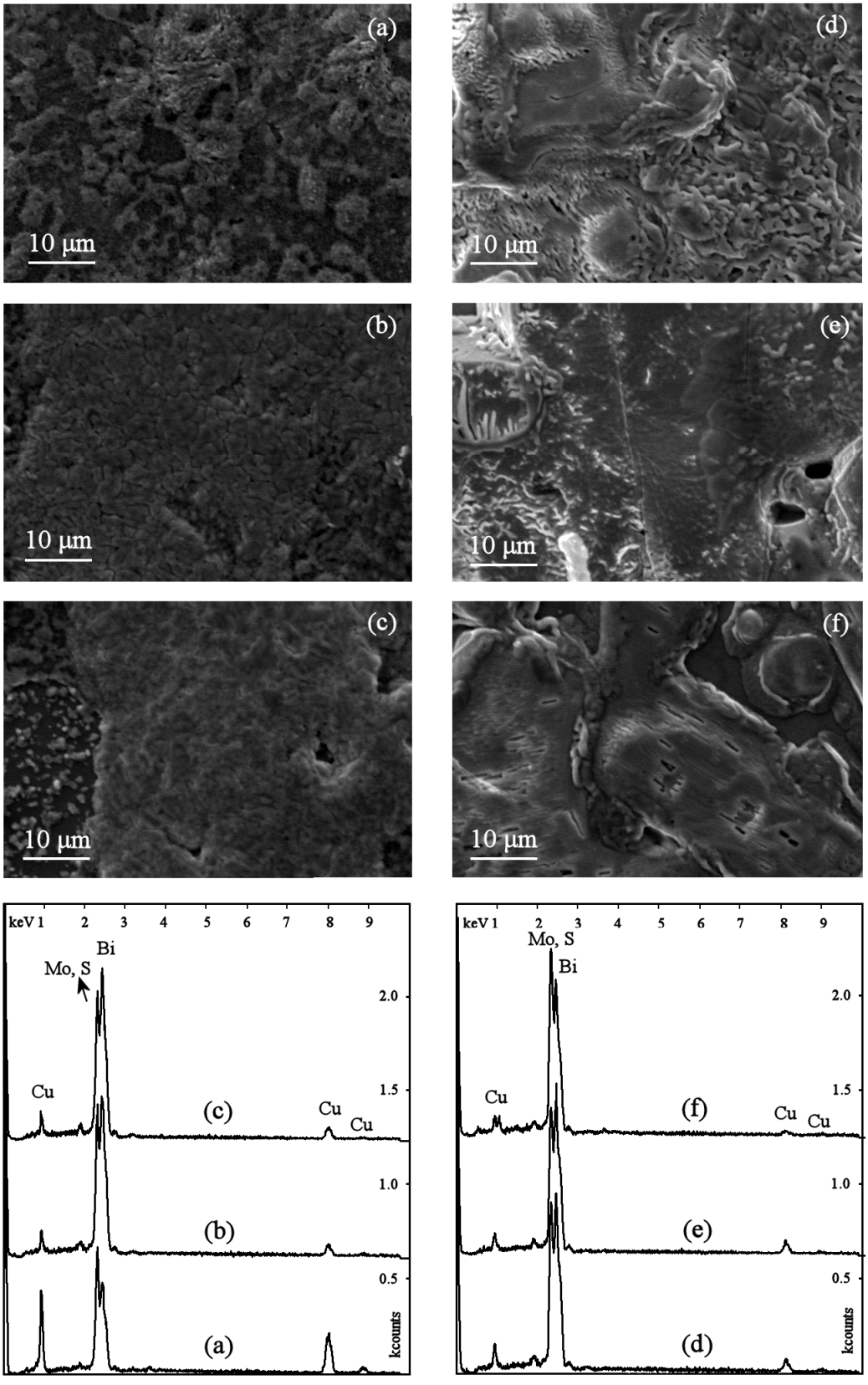

Fig. 3.3.5 Secondary electron images of the sputtered Cu:Bi 1:1 metal precursors after sulfurization at 400 (a,b,c) and 500 °C (d,e,f) with 120 mbar S_2 (a,d) and with 120 mbar (b,e) and 14 mbar H_2S (c,f) for 30 minutes. The corresponding EDS spectra are included.

3.4 Structural characterization of Cu-Bi(S) thin films

A Panalytical X'pert X-ray powder diffractometer was employed for the structural characterization of the as-deposited and annealed electroplated Cu-Bi films (section 3.4.1) and of the samples sulfurized with the RTP furnace (section 3.4.2 and 3.4.3).

3.4.1 Structural properties of annealed electroplated Cu-Bi films

The Cu/Bi/Cu precursor shows the presence of elemental Cu and Bi only, with the XRD spectrum matching the powder patterns of the elements.
XRD spectra of the co-electroplated Cu-Bi films as-deposited and annealed (without sulfur) at 250 and 500 °C for 5 minutes are shown in Fig. 3.4.1.

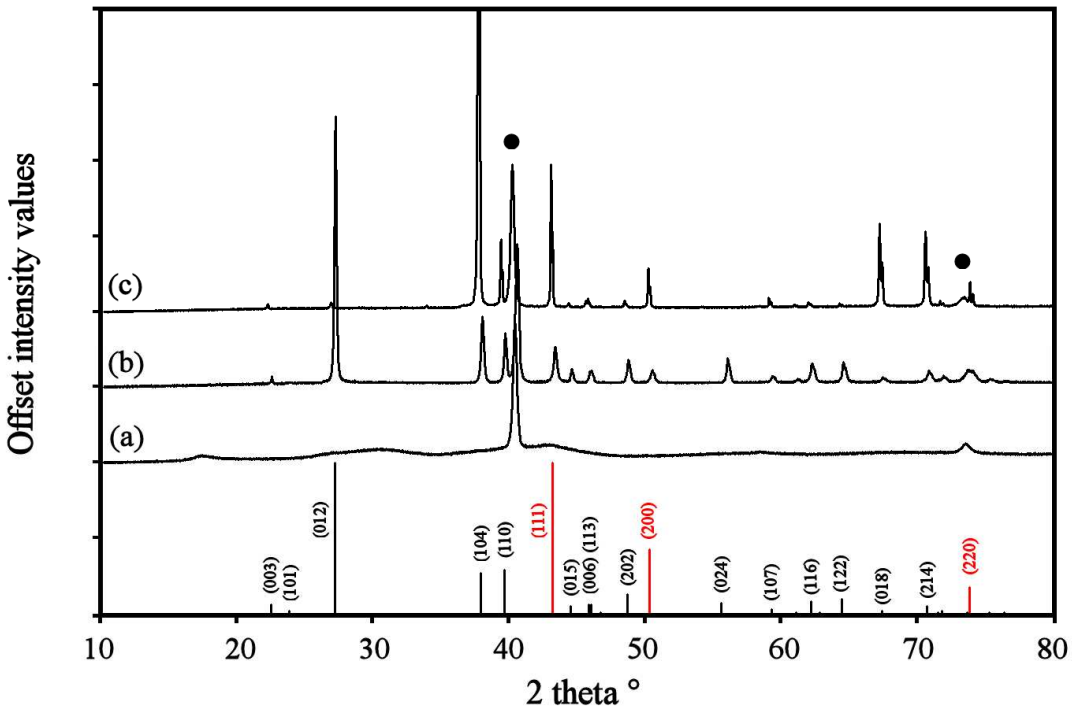

Fig. 3.4.1 XRD spectra of the co-electroplated Cu-Bi precursors as-deposited (at -0.57 V vs SHE with a charge cut-off of -2.1 Ccm^{-2}) (a) and after thermal treatment at 250 (b) and 500 °C (c) for 5 minutes (heating rate: 600 °$Cmin^{-1}$). Standard powder patterns for Bi PDF no 44-1246 (black) and Cu PDF no 70-3038 (red) are included (● labels refer to the Mo substrate) [41].

The as-deposited co-electroplated Cu-Bi precursor shows an XRD spectrum typical of an amorphous material; very broad peaks are seen at ~ 18, 27, 31, 44 and 59 °

(Fig. 3.4.1a), among which only those at 27 and 44 ° are centred in correspondence to Bi and Cu diffractions, while the others do not match the elements' patterns. Such curves might arise from short-range ordered domains [219], whose size and quantity are such that only broad and low diffraction peaks are detectable. On a larger scale, the Cu and Bi atoms within the film are likely to be randomly distributed. Heat treatment at 250 °C for 5 minutes causes the elements in the co-deposit to separate, forming distinct Bi and Cu aggregates which give XRD spectra that match reasonably well with the corresponding powder patterns (Fig. 3.4.1b). Annealing at 500 °C for 5 minutes causes the Bi and Cu aggregates to enlarge, as it is shown by the sharper XRD peaks (Fig. 3.4.1c). The Bi aggregates exhibit strong (104) texturing that may arise from directional crystallisation of Bi caused by the strong cooling rate employed.

3.4.2 Structural properties of sulfurized evaporated Bi films

In order to relate the formation of the ternary chalcogenide to initial conversion of the precursor metals into the corresponding binary sulfides, ex-situ XRD analyses were performed on a series of evaporated bismuth films sulfurized for 5 minutes at different temperatures between 350 and 550 °C (heating rate: 600 °Cmin^{-1}). The analogous treatment on the films of evaporated copper has been discussed for the Cu-Sb system in section 2.4. The previous work showed that Cu can be fully converted to CuS in the presence of elemental sulfur vapour even at temperatures as low as 200 °C, and it was found that its diffraction pattern was consistent with hexagonal CuS (*Covellite*) [146]. The evaporated Bi samples showed a gradual greyscale variation from dark to light as the temperature of the sulfurization treatment was increased. The corresponding series of XRD spectra is shown in Fig. 3.4.2.

The evaporated film of Bi exhibits (*00l*) preferred orientation (fig. 3.4.2a). This is similar to what it was found for the Sb case (Fig. 2.4.1). Sulfurization for 5 minutes up to 350 °C causes the Bi to react partially with sulfur, leading to a mixture of unreacted Bi and Bi_2S_3.

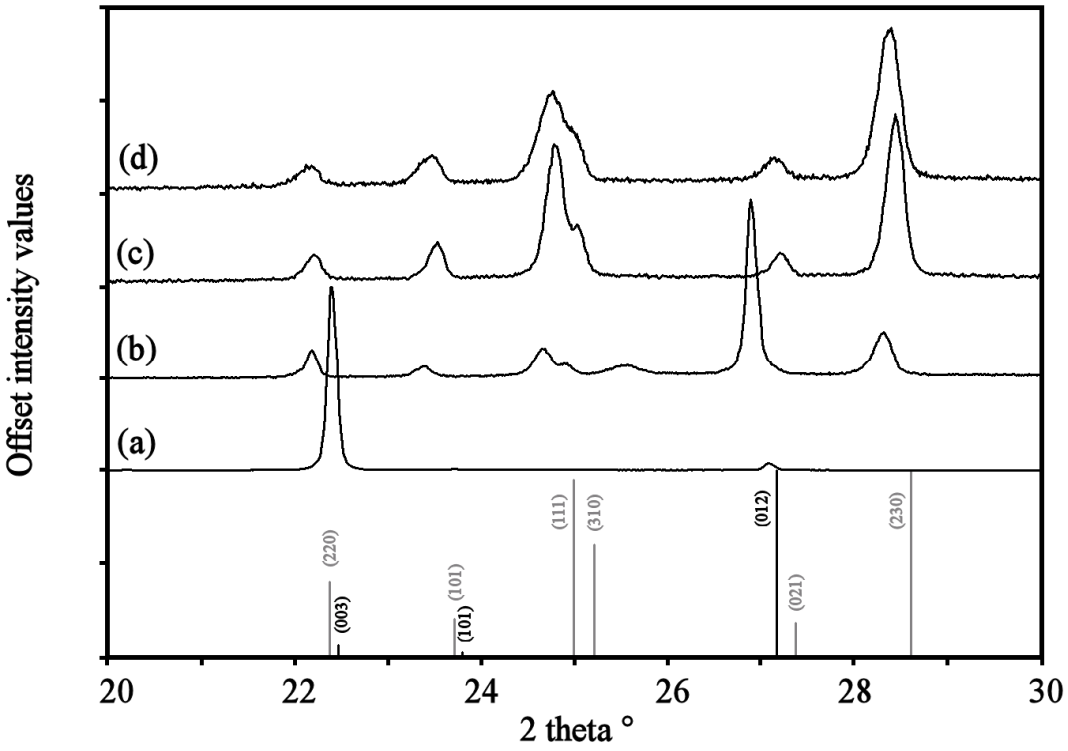

Fig. 3.4.2 Series of XRD spectra of the evaporated as-deposited films of Bi (a) and after sulfurization at 350 (b), 400 (c) and 450 °C (d) for 5 minutes with fast heating rate (600 °C·min^{-1}) (initial sulfur pressure 500 mbar). Standard powder patterns for Bi PDF no 44-1246 (black) and Bi_2S_3 PDF no 6-333 (grey) are included [41]. The substrate employed is soda-lime glass.

It can be observed from Fig. 3.4.2b that the remaining Bi shows a strong (*012*) preferred orientation as opposed to (*001*) for the as-deposited Bi, suggesting that the element has undergone melting and subsequent directional crystallization. It is interesting to note the effect of the different substrate, bare glass or Mo coated glass on the directionality of Bi crystallization, (cf. Fig. 3.4.1).

The sulfurization treatments result in a bismuth sulfide with an XRD spectrum matching that of orthorhombic Bi_2S_3 (*Bismuthinite*), apart from a systematic peak shift towards lower diffraction angles indicative of the presence of expansion strains affecting its lattice. This strain does not seem to be appreciably relieved even if the film is sulfurized up to 550 °C in the time frame of 5 minutes. Since liquid Bi is denser than the solid (in proximity of the melting point) it is probable that Bi_2S_3 formed on the surface of liquid Bi is subject to expansion strains when the substrate of unreacted Bi expands during solidification. Within the 5 minutes period investigated, complete conversion of Bi to Bi_2S_3 occurs at the temperature of 400 °C

(Fig. 2c), when the strong peak at 2θ = 26.9 ° corresponding to the (012) planes of rhombohedral Bi is no longer detectable.

3.4.3 Structural properties of sulfurized electroplated Cu-Bi films

Fig. 3.4.3a,b shows the series of XRD spectra of the sulfurized films obtained from the stacked (a) and from the co-electroplated (b) ternary compound precursors. The standard powder patterns of CuS (*Covellite*), Bi_2S_3 (*Bismuthinite*) and Cu_3BiS_3 (*Wittichenite*) are also shown.

The structural analysis reveals that sulfurization below 400 °C leads only to the binary sulfides, leaving traces of unreacted Bi. For sulfurization at 450 °C, some of the peaks related to the ternary chalcogenide start to appear, but the sample still shows the coexistence of the binary sulfides. At 500 °C, the conversion of the precursors to Cu_3BiS_3 is complete and the treatment at 550 °C does not seem to alter appreciably the structural properties attained at 500 °C.

Comparison of Fig.3.4.3a and Fig.3.4.3b reveals very little dependence of the phase composition of the converted film on the starting precursor configuration. Regardless of whether the stacked or homogenous electroplated films are used as precursor, the formation of the binary sulfides is observed to occur prior to the development of the ternary compound. 5 minute treatments at temperatures above 450 °C resulted in the formation of single-phase films with XRD pattern matching that of Cu_3BiS_3 (*Wittichenite*). Our results are remarkably different from those reported elsewhere on films sulfurized with hydrogen sulfide. In fact, Haber et al. reported that, in order to minimise losses of Bi [155], Cu_3BiS_3 had to be formed at relatively low temperature (270 °C) with a long reaction time (16 hours) in the presence of 6.7 mbar of H_2S [147]. With the sulfurization conditions used in the present work, consisting of an initial sulfur pressure of 500 mbar, up to 16 hours of treatment at the same temperature employed by Haber (270 °C) was insufficient to form the ternary chalcogenide. Furthermore, no appreciable Bi depletion was detected in the films. Even if the treatment was performed at 550 °C for 16 hours, the resulting films were still Cu_3BiS_3 with unaltered lattice parameters. These apparent contradictions between Haber's and our work are discussed in chapter 4.

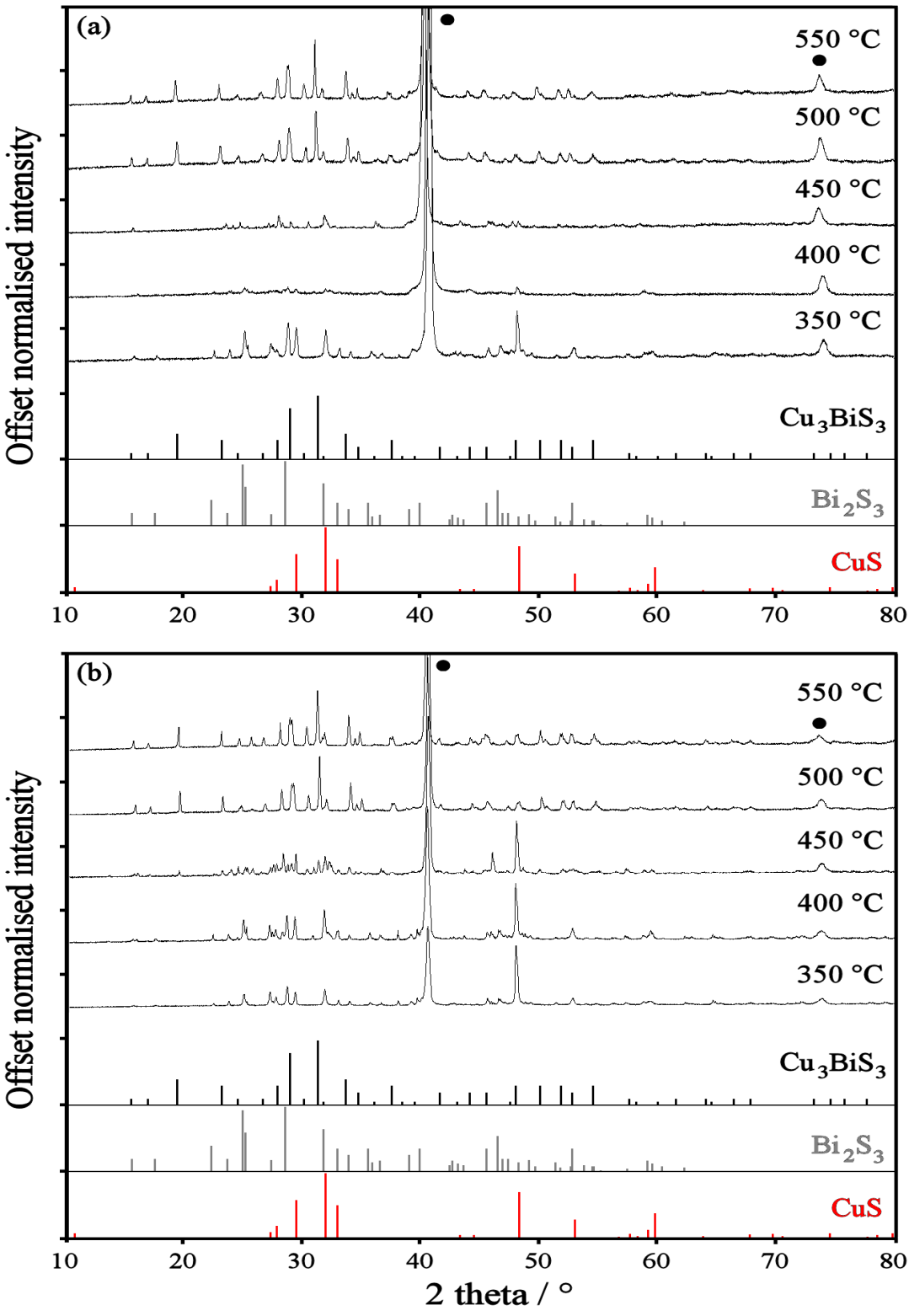

Fig. 3.4.3 Series of XRD spectra of typical Cu/Bi/Cu electroplated stacked (a) and Cu_3Bi co-electroplated (at -0.57 V vs SHE with a charge cut-off of -2.1 Ccm^{-2}) (b) precursors after sulfurization at temperatures between 350 and 550 °C for 5 minutes (heating rate: 600 °C·min^{-1}, initial sulfur pressure 500 mbar). Standard powder patterns of the relevant phases: CuS PDF no 65-3561 (red), Bi_2S_3 PDF no 6-333 (grey) and Cu_3BiS_3 PDF no 9-488 (black) (● labels refer to the Mo substrate) [41].

3.5 Photoelectrochemistry of sulfurized Cu:Bi 3:1 films

The samples obtained by sulfurization of the Cu:Bi 3:1 metal precursor films of the two configurations were characterised photoelectrochemically in order to ascertain their minority carrier type. For this purpose, the same procedures described in section 2.5 were employed. The samples were immersed in a 0.2 M aqueous solution of $Eu(NO_3)_3$ and illuminated with a pulsed white LED while running a cyclic voltammogram. A cathodic photocurrent response was observed that corresponds to the reduction of Eu^{3+} at the surface of the working electrode, showing that the samples are *p*-type.

Similarly to the Cu-Sb case (section 2.5 [146]), the effect of etching by immersion in a 5% wt. KCN solution was tested, to see if improvement of the photoactive properties could be achieved by removal of residual $Cu_{1-x}S$ surface phases. The treatment improved the photoactive properties of the films obtained by sulfurization of the stacked precursors. However, in contrast to the behaviour seen with $CuSbS_2$, etching periods longer than 60 seconds resulted in the sudden and complete suppression of photoactivity. The samples obtained by sulfurization of the co-electroplated precursors were photoactive "as-grown", and etching even with a more dilute solution (0.5% wt. KCN) and even for shorter periods (5 seconds) suppressed their photoresponse.

External Quantum Efficiency (EQE) spectra of the films are illustrated in Fig. 3.5.1. The photoelectrochemical properties of the films are rather poor, with external quantum efficiencies below 12%. Nevertheless, an estimation of the band-gap energy of the compound gives approximately ~1.3 - 1.4 eV, which is consistent with the values reported in the literature [207, 208].

It can be noticed that the onset of the EQE spectra of the samples obtained by sulfurization at low heating rate of the co-electroplated precursor (Fig. 3.5.1b) is sharper than the one of the stacked precursor (Fig. 3.5.1c). The latter was measured after 60 seconds etching, because the photoactive signal of the as-grown film was not detectable. The shape of the EQE spectra of the sulfurized co-electroplated films is similar, although the data corresponding to the sample heated with a rate of 600 °C min^{-1} has been multiplied by a factor of 5 for sake of comparison (note the lower signal to noise ratio). This difference in the magnitude is attributed to the poor

morphology of the co-electroplated films sulfurized with heating rate of 600 °Cmin^{-1}, as it is apparent from Figs. 3.3.2 and 3.3.3.

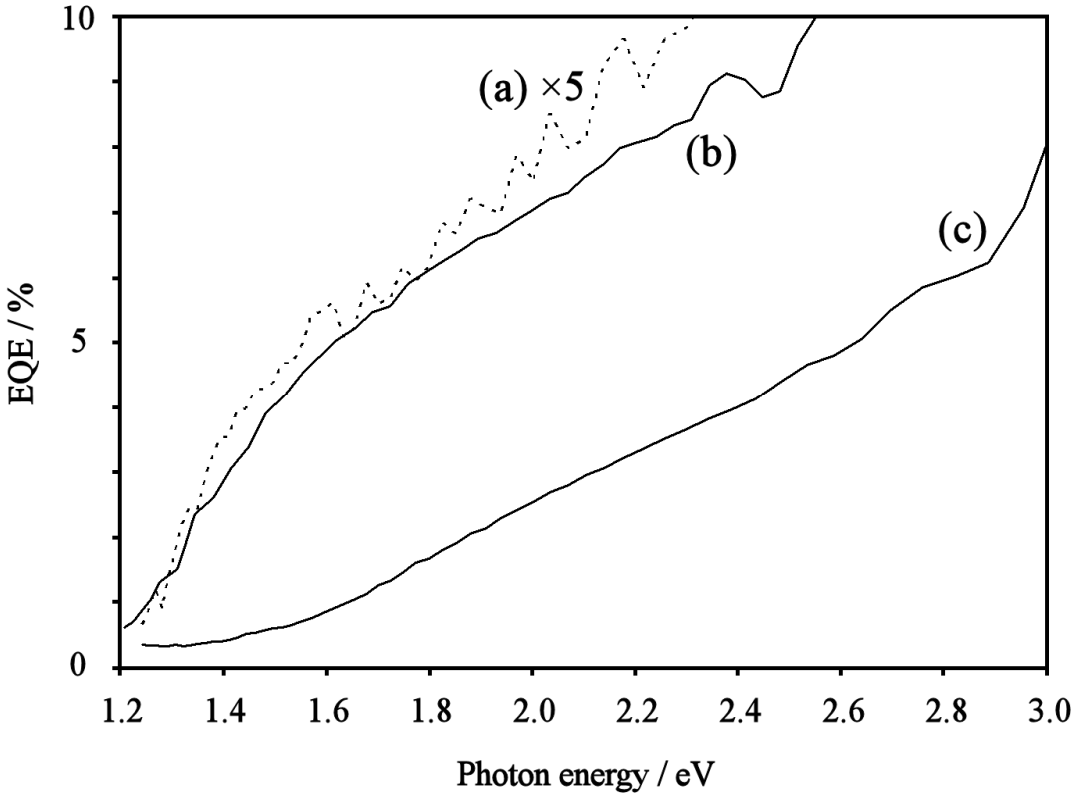

Fig. 3.5.1 EQE spectra of Cu_3BiS_3 films obtained by sulfurization of the Bi-Cu metal precursors at 500 °C for 30 minutes. Co-electroplated precursor (plated at -0.57 V vs SHE with a charge cut-off of -2.1 Ccm^{-2}) sulfurized with heating rate of 600 °C min^{-1} (x5) (a) and 5 °C min^{-1} (b); stacked Cu/Bi/Cu precursor with 60 seconds etching in KCN 5% wt. (c) [41]. Acquisition conditions: 0.2 M Eu^{3+} solution, - 0.5 V vs. Ag/AgCl, chopping frequency 27 Hz.

An order of magnitude estimate for the naturally occurring acceptor density of the Cu_3BiS_3 films produced by sulfurization of the co-electroplated precursors was obtained by analysing the dependence of EQE - measured near the onset region of absorption (photon energy 1.7 eV) - on applied potential.

Fig. 3.5.2 shows a plot of $[\ln(1-\Phi)]^2$ versus E for a typical Cu_3BiS_3 film. The linear section in the onset region has a gradient equal to $2\alpha^2 \varepsilon\varepsilon_0/(eN_a)$, from which N_a can be extracted (see section 1.3 for derivation of such plots).

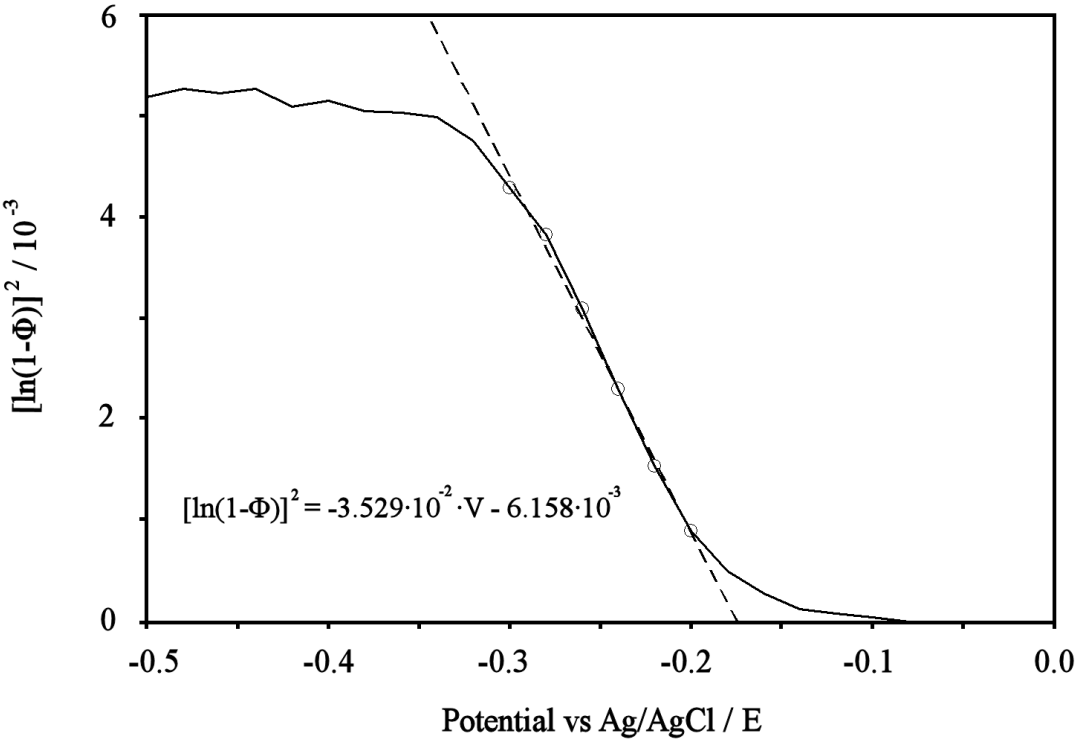

Fig. 3.5.2 Plot of $[\ln (1-\Phi)]^2$ vs applied potential of a typical Cu_3BiS_3 film obtained by sulfurization of a co-electroplated precursor at 500 °C for 30 minutes [41]. Acquisition conditions: 0.2 M Eu^{3+} solution, $h\nu = 1.7$ eV, chopping frequency 27 Hz.

Taking the value of α (at 1.7 eV) reported by Haber et al. [208] (~$6 \cdot 10^4$ cm^{-1}), and a value of ε typical of an inorganic sulfide like $CuInS_2$ (10) [220], gives an acceptor density of ~ $3 \cdot 10^{17}$ cm^{-3}. This is about one order of magnitude higher than that reported by Mesa et al. [221] for Cu_3BiS_3 films obtained by co-evaporation of the elements. For comparison, it is known that typical carrier concentrations of device quality chalcogenide absorbers such as CIGSSe and CZTSSe [222, 223] lie in the region of 10^{16} cm^{-3}.

3.6 Experimental details

The co-electrodeposition of Cu-Bi thin film metal precursors was carried out in an electrolytic cell with the capacity of 150 ml with a rotating disc working electrode (RDE) geometry and a three electrodes configuration, as shown in Fig. 3.6.1a. The Mo coated substrate held as the RDE (house-built) was provided by Stefan Schäfer from Enthone GmbH (RF sputtered on 4 mm thick soda lime glass sheets). The reference electrode (R.E.) employed was saturated calomel electrode (Radiometer Analytical). The counter electrode (C.E.) was a house-built Pt foil (4 cm^2).

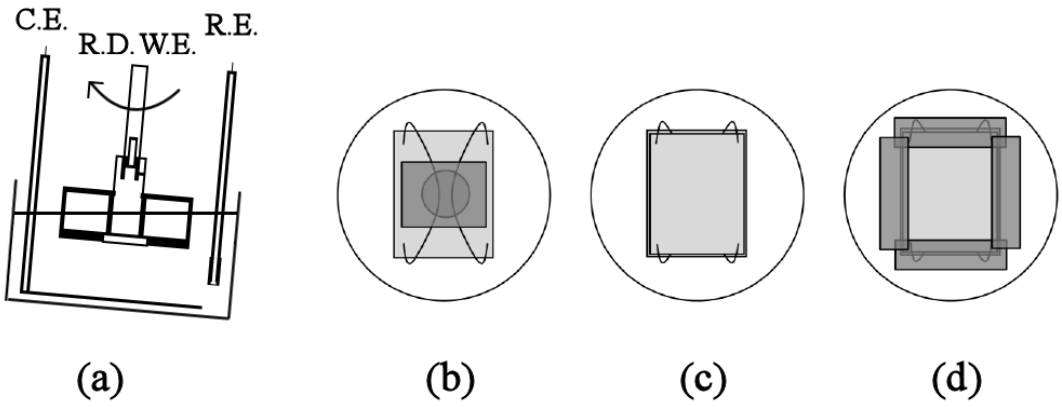

Fig. 3.6.1 Electrolytic cell with RDE geometry and three electrodes configuration employed for the co-electrodeposition of Cu-Bi thin film metal precursors (a). System employed for mounting the Mo coated substrates allowing electrical contacts with the brass core of the RDE head (b-d) [130]. Cu wires are taped onto the brass core of the RDE head (b), the Mo coated substrate is placed into the recess and the ends of the Cu wires are placed in contact with the front surface of the substrate (c), the edges of the substrates are masked with polyimide tape (RS) (d).

The cell was maintained tilted in order to avoid the presence of air bubbles between substrates and the plating bath, as described by Scragg [130]. The Mo coated substrates (4 cm^2) were connected to the RDE head as described in Fig. 3.6.1b-d. The solution composition was: 0.030 M $CuSO_4$, 0.010 M $Bi(NO_3)_3$, 2 M NaOH and 0.1 M D-sorbitol. (Sigma Aldrich). Potentiostatic depositions were performed at -0.57 V vs SHE with a charge cut-off of 2.1 Ccm^{-2} and a rotation speed of 300 rpm. The potential was applied with a μ Autolab type III potentiostat (Fig. 2.6.1b).

The study of the conversion reaction of the Cu-Bi precursors into the sulfide layers of interest was performed with either an AS-Micro Rapid Thermal Processor (AnnealSys) (RTP) furnace or with a wire-wound quartz tubular furnace (Thermo Scientific).

Precursor type(s)	Furnace – heating rate	Max. temperature	Dwell time	Sulfur source pressure
Cu/Bi/Cu electroplated	Tub. – 5 °Cmin^{-1}	300°C	30 min	45 mbar S_2 calculated at 298K
Cu/Bi/Cu electroplated	Tub. – 5 °Cmin^{-1}	350°C	30 min	45 mbar S_2 calculated at 298K
Cu/Bi/Cu electroplated	Tub. – 5 °Cmin^{-1}	400 °C	30 min	45 mbar S_2 calculated at 298K
Cu/Bi/Cu electroplated	Tub. – 5 °Cmin^{-1}	450 °C	30 min	45 mbar S_2 calculated at 298K
Cu/Bi/Cu electroplated	Tub. – 5 °Cmin^{-1}	500 °C	30 min	45 mbar S_2 calculated at 298K
evaporated Bi, Cu/Bi/Cu electroplated, Cu-Bi co-electroplated 3:1	RTP – 600 °Cmin^{-1}	350°C	5 min	500 mbar S_2 calculated at 298K
evaporated Bi, Cu/Bi/Cu electroplated, Cu-Bi co-electroplated 3:1	RTP – 600 °min^{-1}	400 °C	5 min	500 mbar S_2 calculated at 298K
evaporated Bi, Cu/Bi/Cu electroplated, Cu-Bi co-electroplated 3:1	RTP – 600 °min^{-1}	450 °C	5 min	500 mbar S_2 calculated at 298K
evaporated Bi, Cu/Bi/Cu electroplated, Cu-Bi co-electroplated 3:1	RTP – 600 °min^{-1}	500 °C	5 min	500 mbar S_2 calculated at 298K
evaporated Bi, Cu/Bi/Cu electroplated, Cu-Bi co-electroplated 3:1	RTP – 600 °min^{-1}	550 °C	5 min	500 mbar S_2 calculated at 298K
Cu/Bi/Cu electroplated, Cu-Bi co-electroplated 3:1	RTP – 5 °min^{-1}	500 °C	30 min	500 mbar S_2 calculated at 298K
Cu-Bi co-electroplated 3:1	RTP – 5 °min^{-1}	500 °C	5 min	500 mbar S_2 calculated at 298K
Cu-Bi co-electroplated 3:1	RTP – 600 °min^{-1}	270 °C	300 sec	500 mbar S_2 calculated at 298K
Cu-Bi co-electroplated 3:1	RTP – 600 °min^{-1}	270 °C	1800 sec	500 mbar S_2 calculated at 298K
Cu-Bi co-electroplated 3:1	RTP – 600 °min^{-1}	270 °C	7200 sec	500 mbar S_2 calculated at 298K
Cu-Bi co-electroplated 3:1	RTP – 600 °min^{-1}	270 °C	57600 sec	500 mbar S_2 calculated at 298K
Cu-Bi co-electroplated 3:1	RTP – 600 °min^{-1}	350 °C	300 sec	500 mbar S_2 calculated at 298K
Cu-Bi co-electroplated 3:1	RTP – 600 °min^{-1}	350 °C	1800 sec	500 mbar S_2 calculated at 298K

Cu-Bi co-electroplated 3:1	RTP – 600 °min^{-1}	350 °C	7200 sec	500 mbar S_2 calculated at 298K
Cu-Bi co-electroplated 3:1	RTP – 600 °min^{-1}	350 °C	50000 sec	500 mbar S_2 calculated at 298K
Cu-Bi co-electroplated 3:1	RTP – 600 °min^{-1}	400 °C	300 sec	500 mbar S_2 calculated at 298K
Cu-Bi co-electroplated 3:1	RTP – 600 °min^{-1}	400 °C	1800 sec	500 mbar S_2 calculated at 298K
Cu-Bi co-electroplated 3:1	RTP – 600 °min^{-1}	400 °C	7200 sec	500 mbar S_2 calculated at 298K
Cu-Bi co-electroplated 3:1	RTP – 600 °min^{-1}	450 °C	300 sec	500 mbar S_2 calculated at 298K
Cu-Bi co-electroplated 3:1	RTP – 600 °min^{-1}	450 °C	1500 sec	500 mbar S_2 calculated at 298K
Cu-Bi co-electroplated 3:1	RTP – 600 °min^{-1}	450 °C	1800 sec	500 mbar S_2 calculated at 298K
Cu-Bi co-electroplated 3:1	RTP – 600 °min^{-1}	500 °C	30 sec	500 mbar S_2 calculated at 298K
Cu-Bi co-electroplated 3:1	RTP – 600 °min^{-1}	500 °C	100 sec	500 mbar S_2 calculated at 298K
Cu-Bi co-electroplated 3:1	RTP – 600 °min^{-1}	550 °C	57600 sec	500 mbar S_2 calculated at 298K
Cu-Bi co-electroplated 3:1	RTP – 600 °min^{-1}	550 °C	57600 sec	700 mbar N_2 (no sulfur added)
Cu-Bi sputtered 1:1	Tub. – 5 °Cmin^{-1}	400 °C	30 min	120 mbar S_2 calculated at 298K
Cu-Bi sputtered 1:1	Tub. – 5 °Cmin^{-1}	500 °C	30 min	120 mbar S_2 calculated at 298K
Cu-Bi sputtered 1:1	Tub. – 5 °Cmin^{-1}	400 °C	30 min	120 mbar H_2S calculated at 298K
Cu-Bi sputtered 1:1	Tub. – 5 °Cmin^{-1}	500 °C	30 min	120 mbar H_2S calculated at 298K
Cu-Bi sputtered 1:1	Tub. – 5 °Cmin^{-1}	400 °C	30 min	14 mbar H_2S calculated at 298K
Cu-Bi sputtered 1:1	Tub. – 5 °Cmin^{-1}	500 °C	30 min	14 mbar H_2S calculated at 298K

Table 2.6.1 Details of the heating treatments employed for the study of the Cu-Bi-S chalcogenide layers in chapters 3 and 4.

4. Study of the chalcogenization reaction

The reaction chemistries involved in the formation of thin compound films may be complex, but in most cases there appears to be a competition between the rates of reaction and mass transfer [224]. It is known that ternary or multinary sulfide films of good morphological quality can be obtained by heat treatment of stacked layers of the binaries with no additional chalcogen required [82, 90, 132]. Other methods such as co-evaporation [225], reactive magnetron sputtering [128, 143], solution processing [54, 139, 226] and even co-electrodeposition [8, 55], where all the elements are introduced at the same stage, have shown to give very good film properties. In all these methods, suitably designed heat treatments are employed to ensure a high degree of homogenization. Such annealing stages resemble often simple diffusion couple experiments, where entropic gain is the main driving force for compound synthesis. However, the situation becomes more complicated when the formation of a ternary or multinary chalcogenide is achieved through incorporation of the chalcogen into a film of metal precursors. In such cases the chalcogen or chalcogen-bearing molecule needs to react with the elemental or alloyed film and oxidise it to its corresponding sulfides; i.e. enthalpy becomes the dominant term of the free energy of reaction. The reaction of the chalcogen with the elements may lead to the formation of secondary phases that grow and separate, causing a degradation of the original film morphology. As a consequence, it may be difficult to achieve the desired film composition (e.g. a phase-pure ternary sulfide) and morphology (e.g. a defect-free compact layer); simply because phases are inconveniently segregated and the contact area between them is reduced. Furthermore, in the case of chalcogenization of metal binary or ternary precursors, a large number of intermetallic alloys may form over the processing timescale, with further complication of the reaction pathway. In fact, each intermetallic phase may show a different reactivity towards the chalcogen-bearing reactant, with a multiplication of the possibilities for segregation over different timescales, e.g. see von Klopmann [227]. Although the products obtained at the end of the process can be reasonably deduced from the equilibrium phase diagrams (if these are available), the morphology of the resulting film is often driven by the reaction trajectory and associated phase development [147]. As a consequence, aspects related to the preparation via the two-step approach of thin chalcogenide films with suitable

compositional and morphological properties require optimisation. A deeper understanding of the thermodynamics and kinetics of chalcogenization reactions is of crucial importance to solve issues of secondary phase segregation, compositional stability and film morphology.

In this chapter, the phase evolution of stacked and homogeneous Cu-Sb and Cu-Bi metal precursor films during sulfurization with either elemental sulfur vapour or hydrogen sulfide is analyzed critically. The aim is to elucidate the roles of diffusion and phase equilibria in the kinetics of compound formation, film morphology and potential elemental losses due to compound decomposition during the thermal treatments. Section 4.1 outlines the phase evolution study by interpretation of the ex-situ XRD analyses of the "quenched" chalcogenide films reported in chapters 2 and 3. A new "Time-Temperature-Reaction" (TTR) diagram is introduced for the description of the reaction kinetics. The effect of the heating rate of sulfurization on the compositional and morphological properties of the processed Cu-Bi precursor films is considered in section 4.2 through SEM/EDS analyses. Section 4.3 deals with the thermodynamics of chalcogenization and highlights the role of the chalcogenizing conditions on the reaction sequence. Furthermore, modified Pilling-Bedworth coefficients [228] are introduced to provide a plausible interpretation of the kinetic observations. In section 4.4, equilibrium pressure diagrams suggest the possible compound decomposition routes accounting for the elemental losses observed during the thermal processes (section 2.3) [146, 155]. The utility of thermochemistry for computation and prediction of such phenomena is highlighted.

The discussion given here is expected to give a meaningful contribution towards the understanding of several issues associated to the mechanism of reaction/diffusion of the chalcogen from the vapour phase into metallic precursors. Applications of such findings to the synthesis and decomposition prevention of other thin-film PV absorber sulfides obtained through routes equivalent to electroplating/annealing should be possible [55, 154, 229-233]. The approach developed here may also be relevant to other fields of materials science, where the compound of interest is often formed via reaction of a solid precursor with gaseous or liquid species. Examples could be the preparation of $LiCo(Ni)O_2$ cathodes for molten carbonate fuel cells and lithium-ion batteries [234, 235] and the formation of protective barriers by passivation treatments of precursor coatings [236]. Part of this chapter is based on published material [157].

4.1 Following compound formation via structural analysis

The sulfurization reactions of the Cu-Sb and Cu-Bi films can be studied by evaluation of the phase evolution as a function of sulfurization temperature and time. In the absence of in-situ techniques such as Energy Dispersive X-Ray Diffraction (EDXRD)[227, 237], angle dispersive XRD [238] or Raman spectroscopy [239] this evaluation can be attained by ex-situ structural analysis of the films sulfurized at various temperatures for different periods and then cooled down to room temperature [130, 240]. If the cooling employed is sufficiently fast (quenching), it is reasonable to assume that the film phase composition attained at the end of the treatment is preserved, since diffusion mechanisms are extremely hindered at low temperature. Of course, this approximation is as good as the cooling rate employed is high. In this sense, RTP is a valuable tool for investigation of the mechanism of phase formation.

Fig. 4.1.1a-b are plots of the integrated intensity of the main XRD reflections of the relevant phases for samples of Cu-Sb and Cu-Bi precursor films sulfurized with elemental sulfur vapour at given temperatures for 5 and 30 minutes respectively.

The intensity of the scattered X-rays in XRD is a function of several variables. Among these are: incident intensity, texture and scattering factors of the phases under study and their relative volume fraction. Due to samples spinning during acquisition of the diffractograms in Fig. 4.1.1, the effect of texturing can be partially neglected. However, the plots are not intended as quantitative compositional estimations, since the absolute magnitudes of intensity are not normalised to the scattering factors of the different phases. Nevertheless, the changes in relative intensities for each phase provide a valid estimate of the evolution of the different species.

The bright blue colour of the Covellite CuS phase provided a clear indication when the sulfurized samples were not completely converted into the grey $CuSbS_2$ or Cu_3BiS_3 compounds. A good correlation between the visual appearance of the films and their phase composition, as detected by qualitative phase analysis, was always observed. No colour difference was perceived between the samples of the two precursor configurations (stacked and co-electroplated) sulfurized at the same temperature.

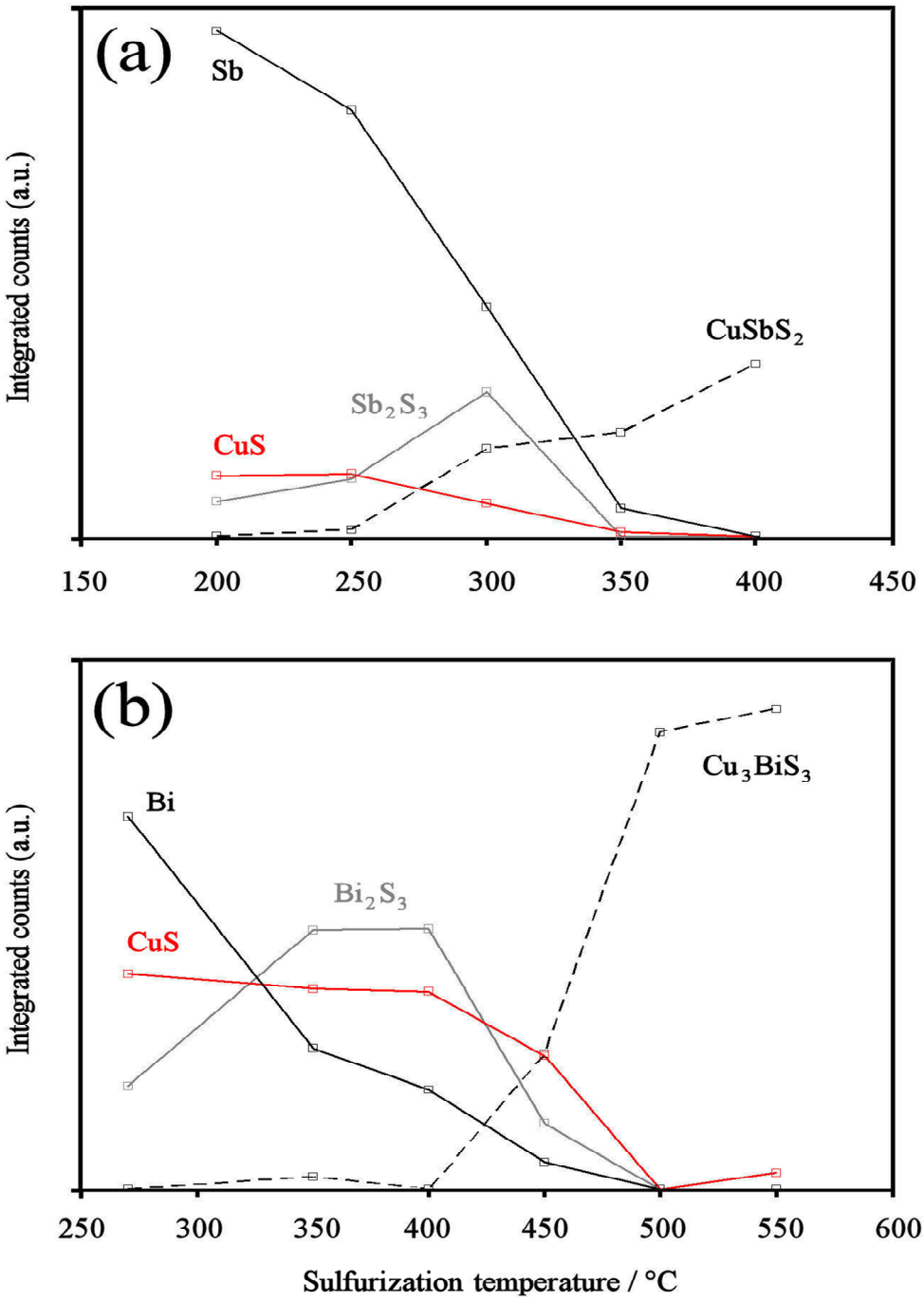

Fig. 4.1.1 Ex-situ XRD integrated peak intensities for Cu:Sb = 1:1 stacked (a) and Cu:Bi = 3:1 co-electroplated (b) precursor films after sulfurization treatments with elemental sulfur vapour lasting 30 and 5 minutes respectively [157].
The contribution of each phase and reflections are considered as follows:
(a): Sb PDF no 35-732 [(003)+(006)+(009)], CuS PDF no 65-3561 [(006)], Sb_2S_3 PDF no 42-1393 [(200)+(020)+(120)+(412)+(214)+(502)+(205)], $CuSbS_2$ PDF no 65-2416 [(102)+(015)+(213)+(017)+(018)].
(b): Bi (black) PDF no 44-1246 [(012)+(104)], CuS PDF no 65-3561 [(101)+(102)], Bi_2S_3 PDF no 6-333 [(121)+(230)+(130)+(310)], Cu_3BiS_3 PDF no 9-488 [(111)+(200)+(012)+(220)+(112)+(130)+(040)].

Considering the minor structural differences between stacked and co-electroplated precursors seen in chapters 2 and 3, there appears to be no obvious effect of the two precursor types on the phase composition, but no further efforts were made to demonstrate this.

The results in Fig. 4.1.1 suggest that the systems follow a sequential reaction/diffusion mechanism, where the metals react selectively with sulfur to form the corresponding binary sulfides. The subsequent emergence of the ternary phases is the result of interdiffusion of the binaries when the temperature and time of the sulfurization treatments are suitable. According to these results, two reaction sequences can be written (Reactions 4.1.1-4.1.5).

Reac. 4.1.1 $2Cu_{(s)} + S_{2\,(g)} \rightarrow 2CuS_{(s)}$

Reac. 4.1.2 $4Sb_{(s)} + 3S_{2\,(g)} \rightarrow 2Sb_2S_{3\,(s)}$

Reac. 4.1.3 $4CuS_{(s)} + 2Sb_2S_{3\,(s)} \rightarrow 4CuSbS_{2\,(s)} + S_{2\,(g)}$

Reac. 4.1.1 $2Cu_{(s)} + S_{2\,(g)} \rightarrow 2CuS_{(s)}$

Reac. 4.1.4 $4Bi_{(g)} + 3S_{2\,(g)} \rightarrow 2Bi_2S_{3\,(s)}$

Reac. 4.1.5 $12CuS_{(s)} + 2Bi_2S_{3\,(s)} \rightarrow 4Cu_3BiS_{3\,(s)} + 3S_{2\,(g)}$

No traces of unreacted Cu were observable at any of the investigated sulfurization temperatures. CuS is formed very quickly at the expenses of Cu, and its integrated XRD peaks remain rather constant until the sulfurization temperature is sufficiently high to allow the formation of the ternary sulfides. At about 300 °C for Cu-Sb and 450 °C for Cu-Bi the CuS peak counts start to decrease and the patterns of $CuSbS_2$ and Cu_3BiS_3 appear thereafter.

Contrary to Cu, the XRD peaks corresponding to elemental Sb and Bi (M) remain clearly visible respectively up to 350 and 450 °C, suggesting that sulfur uptake by these elements is more sluggish. Over the range of dwell times considered, M_2S_3 coexists with M and CuS until the conversion to the ternary sulfide comes to an end. The trend of the corresponding XRD peak counts versus temperature exhibits a maximum corresponding to the temperature at which the rate of M_2S_3 formation equals its rate of consumption in the reactions forming $CuSbS_2$ and Cu_3BiS_3. These phase evolution profiles are consistent with a reaction mechanism in which the rate is determined by the solid state diffusion of the elements across the binary sulfide interfaces. In fact, the binary sulfides build up and decay subsequently. If this were

not the case, the binary phases would react promptly to form the ternaries, and they would not be detected along with the ternaries (Fig. 4.1.1).

The formation of intermediate sulfide phases in the solid state has been studied by Ross [241], who observed the phase evolution in bulk diffusion couples of the binaries. For the Cu_2S-Sb_2S_3 experiment, the rates of intermediate phase formation were reported to obey a parabolic rate diffusion rule that was first described by Tammann [242, 243], Eq. 4.1.1.

Eq. 4.1.1 $$x = [2k(T) \cdot t]^{1/2}$$

where x is the thickness of the developing intermediate phase, $k(T)$ is the rate constant and t is the time.

The temperature dependence of the reaction rate constant is given by the Arrhenius equation, Eq. 4.1.2.

Eq. 4.1.2 $$k(T) = A \cdot e^{-E_a / RT}$$

where A is a pre-exponential factor, E_a is the activation energy of the reaction, R is the universal gas constant and T is the absolute temperature. By substituting Eq. 4.1.2 in Eq. 4.1.1, an expression is obtained that can be used to analyse the kinetics of ternary sulfide formation in thin films (Eq. 4.1.3). This can be achieved through estimation of the temperature dependence of the times required for the ternary phase to appear t_s and form completely t_f.

Eq. 4.1.3 $$\ln[t_{s,f}] = \ln(x^2/2A) + E_a/RT$$

In Ross' investigation, samples obtained compressing powder pellets of the pure sulfides were placed face to face and annealed at different temperatures for different durations. The pellets were then cut-polished lengthwise normal to the interface and analysed visually, i.e. the lengths of the intermediate phases were measured with a caliper. The thin film geometry of our system is very different. In our case, a direct measurement of the thickness of the developing phases would be difficult to achieve, requiring for example EDS elemental linescan with TEM [223]. Alternatively, accurate estimations of the critical times t_s and t_f in thin films would be possible by a

temperature-resolved in-situ isothermal examination. Nevertheless, extensive individual XRD analyses of RTP processed films can provide enough information for approximate studies.

Based on the same principle of the time-temperature transformation (TTT) diagrams, we can introduce a time-temperature reaction (TTR) diagram for the representation of the kinetics of thin film ternary sulfide formation. TTT diagrams have wide application in metallurgy and other fields and are successfully employed to describe the transformation kinetics under different annealing conditions [244]. Similarly, TTR diagrams can be created for the description of the phase composition of samples during sulfurization. Of course, there are obvious differences between TTT and TTR. In TTR there is the introduction of an additional component into the system during the treatment, and the description is valid only for ideally fixed precursor film configuration and chalcogenizing conditions (chalcogen source and its partial pressure). As a consequence, the morphology of the phases will, in principle, depend on the reaction pathway followed during the treatment.

Fig. 4.1.2 shows a hypothetical TTR diagram showing the temperature dependence of the time required for a ternary sulfide phase to form via sulfurization of thin film metal precursor (a).

The t_s and t_f lines (ternary sulfide formation started and finished, respectively) may well be represented by curves (a) and (b) in Fig. 4.1.2. For exact analyses of the kinetics of ternary sulfide formation, these critical times should be ideally plotted after subtraction of the corresponding times required for the binary sulfides to form.

The effect of a film thickness increase and of a pre-exponential factor decrease on the positions respectively of the start and finish curves in the TTR diagram is shown by (Fig. 4.1.2a-c). The Arrhenius equation describing the kinetics of our system predicts for both cases a shift of the lines towards longer times. Let us discuss first the effect of a pre-exponential factor decrease on the position of the Arrhenius line corresponding to t_s and t_f. According to Eq. 4.1.3, the intercept of the line is equal to $\ln(x^2/2A)$. Therefore a decrease of A brings about a shift of the lines towards more positive values on the y axis of the Arrhenius plot. A shift in the same direction is expected if the film thickness (x) is increased, but in this case it is reasonable to suppose that only the line describing the end of the conversion $\ln(t_f)$ is affected.

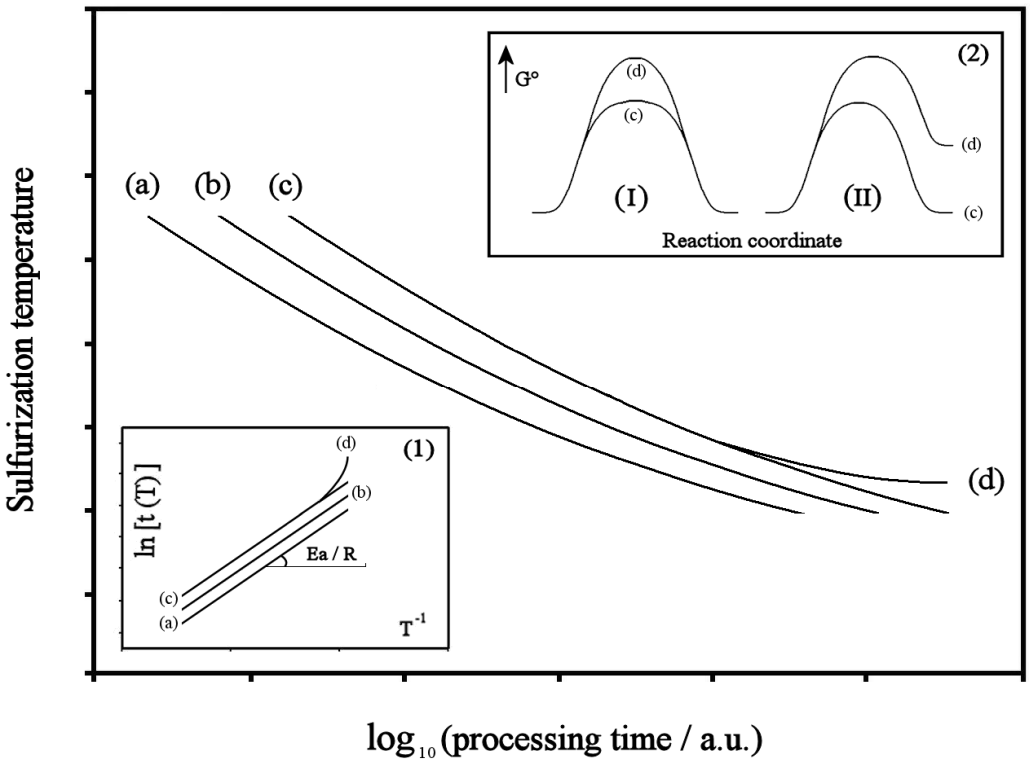

Fig. 4.1.2 Hypothetical TTR diagram showing the temperature dependence of the time required for the ternary sulfide to form via sulfurization of thin film metal precursor (a). Theoretical effects of a film thickness increase or a pre-exponential factor decrease (b,c) and of an activation energy increase (d) on the shape of the reaction curves. Inset (1): corresponding Arrhenius plot. Inset (2): energy profile showing an increase of the activation energy due to either a variation of the reaction mechanism (I) or as a consequence of a variation of the relative thermodynamic stability of the reaction components (II).

In fact, from Eq. 4.1.3 the intercept of the line describing the beginning of the ternary sulfide formation $\ln(t_s)$, can be assumed to depend on a critical thickness (x_c). In principle, the minimum thickness that can be considered as evidence for a phase formation is given by the unit cell parameter of the phase under study. However, in practical terms x_c can be thought as the minimum thickness required for the phase to be detected with the technique employed. Therefore, it is reasonable to assume that the intercept of $\ln(t_s)$ in the Arrhenius plot is independent of the total thickness of the film and depends only on the detection limit for the specific phase and on A.

The t_s and t_f curves divide the time-temperature area into three regions characterised by three different phase compositions. Before (a), the phases observed are the binary sulfides and, in some cases the unreacted metal precursors. At the times indicated by curve (a), the ternary sulfide starts to appear and after (b) its formation is complete and the solid system is monophasic, unless excess binary phases are remain due to non stoichiometry of the precursors employed initially.

As illustrated in the modified Arrhenius plot depicted in Fig. 4.1.2(1), $\ln[t_{s,f}]$ versus *1/T* yields a straight line, with a slope corresponding to E_a/R, according to Eq.4.1.3. Therefore, E_a can be extracted to give useful information on the system under investigation. E_a may vary when nucleation and/or growth mechanisms of the ternary phase are altered. This behaviour is reflected in the modified Arrhenius plot by a variation of the slope. It is generally recognised that at low temperature, the reaction kinetics may become slower. In such cases a limiting situation may occur where the reaction curve in the TTR diagram lies parallel to the abscissa, representing processing times approaching infinity at a critical temperature (Fig. 4.1.2d). This corresponds to a situation in which the growth of the ternary phase ceases, below a certain temperature. If the activation energy of ternary sulfide formation varies due to a variation of the reaction mechanism, the energetic profile is illustrated in Fig. 4.1.2(2I).

In the reacting solid state, interdiffusion of ions such as Cu, Sb Bi and S (of considerably larger size than H, C and N) is likely to be based mainly on a vacancy rather than an interstitial exchange mechanism. The vacancy-assisted diffusion mechanism is ultimately dependent on the concentration of vacancy defects within the crystal structures involved in the reaction, which in turn is known to be an Arrhenius-like thermally activated function (of the type of Eq. 4.1.2) [245, 246]. In this context, the activation energy for vacancy formation can be thought as the energy required to break inter-atomic bonds and let the ions "jump" into the newly formed vacancy. Different types of exchange jumps are theoretically possible. For example, Monte Carlo simulations of the cations diffusion via vacancies in simple spinels have shown that the contributions of the different possible jumps to the overall cation diffusion are a function of the vacancy concentration [247, 248]. Each jump has different activation energy. Therefore, it is possible that the activation energy of ternary sulfide formation, which is ultimately dependent on the activation energy of the different possible vacancy exchange mechanisms, varies as a function of the temperature.

It has also been shown that the temperature dependence of the self-diffusion coefficients of cations in metal sulfides M_2S_n can be expressed empirically by Arrhenius-like functions of the type of Eq. 4.1.4 [249].

Eq. 4.1.4 $$D_{M^{n+}}(T) = B \cdot (p_{S_2})^m \cdot e^{-E_d / RT}$$

where $D_M^{n+}(T)$ is the self-diffusion coefficient of the cation M^{n+} in the sulfide M_2S_n, B is a pre-exponential factor, p_{S2} is the pressure of sulfur in the system, m is an empirical exponent, E_d is the activation energy of self-diffusion (which has also been shown to vary slightly as a function of p_{S2} in some cases [249]).

Although Eq. 4.1.4 refers to self-diffusion, it is reasonable to assume that a similar relationship may still be valid for interdiffusion. Eq. 4.1.4 suggests that the presence of a gaseous sulfur pressure in equilibrium with the solid reacting sulfides may affect the kinetics of ternary sulfide formation. This can be due to variation of both the pre-exponential factor and of the activation energy of interdiffusion.

However, E_a may also change linearly as a consequence of the changes in the relative thermodynamic stability of the reaction components, as per Fig. 4.1.2(2II). Examples of this kind, where sulfur pressure influences the relative stability of sulfide phases, are discussed in section 4.3.

In order to study the kinetics of ternary sulfide formation in a real system, an approximate TTR diagram for the formation of Cu_3BiS_3 from the co-electroplated Cu:Bi 3:1 metal precursors and elemental sulfur vapour has been created. For this purpose, the sulfurization treatments were quenched at logarithmically staggered times up to 16 hours in the range 270-500 °C in order to ascertain the minimum dwell times required for the Cu_3BiS_3 phase to appear and form completely. The results are shown in Fig. 4.1.3. As anticipated, t_s and t_f curves in Fig. 4.1.3(I) are reasonably parallel, and their corresponding Arrhenius plot in Fig. 4.1.3(II) gives lines that are shifted on the y-axis but with a similar slope. Before t_s (region a) $Bi_{(s)}$, $Bi_2S_{3(s)}$ and $CuS_{(s)}$ are the phases present. In region (b), the ternary sulfide starts to appear and in (c) Cu_3BiS_3 is fully formed.

The kinetic model developed by Ross [241] is based on the simultaneous and chemically-equivalent interchange of the two kinds of metal ions, migrating in opposite direction through the sulfur network of the emerging phase. If we assume that the CuS-Bi_2S_3 system follows a similar behaviour, information on the kinetics of Cu_3BiS_3 phase formation can be extracted from the data in the TTR diagram of Fig. 4.1.3. This can be done by analysing the temperature dependence of the time required for the ternary phase to appear and form completely.

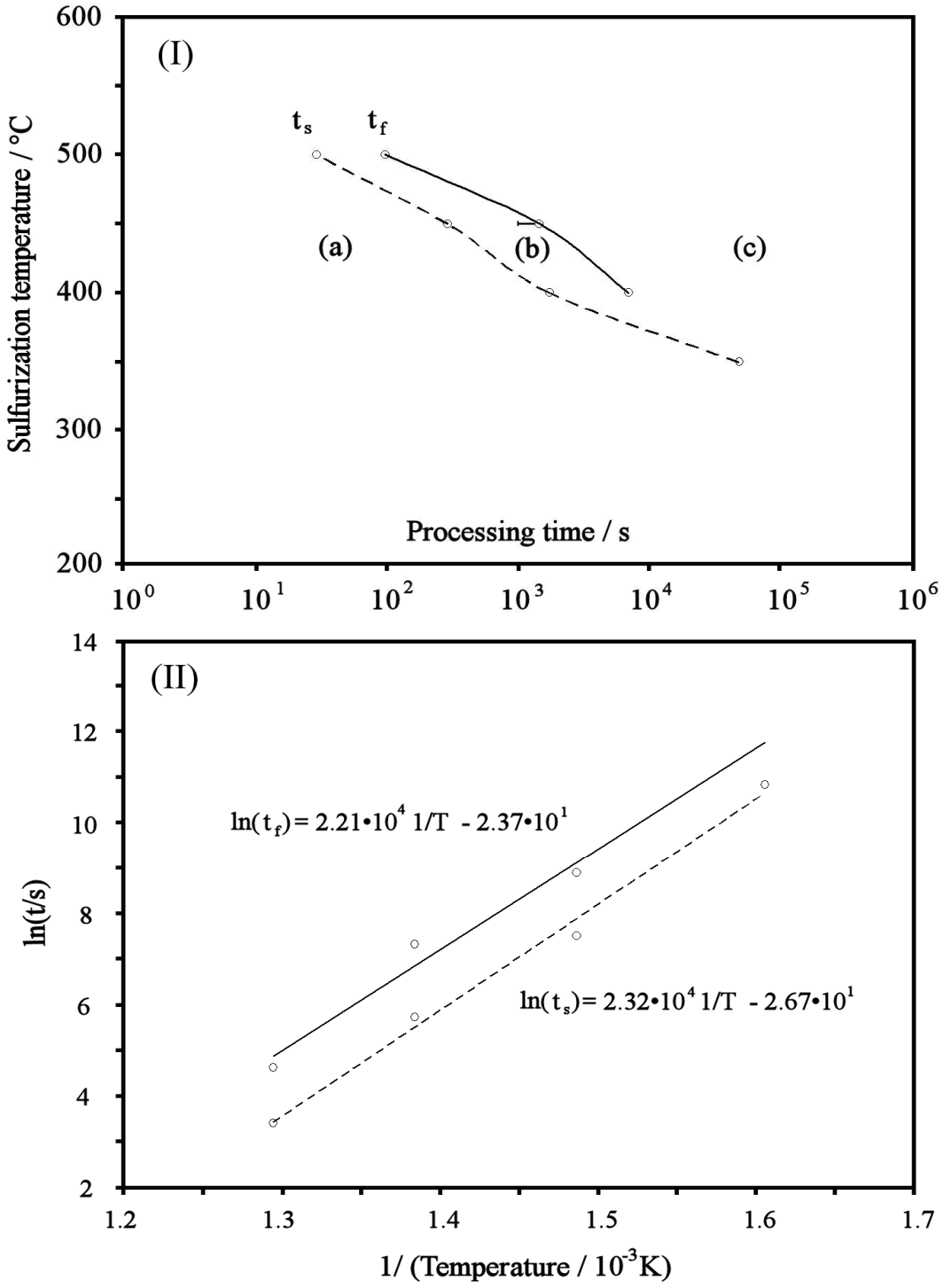

Fig. 4.1.3 (I) Time Temperature Reaction (TTR) diagram for the sulfurization conversion of co-electroplated Cu:Bi 3:1 metal precursor into 2 µm thick Cu_3BiS_3 layers in the presence of elemental sulfur vapour at a partial pressure of 500 mbar. The plot was created from data obtained by ex-situ XRD analysis of rapid thermal processed samples (600 °C·min^{-1}) after quenching. The dashed line represents the emergence of the ternary sulfide (t_s) and the solid line the reaction completion (t_f). The corresponding Arrhenius plot for the estimation of the activation energy of Cu_3BiS_3 formation is shown in (II) [157]. The least squares fitting equations corresponding to the t_s and t_f curves are shown.

To assist the reader, the Arrhenius plot is shown in Fig. 4.1.3(II), with indication of the least squares fitting equations for the lines corresponding to the t_s and t_f curves.

Estimation of the activation energy of Cu_3BiS_3 formation in thin films from CuS and Bi_2S_3 is possible from Fig. 4.1.3(II), according to Eq. 4.1.3. This gives an average value of ~ 180 $kJmol^{-1}$. By comparison, the reported activation energy for the formation of bulk $CuSbS_2$ from Cu_2S and Sb_2S_3 is much lower, ~ 33 $kJmol^{-1}$ [241]. A more sluggish reaction of Bi with elemental sulfur vapour compared to Sb was already deduced from comparison of the series of XRD analyses of sulfurized evaporated films of Sb (section 2.4) and Bi (section 3.4). An explanation for this different behaviour can be found from the comparison of the two binary sulfides Bi_2S_3 (*Bismuthinite*) and Sb_2S_3 (*Stibnite*). These are isostructural compounds [250] with the group-five element in the trivalent state and a structure characterised by tightly-bonded M_4S_6 rods displaced in a herring bone arrangement [251], with pronounced steric requirements of the lone electron pairs accommodated between the rods [252]. It is known that the effective ionic radii [253] of Bi in trivalent form are on average about 36% larger than those of Sb [254]. This is likely to lead to more sluggish diffusion of Bi through the M_2S_3/CuS crystallite interface, and to a higher value of the activation energy for the corresponding ternary sulfide formation. Although a direct comparison is not strictly legitimate due to the different thermal mass of the furnaces employed, a higher activation energy for the formation of Cu_3BiS_3 compared to $CuSbS_2$ is consistent with the times required for the phases to appear at 350 °C, which were respectively 16 hours and 30 minutes (section 2.4). Analysis of the thermodynamics and kinetics of sulfide formation under different sulfurizing or annealing conditions allows comparison between the synthesis procedure utilised in this work and those employed by Haber et al. [147, 208] and Nair et al. [84]. This comparison involves a discussion of the morphological (section 4.2) and thermochemical/kinetic (section 4.3 and 4.4) consequences on the shape of the TTR curves.

4.2 Morphological implications of the reaction sequence

The results of the morphological and compositional analyses of the sulfurized samples of Cu-Sb and Cu-Bi thin films are consistent with the reaction sequences drawn from the structural investigations and reported in section 4.1. As seen by the SEM/EDS analyses in sections 2.3 and 3.3, most of the Cu contained in the metal precursors reacts selectively with sulfur at temperatures ranging between 200 and 300 °C, leading to the "bloom" of abundant CuS crystals that tend to segregate on top of the former precursor surface. To some degree, this was also observed for CuSe during the selenization conversion of the amorphous $CuSbS_2$ films at 300 °C (section 2.3). By contrast, the conversion of Sb and Bi into the corresponding sulfides is slower (section 4.1), reducing their segregation substantially compared to CuS.

As reported in section 2.3, in the time frame of 30 minutes the Cu-Sb precursors with both configurations are converted into $CuSbS_2$ at 350 °C. The EDS analyses of these films gave a Cu:Sb ratio that approached 2.6. The penetration depth of the electron beam was evidently lower than the thickness of the absorber layer, as no signal from the Mo substrate was detected. This gives further support to the proposed reaction sequence that implies the formation of the ternary sulfide by interdiffusion of the two metal cations in opposite directions, which for the case of Cu means a concentration decrease from the surface to the bottom of the films. A similar situation is observed for Cu-Bi, where the cross-section compositional profile of the Cu_3BiS_3 films shows a slight elemental gradient (Fig. 3.3.4) that is consistent with the supposed mechanism.

Fig. 4.2.1 illustrates the top and cross sectional morphologies of the Cu:Bi 3:1 stacked and co-electroplated metal precursors before (a,h,o) and after sulfurization treatments with heating rates of 600 (f-g,m-n) and 5 °$Cmin^{-1}$ (t-u). From the morphological standpoint, there appear to be meaningful differences between the behaviours of the stacked (a-g) and co-electroplated precursors (h-n) during sulfurization at a fast heating rate as well as between the co-electroplated precursor under fast (h-n) and slow heating rates (o-u). The same figure proposes a phase evolution model consistent with the structural findings of section 4.1 designed to be consistent with these different morphological behaviours.

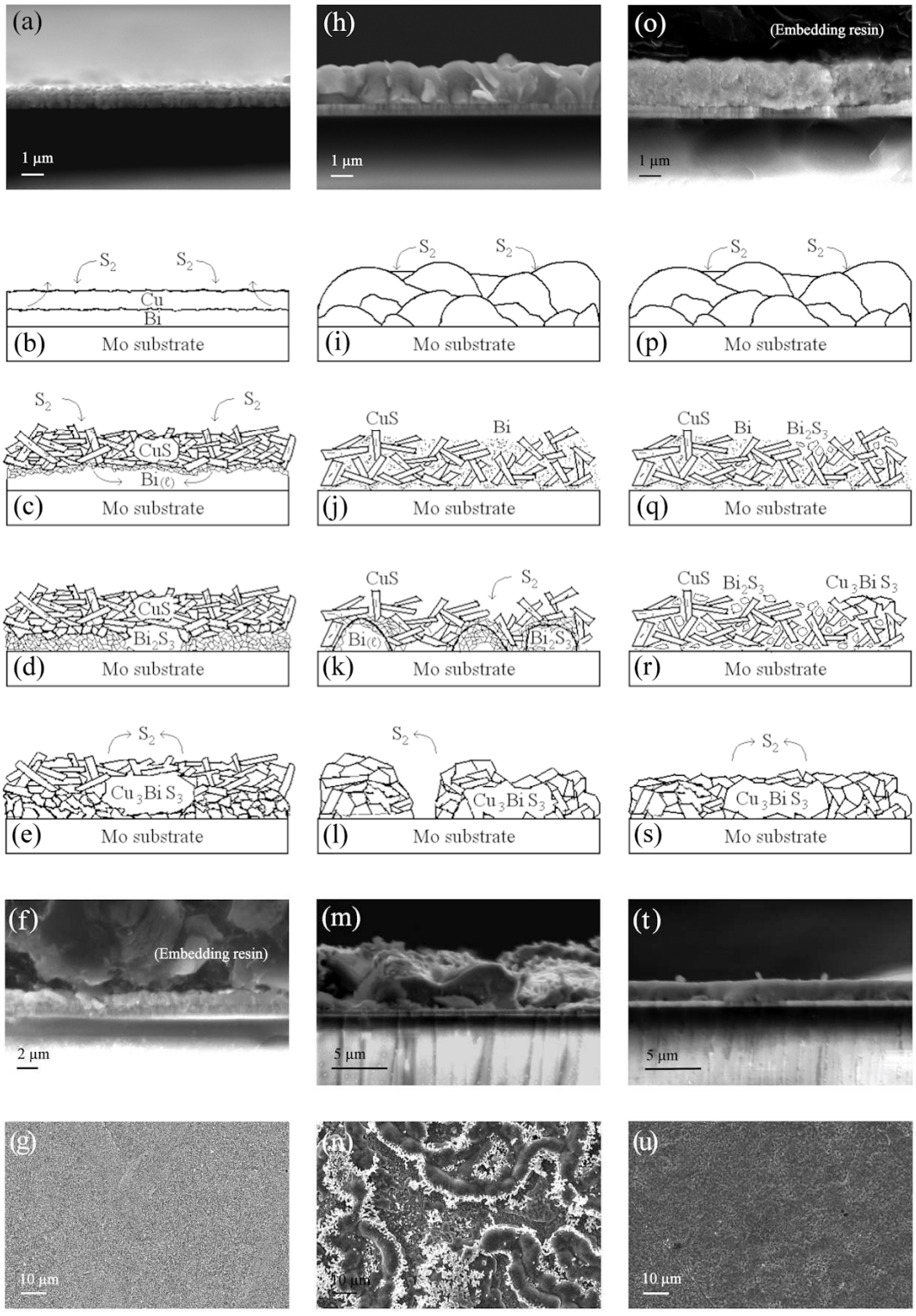

Fig. 4.2.1 Phase evolution model for the interpretation of the structural and morphological results of the sulfurization of stacked (a) and co-electroplated (h,o) Cu:Bi 3:1 metal precursor films in the presence of elemental sulfur vapour at 500 °C with heating rates of 600 °Cmin^{-1} (b-e,i-l) and 5 °Cmin^{-1} (p-s); the corresponding SEM cross sectional (f,m,t) and top views (g,n,u) are included [157].

Initially, crystallites of CuS segregate at the surface of the former precursor film leaving the unreacted Bi underneath (Fig. 4.2.1c) or dispersed amongst the CuS crystals (Fig. 4.2.1j-q). A similar behaviour was shown by the Cu-Sb films at this early stage. If the heating rate employed is such that the conversion of Bi into Bi_2S_3 is not complete when the sample reaches ~270 °C, the unreacted Bi undergoes melting. If Bi in the film precursor is segregated in a morphologically ordered manner (e.g. if it forms a compact metal layer, as in the stacked Cu-Bi configuration), melting does not lead to a degradation of the film morphology (Fig. 4.2.1d). On the other hand, if the Bi contained in the precursor film is homogeneously dispersed (e.g. within the Cu-Bi co-electrodeposit, as suggested by Fig. 3.3.4), there is a driving force for it to coalesce in order to minimise the surface energy. This was observed to occur in the form of "dewdrops" that segregate at the bottom of the film (Fig. 4.2.1k). This coalescence process exposes the underlying Mo substrate layer, as shown by the EDS mapping and elemental analysis (Fig. 3.3.3). If the heating rate employed is low enough to allow a substantial conversion of Bi into Bi_2S_3 (5 $^{o}Cmin^{-1}$), melting is not observed. In the case of the co-electroplated precursor this means that morphological degradation is minimised (Fig. 4.2.1q). Bi_2S_3 is formed slowly by reaction of the remaining Bi with sulfur, and a reasonable preservation of the Bi morphology is observed in all cases (Fig. 4.2.1d,k,r). Eventually, the ternary sulfide appears at the interface between the binary crystallites and grows with a morphology that again depends largely on that of the film attained up to that stage (Fig. 4.2.1e-f,l-m,s-t).

It follows from the preceding discussion that the key for obtaining morphologically good films of Cu_3BiS_3 by sulfurization of co-electroplated precursors with elemental sulfur vapour (under 500 mbar $S_{2\,(g)}$ at the early stages of treatment) is to employ a low heating rate. Under these conditions, the conversion of Bi into Bi_2S_3 occurs before the temperature reaches the melting point of the element, which causes the formation of the liquid framework responsible for the poor film morphology and adhesion (Fig. 4.2.1k,n). The morphological issue linked to high heating rates during sulfurization has not been observed for the Cu-Sb precursor films, although RTP treatments have not been performed and a maximum heating rate of 15 $^{o}Cmin^{-1}$ was used. This difference can be ascribed to the particular dissimilarity between Cu-Bi (Fig. 3.1.1) and Cu-Sb equilibria (Fig. 2.1.1). In fact, negligible mutual solubility of Cu and Bi is shown in the solid state, with no other intermediate compounds, and only a eutectic transformation at 270.6 °C (just below

the melting temperature of pure Bi, 271.4 °C) of composition 99.5% molar Bi [255]. With an initial molar composition of ~25% Bi and ~75% Cu, it can be estimated that ~25% at. of the film precursor forms a liquid (with composition ~98.5% molar Bi) at the eutectic temperature. The steepness of the liquidus boundary will cause only a limited additional part (~1.3% at.) of the precursor to melt and form a liquid of slightly increased Cu concentration (~95% molar Bi) if the temperature is increased up to 500 °C. Considering that most of the Cu has already reacted with sulfur at the eutectic temperature, it is apparent that the large majority of the Bi originally dispersed in the deposit undergoes melting and causes the observed morphological issues.

It was reported in section 3.4.3 that in the present work for processing time up to 16 hours at 270 °C with 500 mbar of sulfur vapour, the ternary sulfide Cu_3BiS_3 was not detected at all, and even at 350 °C the reaction was largely incomplete. This behaviour was shown in Fig. 4.1.3, where the TTR diagram is clearly incomplete in the low temperature range. Dwell periods longer than 16 hours may be necessary in order to identify the critical times in such cases. This behaviour contrasts with the observations of Haber et al. [147] who obtained a phase pure film at 270 °C within 16 hours of treatment, using 7 mbar of hydrogen sulfide instead of sulfur (Fig. 4.2.2a). Furthermore, with a different synthesis route consisting of the thermal annealing of multilayered metal sulfide precursor films, Haber et al. reported on the same article the formation of a phase-pure Cu_3BiS_3 film at 300 °C in 2 hours (Fig. 4.2.2b) [147].

In order to facilitate comparison between the three synthesis routes, the two experimental points obtainable from Haber's works (a,b) have been included in the TTR diagram of Fig. 4.2.2, with the addition of a hypothetical t_f curve. This t_f curve describes the end of ternary sulfide formation in Haber's works. Its position lies at shorter times than the t_s curve corresponding to the beginning of the conversion in the present investigation.

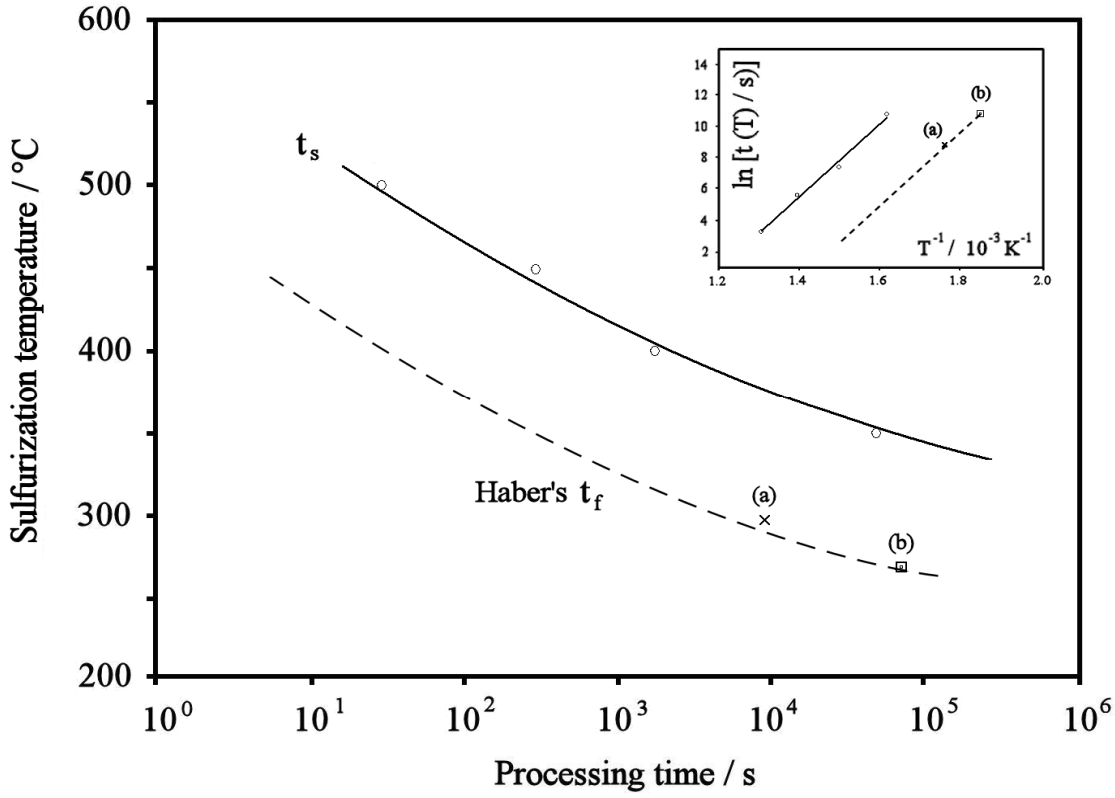

Fig. 4.2.2 TTR diagram of Cu_3BiS_3 formation showing the comparison between the experimentally observed t_s line (solid) (sulfurization with 500 mbar sulfur vapour) and a hypothetical t_f line extrapolated from the data points reported by Haber et al. [147] (dashed). (a) heat treatment of multilayered metal sulfides precursors, (b) sulfurization with 7 mbar H_2S. Inset: corresponding Arrhenius plot.

If the assumptions regarding diffusion made in section 4.1 are valid, the slope of the ln(t_f) line in the Arrhenius plot depends on the activation energy of the reaction and, therefore, on the species involved in the rate limiting step of the reaction. If the ternary sulfide formation in the two Haber's works follows the same reaction observed in the present investigation, the two corresponding ln(t_f) lines should be parallel. Let us consider the three cases in order to make an appropriate comparison. To assist the discussion, the Arrhenius plot in the inset of Fig. 4.2.2 is shown in Fig. 4.2.3 enlarged and enriched with hypothetical cases.

The thickness of the converted films in Haber's work was reported to be 1 μm, which is less than the 2 μm obtained in the present work. However, it is obvious that the t_s points of Haber's experiments must lie at shorter times than the t_f ones reported in Fig. 4.2.2. As discussed in section 4.1, the effect of film thickness on the position of the ln(t_s) lines in the Arrhenius plot should be negligible. Therefore, comparing the three experiments using the ln(t_s) line of the current study and extrapolated Haber's ln(t_f) lines with appropriate slopes should be legitimate.

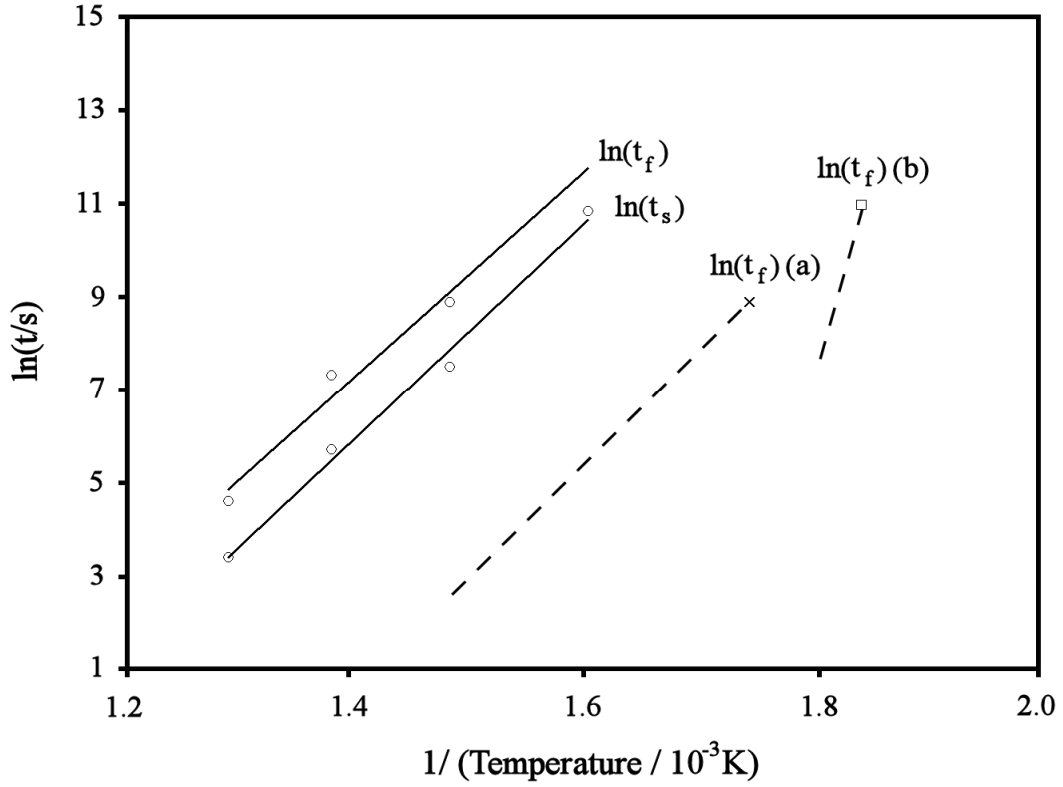

Fig. 4.2.3 Arrhenius plot showing the comparison between the experimentally observed ln(t_f) and ln(t_s) lines of the present work (solid lines) (sulfurization with 500 mbar sulfur vapour) and hypothetical ln(t_f) lines for heat treatment of multilayered metal sulfides precursors (a) and sulfurization of co-sputtered metal precursors with 7 mbar H_2S (b) extrapolated from the data points reported by Haber et al. [147] (dashed lines). In (a) the line slope assumes that the formation of the ternary sulfide follows the same reaction reported in the present work, while in (b) a different activation energy is assumed, accounting for the fact that in process (b) the rate determining step seems to be the sulfur uptake by Bi.

The comparison of the present work with the case (a) reported in Fig. 4.2.3 is interesting. In case (a) Haber et al. employed a multilayered precursor film containing CuS and Bi_2S_3 [147]. The binary phases involved are the same as those observed in the present study; therefore we can assume that the reactions are governed by the same activation energy. This situation is depicted in Fig. 4.2.3 with the ln(t_f) (a) line extrapolated at higher temperature using the same slope as the ln($t_{s,f}$) lines reported in the present study. As a consequence, ln(t_f) (a) is shifted on the y-axis towards lower values compared to the ln($t_{s,f}$) lines of the present study, and its intercept is consistently more negative. If we rule out the effect of the film thickness as discussed earlier, according to Eq. 4.1.3, this situation is the symptom of a higher pre-exponential factor, A.

The pre-exponential factor is a characteristic of the thin-film synthesis. A higher value of A may be correlated with a higher contact area between the intermediate phases, which could be associated with a lower degree of phase segregation and/or to smaller crystallite size. As indicated by the XRD analyses, the multilayered precursors employed by Haber in case (a) contained CuS and Bi_2S_3 but were largely amorphous [147]. It is reasonable to believe that the contact area between the reactants was much higher in case (a) than in the present study. In this context, the reduced time required for the formation of Cu_3BiS_3 at 300 °C may be explained. Similar considerations may apply to the synthesis routes undertaken by Nair et al. [84] and Estrella et al. [209]. In these two cases the formation of Cu_3BiS_3 thin-films was achieved with chemical bath deposited precursor with grain size lower than 5 nm annealed in air at 300°C for 1 hour.

The comparison of the present study with the results of Haber et al. [147] illustrated by case (b) in Figs. 4.2.2-4.2.3 is less obvious. In fact, $Cu_{1.8}S$ and Bi were detected as secondary phases in the films sulfurized with 7 mbar H_2S at 270 °C when the reaction was incomplete [147, 155]. In case (b), the absence of Bi_2S_3 as intermediate phase suggests that the rate limiting step for the ternary sulfide formation may be the sulfur uptake by Bi. In such a scenario, the supply of Bi_2S_3 is promptly converted into the ternary sulfide and is hardly detected in the films. Due to the different activation energy for the rate limiting step, the slope of line (b) in Fig. 4.2.3 may be different from the one observed in the present investigation. However, without further information it is not possible to know whether the sulfurization of Bi is limited by a high value of E_a or by a too low value of A (e.g. by a too low H_2S concentration). That is why a direct comparison of this case with the present study is not straightforward. It would be interesting to investigate the effects of temperature and H_2S concentration on the $\ln(t_f)$ line (b), which would help clarifying if the rate of ternary sulfide formation is really governed by the reaction of Bi and H_2S to form Bi_2S_3 (although it may be difficult to discriminate the direct kinetic influence of these parameters from the indirect kinetic consequences caused by the morphology of the intermediate phases formed). A discussion on this aspect is given in section 4.3.

It is clear that the different reactivity of the metallic elements towards the sulfur source has a strong role on the phase/morphology evolution within the systems, which in turns affects the kinetics of ternary sulfide formation. An investigation of such aspects is given in section 4.3. We believe that morphology and crystallite size of the binary sulfides formed at the early stages of the sulfurization treatments

influence the position of the reaction curve in the TTR diagram. As discussed in section 4.3, phase segregation and crystallite size may be the cause for the delayed ternary sulfide formation observed in our experiments, compared to the sulfurization with H_2S performed by Haber et al. [147]. Some evidence of reduced secondary phase segregation, resulting in an improvement of the film morphology can also be perceived in Fig. 3.3.5, where sulfurization of the Cu:Bi 1:1 sputtered metal precursors with either elemental sulfur vapour or hydrogen sulfide under virtually the same conditions was investigated.

Apart from increasing the contact area (resulting in higher pre-exponential factor in the Arrhenius equation), smaller crystallite sizes of reagents in solid state reactions may be a source of higher reactivity due also to the role of surface energy. In fact, as the particle size decreases, the surface-to-volume ratio increases and this can lead to a sharp alteration of the thermodynamic properties of materials. An example is given by the melting point depression that is known to occur in nanometer-sized metal powders [256, 257]. Although analogous effects on compounds are very little studied [258], they may have a crucial importance in the synthesis of thin films via the two-stage route. The possibility to engineer precursor films with very small particle size may present considerable advantages. Such an approach deserves appropriate attention for further expansion.

4.3 The role of the sulfurizing conditions in phase evolution

Section 4.2 explored the implications of the pressure and type of sulfurizing agents on the kinetics of ternary compound formation. A comparison was made between sulfurization of Cu-Bi thin film metal precursors with sulfur vapour at 500 mbar and hydrogen sulfide at 7 mbar [147]. It was found that the treatment with pure chalcogen required higher temperatures and longer times for Cu_3BiS_3 to appear. If we consider thickness-equivalent converted films, it can be concluded that the reacting species employed in the sulfurizing atmosphere play a major role in determining the kinetics of ternary sulfide formation. In this section, thermodynamic and kinetic assessments of the reactions of elemental Cu, Bi and Sb with either $S_{2(g)}$ or $H_2S_{(g)}$ are given.

The thermodynamics of the relevant sulfurization reactions (4.3.1-4.3.4) is investigated by comparing the temperature dependence of the Gibbs free energies changes.

Reac. 4.3.1a $2Cu_{(s)} + S_{2(g)} \rightarrow 2CuS_{(s)}$

Reac. 4.3.1b $2Cu_{(s)} + 2H_2S_{(g)} \rightarrow 2CuS_{(s)} + 2H_{2(g)}$

Reac. 4.3.2a $4Cu_{(s)} + S_{2(g)} \rightarrow 2Cu_2S_{(s)}$

Reac. 4.3.2b $2Cu_{(s)} + H_2S_{(g)} \rightarrow Cu_2S_{(s)} + H_{2(g)}$

Reac. 4.3.3a $4Sb_{(s,l)} + 3S_{2(g)} \rightarrow 2Sb_2S_{3(s)}$

Reac. 4.3.3b $4Sb_{(s,l)} + 6H_2S_{(g)} \rightarrow 2Sb_2S_{3(s)} + 6H_{2(g)}$

Reac. 4.3.4a $4Bi_{(s,l)} + 3S_{2(g)} \rightarrow 2Bi_2S_{3(s)}$

Reac. 4.3.4b $4Bi_{(s,l)} + 6H_2S_{(g)} \rightarrow 2Bi_2S_{3(s)} + 6H_{2(g)}$

Fig. 4.3.1 shows the standard Gibbs free energies of reactions 4.3.1-4.3.4 normalised per one mole of metal for the sake of comparison. The calculations are based on the thermochemical parameters reported by Knacke et al. [259], and the procedure is described briefly in section 5.1 (see also Appendix 3).

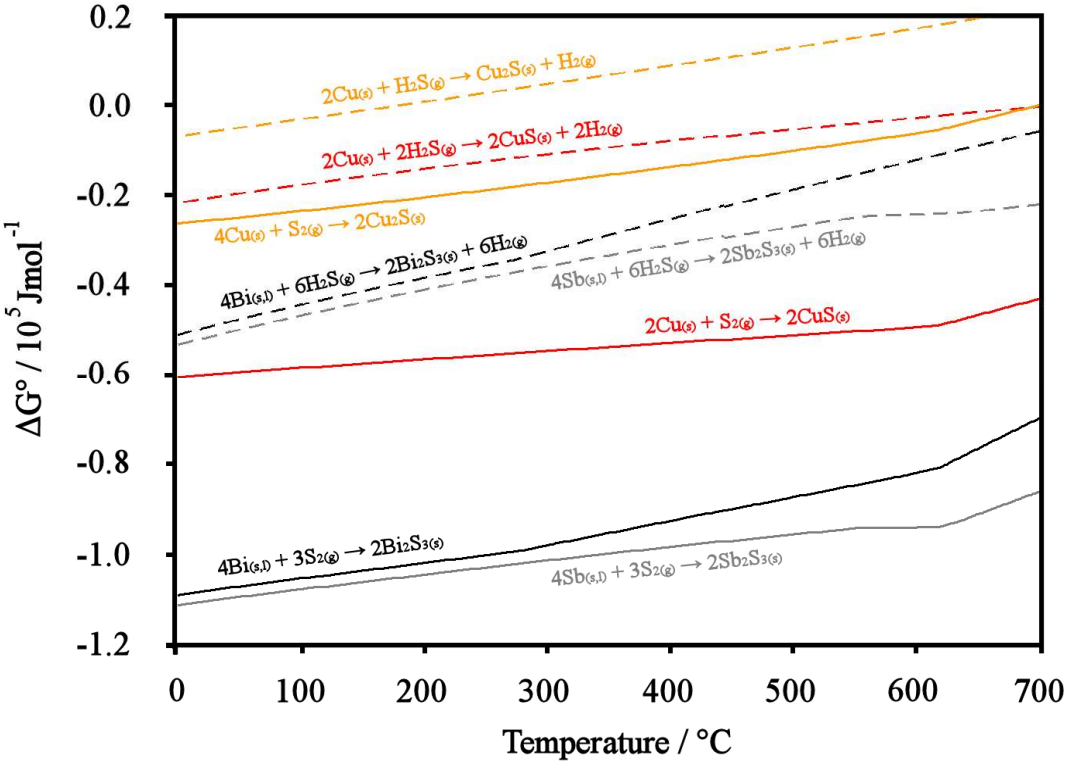

Fig. 4.3.1 Standard Gibbs free energies of the sulfurization reactions of Cu, Bi and Sb with $S_{2(g)}$ (solid lines) and $H_2S_{(g)}$ (dashed lines), as functions of temperature [157].

It is known that up ~620 °C, sulfur vapour is mostly composed of $S_{8(g)}$ – $S_{6(g)}$ ring molecules, whereas the $S_{2(g)}$ species becomes predominant at higher temperatures [260]. Therefore the thermodynamic calculations were based on the data for the most stable molecular sulfur species at each temperature, although little effect of the specific sulfur species considered is expected on the conclusions that can be drawn by comparison of the reactions.

The trends in Fig. 4.3.1 reveal that the sulfurizations via $H_2S_{(g)}$ (dashed lines) are associated with a smaller free energy gain than the corresponding reactions involving $S_{n(g)}$ (solid lines). This behaviour is analogous in any other metal system and is a consequence of the Gibbs free energy of formation of H_2S from elemental H_2 + S_2 (reaction 4.3.5).

Reac. 4.3.5 $H_{2\,(g)} + S_{2\,(g)} \rightarrow H_2S_{\,(g)}$

As calculated in Fig. 4.3.2, ΔG° for reaction 4.3.5 (curve b) is lower than about -40 kJ·mol^{-1} from 0 up to 700 °C, even if the calculation is based on the thermochemical data of the most stable molecular species of sulfur (c). ΔG° is even more negative if the reaction involves atomic sulfur (a).

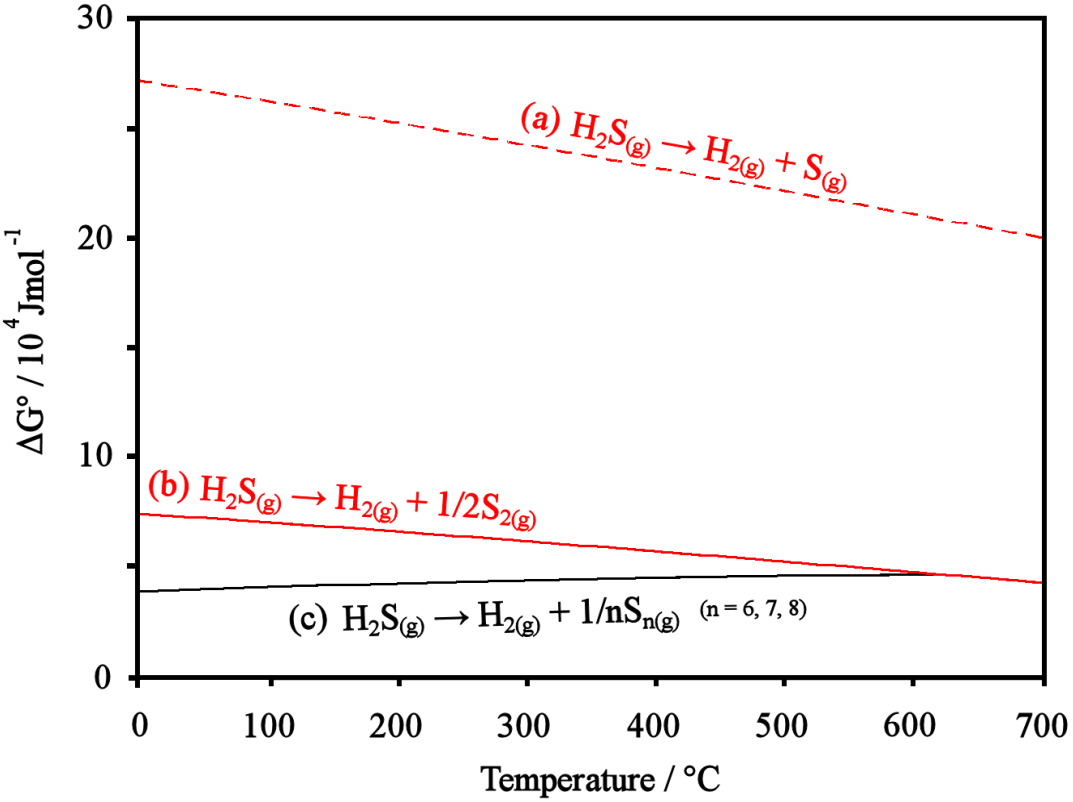

Fig. 4.3.2 Temperature dependence of the Gibbs free energy changes for the decomposition reactions of gaseous hydrogen sulfide into gaseous atomic (a), diatomic (b) and polyatomic (most stable) sulfur species (c) plus hydrogen. The reactions have a ΔG° higher than +40 kJmol^{-1} between 0 and 700 °C. This figure translates into a lower exoergonicity for the sulfurization reactions of metals carried out with hydrogen sulfide rather than elemental sulfur vapour.

A schematic diagram of the relative free energy levels between a metal plus either elemental sulfur vapour or hydrogen sulfide and the metal sulfide is depicted in Fig. 4.3.3, with indication of the free energy changes. This diagram applies to any metals at least in the temperature range of interest for thin-film sulfide formation (considered in Fig. 4.3.3 between 0 and 700 °C).

As shown in Fig. 4.3.1, the ΔG° plots for the sulfurizations of Sb and Bi (with either $H_2S_{(g)}$ or $S_{2(g)}$) are very similar, with the exoergonicity for Bi sulfurizations being slightly lower than those for Sb (ΔΔG° ~2 kJmol^{-1} at 298 K). On the other hand, the free energy changes for the corresponding sulfurizations of Cu are significantly lower than those of Sb and Bi (ΔΔG° >30 kJmol^{-1} at 298 K).

In section 4.2 it was emphasised how Cu reacts with 500 mbar of $S_{2(g)}$ (to form CuS) much more rapidly than Bi and Sb. Furthermore, it was reported that the intermediate phases found by Haber et al. [147, 155] in the Cu-Bi precursor films during incomplete sulfurization with 7 mbar H_2S were $Cu_{1.8}S$ and Bi. It was deduced

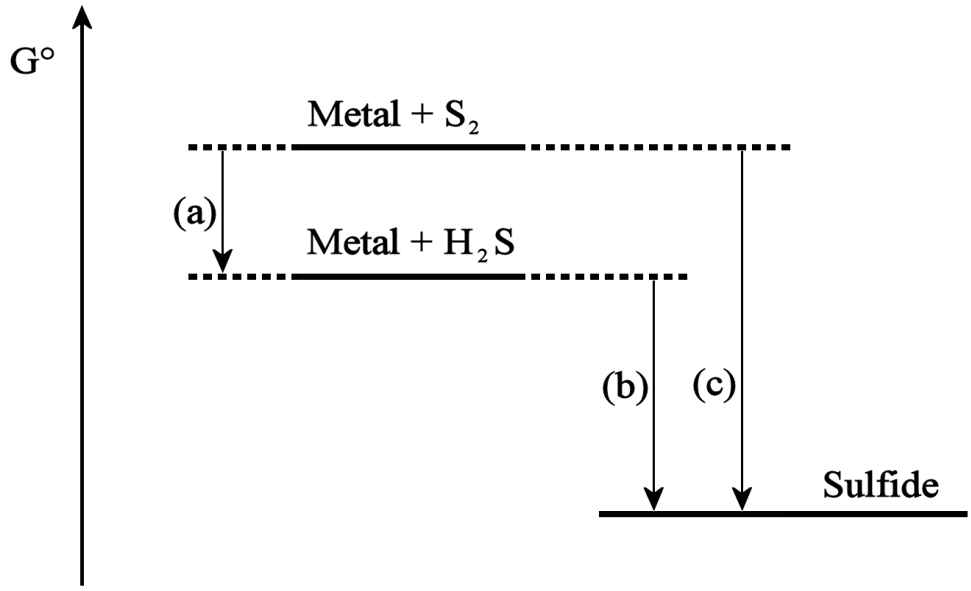

Fig. 4.3.3 Schematic diagram showing the relative free energy levels of a metal plus either $S_{2\,(g)}$ or $H_2S_{\,(g)}$ and the metal sulfide. $\Delta G°$(a) corresponds to the free energy change of reaction 4.3.5 and is lower than -40 $kJmol^{-1}$ from 0 up to 700 °C. As a consequence $\Delta G°$(c), corresponding to the sulfurization reaction with elemental sulfur vapour, is always more negative than $\Delta G°$(b), corresponding to the analogous reaction with $H_2S_{\,(g)}$.

that in Haber's work the rate limiting step for the formation of Cu_3BiS_3 is the sulfurization of Bi.

The existence of correlations between thermodynamic properties and reactivity of substances is important for prediction and interpretation of the kinetics in a variety of systems. The first linear free energy relationship was reported by Hammett in organic chemistry [261], and further extension was made to inorganic crystalline solids by Sverjensky and Molling [262, 263]. Estimations of the relative rates for reactions 4.3.1-4.3.4 are plotted as functions of the corresponding calculated thermodynamic equilibrium constants in Fig. 4.3.4. This figure is a semi-quantitative plot, where correctly determined x-values are associated with y-values that are arbitrarily chosen to be consistent with the qualitative kinetic information extracted from the present and from Haber's works [147, 155]. As such, there is no intention to ascertain any quantitative free energy relationship between the sulfurization reactions considered. The intent of Fig. 4.3.4 is to give the reader a picture of the relative elemental reactivity towards sulfur vapour and hydrogen sulfide, and to serve as basis for further discussion.

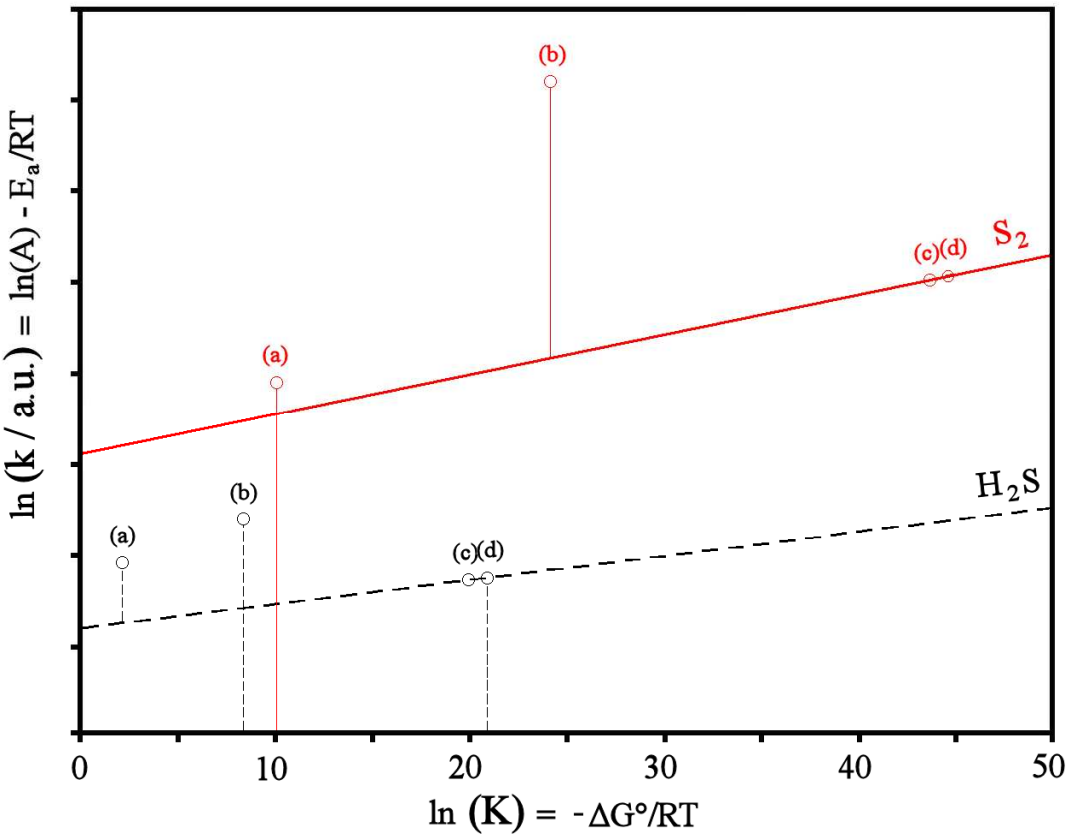

Fig. 4.3.4 Semi-quantitative plot showing the relative sulfurization rates for Cu into Cu_2S (a) and CuS (b) and for Bi and Sb into Bi_2S_3 (c) and Sb_2S_3 (d) with either elemental sulfur vapour (solid) or hydrogen sulfide (dashed), as functions of the corresponding calculated equilibrium thermodynamic constants. The y-values are arbitrarily chosen in order to fit the qualitative kinetic information obtainable from the present and from Haber's works [147, 155]. The proposed relative y-values with no experimental evidence are depicted by bars starting from the abscissa.

The solid lines in Fig. 4.3.4 correspond to the sulfurizations with 500 mbar $S_{2(g)}$ in the present study. The reactivity of Cu to form CuS is represented by point (b) in the solid line. For comparison, (c) and (d) are the relative reactivities of Bi and Sb forming Bi_2S_3 and Sb_2S_3, as extracted from the qualitative information of Fig. 4.1.1. The dashed lines in Fig. 4.3.4 correspond to the sulfurizations with 7 mbar $H_2S_{(g)}$ in the work by Haber at al. [147, 155]. In this case, the formation of $Cu_{1.8}S$ from elemental Cu is represented by point (a), and the corresponding thermodynamic equilibrium constant was calculated using the data of the compositionally similar Cu_2S. As inferred from Haber's work, the lower sulfurization rate of Bi with H_2S compared to Cu is represented by point (c) in the dashed line. In the diagram of Fig. 4.3.4, the linear relationship between the observed sulfurization rates of Bi and Sb with elemental sulfur vapour and the corresponding thermodynamic equilibrium constants is represented by the solid line that joins points (c) and (d). Such linear

relationships may be due to a similar mechanism of sulfide formation. In this respect, it is relevant to highlight that Bi_2S_3 (*Bismuthinite*) and Sb_2S_3 (*Stibnite*) are isostructural [250]. By extrapolation of this free energy relationship to lower values of the thermodynamic equilibrium constant, it is possible to estimate the relative reactivity that Cu would show if the structures of its sulfides were similar to that of Bi_2S_3 and Sb_2S_3 and if their growth would also occur in a comparable way.

Although no data about the sulfurization of Sb with hydrogen sulfide were found, Fig. 4.3.4 assumes that a free energy relationship similar to the one seen for $S_{2(g)}$ may exist between the sulfurization of Bi and Sb with $H_2S_{(g)}$ (dashed line). Analogous considerations apply to the extrapolation of this line towards lower values of the equilibrium thermodynamic constant.

Based on the assumption of linear free energy relationships, the sulfurization rates of Cu with both $S_{2(g)}$ and $H_2S_{(g)}$ are expected to be lower than the corresponding reaction rates of Bi and Sb. The experimental evidence from the present and Haber's works [147, 155] contradicts this expectation. In both cases, Cu seems to react more quickly with the sulfur-bearing molecule compared to Bi and Sb. Discussion of the possible causes for this disagreement follows.

It is clear that the rates of formation of binary sulfides are affected by the morphology of the sulfide crystals that nucleate and grow on the surface of the base metal, since these interpose physically between the two reactants. For example, experiments on the electrochemical anodisation of Sb and Bi have shown that the nucleation and growth of the sulfides give rise to adherent films that envelop the unreacted metal [169, 170], so that one or both the reaction components need time to diffuse through the newly formed phase.

For a qualitative indication of the structural compatibility between a metal and its own sulfide growing onto its surface, we can adapt the concept of the Pilling-Bedworth ratio (R_{PB}), originally developed by corrosion scientists for the investigation of metal oxide formation [228]. For a generic metal sulfide of formula M_xS_y, the adapted Pilling-Bedworth ratio R_{PB} is given by Eq. 4.3.1.

Eq. 4.3.1 $$R_{PB} = V_{M_xS_y} \Big/ xV_M = \rho_M W_{M_xS_y} \Big/ x\,\rho_{M_xS_y} W_M$$

where V, ρ and W are the molar volume ($mol \cdot cm^{-3}$), the density ($g \cdot cm^{-3}$) and the molar mass ($g \cdot mol^{-1}$) of the metal (M) and its sulfide (M_xS_y), respectively. Fig. 4.3.5 is a qualitative representation of the effects of the Pilling-Bedworth ratio on the

morphology of the growing sulfide layer. If this ratio is less than 1, the volume of the grown sulfide is smaller than that of the metal which it replaces, so that the sulfide film will be under expansion strain and will ultimately crack to form a cellular, porous structure (Fig. 4.3.5a). In such a case, the reaction rate may initially decrease, but it rises as soon as a critical sulfide thickness is attained and cracking occurs. If the R_{PB} exceeds unity, a continuous enveloping film of sulfide should form which is free to expand outwards. This isolates the surface of the underlying metal from free contact with the sulfur atmosphere, hindering completion of the conversion (Fig. 4.3.5b). However, if R_{PB} is too high, the sulfide layer may flake off due to excess compression strains (Fig. 4.3.5c) [157].

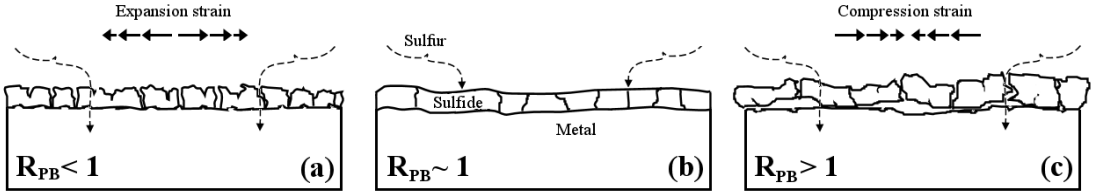

Fig. 4.3.5 Schematic depiction of the effects of mutual density compatibility between a metal and its own sulfide growing onto the metal's surface. Three cases are shown where the Pilling-Bedworth ratio is lower than (a), approximately (b) or exceeding one (c).

The modified Pilling-Bedworth ratio provides a real estimate of the volume compatibility between metals and their sulfides. However, its consequences may vary depending on other anisotropic properties of both phases such as hardness, resilience and surface tension that are all complex functions of the crystallographic direction. Clearly, the processing conditions, as well as the sulfurizing agent employed and its pressure will have an effect on the formation of nuclei and on possible preferential directions of growth [264, 265]. In any case, the following qualitative results are obtained from computation of the Pilling-Bedworth ratios of the interfaces relevant to our study: 2.87 for Cu/CuS, 1.93 for Cu/Cu_2S, 2.00 for Cu/$Cu_{1.8}S$, 2.02 for Sb/Sb_2S_3 and 1.77 for Bi/Bi_2S_3. Among these cases, Cu/CuS has by far the highest R_{PB}. Conversely, Bi/Bi_2S_3 has a particularly low value of R_{PB} (>1) that could make Bi_2S_3 a physical barrier for the conversion reaction. Cu/Cu_2S, Cu/$Cu_{1.8}S$ and Sb/Sb_2S_3 have very similar R_{PB}.

Overall, this simple approach seems to agree with the relative reactivity of Cu, Bi and Sb towards elemental sulfur vapour observed in this work, but fails in explaining

the relatively higher reactivity of Cu compared to Bi in the presence of hydrogen sulfide, as found by Haber [147, 155]. We now consider why the Pilling-Bedworth principle is not enough to explain the relative reactivity of Cu, Sb and Bi with H_2S. Sulfurization of homogenous bulk brass with both sulfur and hydrogen sulfide has been shown to occur with selective reaction of Cu, forming a Cu_2S layer that grows via outward cation migration accompanied by the appearance of pores localised at the alloy/Cu_2S interface [266]. Similar kinetics of sulfide growth has been reported to occur under conditions where covellite (CuS) forms on the surface of bulk Cu [267] and, given the morphological and compositional analyses reported in sections 2.3 and 3.3, it is likely to be the case also for the present study. It is known that the non stoichiometric phases $Cu_{2-x}S$ with x up to 0.066 show exceptionally high copper mobility, due to a mechanism based on cation vacancy exchange [268, 269]. During electrochemical anodisation of Cu electrodes, thin films of Cu_2S are formed first, followed by CuS growth with anodic charge/time profile typical for control of the process via diffusion of Cu ions through the growing film [270, 271]. It has been suggested that if the grown sulfide phase shows defects only in the cation sublattice, the outward diffusion of metal is the main process occurring during the sulfurization (in terms of transport numbers, this corresponds to: $t_+ > t_-$) [272]. In such cases, the oxidation occurs at the metal sulfide/sulfur-source interface and voids are formed at the metal/metal sulfide interface, with degradation of the morphology and breakage of the film.

On the other hand, the reported *n*-type conductivity of both Bi_2S_3 [273] and Sb_2S_3 [274] may suggest that in both cases the defects involve mainly the anion skeleton so that the inward diffusion of the oxidizer is energetically more favourable than outward diffusion of Bi and Sb cations (in terms of transport numbers, this corresponds to: $t_- > t_+$). Indeed, a recent electrochemical impedance spectroscopy model is based on the assumption that anodic Bi_2S_3 grows via transport of sulfide vacancies [275].

It has been proposed that the sulfurization of metals by H_2S involves a dissociative adsorption on the metal surface via reaction 4.3.6 [276].

Reac. 4.3.6 $H_2S_{(g)} \rightarrow H_{2\,(g)} + S^{2-} + 2(+)$

where (+) represents a positive elementary charge shared by the whole metal lattice. This process can also be seen as a reduction of the protons of H_2S by free electrons

of the metal film. The sulfurization of Cu by H_2S has been shown to initiate by germination [277]. This process is likely to occur at a surface defect, where the normal bonding in the metal lattice is unsatisfied [278]. The islands of the new phase grow laterally until they coalesce into a continuous film. At this point the growth is limited by the supply of metal cations towards the metal sulfide/gas interface [279], with the electroneutrality ensured by electron tunnelling [280]. As discussed earlier, the vacancy of the cation sublattices of Cu_2S and $Cu_{1.8}S$ are responsible for the high mobility of Cu in these solids. Therefore, the reduction of the hydrogen atoms at the surface of the sulfide film is limited by Cu out-diffusion. On the other hand, Bi_2S_3 is likely to grow by S anions diffusion from the surface towards the inner part of the film. The average radius of the S^{2-} anion (1.7 Å) is larger than the radii of Bi^{3+} (1.2 Å) and Cu^{+} (0.9 Å) cations [254]. In the presence of H_2S, Cu_2S is likely to grow more rapidly than Bi_2S_3 because of the mechanism involving diffusion of the smaller Cu^{+} cations rather than the larger S^{2-} anion.

If we compare our sulfurization experiment with Haber's based on H_2S [147], it is possible to make some interpretations. The $\Delta G°$ of Cu sulfurization with elemental sulfur vapour is almost 3 times the one for sulfurization with hydrogen sulfide. Furthermore, the initial $S_{2(g)}$ pressure employed in our experiments is about 70 times the H_2S pressure utilised in Haber's work, which translates into a further enhancement of the thermodynamic driving force for formation of the binary sulfides. Due to the different mechanisms of sulfide growth, Bi and Sb are less affected than Cu by the concentration of the oxidizing agent. Therefore, due to the high sulfur partial pressure employed in the present work, Cu tends to react more quickly than Sb and Bi, forming segregated CuS crystals at the surface of the former precursor film. If the sulfur vapour is replaced by hydrogen sulfide at much lower pressure [147], the sulfurization reaction of Cu is slower (possibly also for kinetic reasons), and it occurs on a time scale that is more similar to the sulfurization of Bi and Sb.

Gerein et al. [155] have shown that sulfur incorporation into co-sputtered Cu-Bi films from H_2S at lower temperatures (300 °C) leads to amorphous copper sulfide with reduced lateral segregation of the binary phases and facilitated interdiffusion of Cu and Bi. The kinetic considerations of binary sulfide formation also serve as an explanation for the observed differences in the kinetics of ternary sulfide formation under different sulfurization conditions, as highlighted in Fig. 4.2.2. These differences are due to the consequences of the morphologies of the binary sulfides

grown. For example, CuS segregation at the film surface and the larger crystallite size observed in the present work translate into longer times and/or higher temperatures required for Cu_3BiS_3 to emerge and form completely, compared to the work by Haber et al. [147]. This phenomenon is probably due to compensation of the reduced CuS/Bi_2S_3 contact area that decreases the pre-exponential factor in the Arrhenius equation.

Further support for the proposed explanation is also found in work by Binsma et al. [85], where sulfurization of stacked and co-deposited Cu-In films with either elemental sulfur vapour or hydrogen sulfide was investigated. The critical temperature for the formation of the ternary sulfide $CuInS_2$ was more than 100 °C higher if elemental sulfur was employed in lieu of hydrogen sulfide. Furthermore, if sulfur was used as the sulfurizing agent, the stacked configuration with In on the top showed that $CuInS_2$ can form at lower temperature, compared to the homogeneous configuration. The computed Pilling-Bedworth ratio for In/In_2S_3 is 2.03, which is very close to the corresponding value for Sb. In fact, this behaviour was originally attributed to the protection of the Cu layer by In. The resulting prevention of surface segregation of CuS ensures the preservation of the contact area between the phases and may be responsible for the reported improved kinetics of ternary sulfide formation.

We have seen in section 4.2 the effects of increasing film thickness and decreasing pre-exponential factor on the kinetics of ternary sulfide formation. We can now investigate the effect on the TTR diagram of an increase of the activation energy for the ternary sulfide formation. An increase of the slopes for the lines corresponding to t_s and t_f in the modified Arrhenius plot is an indication of higher activation energy for nucleation and growth of the ternary sulfide. This may be caused by either a different (slower) diffusion mechanism, or by a change of the sign of the Gibbs free energy of reaction 4.1.5 in the low temperature regime. As is emphasized in section 4.4, sulfur pressure has an important thermodynamic (de)stabilization effect on sulfide phases. For example, Nair et al. demonstrated that it is possible to obtain Cu_3BiS_3 by interfacial diffusion of metal atoms in $CuS\text{-}Bi_2S_3$ films annealed in air at temperatures as low as 250 °C for 1 hour [84]. These results suggest that under the conditions employed by Nair, the ternary sulfide formation is thermodynamically favourable and occurs at a much higher rate than in the present and Haber's works where sulfur is introduced by reaction between a sulfur-bearing gas phase and the

metal films. As already mentioned in section 4.1, reaction 4.3.7 requires some sulfur to be released from the solid chalcogenide film.

Reac. 4.3.7 $12CuS_{(s)} + 2Bi_2S_{3\,(s)} \rightarrow 4Cu_3BiS_{3\,(s)} + 3S_{2\,(g)}$

At temperatures where sulfur vapour is stable, annealing in air provides no thermodynamic constraint on its release, as is apparent from the results of Nair et al. [84]. However, this may not be the case if the thermal treatment is performed in the presence of an excess sulfur vapour, e.g. in the present work.

It is reasonable to believe that in our case the stabilization of CuS offered by the excess sulfur vapour may also be the cause for the delayed or even unobserved Cu_3BiS_3 formation in the time frame up to 16 hours at 350 and 270 °C, respectively (Fig. 4.1.3). In Haber's work, where hydrogen sulfide is employed, the Cu intermediate phase is $Cu_{2-x}S$ [147]. The reaction of $Cu_{2-x}S$ with Bi_2S_3 occurs with a reduced amount of evolving sulfur (cf. reaction 4.1.5). The critical times t_s and t_f should be determined in order to estimate the rate of ternary sulfide formation at low temperature, and investigate if the completion delay observed in the present work is simply due to reduced contact area or it is also affected by the residual sulfur pressure inside the vessel. In fact, different sulfurizing conditions such as a different sulfur source and/or its pressure are expected to affect the shape of the TTR diagram, not just because of kinetic factors (e.g. due to different morphology of the grown binary sulfides), but also for thermodynamic reasons (e.g. mass action in reaction 4.1.5). Fig. 4.3.6 shows the theoretical effect on a hypothetical TTR diagram of an increase of the activation energy for ternary sulfide formation at low temperature, due to the presence of elemental sulfur vapour at different pressures.

A similar explanation can be given for the interesting kinetic observations reported by Binsma et al. on $CuInS_2$ [85]. At 375 °C they observed the formation of a single-phase $CuInS_2$ film via sulfurization of co-deposited Cu-In metal precursors with elemental sulfur vapour within 2 hours. However, a similar process carried out at 325 °C resulted in the presence of additional binary sulfides, even after 100 hours of treatment. No explanation for this phenomenon was provided by Binsma et al. [85], but it seems reasonable to think that thermodynamic stabilization of CuS by the high sulfur pressure (liquid sulfur in equilibrium in a sealed glass ampoule) may be the cause for the failure of the interdiffusion reaction to reach completion.

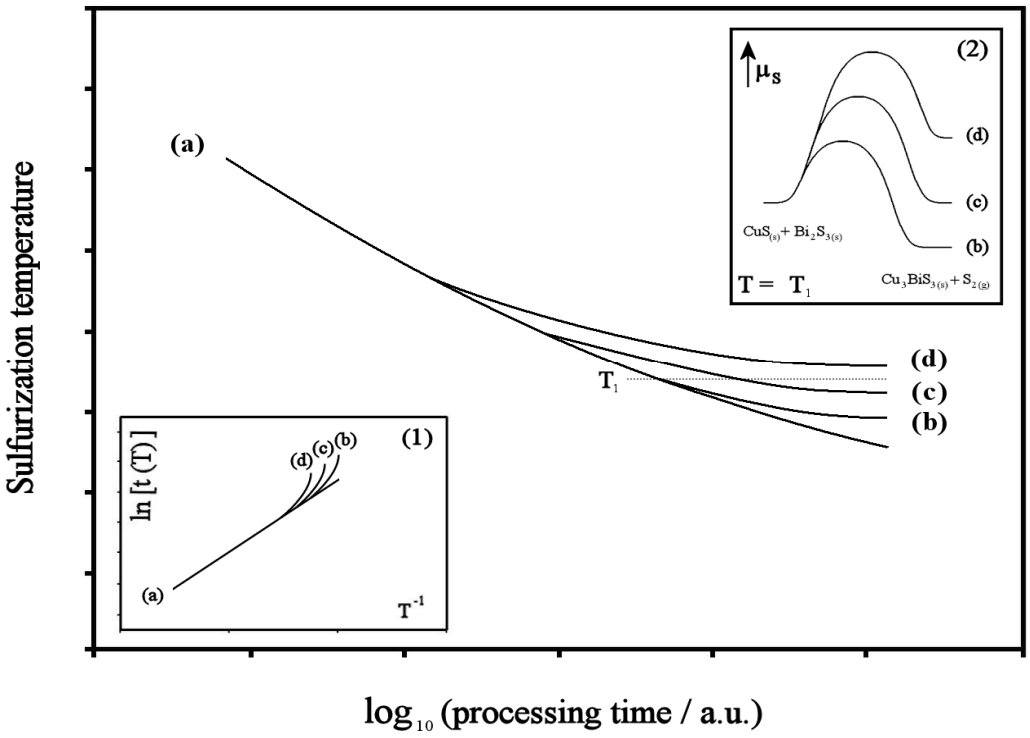

Fig. 4.3.6 Theoretical effect (drawn) of an activation energy increase (b,c,d), on the shape of the reaction curve (a) of a TTR diagram at low temperature. Inset (1): corresponding Arrhenius plot. Inset (2): example of sulfur chemical potential profile at $T = T_1$ for increased sulfur partial pressure (b,c,d) for $CuS+Bi_2S_3$ vs $Cu_3BiS_3+S_2$.

Section 4.4 analyses potential compound decomposition during thermal treatments, with emphasis on the thermodynamic and kinetic aspects.

4.4 Elemental losses during the thermal treatments of chalcogenide layers

The formation of a functional film, such as the absorber layer in a solar cell device, must be performed under conditions where decomposition of the compound of interest is prevented as far as possible. For example, the loss of Sn from CZTS thin films is a well known issue [154], and it has attracted recent attention in several important fundamental studies [143, 281].

In our specific case, the losses of Sb and Bi are also a matter of concern for the achievement of good quality single-phase $CuSbS_2$ and Cu_3BiS_3 films. In fact, we have seen in section 2.3 that evaporated Sb films treated at 350 and 400 °C in excess sulfur vapour under a N_2 flux of about 10 ml·min^{-1} became semi-transparent, showing evidence of elemental depletion [146], while evaporated films of $CuSbS_2$ underwent substantial morphology degradation and Sb depletion to the composition Cu_3SbS_3, when annealed in the absence of chalcogen up to 500 °C.

An overview of the tabulated vapour pressures above solid Sb_2S_3 and Bi_2S_3 is provided in Fig. 4.4.1 [282-284].

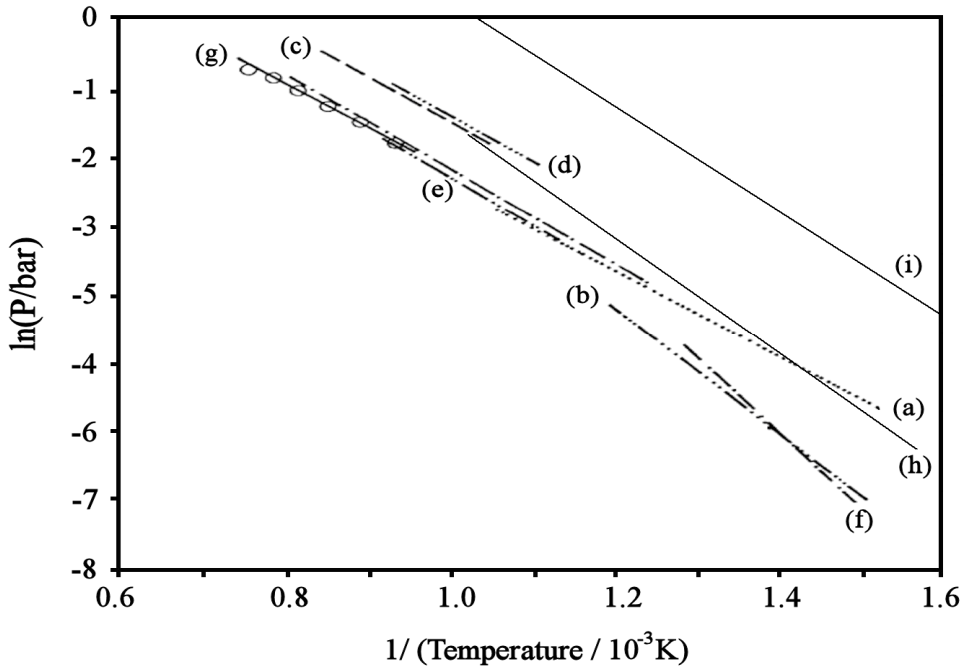

Fig. 4.4.1 Overview of the tabulated vapour pressures of Sb_2S_3 according to (a) Veselovskii [285], (b) Gospodinov et al. [286], (c) Ustyogov et al. [287], (d) Ryazantsev et al. [288], (e) Jones [289], (f) Matei et al. [282], (g) Piacente et al. [284], and of Bi_2S_3 (h) according to Piacente et al. [283]. (The data were taken from [282-284]).

The phenomenon of Sb depletion is attributed to a chemical vapour transport process caused by the excess sulfur with the formation of an Sb-bearing volatile compound such as Sb_2S_4, as discussed later. Yang et al. were the first to report on this transport behaviour, and they made use of it for the synthesis of hollow Sb_2S_3 nanotubes, although no explanation was offered [290]. The method consisted of a treatment of Sb_2S_3 powder at 500 °C in excess sulfur and under a flux of 10 ml·min^{-1} of Ar. These conditions resemble closely our sulfurization treatments of the Cu-Sb metal precursor films reported in section 2.2, therefore it is reasonable to expect an analogy between the two cases.

Gerein et al. [155] first reported the issues concerning the synthesis of morphologically good single phase Cu_3BiS_3 films by sulfurization of metal precursors with hydrogen sulfide over a reasonably short time. In fact, they reported that heat treatment in vacuum at 600 °C resulted in the decomposition of Cu_3BiS_3 from the films, with losses of Bi_2S_3 and the sole preservation of crystalline Cu_2S (*Chalcocite*). Similarly, any treatment performed at temperature higher than 300 °C caused some Bi losses, restricting the upper temperature limit of the process, which in turn imposed long times (>16 hours) to accomplish the full metal conversion [147]. Piacente et al. have shown that solid Bi_2S_3 decomposes into liquid Bi and gaseous S_2 in the temperature range 341-422 °C (Fig. 4.4.0h) [283]. However, due to the extremely low vapour pressure of elemental Bi [291] (~10^{-9} bar at 400 °C), such a reaction does not explain the Bi losses reported by Gerein et al. [155]. A one-step method for the synthesis of Cu_3BiS_3 thin films with good compositional and morphological properties was designed by the same group, with the intent to overcome these restrictions. This process is based on reactive RF and DC sputter deposition of CuS and Bi on substrates held at 250-300 °C [208]. Although this approach is appealing for its simplicity on a laboratory scale, the combined use of DC and RF sputtering might pose technical and economical issues for potential scale-up. Therefore, the development of a two-stage process may be desirable.

As reported in section 3.4.3, no appreciable Bi depletion was found in the present work for converted films of Cu_3BiS_3 even at 550 °C in the time frame up to 16 hours under an estimated $S_{2(g)}$ pressure of 23 mbar. The comparison with Haber's work [147] (where sulfurization in H_2S at 7 mbar at temperatures higher than 300 °C resulted in Bi depletion), suggests that the presence of a background pressure of sulfur vapour has a critical effect on the decomposition equilibria of Cu_3BiS_3, which seem to involve molecular sulfur.

If effective routes for the synthesis of $CuSbS_2$ and Cu_3BiS_3 thin films are to be designed, the chemical equilibria that hide behind these reported elemental losses deserve further attention. This is the intent of the present section. A thermochemical approach is introduced here, in order to investigate the plausible decomposition reactions of the Sb and Bi sulfides in more detail. Hua et al. [292] reported an extensive review of the complex chemistry of the gaseous Sb-S system for their work on the volatilisation kinetics of Sb_2S_3 in steam atmosphere. More than 22 species seem to be involved. In our treatment, the Sb-bearing decomposing species considered is Sb_2S_3, because no experimental thermochemical data are available for $CuSbS_2$. We now demonstrate with Hess' law that the figures resulting from this approximation can only overestimate the losses. Indeed $CuSbS_2$ is more stable than Sb_2S_3 and Cu_2S up to 551 °C, where it melts congruently [293]. Therefore, reaction 4.4.1 can be assumed to have a positive free energy change up to 551 °C.

Reac. 4.4.1 $2CuSbS_{2\,(s)} \rightarrow Cu_2S_{\,(s)} + Sb_2S_{3\,(s)}$

A similar consideration applies to Cu_3BiS_3, with Bi_2S_3 being the solid Bi-bearing decomposing species considered, since the binary sulfide (as for $CuSbS_2$) would ultimately be the result of the solid state decomposition [218] (reaction 4.4.2).

Reac. 4.4.2 $2Cu_3BiS_{3\,(s)} \rightarrow 3Cu_2S_{\,(s)} + Bi_2S_{3\,(s)}$

Fig. 4.4.2 shows the Cu_2S-Sb_2S_3 and the Cu_2S-Bi_2S_3 pseudo-binary equilibrium phase diagrams, as reported by Sugaki et al. [218, 293]. From such diagrams is apparent that the free energy changes of reactions 4.4.1 and 4.4.2 are positive respectively up to 551 °and 527 °C.

Fig. 4.4.3 is a graphical representation of the energetic diagrams of the binary sulfides (Cu_2S + Sb_2S_3 and Cu_2S + Bi_2S_3), ternary sulfides ($CuSbS_2$ and Cu_3BiS_3) and of generic Sb- and Bi-bearing gaseous compounds. Since $\Delta G°(a) < 0$, it follows that $\Delta G°(c) > \Delta G°(b) > 0$. By substitution in Eqs. 4.4.1 and 4.4.2 it follows that the equilibrium pressure of the Sb- and Bi-bearing gaseous compounds above solid Sb_2S_3 and Bi_2S_3 are higher than respectively above solid $CuSbS_2$ and Cu_3BiS_3.

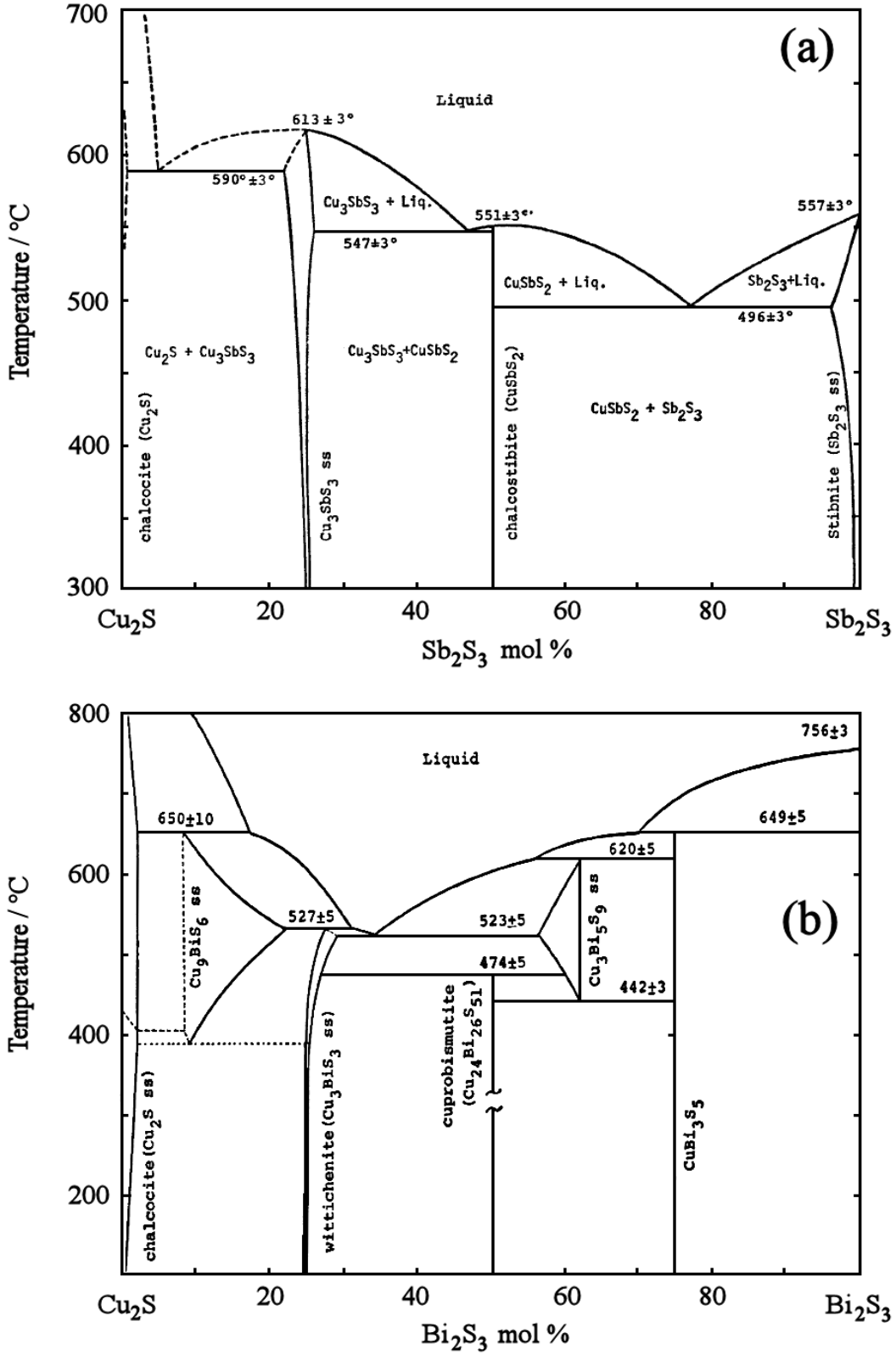

Fig. 4.4.2 Cu_2S-Sb_2S_3 (a) and Cu_2S-Bi_2S_3 (b) equilibrium pseudo-binary phase diagrams, as reported by Sugaki et al. [218, 293]. The $CuSbS_2$ phase (*Chalcostibite*) melts congruently at 551 °C (a), while Cu_3BiS_3 (*Wittichenite*) decomposes peritectically at 527 °C (b).

As a consequence, the computation performed in the present study is an overestimation of the Sb and Bi losses that would occur at equilibrium.

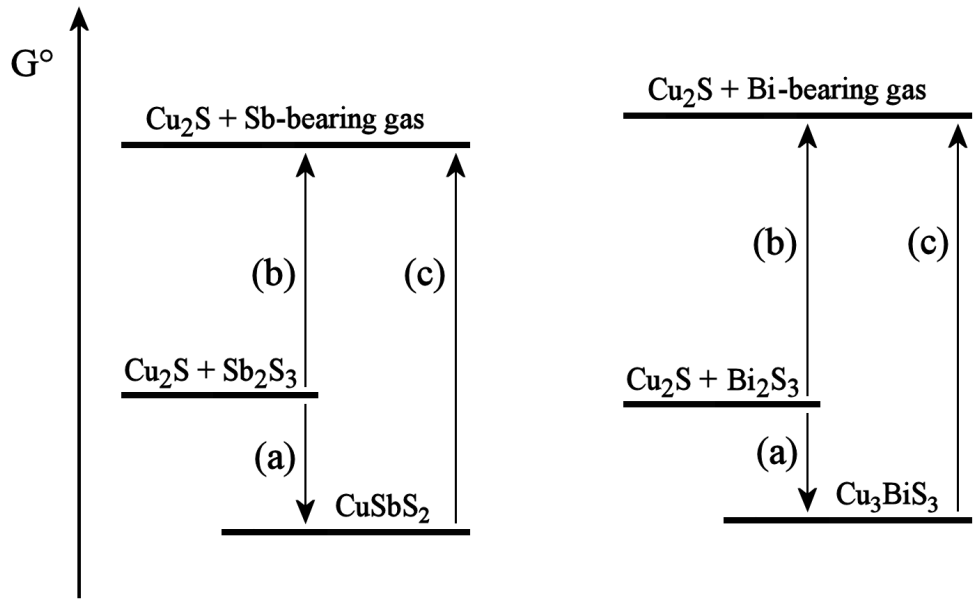

Fig. 4.4.3 Graphical representation of the energetic diagram of condensed Cu_2S + Sb_2S_3, $CuSbS_2$ and of a generic gaseous Sb-bearing compound. Since $\Delta G°(a) < 0$, $\Delta G°(c) > \Delta G°(b) > 0$, meaning that the pressure of the Sb-bearing gaseous compound in equilibrium with solid Sb_2S_3 is higher than with solid $CuSbS_2$ (see Eqs. 4.4.1 and 4.4.2). Therefore, the computation performed in the present study gives an overestimation of the Sb losses that would occur at the equilibrium.

Many Sb- and Bi-bearing species could potentially be involved, but the following are those for which thermochemical data in the temperature range of interest are available: $Sb_{(g)}$, $Sb_{2\,(g)}$, $Sb_{4\,(g)}$, $SbS_{(g)}$, and $BiS_{(g)}$, $Bi_{2\,(g)}$ and $Bi_{(g)}$ [259, 294]. These product species have a high free energy content, and they have only been reported in the gaseous form (with the exception of condensed Sb and Bi). Consequently, the scenario is slightly different from CISSe [295, 296] and CZTSSe [156], because the corresponding decompositions cannot occur in multiple steps, as proposed by Scragg et al. for CZTS [281].

The decomposition reactions investigated are as follows (4.4.3-4.4.9) [157].

Reac. 4.4.3 $Sb_2S_{3\,(s)} \rightarrow 2Sb_{(g)} + 3/2S_{2\,(g)}$

Reac. 4.4.4 $Sb_2S_{3\,(s)} \rightarrow Sb_{2\,(g)} + 3/2S_{2\,(g)}$

Reac. 4.4.5 $Sb_2S_{3\,(s)} \rightarrow 1/2Sb_{4\,(g)} + 3/2S_{2\,(g)}$

Reac. 4.4.6 $Sb_2S_{3\,(s)} \rightarrow 2SbS_{\,(g)} + 1/2S_{2\,(g)}$

Reac. 4.4.7 $Bi_2S_{3\,(s)} \rightarrow 2BiS_{\,(g)} + 1/2S_{2\,(g)}$

Reac. 4.4.8 $Bi_2S_{3\,(s)} \rightarrow 2Bi_{\,(g)} + 3/2S_{2\,(g)}$

Reac. 4.4.9 $Bi_2S_{3\,(s)} \rightarrow Bi_{2\,(g)} + 3/2S_{2\,(g)}$

For each of the above reactions, the equilibrium pressure constant can be calculated according to equation 4.4.1.

Eq. 4.4.1 $$K_{P_j} = \prod_i P_i^{\nu}$$

where *j* is the reaction number, *i* is the chemical species in each reaction and ν is the corresponding stoichiometric coefficient (N.B. that the convention employed for the sign of ν is minus for the reagents and plus for the products).

The relationship between equilibrium constant and standard Gibbs free energy change (ΔG°) of a reaction is known (Eq. 4.4.2).

Eq. 4.4.2 $$\Delta G° = -RT\ln(K_P)$$

where *R* is the universal ideal gas constant and *T* is the absolute temperature.

The pressures of the Sb- or Bi-bearing molecules of interest can be obtained combining Eqs. 4.4.1 and 4.4.2 (Eqs. 4.4.3-4.4.9) [157].

Eq. 4.4.3 $$P_{Sb_{(g)}} = e^{-\Delta G°/2RT} \Big/ P_{S_{2(g)}}^{3/4}$$

Eq. 4.4.4 $$P_{Sb_{2(g)}} = e^{-\Delta G°/RT} \Big/ P_{S_{2(g)}}^{3/2}$$

Eq. 4.4.5 $$P_{Sb_{4(g)}} = e^{-2\Delta G°/RT} \Big/ P_{S_{2(g)}}^{3}$$

Eq. 4.4.6 $$P_{SbS_{(g)}} = e^{-\Delta G^\circ/2RT} \Big/ P_{S_{2(g)}}^{1/4}$$

Eq. 4.4.7 $$P_{BiS_{(g)}} = e^{-\Delta G^\circ/2RT} \Big/ P_{S_{2(g)}}^{1/4}$$

Eq. 4.4.8 $$P_{Bi_{(g)}} = e^{-\Delta G^\circ/2RT} \Big/ P_{S_{2(g)}}^{3/4}$$

Eq. 4.4.9 $$P_{Bi_{2(g)}} = e^{-\Delta G^\circ/RT} \Big/ P_{S_{2(g)}}^{3/2}$$

An estimation of the tendency for the Sb- and Bi-containing gaseous species to evolve from solid Sb_2S_3 and Bi_2S_3 can be obtained if the temperature dependence of the standard Gibbs free energy changes for reactions 4.4.3-4.4.9 is known. Equations 4.4.3-4.4.9 are computed as functions of both the temperature and the $S_{2\,(g)}$ partial pressure within the chamber. Figs. 4.4.4-4.4.5 are the graphical representations of these pressure equilibria for the Sb-S and Bi-S systems respectively.

In principle, all these processes can occur simultaneously, and their relative importance can be understood if a 2D projection of the 3D intersections among all the surfaces is plotted (Figs. 4.4.4d and 4.4.5d).

Figs. 4.4.4d and 4.4.5d give only the relative importance of each process, but they do not help to identify the actual equilibrium extent of the corresponding processes. On the other hand, 3D plots like Figs. 4.4.4a-b and 4.4.5a-b are often not easy to understand. Therefore, the 2D projections in Figs. 4.4.4c and 4.4.5c are shown, in an attempt to quantify the magnitude of each process. As indicated in the 3D plots, a linear plane is added representing a "threshold pressure" that is identified by Eq. 4.4.10.

Eq. 4.4.10 $P^* = 10^{-8}$ bar $K^{-1} \cdot T$

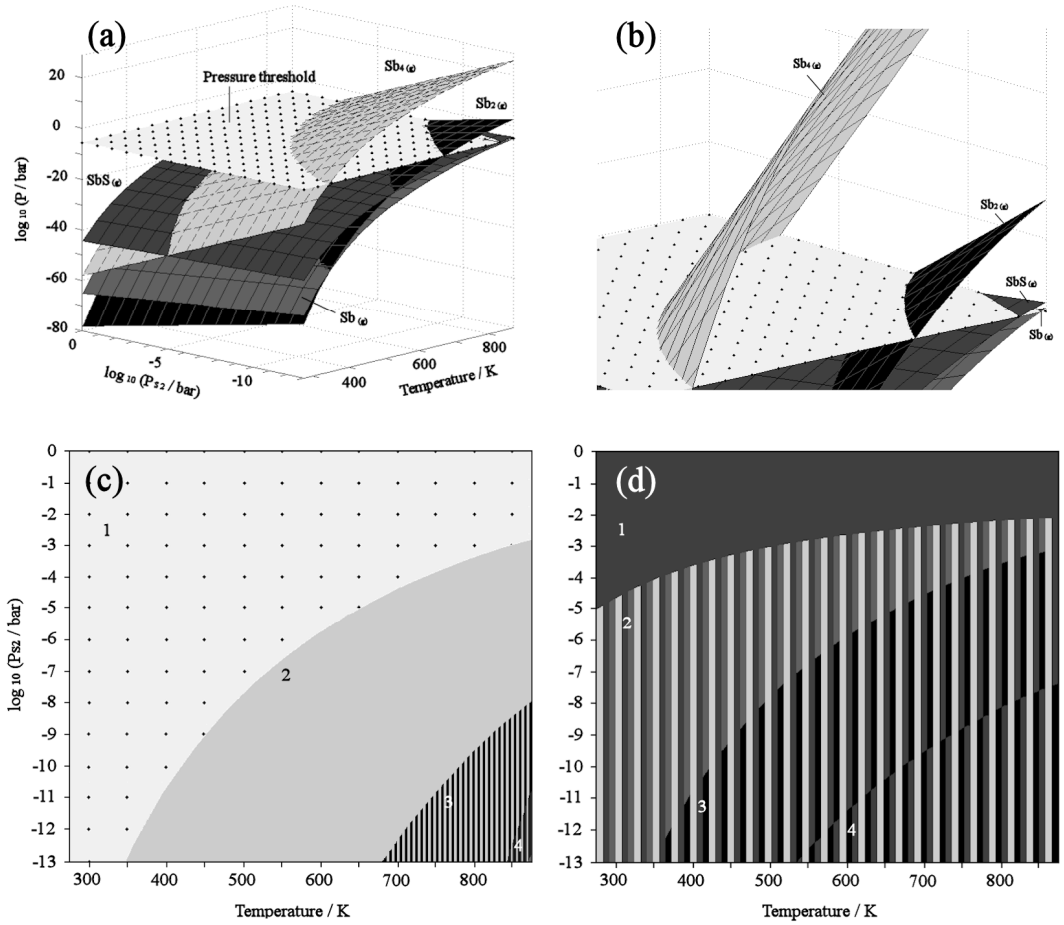

Fig. 4.4.4 3D plot showing the pressures of $Sb_{(g)}$, $Sb_{2\ (g)}$, $Sb_{4\ (g)}$ and $SbS_{\ (g)}$ (Eqs.4.4.3-4.4.6) as functions of temperature and partial pressure of $S_{2\ (g)}$ in equilibrium with $Sb_2S_{3\ (s)}$, as per reactions (4.4.3-4.4.6) with the addition of the threshold pressure plane (Eq. 4.4.10) (a-b).
Intersection among the pressure equilibria functions of the Sb-bearing gaseous species (d) and of the latter with the threshold pressure plane (c) plotted as 2D projections of the 3D plot on the x-y plane.
Fig. 4.4.4c can be divided into four regions. In region 1 the pressure of the Sb-bearing gaseous species is below the threshold pressure value. In region 2, $Sb_{4\ (g)}$ is the only species that shows a pressure exceeding the threshold value, while in region 3 and 4, $Sb_{2\ (g)}$ and $SbS_{(g)}$ also contribute progressively to the Sb depletion process. Careful inspection of Fig. 4.4.4b, also reveals that $Sb_{(g)}$ satisfies the threshold conditions at the very corner of minimum sulfur pressure and maximum temperature considered. Fig. 4.4.4d shows the regions of the sulfur pressure/temperature diagram with different relative magnitude of the pressure for each volatile species, which is as follows [157].

Region 1: $SbS_{\ (g)} > Sb_{4\ (g)} > Sb_{\ (g)} > Sb_{2\ (g)}$
Region 2: $Sb_{4\ (g)} > SbS_{\ (g)} > Sb_{\ (g)} > Sb_{2\ (g)}$
Region 3: $Sb_{4\ (g)} > SbS_{\ (g)} > Sb_{2\ (g)} > Sb_{\ (g)}$
Region 4: $Sb_{4\ (g)} > Sb_{2\ (g)} > SbS_{\ (g)} > Sb_{\ (g)}$

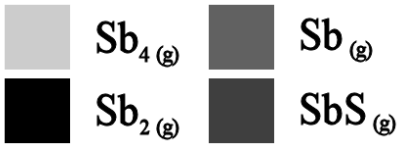

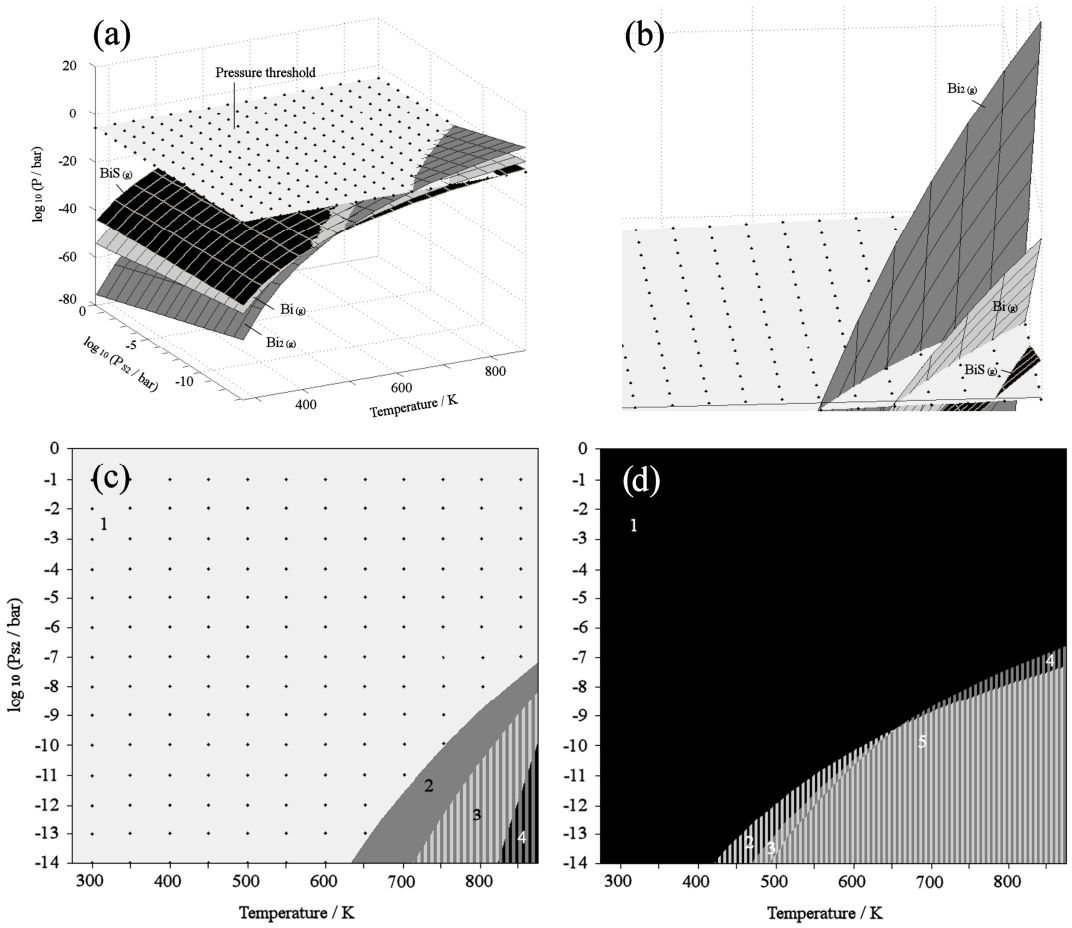

Fig. 4.4.5 3D plot showing the pressures of $Bi_{(g)}$, $Bi_{2\,(g)}$, and $BiS_{(g)}$ (Eqs.4.4.7-4.4.9) as functions of temperature and partial pressure of $S_{2\,(g)}$ in equilibrium with $Bi_2S_{3\,(s)}$, as per reactions (4.4.7-4.4.9) with the addition of the threshold pressure plane (Eq. 4.4.10) (a-b).
Intersection among the pressure equilibria functions of the Sb-bearing gaseous species (d) and of the latter with the threshold pressure plane (c) plotted as 2D projections of the 3D plot on the x-y plane.
Fig. 4.4.5c can be divided into four regions. In region 1 the pressure of the Bi-bearing gaseous species is below the threshold pressure value. In region 2, $Bi_{2\,(g)}$ is the only species that shows a pressure exceeding the threshold value, while in region 3 and 4, $Bi_{(g)}$ and $BiS_{(g)}$ contribute progressively to the Bi depletion process, as can be also inferred from Fig. 4.4.5b.
Fig. 4.4.5d shows the regions of the sulfur pressure/temperature diagram with different relative magnitude of the pressures for each volatile species, which are as follows [157].

Region 1: $BiS_{(g)} > Bi_{(g)} > Bi_{2\,(g)}$
Region 2: $Bi_{(g)} > BiS_{(g)} > Bi_{2\,(g)}$
Region 3: $Bi_{(g)} > Bi_{2\,(g)} > BiS_{(g)}$
Region 4: $Bi_{2\,(g)} > BiS_{(g)} > Bi_{(g)}$
Region 5: $Bi_{2\,(g)} > Bi_{(g)} > BiS_{(g)}$

The choice for the temperature coefficient in Eq. 4.4.10 that defines the plane is arbitrary. In Figs. 4.4.4-4.4.5 the value 10^{-8} bar K^{-1} has been chosen, as to delineate the pressure limit above which the loss of Sb and Bi from films of $CuSbS_2$ and Cu_3BiS_3 1 μm thick exceeds 10% of the original content per cm^2 area of film and dm^3 capacity of sulfurization furnace (calculated from P = nRT/V, based on the difference between the number of moles of Sb per cm^2 of film and the number of moles of Sb-bearing gas at the equilibrium per dm^3 of furnace under static atmosphere conditions). The P^* plane cuts the pressure equilibria functions of the Sb- and Bi-bearing gaseous species in Figs. 4.4.4a-c and 4.4.5a-c respectively. By doing so it identifies the species that have the potential to contribute most to the loss mechanisms. The 2D projections obtained from these intersections (Figs. 4.4.4c and 4.4.5c) define the sulfur pressure / temperature conditions under which these processes occur and exceed the chosen extent.

Among the decomposition routes computed in Fig. 4.4.4, the evolution of $Sb_{4(g)}$ and $S_{2(g)}$ through reaction 4.4.5 should be the major contributor to Sb depletion in the ranges of $S_{2\,(g)}$ pressure and temperature of our interest. At 400 °C and 10^{-10} mbar of $S_{2\,(g)}$, an equilibrium partial pressure of ~ 10^{-1} mbar can be estimated for the $Sb_{4\,(g)}$ species in equilibrium with solid Sb_2S_3. In these conditions it is very likely that the use of a gas flux and/or a large volume of the furnace would determine Sb losses. This may occur via mass transport and/or saturation of the vessel, especially with prolonged dwell times that would allow the equilibrium to be reached. From Fig. 4.4.4c it is apparent that a $S_{2\,(g)}$ partial pressure of 0.1 mbar is sufficient to bring down the equilibrium pressures of the Sb-bearing gas species to negligible values. However, mass spectrometric studies of the vapour phase above solid Sb_2S_3 indicate $SbS_{(g)}$ as the dominant component. As a consequence, some thermodynamic models developed to describe the composition of epithermal ore fluids (volcanic eruptive gases) are based on the assumption that Sb is transported primarily through this diatomic molecule (Spycher et al. [297] in Zakaznova-Iakovleva et al. [298]). As reported in section 2.2, this may be the case for the evaporated $CuSbS_2$ samples annealed in absence of chalcogen, but for the Cu-Sb metal precursor films, a large excess of elemental sulfur vapour was employed during the sulfurization treatment. Therefore, the Sb losses observed in that case cannot be attributed to reactions 4.4.3-4.4.6, because they would be all effectively suppressed by Le Chatelier effect. It follows that a different process must have occurred: one in which sulfur molecules take part on the left hand side of the chemical equation. A possibility might be given

by the molecule Sb_2S_4, which was suggested from mass spectrometric studies by Steblevskii et al. [299] to compose part of the vapour above Sb_2S_3 in the temperature range 377-467 °C. Antimony thioantimonate (Sb_2S_4) is also known as an amorphous solid. This suggests it may not be an incommensurate species resulting from elemental sulfur intercalation into the lattice of Sb_2S_3 [300], but it may rather exists as a molecular solid. Its decomposition into solid Sb_2S_3 and sulfur in the temperature range 200-400 °C is a process exploited in rheology, because the formation of gaseous sulfur decreases friction between gears [301]. The reverse reaction may occur (reac. 4.4.10).

Reac. 4.4.10 $Sb_2S_{3\,(s)} + 1/2S_{2\,(g)} \rightarrow Sb_2S_{4\,(g)}$

Steblevskii et al. [302] suggest that reaction 4.4.10 occurs between $S_{2\,(g)}$ and either gaseous or molecular Sb_2S_3. Such a scenario would open the possibility for Sb to be transported in excess sulfur and would explain the Sb_2S_3 transport in excess sulfur reported by Yang et al. [290]. Depending on the sign of the reaction enthalpy, gaseous Sb_2S_4 will then incur decomposition back to $Sb_2S_{3\,(s)} + S_{2\,(g)}$ in the hot or cold parts of the furnace.

As in the Sb-S case, Fig. 4.4.5 can help identify the processes that are most likely to be responsible for the depletion of Bi from Bi_2S_3, and so from Cu_3BiS_3 too. At high temperature, according to the thermochemical computation, the species mostly contributing to the Bi losses is $Bi_{2\,(g)}$ through reaction 4.4.9. This reaction could be responsible for the Cu_3BiS_3 decomposition from the films annealed in vacuum at 600 °C, as reported by Gerein et al. [155] and for any Bi losses reported for treatments at temperatures higher than 300 °C [147]. Furthermore, it would explain why Bi depletion was not observed in the present work. Indeed an atmosphere containing 23 mbar of sulfur vapour (at equilibrium) is more than capable of suppressing the compound decomposition by exerting mass action.

It must be highlighted that this is a purely thermodynamic treatment and, therefore, it only gives the conditions of surface instability. Information on the actual decomposition rates can only be attained with kinetic investigations. It is reasonable to think that the reactions involving the least number of metal-S bond breakages are those showing the lowest activation energy and may dominate for kinetic reasons.

As seen in section 4.3 for the low temperature region of the TTR diagram, due to the equilibria of reactions 4.4.3-4.4.9 the pressure of sulfur within the system also

affects the shape of the reaction curves in the upper region of temperatures. Fig. 4.4.6 is a schematic representation of the effect of sulfur pressure on the upper limit of the curves for ternary sulfide formation.

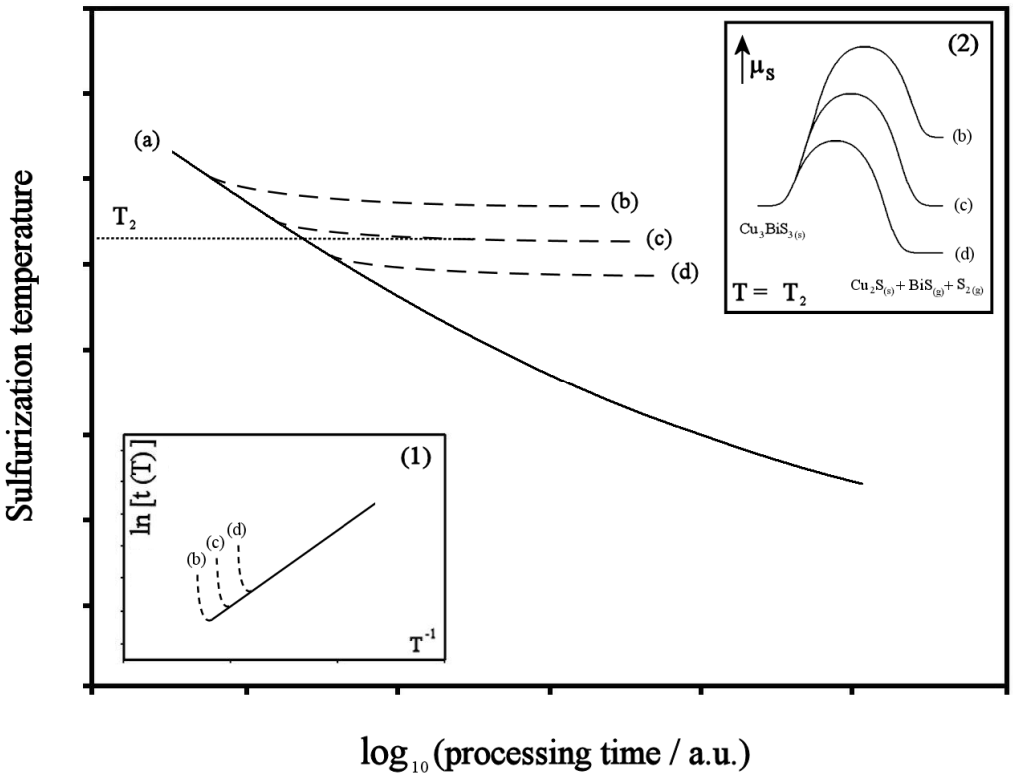

Fig. 4.4.6 Schematic representation of the effect of decreasing sulfur pressure (b,c,d) on the ternary sulfide formation curve (a) in the high temperature range due to compound decomposition. Inset (1): corresponding Arrhenius plot. Inset (2): example of sulfur chemical potential profile at $T = T_2$ for decreasing sulfur pressure (b,c,d) for a potential decomposition route.

Concluding remarks for part A

In chapters 2 and 3 experimental details concerning the formation of $CuSb(S,Se)_2$ and Cu_3BiS_3 thin films have been outlined, along with the morphological, compositional, structural and photoelectrochemical results. The synthesis followed a two-stage route consisting of the formation of metal or chalcogenide precursor films and subsequent conversion into the desired compound by reaction with chalcogenizing atmospheres. Conditions were identified for the formation of semiconductor thin films with band-gap energies suitable for photovoltaic applications, ranging from ~1.2 to ~1.5 eV. However, the measured photocurrent conversion efficiencies of these films were too poor to deserve device completion tests.

Based on the conclusion that good semiconductor properties can only be attained if suitably compact single-phase layers are synthesised, efforts were directed to the study of the reaction chemistry of ternary sulfide formation (chapter 4). This study was made possible by the combined structural and morphological characterization of Cu-Bi-S films obtained with an RTP furnace. Such an approach allowed determination of the phase evolution of the system as a function of sulfurization time and temperature. It became clear that the conversion of the metal precursor films into ternary sulfides in the presence of elemental sulfur vapour occurs via prior separation of the binary sulfides and their subsequent solid state reaction. The analysis of these results allowed the construction of Time-Temperature-Reaction diagrams for the description of the sulfurization reaction under different conditions. Important kinetic information was extracted from the TTR diagram. Particularly, it was found that the activation energy for the formation of Cu_3BiS_3 thin films by diffusion across the CuS-Bi_2S_3 interface is considerably higher than the corresponding energy for $CuSbS_2$ reported in the literature for bulk diffusion couple experiments. This result seems consistent with the comparative atomic radii of Bi and Sb in similar sulfides.

The thermodynamics of sulfurization reactions were assessed via computation of the free energy changes as a function of the temperature. A linear relationship was found between the free energy changes and the relative reaction rates for the reactions of Sb and Bi. By contrast, the sulfurization reactions of Cu with both elemental sulfur vapour and hydrogen sulfide do not fit in the linear free energy relationship found for Sb and Bi. This is explained by the fact that, despite the lower

exoergonicity, Cu is much more reactive than Sb and Bi with both elemental sulfur vapour and hydrogen sulfide. A plausible explanation for this phenomenon was given. This takes inspiration from Corrosion Science and considers the role of density compatibility between metals and corresponding binary sulfides growing onto their surface. Modified Pilling-Bedworth coefficients were calculated for the interfaces relevant to our experimental work: Cu/CuS, Sb/Sb_2S_3, Bi/Bi_2S_3, as well as Cu/Cu_2S, Cu/$Cu_{1.8}S$ and In/In_2S_3 for comparison with key articles from the literature. The coefficients seem to be in qualitative agreement with the proposed different mechanisms of binary sulfide growth, which in turn are the cause for prominent phase segregation of CuS in the presence of elemental sulfur vapour observed for both Cu-Sb and Cu-Bi systems. These considerations allowed a sound interpretation of the results obtained in this work and made possible a critical comparison with those reported in other literature resources. Particular attention was given to the different sulfurizing conditions and their effects on the structural and morphological properties of the films produced. For example, it was found that the Pilling-Bedworth argument fails to explain the higher reactivity of Cu towards hydrogen sulfide, compared to Bi. In such case the different reactivity may be attributed to the different radii of the ions involved in the growth of the binary sulfide (either Cu^+ or S^{2-}). In fact, diffusion of Cu cations is expected for Cu-S phases, where the cation sublattice is generally defective, while sulfide anions are likely responsible for the growth of Sb_2S_3 and Bi_2S_3.

Our findings indicate that the early stages of the processing have a strong effect on the growth of the intermediate phases, which were shown to influence the kinetics of ternary sulfide formation and the morphological quality of the layers. Furthermore, the composition of the atmosphere during the process determines if the ternary sulfide can grow or is subject to decomposition or incomplete formation.

In summary, the following aspects and their impact on the kinetics of ternary sulfide formation have been identified (Fig.CA1), with the objective of formulating some general rules for the design of effective synthetic routes.

(1) Extent of intermediate phase segregation and/or crystallite size (section 4.2)

(2) Thermodynamic (de)stabilization at low temperature (section 4.3)

(3) Thermodynamic (de)stabilization at high temperature (section 4.4)

All these points are related to the chalcogenizing conditions employed during the synthesis, either directly, as per (2) and (3) or indirectly (1).

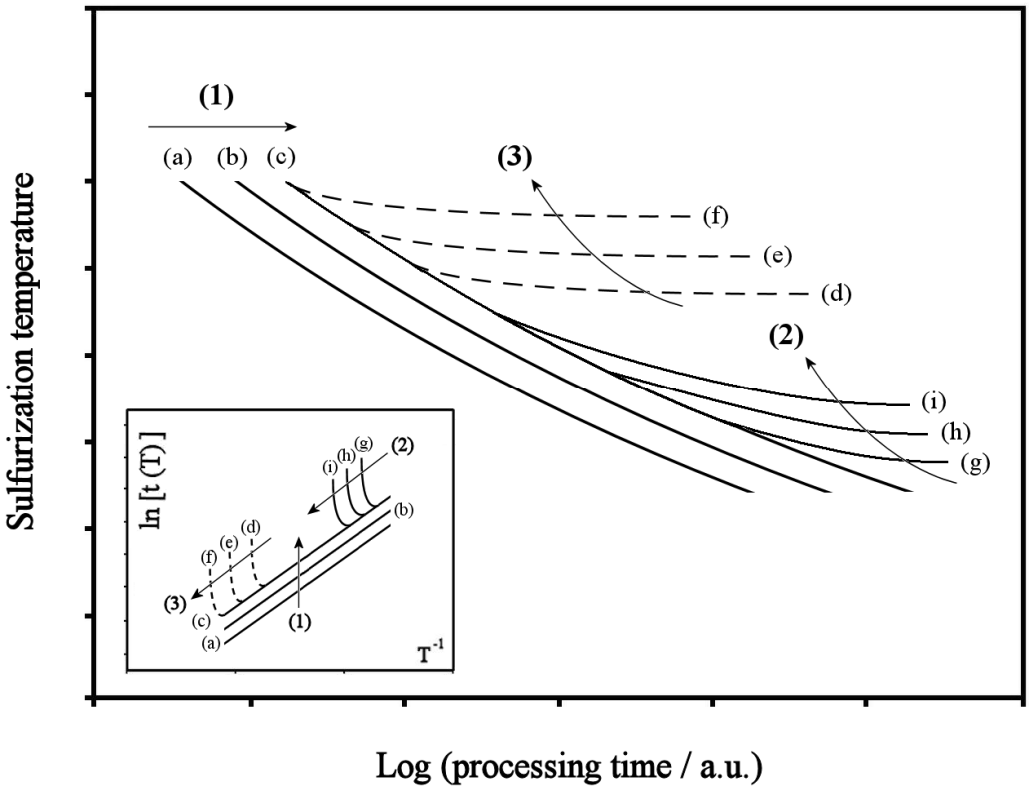

Fig. CA1 Schematic summary of the effects of secondary phase segregation and/or crystallite size (1) and phase (de)stabilization due to an increase of sulfur partial pressure (2,3) on the shape and position of the ternary sulfide formation curves in a TTR diagram. Inset: corresponding Arrhenius plot.

Other parameters can affect point (1). One example can be the configuration of the metal precursor film. Although this aspect has not been thoroughly investigated, it can be concluded that the sulfurization of homogeneous Cu-Bi metal precursors did not seem to involve a simpler reaction pathway compared to the stacked configuration. This was attributed to both the particularly low temperature of the eutectic reaction in the Cu-Bi phase equilibria and to the strongly different reactivity of Cu and Bi towards sulfur. As discussed in section 4.2, the combination of these two aspects was believed to be the cause of the more pronounced detrimental phase segregations observed with the co-electroplated metal precursors compared to the stacked films.

Phase segregation is inherently expected with any two-stage process consisting of precursor film conversion by mass transfer from a gas or liquid phase followed by solid state reaction. It is obvious that this intrinsic process flaw becomes more important as the complexity of the system considered increases [56]. On the other hand, since the simplicity of such a process makes it a route with great industrial

appeal, endeavouring to find possible ways to minimise intermediate phase segregations is worthwhile. In fact, it seems clear that the promising results recently reported on thin CIGSSe and CZTSSe films obtained with a solution-particle approach (e.g. where the binary sulfides are dissolved in hydrazine and spin-coated) have to do with the fact that the chalcogen in already present in the precursor film and does not have to be introduced at a second stage [54, 58, 303]. Therefore, the design of the conditions for successful thin-film formation with the two-stage process requires the choice of an appropriate precursor film configuration as well as fine-tuning of the reactive atmosphere composition. This may involve variation of temperature, pressure and kind of chalcogenizing species during the conversion treatment, in order to suit the metal precursor chemistries. For example, a less reactive chalcogenizing atmosphere may be chosen at the early stages of the treatment in order to reduce detrimental phase segregations of the more reactive components of the system. The conditions can then be made more reactive to accommodate the lower reactivity of the other components. In this context, Merdes et al. have reported excellent improvements of CIGS reaction progress using an RTP procedure with careful adjustment of temperature profile and sulfur partial pressure [304]. Enhancement of morphological and photoactive properties of CZTS thin-films have been reported by Maeda et al. with a sulfurization method employing hydrogen sulfide at low concentration (3%) and CZTS metal precursors with presumably high (although not reported) surface area obtained with a sol-gel method [305]. The nucleation rate of the binary chalcogenides is likely to be reduced by less reactive chalcogenizing atmospheres. This should lead to a reduction of the extent of secondary phase segregation and, in some cases, to the formation of amorphous intermediate films [155]. Unfortunately if the surface area of the metal precursor is low, this procedure may have the side effect of reducing the overall reaction rate, with the result that longer times may be required for the chalcogen uptake to complete [147]. The use of porous metal precursor films may help to compensate for the reduced driving force. High surface areas should also contribute to compensate for the differing levels of reactivity of the precursor metals (e.g. Cu and Bi or Sb), with potential morphological benefits. In the present work, porous Cu-Bi metal precursors were serendipitly produced via co-electrodeposition from an alkaline aqueous solution. Unfortunately, the novelty of these precursors and their potential value for conversion into Cu_3BiS_3 with a reduced reactivity of the sulfurizing atmosphere were not appreciated sufficiently. The Cu-Bi porous precursors were

sulfurized under highly reactive conditions (500 mbar S_2). Despite this high reactivity, the low melting temperature of Bi (270 °C) made difficult to prevent Bi melting and segregation from the homogeneous matrix of the precursor film if the heating rate employed during the sulfurization treatment was 600 °C·min^{-1}. Nevertheless, heating rate of 5 °C·min^{-1} resulted in the formation of films with compact morphology and virtually no volume change from the precursor. Small grain size may be expected if a high surface area metal precursor is sulfurized at low temperature. Consequently, a subsequent annealing stage at higher temperature may be necessary to ensure complete diffusion of the binary sulfides and enhancement of the crystalline properties of the films. In the present work, sulfurization of Cu-Bi porous precursors at 500 °C (with 500 mbar S_2 and at a rate of 5 °C·min^{-1}) produced phase pure Cu_3BiS_3 films with average grain size of 1 μm.

As highlighted by points (2) and (3), there are upper and lower limits to the temperatures that can be employed during the treatment if single-phase ternary sulfide films are to be obtained. These limits depend on the partial pressure of chalcogen within the system, and attention should be given to them at the stage of conversion treatment design. The lower temperature limit is set by the equilibrium between the ternary (multinary) chalcogenide and any binary (lower order) chalcogenide in which the metal shows a higher oxidation state. Such equilibria are governed by the partial pressure of chalcogen in the system in such a way that an increase of sulfur pressure destabilises the ternary sulfide and favours the formation of sulfides with higher oxidation state of the metal cation. A typical example of equilibrium governed by the sulfur partial pressure is given by Cu, which is often present as Cu(I) in the compounds of interest, but can be oxidised to Cu(II) by a sulfur excess. Conversely, the upper temperature limit is set by the potential compound decompositions with formation of gaseous phases, subject to depletion. In such cases, the effect of the chalcogen pressure is opposite. An extension of the time-temperature stability range can often be achieved with an increase of the chalcogen partial pressure. The stoichiometry of the process will determine the effect of the chalcogen excess on the reaction suppression.

When designing the annealing treatment of a new compound, care should be taken to identify any possible volatile species and quantify the extent of the decomposition reaction at the temperature of interest in a closed system. This information will allow the determination of the appropriate atmosphere composition for a process that will preserve the stability of the compound. Due to their relatively low decomposition

temperatures, $CuSb(S,Se)_2$, $CuBiS_2$ and Cu_3BiS_3 may present intrinsic limitations to the achievement of device-quality semiconductor properties. Indeed, we have seen in section 1A that for CI(G)S these properties are only attained if the level of crystalline defects detectable with Raman spectroscopy is strongly reduced [149].

In our experiments we investigated the conditions for the formation of single-phase films, and XRD was employed to estimate their quality. The poor photoelectrochemical properties observed may arise from a high level of XRD-invisible defects, whose concentration may not be reduced any further due to the temperature limitations imposed by the decomposition equilibria. The conditions for the formation of device-quality absorber films should be obtained with the addition to the TTR diagram of isopleths curves representing the points where the defect concentration, as obtained e.g. from Raman spectroscopy [306], is below a suitably defined level.

Part B

Dai diamanti non nasce niente
dal letame nascono i fior.

Fabrizio De André

Introduction to part B: fundamental debates on CZTS

$Cu_2ZnSnS_{4-x}Se_x$ (CZTS) is currently attracting a great deal of attention for application as absorber material in thin film solar cells due to its low cost, low toxicity and suitable optoelectronic properties [47]. To date, the record efficiency for photovoltaic devices based on this sulfoselenide is about 10%, with cells containing a liquid-processed layer [54, 58]. Although many studies are being performed on thin films of this material, some key information may better be obtained by studying it in a single crystalline or bulk form: crystal and electronic structures [72], phonon frequencies and line widths of Raman active modes, extension of the compositional homogeneity range [76].

We reported in section 1.4 on the structural derivation of CZTS from the crystalline lattice of diamond [45], described as two interpenetrated face centred cubic sub-lattices. Each atom in the "adamantine" structures is tetrahedrally coordinated. Following the principle of *isoelectronic* substitution [44], atoms of the group IV are substituted by an equal number of cations and anions of valence III and V or II and VI respectively, to form binary compounds such as GaAs or ZnS. The structure of these compounds consists of cations and anions ordered in the two sub-lattices. The substitution can proceed involving the cation sub-lattice. For example an equal number of cations of valence I and III can replace the cations of valence II, with the formation of ternary chalcogenides (e.g. $CuInS_2$). Similarly, a third level of substitution of the valence III atoms on the cation sub-lattice brings about I_2-II-IV-VI_4 compounds, like the quaternary chalcogenides Cu_2FeSnS_4 and $Cu_2ZnSnSe_4$ known as the minerals *Stannite* and *Kesterite*. At each level of substitution, the symmetry of the structure decreases from the space group no. 227 of the diamond (*Fd-3m*) down to the group no. 121 of the *Stannite*-type structure of Cu_2FeSnS_4 (*I-42m*). Mineralogically, *Stannite* may occur in nature as $Cu_2Fe(Zn)SnS_4$ with Fe partially substituted by Zn, and vice-versa *Kesterite* can show some substitution of Zn by Fe, leading to $Cu_2Zn(Fe)SnS_4$. Due to the formula similarity and the reported natural intergrowth between these two minerals, the pseudo-binary system Cu_2FeSnS_4-Cu_2ZnSnS_4 has been investigated synthetically by Springer [59]. His results, based on combined ex-situ XRD powder analysis, differential thermal analysis (DTA) and reflected light microscopy, are summarised by Fig. 1.B.1.

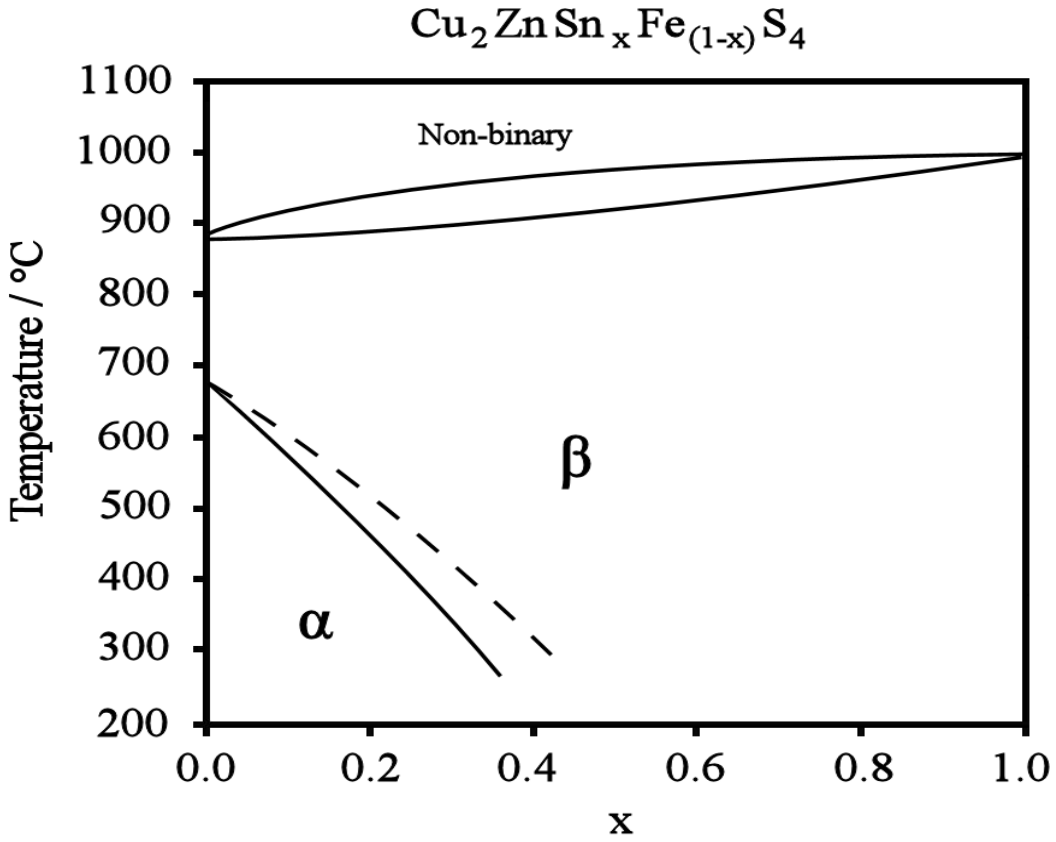

Fig. 1.B.1 Pseudo-binary phase diagram of the Cu_2FeSnS_4- Cu_2ZnSnS_4 system, as determined by Springer via DTA and ex-situ XRD analyses, modified from [59], where α and β represent two distinct phase homogeneity regions. (N.B. a more recent investigation of this pseudo-binary phase diagram has been reported by Kissin [63], but the considerations that follow in the text are still valid).

The samples were synthesised by Springer within sealed silica tubes by heating either the elements or stoichiometric amounts of pre-synthesised end-members. Samples quenched at different temperatures were analysed, and a salt flux (eutectic mixture of 44 % wt. NH_4Cl 56 % wt. LiCl) was added to the charges tested at temperature lower than 300 °C to accelerate the kinetics of phase transformation. The diagram in Fig. 1.B.1 shows the existence of a homogeneity range labelled β, where a single phase was found. At temperature lower than ~680 °C, the Fe-rich member shows the separation of another phase labelled α, as observed from the disappearance of several lines in the X-ray powder pattern. The occurrence of missing reflections may be attributed to a cation reordering responsible for the transition from a lower to a higher symmetry unit cell. Therefore, at room temperature the pseudo-binary system is biphasic. The variations of lattice parameters with composition reported by Kissin et al. [62] confirm the miscibility gap at low temperature, while continuity of the cell parameters for samples quenched at 750 and 550 °C reported by Bernardini

et al. [64] indicates the presence of a solid solution at higher temperature. Bonazzi et al. [65] have found that the unit cell volume increases with increasing the Zn content in the pseudo-binary system, despite the ionic radius of Zn^{2+} being smaller than that of Fe^{2+}. This suggests that the character of the chemical bonds in *Kesterite* is more covalent than in the *Stannite*. The structural distinction between *Stannite* and *Kesterite* was further questioned by Hall et al [60, 61]. Based on the relative magnitudes of the refined thermal parameters of Cu and Zn, they provided support for two different space groups: *I-42m* for $Cu_2Fe(Zn)SnS_4$ and *I-4* for $Cu_2Zn(Fe)SnS_4$ [61]. The structural diversity between these two compounds is given by the different ordering in the cation sub-lattice. The sequence of cation planes in pure *Stannite* is Fe-Sn/Cu-Cu, while in pure *Kesterite* is Cu-Sn/Cu-Zn. The two mirror planes at (110) and (-110) present in the structure of *Stannite* are removed from the unit cell of *Kesterite* (as well as the the 2-fold rotation axes, the double-glide planes and the screw axes), lowering the symmetry of *Kesterite* further down to the space group no. 82 (*I-4*). This difference is highlighted in Fig. 1.B.2, where the unit cells of *Stannite* and *Kesterite* and the corresponding space group diagrams are shown (see also Appendix 2).

The attribution of the space groups of *Stannite* and *Kesterite* given by Hall et al. [61] was recently confirmed by Schorr et al. [68] with combined X-ray and neutron diffraction analysis of powder samples. Due to the same number of electrons, Cu^+ and Zn^{2+} ions have virtually equal atomic form factors [307]. For this reason these two cations are not easily distinguished by conventional X-ray diffraction. However, they do show different neutron scattering cross sections [67], allowing the Cu-Zn cation ordering in the *Kesterite* structure of CZTS to be solved. Schorr's findings indicate that the occupancy of Cu and Zn on the (001) planes of CZTS samples quenched at 750 ºC is completely random (raising objection on the formal attribution of the *I-4* space group), while a 60 % ordering was found for the same samples cooled down to room temperature with a rate of 1 ºC h^{-1} [71]. These results are consistent with DFT calculations showing that Cu_{Zn} and Zn_{Cu} antisite defects are energetically less expensive to form compared to Zn_{Sn}, Sn_{Zn}, Cu_{Sn} and Sn_{Cu} [118].

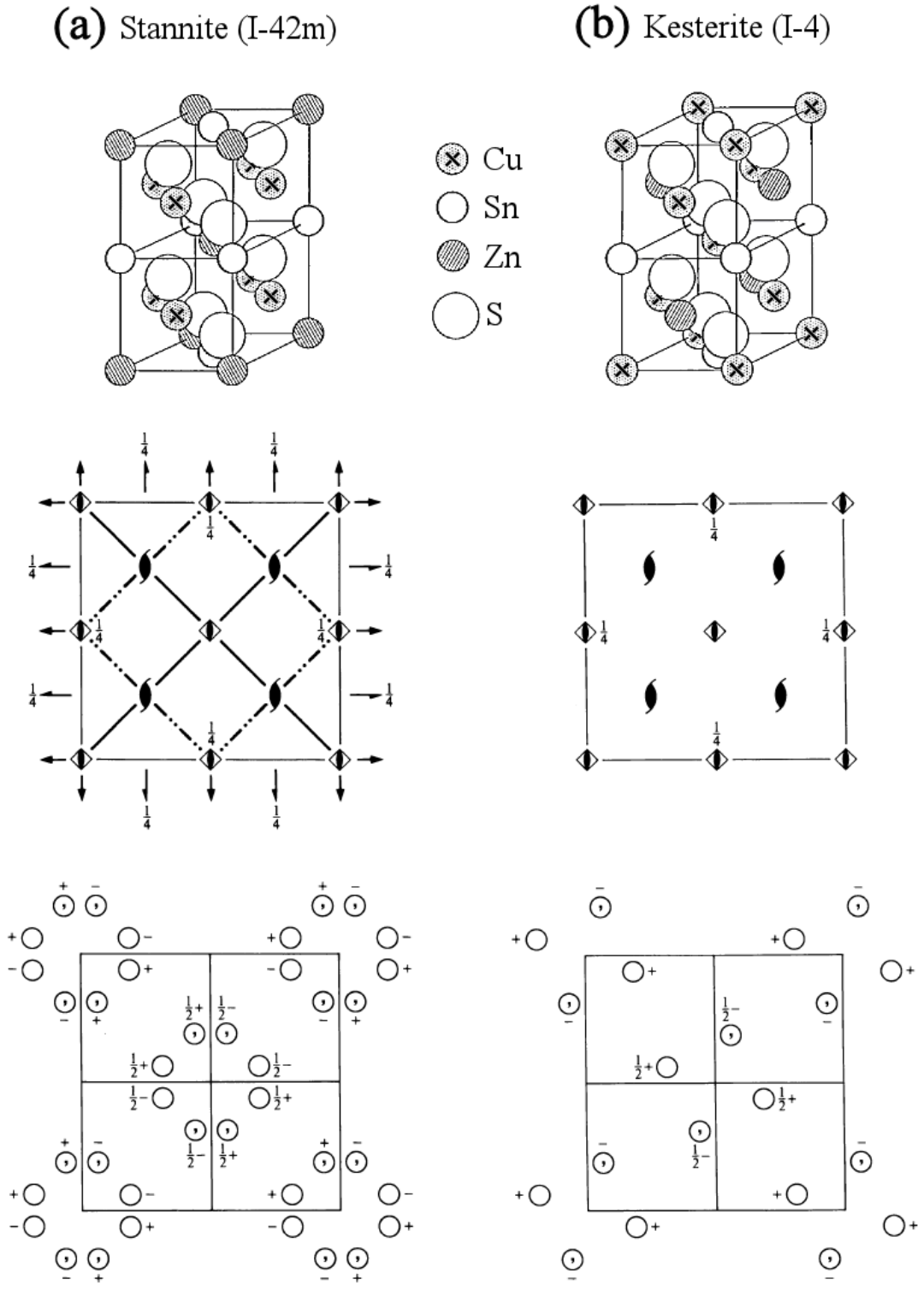

Fig. 1.B.2 Representation of the unit cell and cation ordering in *Stannite* (a) and *Kesterite* (b) [61] and corresponding *I-42m* and *I-4* space group diagrams [308].

The *Kesterite* structure of CZTS is consistent with the relative configuration stabilities of *Kesterite* and *Stannite* calculated by DFT [309, 310]. The same computations predict an energetic difference of ~3-50 meV/formula unit between the two structures, corresponding to ~0.3-5 kJmol^{-1}. Thermal energy at ~330 °C is

enough to exceed the upper limit of this range; therefore formation of *Stannite* may occur during the synthesis of CZTS in either bulk or thin-films. Clearly, both the nature and concentration of defects and the possible presence of solid solutions or domains of *Kesterite-Stannite* in thin CZTS absorber layers have an effect on its optoelectronic properties. For example, it has been shown by Scragg that a smooth bowing variation of the band-gap energies from ~1.45 to ~1.55 eV is achieved for thin CZTS films as a function of the sulfurization time, as shown in Fig. 1.B.3 [130].

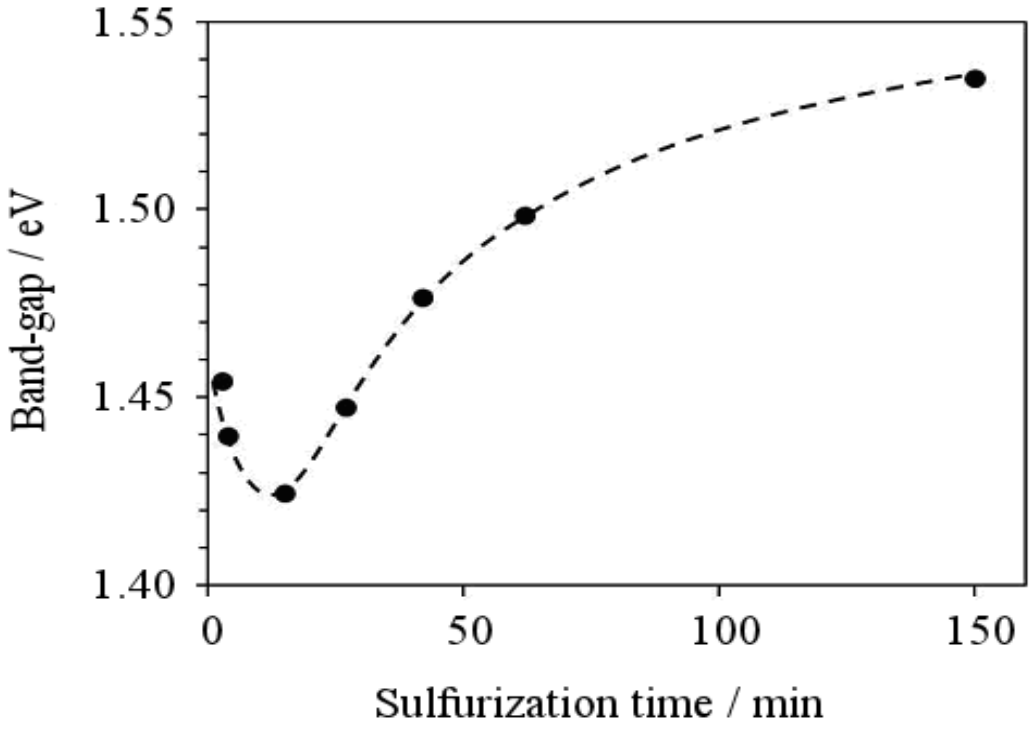

Fig. 1.B.3 Bowing variation of the band-gap of CZTS thin films as a function of the sulfurization time at 560 °C, as reported by Scragg [130]. The variation may be due to the transition from a *Stannite* to a *Kesterite* crystalline structure.

An interesting hypothesis was proposed by Scragg for the behaviour shown in Fig. 1.B.3. It is based on the possibility that *Stannite* may form at the early stages of CZTS synthesis and that a slow conversion into the thermodynamically more stable *Kesterite* is achieved in the time frame of 2 hours at 560 °C. This hypothesis is supported by the calculated band-gap energies of *Stannite* (~1.3-1.4 eV), *Kesterite* (~1.4-1.6 eV) [121, 311] and of an intermediate solid solution (~1.1 eV)[309]. Determination of the space group of CZTS from single-crystal neutron diffraction has never been performed. Section 7.1 shows the results of the space group refinement from X-ray and neutron diffraction of single crystals synthesised in the present study via the CVT with I_2.

The electronic structure of semiconductors can be assessed with photoluminescence spectroscopy (PL). With this technique, transitions between electronic energetic levels of the material are induced with a light beam, and the emission spectrum is recorded. Analysis of the emission spectrum may be very complex, but it can provide information on the value of the band-gap energy and on the presence of energetic levels associated with the defect structure of the material. The formation energy of the possible defects in CZTS have been computed with DFT by Chen et al. [153], and the positions of the corresponding energy levels relative to VBM and CBM of CZTS are shown in Fig. 1.B.4.

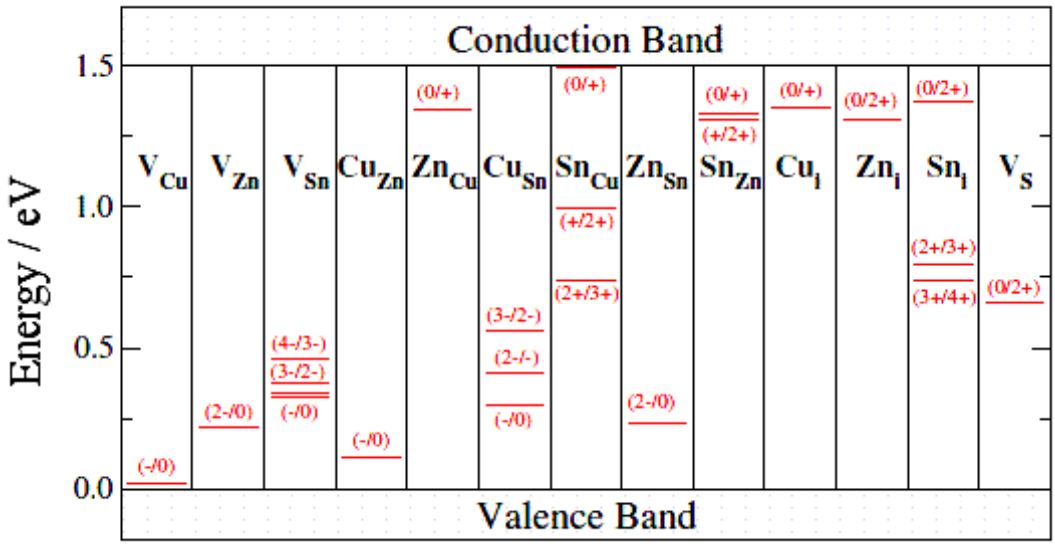

Fig. 1.B.4 Diagram of the electronic transition-energy levels of intrinsic defects in CZTS relative to the VBM and CBM, as reported by Chen et al. [153].

The type and concentration of defects present in CZTS affect its electronic properties. Experimental corroborations of the CZTS defect electronic structure obtained by computation are still limited, and only a preliminary study was undertaken in this work. The results of the PL analyses of CZTS single crystals are reported in section 7.3.

Clearly, if the concentration of some intrinsic defects in CZTS exceeds a critical value, phase separation is likely to occur [118]. The current knowledge of the equilibrium phase relations in the Cu_2S-ZnS-SnS_2 system is limited to the work reported by Olekseyuk et al. [133]. The isothermal section at ~400 °C that they constructed is reproduced in Fig. 1.B.5.

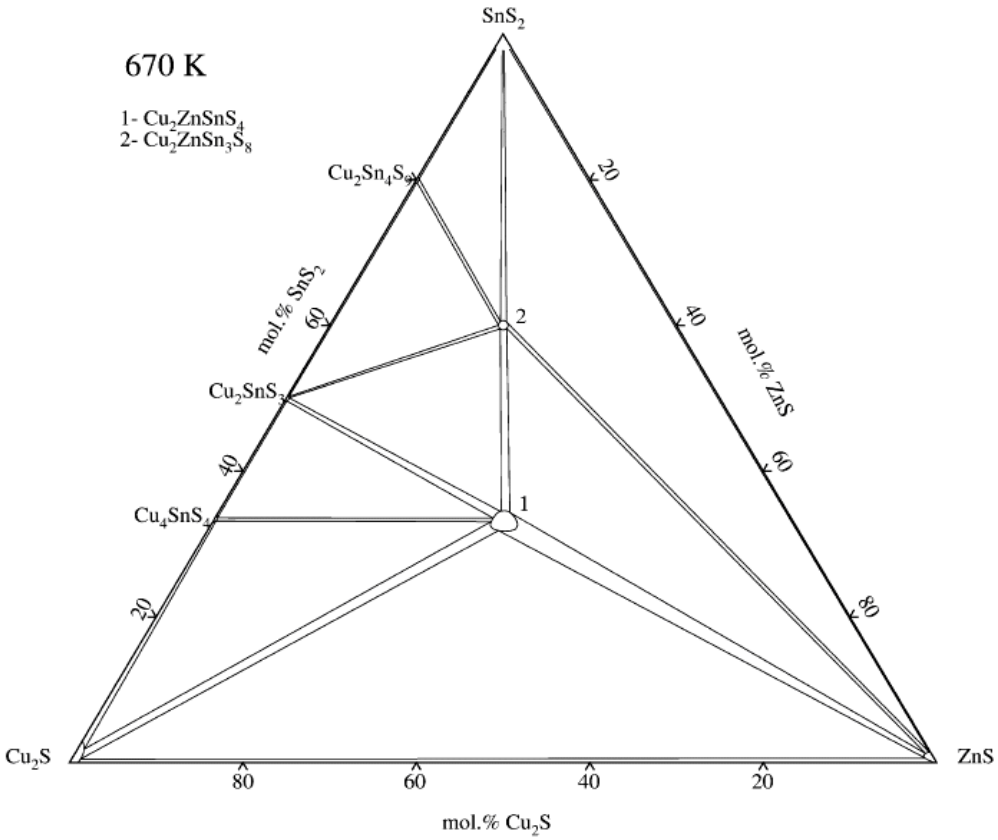

Fig. 1.B.5 Isothermal section at 670 K of the Cu_2S-ZnS-SnS_2, as reported by Olekseyuk et al. [133].

Fig. 1.B.5 shows the existence of another quaternary phase with stoichiometry $Cu_2ZnSn_3S_8$, which can be regarded as $Cu_2ZnSnS_4 \cdot 2\ SnS_2$. This sulfide has been indexed with tetragonal structure, but no space group determination was reported. Fig. 1.B.5 shows also that the homogeneity range of the phase Cu_2ZnSnS_4 at ~400 °C is limited approximately by a circle with a diameter of about 4 atomic percent. This information is very important for the prediction of secondary phase segregation during the synthesis of CZTS. However, the diagram in Fig. 1.B.5 illustrates the phase relations as determined at ~400 °C. No information on the phase homogeneity range at other temperatures can be extrapolated. Furthermore, it must be borne in mind that the Cu_2S-ZnS-SnS_2 is a pseudo-ternary system. Therefore, due to the stoichiometric constraints, it does not show the equilibrium relations with other potential intermediate phases that may form during the processing of the quaternary Cu-Zn-Sn-S system. Such other phases may be: CuS, $Cu_{1-x}S$, Sn_2S_3, Sn_3S_4, SnS. If the CZTS synthetic procedure employs Cu-Zn-Sn metal precursors and a sulfur-bearing reactant, the phase relations in the cation ternary system would be appropriately described only by a 5-axis graph. Indeed, a 3D plot (e.g. as described by Kartzmark [312]) would only suffice in describing the phase relations of the

quaternary system at fixed temperature and reactant partial pressure. In fact, such 3D plots would be nothing but 3D isothermal and isobaric sections of the much more complex 5D phase diagram.

ZnS and Cu_2SnS_3 (CTS) may be encountered as secondary phases in CZTS films if the samples are not fully converted and/or non-equilibrium growth conditions are employed. Due to the similar lattice parameters of ZnS, Cu_2SnS_3 and Cu_2ZnSnS_4, these three phases display very similar XRD patterns. Both CZTS and CTS (the latter can be tetragonal, monoclinic or triclinic) have lower symmetry than cubic ZnS. Therefore the XRD patterns of CZTS and CTS show some characteristic low intensity peaks that can help in detecting their presence. Nevertheless, the absence of these unique peaks is not conclusive for identification of the phase composition, as has been highlighted by several authors [130, 132, 154, 313, 314]. Raman spectroscopy has been suggested as a viable alternative to XRD for the discrimination of such phases [314, 315]. However, high quality crystalline reference samples are required for the accurate determination of the line widths of the Raman active modes. Ideally, single crystals of CZTS in the two structures *Kesterite* and *Stannite* are needed. Raman spectroscopy analyses of CZTS crystals produced in this work are shown in sect. 7.2.

In the present study, the synthesis of CZTS single crystals was carried out with the technique of chemical vapour transport (CVT) using iodine as the transporting agent. The thermochemistry of the pentenary system Cu-Zn-Sn-S-I was assessed computationally to assist design of the crystal growth experiments. In particular, the thermochemistry of CVT in the Cu-Zn-Sn-S system by the action of I_2 was assessed by computation of the Gibbs free energies of the independent chemical reactions. The relative stability of the unary volatile components with respect to the corresponding binary sulfides and the quaternary compound Cu_2ZnSnS_4 were computed as functions of the temperature. With the aim of assessing the risk of compositionally incongruent mass transport, the effects of I_2 and S_2 partial pressures on the phase stabilities were estimated. The results of the thermochemical analysis were helpful for the design of single crystal growth experiments and gave valuable insights for the formulation of a hypothetic nucleation mechanism. These results are reported in chapter 5.

Experiments of CVT growth of CZTS were performed, and the effects of temperature gradient and iodine pressure on composition, morphology and crystal structure were investigated. The results are presented in chapter 6.

5. Thermodynamics of the Cu-Zn-Sn-S-I system

The first attempt to produce single crystals of CZTS was made by Nitsche et al. [316] who employed the Chemical Vapour Transport (CVT) technique using I_2 as the transporting agent. This technique is based on the principle that a transport of matter may take place when a solid reacts reversibly with a transport gas, forming volatile compounds that can be decomposed as to yield the original solid. A net transport of mass is observed if the system is set up to provide a concentration gradient. If the equilibrium constant of the reaction varies with temperature, a convenient procedure to create such gradient is by applying a gradient of temperature. The direction of transport depends on the sign of the enthalpy of the solid-gas reaction (ΔH), according to the Van t'Hoff equation (Eq. 5.1).

Eq. 5.1 $$\partial \ln[K(T)]/\partial T = \Delta H^{\circ}/RT^2$$

If the reaction is exothermic ($\Delta H < 0$) the transport occurs from the cold to the hot zones of the system. Vice-versa, with endothermic reactions ($\Delta H > 0$) the transport occurs from hotter to colder zones.

It is known that the successful growth of single crystalline compounds via CVT is a trade-off between duration of the experiment and size/quality of the products (see e.g. Schäfer [317] and Faktor et al. [318]). These two characteristics are a consequence of the material flux typical for the system investigated and of the specific experimental conditions employed. Eq. 5.2 is a function that describes the dependence of the transport rate through a unit cross-sectional area (F_s) on various parameters [319].

Eq. 5.2 $$F_s = \frac{\Delta H \cdot \Delta T}{R^2 \cdot \overline{T}^3 \cdot L} \cdot \left\{ \sum_i \frac{q_i}{p_i} \left(\sum_j \frac{q_j \cdot \overline{p_i} - q_i \cdot \overline{p_j}}{P \cdot D_{ij}} \right) \right\}^{-1}$$

where ΔT is the temperature gradient, $\overline{T}$ is the average absolute temperature, $\overline{p_i}$ and $\overline{p_j}$ are the average partial pressures of the components *i* and *j*, *P* is the total pressure, D_{ij} are the diffusion coefficients for the binary mixture of components *i* and *j*, and *q* are the stoichiometric coefficients of the reaction. Eq. 5.2 shows that the transport

rate increases with an increase of the temperature gradient and decreases with an increase of the total pressure in the ampoule; the right balance between these parameters must be found so that the crystal nucleation is minimised without slowing too much down the growth stage. The best experimental conditions are those for which, once a small number of seeds are formed at the growth end, the transport rate does not exceed the velocity of growth of the seeds [320]. Expedients based on the gradual rising of the source temperature were proposed by Paorici et al. [321], to allow for reduced primary nucleation and avoidance of constitutional undercooling during the first stages of the transport experiments. Iterative swaps of the temperature gradient can also be thought as a viable means of increasing the average size of the growing crystals.

Despite the fact that concentrations of transporting agents far below stoichiometry are usually recommended for balancing the supersaturation conditions [317], recent findings by Senthil Kumar et al. [322] suggest that iodine concentrations above a certain level may, in fact, have little influence on the nucleation and growth of crystals. As shown by Schäfer et al. [323], at low pressure of the transporting agent, the heterogeneous reactions occurring at the source end become the rate limiting step for the transport process. Under these conditions an increase of the transporting agent concentration leads to an increase of the transport rate until a maximum is reached due to diffusion control. These two situations can be depicted geometrically as two vessels with different shape: a beaker and a bottle. While the neck of a bottle (diffusion rate control) acts as an obstruction for mass transport allowing enough time for the reagents to equilibrate, in a beaker (heterogeneous reaction rate control) there are no such barriers, thus it may happen that a sample of transported gas does not reflect the composition that would be achieved at equilibrium.

The experimental studies described in chapter 6 deal with the effects of temperature gradient and I_2 load on the mechanism of mass transport and their consequences on composition and habit of the resulting crystals. Higher crystal perfection was obtained in the case of lower concentration of the transporting agent. It was deduced that a further decrease of the I_2 concentration might be necessary to allow the formation of bigger crystals. Therefore, our concern is about the potential selective leaching of the source material by the action of the transporting agent in the low pressure regime. Such a matter may well become significant in multinary systems, where the relative stabilities of the unary transported species can lie over a wide thermodynamic range.

It is only with the recent studies of Richter et al. [324] that a more systematic analysis of the chemical vapour transport in a multi-component system has been attempted. Particularly, their work highlights the importance of incongruent transport as the main issue for the formation of compositionally well defined sinks. An assessment of the competing chemical reactions potentially occurring under different I_2 and S_2 partial pressures is a compulsory requirement for deeper understanding and description of the phenomenon. This is addressed in the present study, where the constraints for CZTS crystallization are defined with the aim of tailoring the design of successful growth experiments. Our aim is to qualitatively assess whether the transport of the unary volatile components $(CuI)_3$, ZnI_2 and $SnI_{2(w+1)}$ occurs evenly or if preferential leaching of the source material is such that formation of compounds with fixed stoichiometry is unlikely to be merely controlled by the initial load composition.

The review paper by Lenz et al. [325] provides a remarkable overview of the state-of-the-art on the large number of models developed for the interpretation and thermochemical treatment of CVT phenomena. The thermochemical computation that follows is based on simplistic assumptions and therefore it is not intended as an exhaustive treatment.

5.1 Computational procedure

The approach undertaken for the thermochemical assessment of the reactions occurring in the Cu-Zn-Sn-S-I system involves only the minimisation of the Gibbs free energy for each process taken separately and it is not intended as a thorough equilibrium computation. The reader is referred to the works by Zeleznik et al. [326], Vonka et al. [327] and Noläng et al [328, 329] for more advanced, rigorous computational approaches that may be applied to our system. Unfortunately such models would require a much deeper knowledge of computational science that is not within our expertise.

The temperature dependence of the Gibbs free energy of reaction for several possible equilibria in the system Cu-Zn-Sn-S by the action of I_2 as the transporting agent were considered, following the approach of Mariolacos [1] and Jeffes [330]. All the calculations reported in this section are based on the thermochemical data by Knacke et al. [259]. The interpolating thermochemical functions employed and the values of the coefficients for each of the 46 compounds considered in this work are reported in Appendix 3. More specifically, for each of the investigated reactions the most stable forms of the involved reagent and product species (of which thermochemical data are available) were considered, so that the equilibrium thermodynamic parameters $\Delta G°$ and K_P could be determined as functions of the temperature, regardless of their actual kinetic significance.

It is known (see e.g. [318]) that systems at equilibrium containing reactive components obey the Gibbs phase rule of variance *f* if *N* chemical species, *P* phases and *R* independent reactions are defined.

Eq. 5.1.1 $f = N - R - P + 2$

In systems of restricted chemical stoichiometry (i.e. when fixed stoichiometric ratios apply to the chemical reactions taking place) the number of linearly dependent equations *R* equals the number of chemical species *N* minus the chemical components *C* according to the Jouguet's definition [331].

Eq. 5.1.2 $R = N - C$

However, if the stoichiometric ratios are unknown, it is still possible to estimate the number of components *C'* according to Blinkey's definition [332]. Simply, in that case *R'* will not account for the degrees of freedom subtracted by the experimental chemical information (the stoichiometric relationship).

Eq. 5.1.3 $f < f' = N - R' - P + 2 = C' - P + 2$

The mathematical procedure for determination of *C'* and *R'* was described by Samuels [333] by extension of the method of White et al. [334] to mixtures involving condensed phases, and it is thoroughly explained by Smith and Missen [335, 336]. The rank of matrixes *M* of the atomic coefficients m_{ij} was shown to be equal to the number of components *C'*; therefore the number of linearly dependent reactions *R'* is equal to the difference between the total number of chemical species present *N* and the rank of the matrix.

Eq.5.1.4 $rank\,(M) = C'\ R' = N - rank\,(M)$

The linearly independent columns of the matrix M^* resulting from the Gauss Jordan reduction of matrix *M* [337] represent the components *C'* of the system. The solution matrix *X* obtained by appending the identity matrix of dimension *R'*×*R'* below the linearly dependent vectors of matrix $-M^*$ gives the stoichiometric coefficients of the reactions *R'*. Such treatment may be performed separately for each subgroups of unary (S,I), binary (Cu,Zn,Sn-S and Cu,Zn,Sn-I) and ternary/quaternary (Cu_2ZnSnS_4,$Cu_2ZnSn_3S_8$,Cu_2SnS_3) components. The relevant reactions arising from this procedure are computed thermochemically.

5.2 Unary components: S and I

Table 5.2.1 shows the matrix A of the atomic coefficients a_{ij} for the system of unary components, where a_{ij} is the number of atoms of element i in the chemical species j.

	j	**1**	**2**	**3**	**4**	**5**	**6**	**7**	**8**	**9**	**10**	**11**	**12**	**13**	**14**	**15**
i		**I_2 (s)**	**I_2 (l)**	**I_2 (g)**	**I (g)**	**S_8 R**	**S_8 M**	**S_8 (l)**	**S_8 (g)**	**S_7 (g)**	**S_6 (g)**	**S_5 (g)**	**S_4 (g)**	**S_3 (g)**	**S_2 (g)**	**S (g)**
1	**I**	2	2	2	1	0	0	0	0	0	0	0	0	0	0	0
2	**S**	0	0	0	0	8	8	8	8	7	6	5	4	3	2	1

Table 5.2.1 Matrix A of the atomic coefficients $a_{i\,j}$ for the possible compounds shown by the unary components S and I.

The number of chemical species in our system is 15 and the rank of matrix A (Table 5.2.1) is 2. Table 5.2.2 shows the matrix A^* resulting from the Gauss Jordan reduction of matrix A, where the 2 linearly independent columns represent the components $C'(A)$ of the system: $I_{2\,(s)}$ (3) and $S_{8\,(g)}$ (8).

	j	**1**	**2**	**3**	**4**	**5**	**6**	**7**	**8**	**9**	**10**	**11**	**12**	**13**	**14**	**15**
i		**I_2 (s)**	**I_2 (l)**	**I_2 (g)**	**I (g)**	**S_8 R**	**S_8 M**	**S_8 (l)**	**S_8 (g)**	**S_7 (g)**	**S_6 (g)**	**S_5 (g)**	**S_4 (g)**	**S_3 (g)**	**S_2 (g)**	**S (g)**
1	**I**	1	1	1	1/2	0	0	0	0	0	0	0	0	0	0	0
2	**S**	0	0	0	0	1	1	1	1	7/8	3/4	5/8	1/2	3/8	1/4	1/8

Table 5.2.2 Matrix A^* obtained by Gauss-Jordan reduction of matrix A for the unary components S and I.

The remaining 13 linearly dependent columns of matrix A^* represent the number of reactions $R'(A)$. Table 5.2.3 shows the solution matrix $X(A)$ (note the rearrangement of the rows indexes).

	(1)	(2)	(3)	(4)	(5)	(6)	(7)	(8)	(9)	(10)	(11)	(12)	(13)
1	-1	-1	-1/2	0	0	0	0	0	0	0	0	0	0
8	0	0	0	-1	-1	-1	-7/8	-3/4	-5/8	-1/2	-3/8	-1/4	-1/8
2	1	0	0	0	0	0	0	0	0	0	0	0	0
3	0	1	0	0	0	0	0	0	0	0	0	0	0
4	0	0	1	0	0	0	0	0	0	0	0	0	0
5	0	0	0	1	0	0	0	0	0	0	0	0	0
6	0	0	0	0	1	0	0	0	0	0	0	0	0
7	0	0	0	0	0	1	0	0	0	0	0	0	0
9	0	0	0	0	0	0	1	0	0	0	0	0	0
10	0	0	0	0	0	0	0	1	0	0	0	0	0
11	0	0	0	0	0	0	0	0	1	0	0	0	0
10	0	0	0	0	0	0	0	0	0	1	0	0	0
13	0	0	0	0	0	0	0	0	0	0	1	0	0
14	0	0	0	0	0	0	0	0	0	0	0	1	0
15	0	0	0	0	0	0	0	0	0	0	0	0	1

Table 5.2.3 Solution matrix *X(A)* containing the stoichiometric coefficients of the 13 linearly dependent reactions *R'(A)* for the unary components S and I.

Each column in Table 5.2.3 gives the stoichiometric coefficient for the corresponding reaction. By linear combination of *R'(A)*, the two (obvious) reaction sequences for I and S are as follows.

Reac. 5.2.1 $I_{2\,(s)} \rightarrow I_{2\,(l)} \rightarrow I_{2\,(g)} \rightarrow 2\ I_{(g)}$

Reac. 5.2.2 $S_{8\,R} \rightarrow S_{8\,M} \rightarrow S_{8\,(l)} \rightarrow S_{8\,(g)} \rightarrow 8/7\ S_{7\,(g)} \rightarrow 4/3\ S_{6\,(g)} \rightarrow 8/5\ S_{5\,(g)} \rightarrow 2\ S_{4\,(g)} \rightarrow 8/3\ S_{3\,(g)} \rightarrow 4\ S_{2\,(g)} \rightarrow 8\ S_{(g)}$

The standard chemical potential of the unary species is plotted in Fig. 5.2.1 as a function of the absolute temperature.

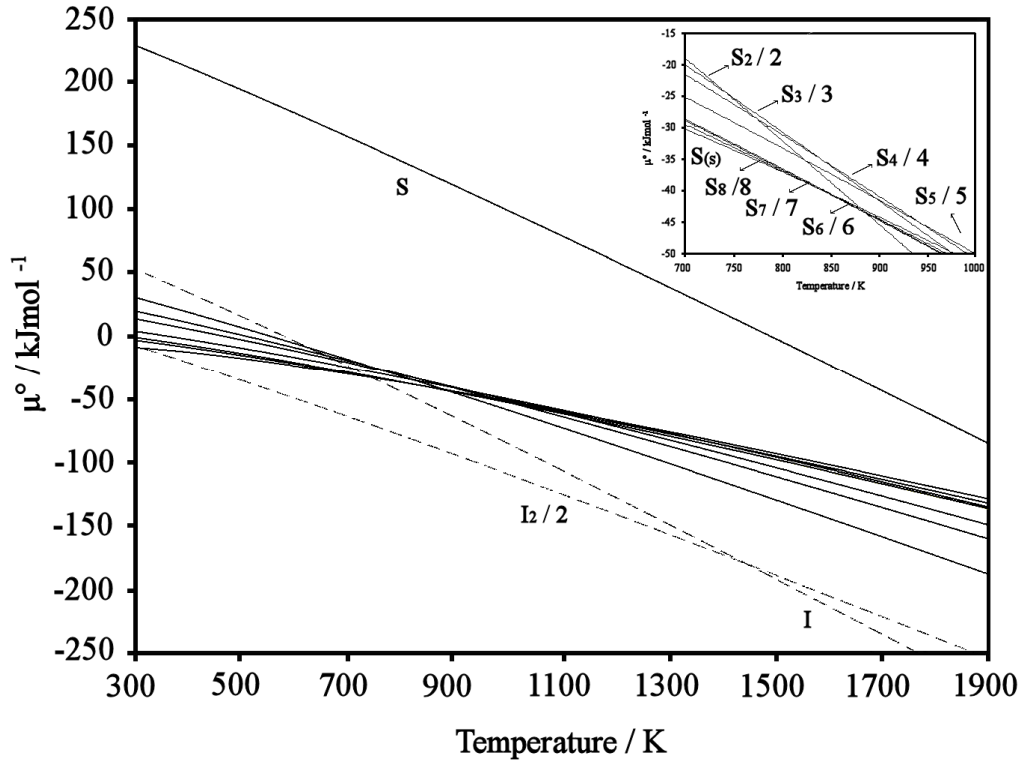

Fig. 5.2.1 Standard chemical potential of the iodine (dashed lines) and sulfur species considered in the present study as a function of the temperature normalised per number of atoms for sake of comparison (i.e.: $\mu°(I_{2\,(g)})/2$, $\mu°(I_{(g)})$, $\mu°(S_{(s)})$, $\mu°(S_{(g)})$, $\mu°(S_{2\,(g)})/2$, $\mu°(S_{3\,(g)})/3$, $\mu°(S_{4\,(g)})/4$, $\mu°(S_{5\,(g)})/5$, $\mu°(S_{6\,(g)})/6$, $\mu°(S_{7\,(g)})/7$, $\mu°(S_{8\,(g)})/8$). The inset is a zoom of the plot to clarify the complexity of the polyatomic molecular sulfur thermochemistry.

From Fig. 5.2.1 it is possible to extract information on the temperature stability regions for each iodine and sulfur species and on the series of their decomposition temperatures. $I_{2\,(g)}$ decomposes at ~ 1470 K to monoatomic $I_{(g)}$, while for $S_{8\,(s)}$ the subsequent decomposition reactions up to the monoatomic $S_{(g)}$ occur in the temperature range 800-900 K. Since these data have first been determined experimentally, one might think that the computational procedure employed to extract them is a purely speculative exercise and the results produced are trivial. However, these thermochemical functions are needed for the computation of the possible reactions occurring in the system Cu-Zn-Sn-S-I, for which experimental data are limited. For this purpose, they will be used in linear combination with the other relevant functions obtainable from Knacke's work [259].

Because of the variety of species shown by sulfur and iodine, the functions corresponding to the minimum of the chemical potential as attained in Fig. 5.2.1 are employed in the subsequent computations. This requires the formal consideration of I_x and S_y in lieu of the simpler I_2 and S_2 molecules.

The following treatments take into account the chemical potential variation due to phase transition of the species, but the corresponding discussion is omitted. Instead, emphasis is given to the chemical reactions, including the decomposition of the binary sulfides and the tentative estimation of ternary and quaternary sulfides formation from the gaseous iodides.

5.3 Binary components: Cu-S, Cu-I, Sn-S, Sn-I, Zn-S, Zn-I

Similarly to the unary components considered in section 5.2, the stability region for each compound involved in a chemical process is found by minimizing the sum of the chemical potentials of reagents and products respectively, as a function of the temperature.

A review of Cu-S phase equilibria is provided in Appendix 4. This system was studied only through the phases CuS and Cu_2S, correlated by the equilibrium reaction 5.3.1 with $S_{y\,(g)}$ evolution (Fig. 5.3.1).

Reac. 5.3.1 $2\ CuS_{(s)} \rightarrow Cu_2S_{(s)} + 1/y\ S_{y\,(g)}$

Fig. 5.3.1 is computed under standard conditions, i.e. 1 bar S_y partial pressure. Under these conditions, the gaseous molecular species $CuS_{(g)}$ has a higher chemical potential than solid CuS (*Covellite*) and solid Cu_2S (*Chalcocite*) plus gaseous S_y throughout the temperature range considered. Therefore, the presence of $CuS_{(g)}$ in our study can be neglected. Fig. 5.3.1 also predicts the decomposition temperature of *Covellite* into *Chalcocite* to be ~800 K (under 1 bar $S_{y\,(g)}$).

According to reaction 5.3.1, the partial pressure of sulfur in the system has an effect on the relative stabilities of CuS and Cu_2S. In order to investigate this effect, the Gibbs free energy of reaction 5.3.1 as a function of both temperature and sulfur pressure was computed with Eq. 5.3.1. The results are shown in Fig. 5.3.2.

Eq. 5.3.1 $\Delta G = \Delta G° + RT/y \ln(P(S_y))$

The Cu-I system shows the existence of two gaseous species besides the condensed CuI that is stable up to 1680 K: the monomeric $CuI_{(g)}$ and the trimeric $(CuI)_{3\,(g)}$. The most stable of these two gaseous forms is the trimeric molecule up to ~1560 K (Fig. 5.3.1), which is far above the temperature range considered for the growth of crystals by the CVT technique.

The complexity of the Sn-S and Sn-I equilibria are likewise assessed. Up to six species are potentially formed: SnI_4, SnI_2, SnS_2, Sn_2S_3, Sn_3S_4 and SnS. A review of the Sn-S phase equilibria is provided in Appendix 5. The results computed under standard conditions are shown in Fig. 5.3.3.

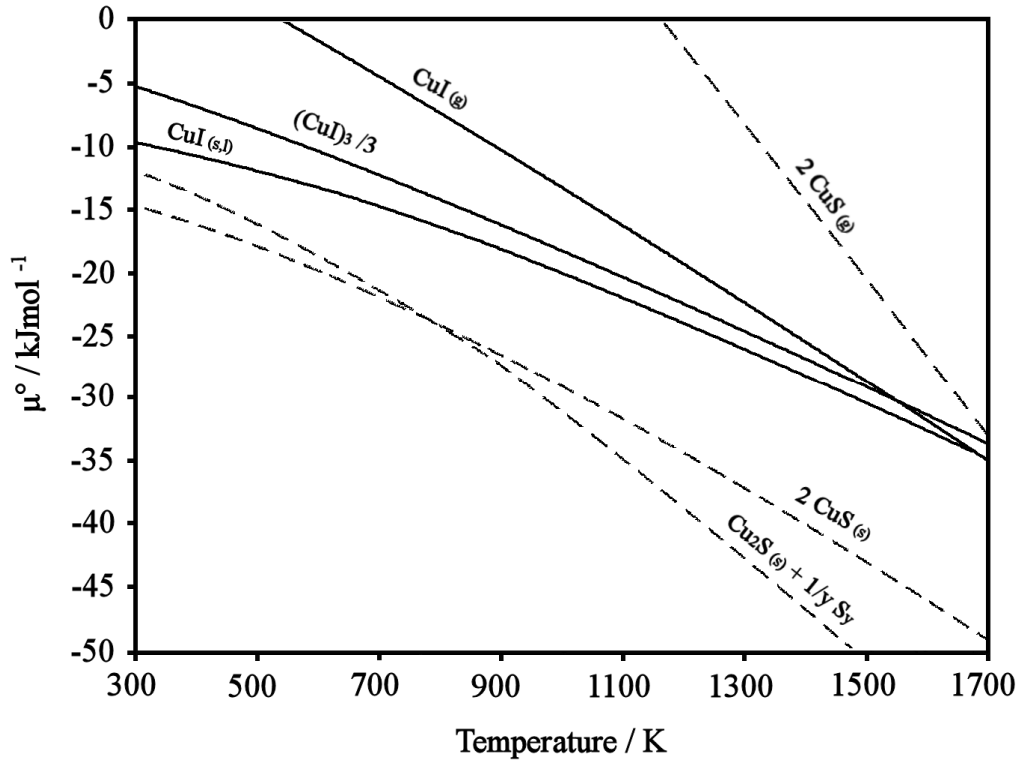

Fig. 5.3.1 Standard chemical potential of the copper sulfide (dashed lines) and copper iodide species considered in the present study as a function of the temperature normalised per number of atoms for sake of comparison (i.e.: $\mu°(Cu_2S_{(s)} + 1/y\ S_{y\,(g)})$, $\mu°(2\ CuS_{(s)})$, $\mu°(2\ CuS_{(g)})$, $\mu°(CuI_{(g)})$, $\mu°((CuI)_{3\,(g)})/3$, $\mu°(CuI_{(s,l)})$).

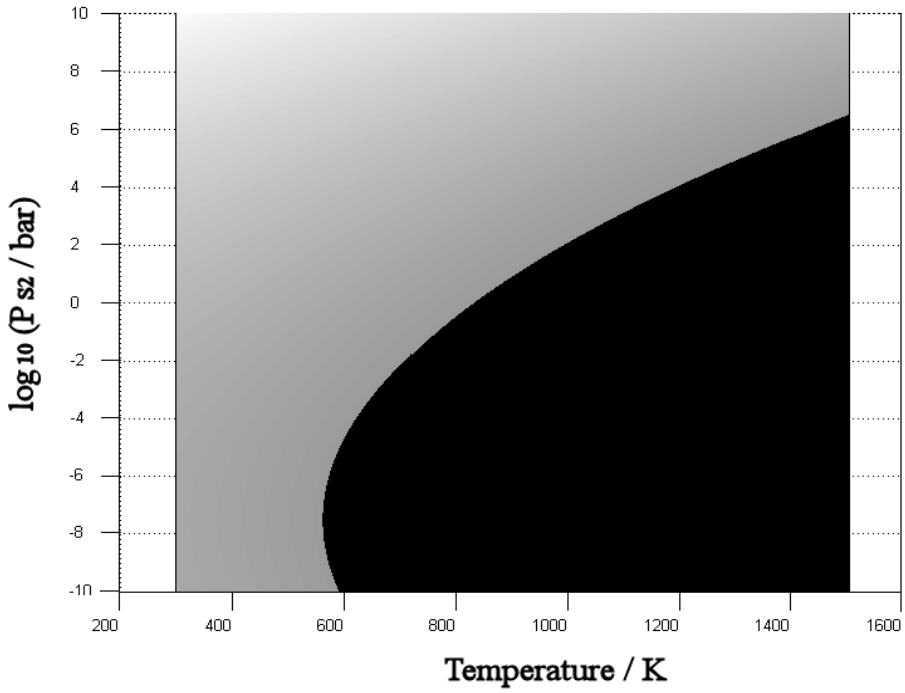

Fig. 5.3.2 2D plot showing the stability regions of CuS (shaded grey) and Cu_2S (black) in the $P(S_{y(g)})$-T plane.

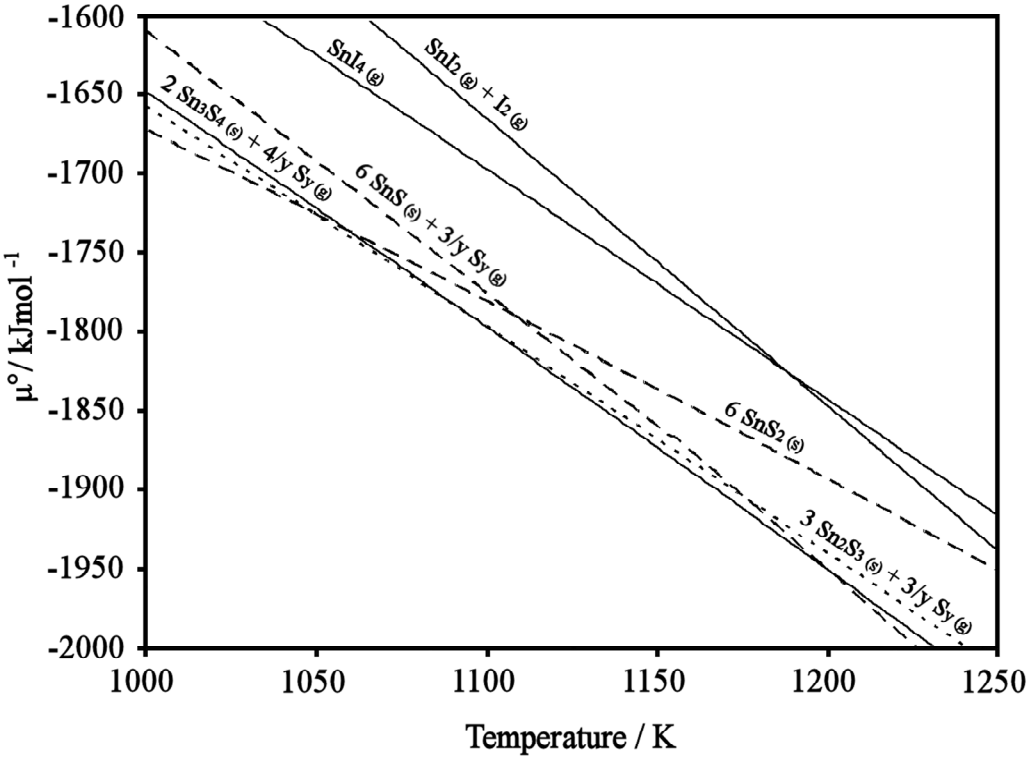

Fig. 5.3.3 Standard chemical potential of the tin sulfide and tin iodide species considered in the present study as a function of the temperature normalised per number of atoms for sake of comparison (i.e.: $\mu°(6\ SnS_{2\ (s)})$, $\mu°(3\ Sn_2S_{3\ (s)} + 3/y\ S_{y\ (g)})$, $\mu°(2\ Sn_3S_{4\ (s)} + 4/y\ S_{y\ (g)})$, $\mu°(6\ SnS_{\ (s)} + 3/y\ S_{y\ (g)})$, $\mu°(2\ CuS_{\ (g)})$, $2.5x\ \mu°(SnI_{4\ (g)})$, $2.5x\ \mu°(SnI_{2\ (g)} + I_{2\ (g)})$). (The chemical potentials of the tin iodide species were multiplied by a factor of 2.5 for graphical purposes).

The decomposition temperatures predicted for the Sn-S and Sn-I species under standard conditions are as follows (reactions 5.3.2-5.3.5).

Reac. 5.3.2 $SnI_{4\ (g)} \rightarrow SnI_{2\ (g)} + I_{2\ (g)}$ (1188 K)

Reac. 5.3.3 $6\ SnS_{2\ (s)} \rightarrow 3\ Sn_2S_{3\ (s)} + 3/y\ S_{y\ (g)}$ (1049 K)

Reac. 5.3.4 $3\ Sn_2S_{3\ (s)} + 3/y\ S_{y\ (g)} \rightarrow 2\ Sn_3S_{4\ (s)} + 4/y\ S_{y\ (g)}$ (1096 K)

Reac. 5.3.5 $2\ Sn_3S_{4\ (s)} + 4/y\ S_{y\ (g)} \rightarrow 6\ SnS_{\ (s)} + 6/y\ S_{y\ (g)}$ (1200 K)

Similarly to the Cu-S system, the equilibria of reactions 5.3.3-5.3.5 are influenced by the pressure of $S_{y\ (g)}$. Particularly, the dependence of the chemical potentials of Sn_2S_3, Sn_3S_4 and SnS as functions of T and $P(S_y)$ are given by Eqs, 5.3.2-5.3.4.

Eq. 5.3.2 $G\ (Sn_2S_3) = G°\ (Sn_2S_3) + 3RT/y\ \ln(P(S_y))$

Eq. 5.3.3 $G\ (Sn_3S_4) = G°\ (Sn_3S_4) + 4RT/y\ \ln(P(S_y))$

Eq. 5.3.4 $G(SnS) = G°(SnS) + 6RT/y \ln(P(S_y))$

The intersections among the surfaces given by Eqs. 5.3.2-5.3.4 and the standard chemical potential of SnS_2 delimit the boundaries between the relative stability regions of the tin sulfide phases. The results are shown in Fig. 5.3.4.

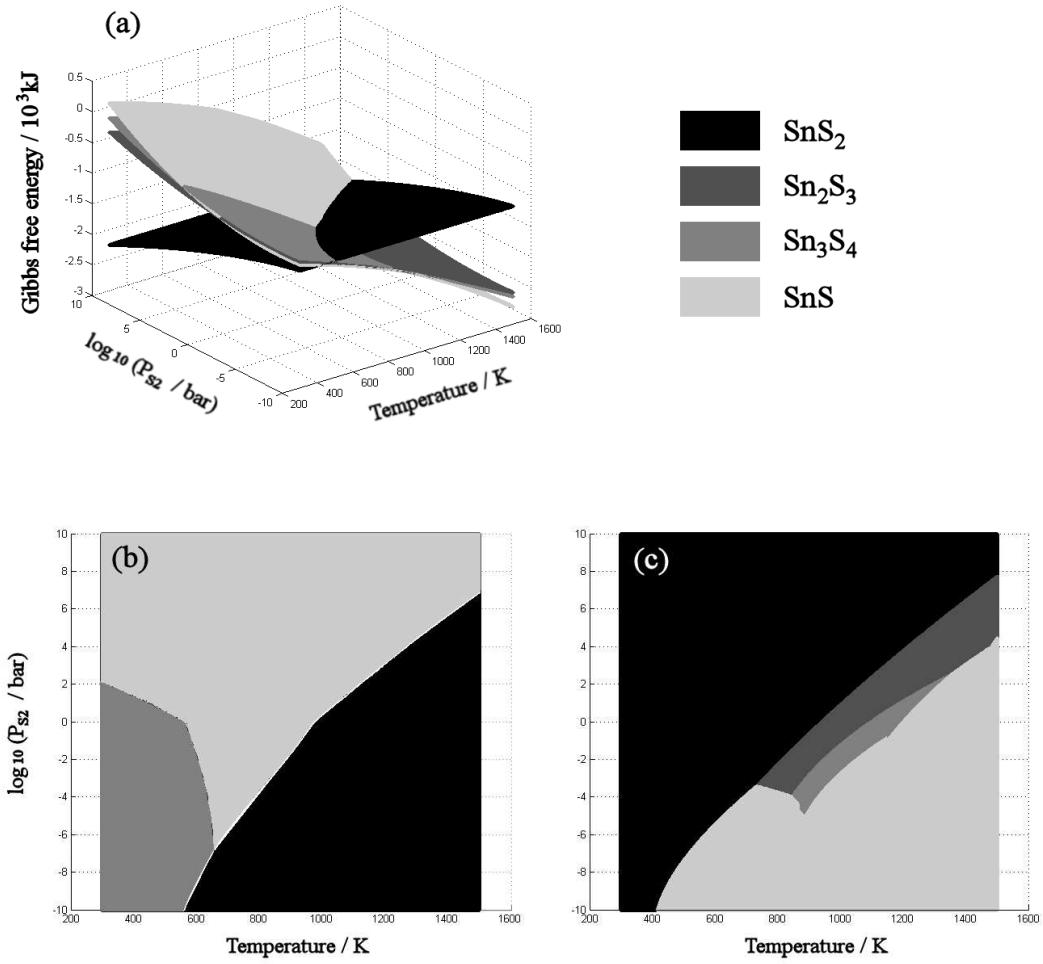

Fig. 5.3.4 (a) 3D plot showing the intersection framework among the surfaces representing the chemical potentials of SnS_2, Sn_2S_3, Sn_3S_4 and SnS as functions of the absolute temperature and of the sulfur partial pressure. Corresponding 2D plots showing the maximization (b) and minimization (c) of the chemical potential in the system. The regions in (c) can be regarded as the T-p($S_{y\,(g)}$) stability regions of the tin sulfide phases in the system.

The Zn-S system is less complicated, because ZnS is the only allowed binary component, either in its cubic (*Sphalerite*) or in its hexagonal (*Wurtzite*) forms (see Appendix 6). The Zn-I system presents only ZnI_2 in both condensed and gaseous forms.

5.4 Ternary systems: Cu-S-I, Sn-S-I, Zn-S-I

As seen in Fig. 5.3.1, the trimeric form of copper iodide is the most stable gas species in the Cu-I system. Therefore, the transport of Cu was computed considering the action of $I_{x\,(g)}$ on $CuS_{\,(s)}$ or $Cu_2S_{\,(s)}$ depending on the temperature range.

Reac. 5.4.1 $(v+1)Cu_{2-v}S_{\,(s)}+(v+1)(2-v)/x\ I_{x\,(g)}\rightarrow(v+1)(2-v)/3(CuI)_{3\,(g)}+(v+1)/y\ S_{y\,(g)}$

Reac. 5.4.2 (v = 1)

$2\ CuS_{\,(s)} + 2/x\ I_{x\,(g)} \rightarrow 2/3\ (CuI)_{3\,(g)} + 2/y\ S_{y\,(g)}$

Reac. 5.4.3 (v = 0)

$Cu_2S_{\,(s)} + 2/x\ I_{x\,(g)}\ 1/y\ S_{y\,(g)} \rightarrow 2/3\ (CuI)_{3\,(g)} + 2/y\ S_{y\,(g)}$

Now, an equilibrium cycle involving three processes can be considered, as shown in Fig. 5.4.1: $2CuS_{\,(s)} + 2/x\ I_{x\,(g)} \rightleftharpoons 2/3\ (CuI)_{3\,(g)} + 2/y\ S_{y\,(g)} \rightleftharpoons Cu_2S_{\,(s)} + 2/x\ I_{x\,(s)}\ 1/y\ S_{y\,(g)}$. This can be depicted by an energy diagram with three relative minima and three relative maxima (the energy level attributed to the transition-state has no actual meaning). The diagram of chemical potential vs temperature for the Cu-S-I system (Fig. 5.4.1) for the three members of the process can be divided into three temperature ranges:

(1) T < 800 K:

$\mu°[2CuS_{\,(s)} + 2/x\ I_{x\,(g)}] < \mu°[Cu_2S_{\,(s)} + 2/x\ I_{x\,(s)}\ 1/y\ S_{y\,(g)}] < \mu°[2/3(CuI)_{3\,(g)} + 2/y\ S_{y\,(g)}]$

(2) 800 K < T < 1223 K:

$\mu°[Cu_2S_{\,(s)} + 2/x\ I_{x\,(s)}\ 1/y\ S_{y\,(g)}] < \mu°[2/3(CuI)_{3\,(g)} + 2/y\ S_{y\,(g)}] < \mu°[2CuS_{\,(s)} + 2/x\ I_{x\,(g)}]$

(3) T > 1233 K:

$\mu°[Cu_2S_{\,(s)} + 2/x\ I_{x\,(s)}\ 1/y\ S_{y\,(g)}] < \mu°[2CuS_{\,(s)} + 2/x\ I_{x\,(g)}] < \mu°[2/3(CuI)_{3\,(g)} + 2/y\ S_{y\,(g)}]$

The Gibbs free energies of reaction 5.4.1 as a function of the temperature are shown in Fig. 5.4.2, where the formation of CuI is computed for both the condensed (solid or liquid) and gaseous forms. The Gibbs free energy of the conversion of $CuS_{\,(s)}$ to $Cu_2S_{\,(s)}$ and $S_{y\,(g)}$ (reaction 5.3.1) is also reported (N.B. the negative slope and the intercept with $\Delta G° = 0$ at T = 800 K).

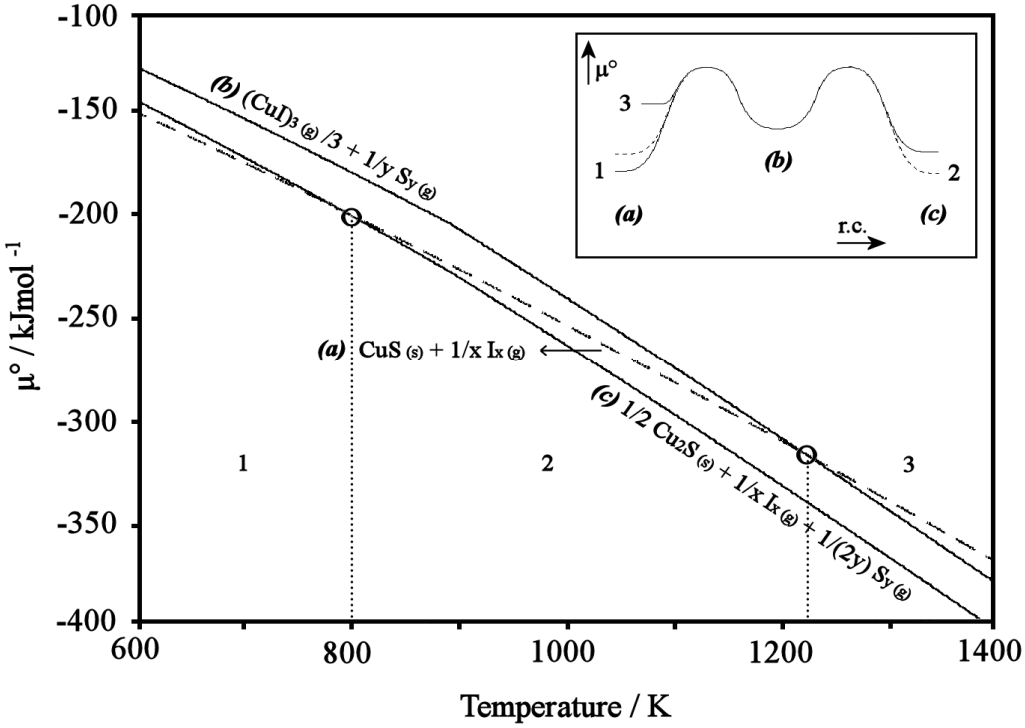

Fig. 5.4.1 Standard chemical potential of the Cu-S-I equilibria (reactions 5.4.1-5.4.3) as a function of the temperature. Inset: schematic representation of the relative stabilities for the three-reaction process (the transition states are a guide to the eye).

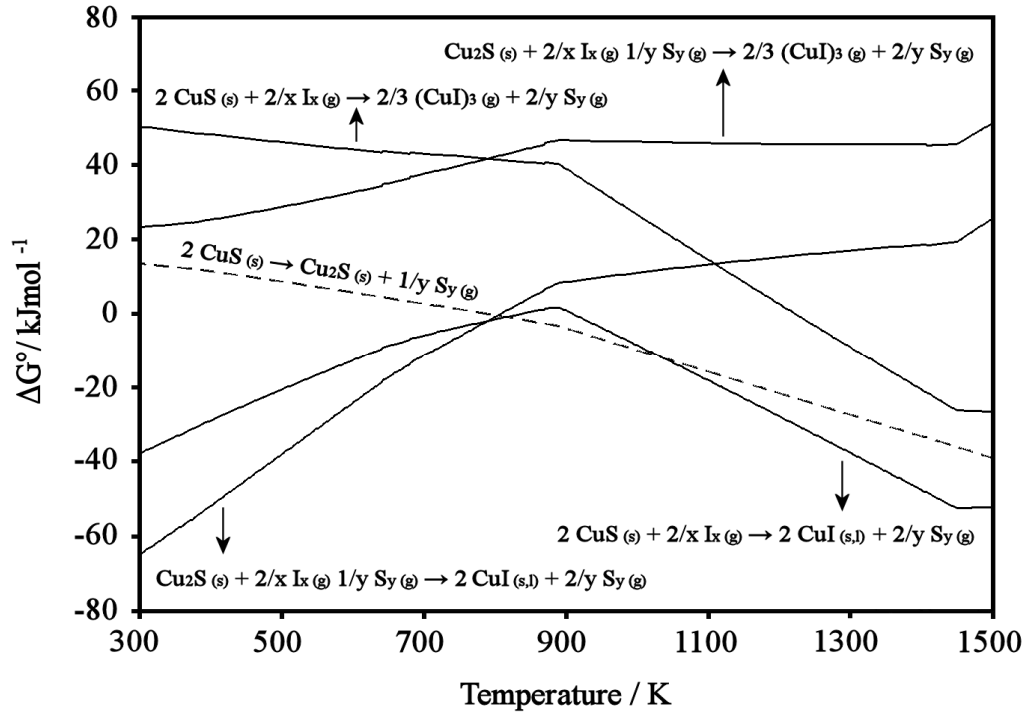

Fig. 5.4.2 Standard Gibbs free energy changes of reactions 5.4.2-5.4.3 as a function of the temperature. Reaction 5.4.1 is plotted for v = 0 and 1 and for the species $(CuI)_{3\,(g)}$ and $CuI_{(s,l)}$.

The equilibria in Fig. 5.4.2 show that there is a strong driving force for crystallization of solid CuI. This suggests that CuI segregation along the length of the ampoule could be an issue for both the effectiveness of the overall transport process and the purity of the resulting crystals.

The equilibria of the Sn-S-I system are expressed by reactions 5.4.4-5.4.5, where the formation of the most stable gaseous form of $SnI_{2(w+1)}$ (w = 0 and 1) is computed from the most stable Sn-S phases.

Reac. 5.4.4 $SnS_{(s)} + (4/x - 2(1-w)/x)\ I_{x\,(g)} + 1/y\ S_{y\,(g)} \rightarrow SnI_{2(w+1)\,(g)} + 2/y\ S_{y\,(g)}$

Reac. 5.4.5 $Sn_zS_{z+1\,(s)} + (4z/x - 2z(1-w)/x)\ I_{x\,(g)} \rightarrow z\ SnI_{2(w+1)\,(g)} + (z+1)/y\ S_{y\,(g)}$

The computation is performed analysing the specific reactions separately (5.4.6-5.4.8) each with its corresponding tin sulfide (z = 1, 2 and 3):

Reac. 5.4.6 (z = 1)

$SnS_{2\,(s)} + 24/xI_{x\,(g)} \rightarrow 6SnI_{2(w+1)\,(g)} + 12/yS_y + 6(2+2w)/xI_{x\,(g)}$

Reac. 5.4.7 (z = 2)

$3Sn_2S_{3\,(s)} + 24/xI_{x\,(g)} + 3/yS_{y\,(g)} \rightarrow 6SnI_{2(w+1)\,(g)} + 12/yS_y + 6(2+2w)/xI_{x\,(g)}$

Reac. 5.4.8 (z = 3)

$2\ Sn_3S_{4\,(s)} + 24/x\ I_{x\,(g)} + 4/y\ S_{y\,(g)} \rightarrow 6\ SnI_{2(w+1)\,(g)} + 12/y\ S_y + 6(2+2w)/x\ I_{x\,(g)}$

The Gibbs free energies of reactions 5.4.4-5.4.5 as a function of the temperature are reported in Fig. 5.4.3.

The transport of Zn by $I_{x\,(g)}$ can be studied by considering the simple formation of $ZnI_{2\,(g)}$ from $ZnS_{(s)}$ (reaction 5.4.9).

Reac. 5.4.9 $ZnS_{(s)} + 2/x\ I_{x\,(g)} \rightarrow ZnI_{2\,(g)} + 1/y\ S_{y\,(g)}$

The computation of reaction 5.4.9 predicts a negative slope of ΔG vs. temperature for $T < 1470$ K (x = 2), while for $T > 1470$ K (x = 1) the slope becomes positive, in agreement with the positive and negative variation of the number of moles of the gaseous species in those temperature ranges. The reaction is exoergonic up to ~ 1232 K, where the curve intersects the abscissa axis.

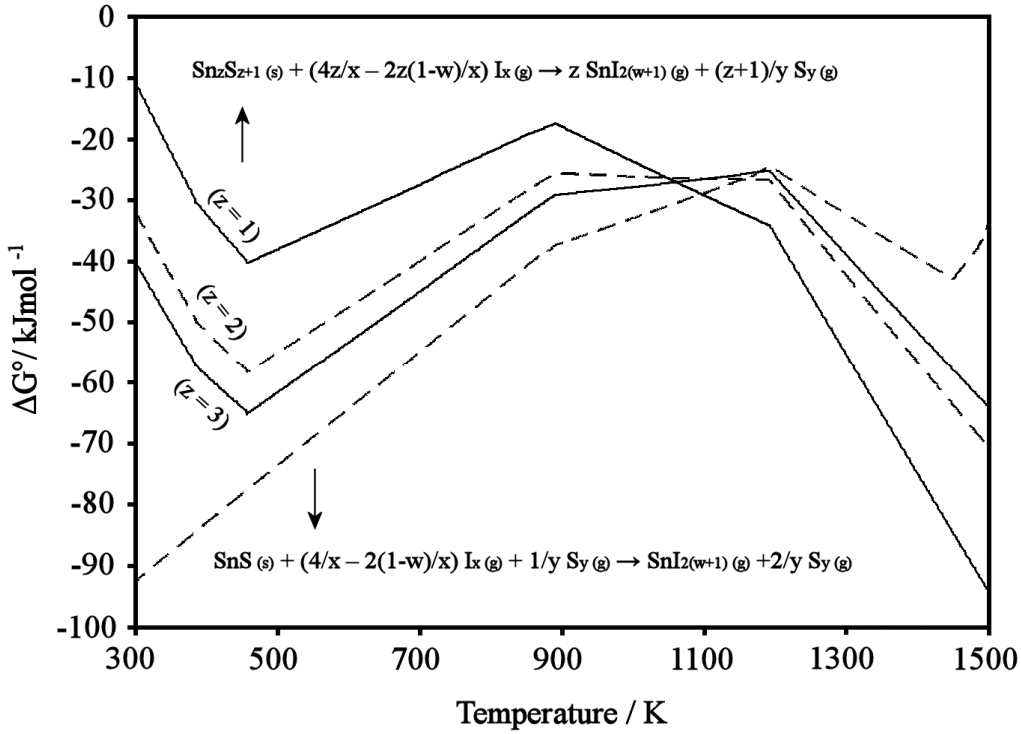

Fig. 5.4.3 Standard Gibbs free energies of reactions 5.4.4-5.4.5 as a function of the temperature. Reaction 5.4.5 is plotted for z = 1, 2 and 3 respectively for the species $SnS_{2\,(s)}$, $Sn_2S_{3\,(s)}$ and $Sn_3S_{4\,(s)}$ (reactions 5.4.6-5.4.8).

If we assume that the species in reactions 5.4.1, 5.4.5, 5.4.6, 5.4.9 are in equilibrium with each other, i.e. the activation energies of the corresponding processes are negligible, the following statement is valid. Having considered the most stable among the possible products at each temperature, the process that maximizes the algebraic magnitude of $\Delta G°$ of reaction is the one that also minimizes the chemical potential of the reagents, and therefore it is the most favourable process. From the relationship between the standard Gibbs free energy of a reaction and its thermodynamic equilibrium constant (Eq. 4.4.2), it is possible to compare the spontaneity of the formation of the gaseous iodide compounds of Cu, Zn and Sn from their sulfides (taken separately).

Eq. 5.4.1 $K_P = e^{-\Delta G°/RT}$

Fig. 5.4.4 shows the temperature dependence of the thermodynamic equilibrium constants (K_P) for the formation of the gaseous binary iodides of Cu, Zn and Sn by the action of $I_{x\,(g)}$ on the corresponding most stable sulfides, as resulting from the computation.

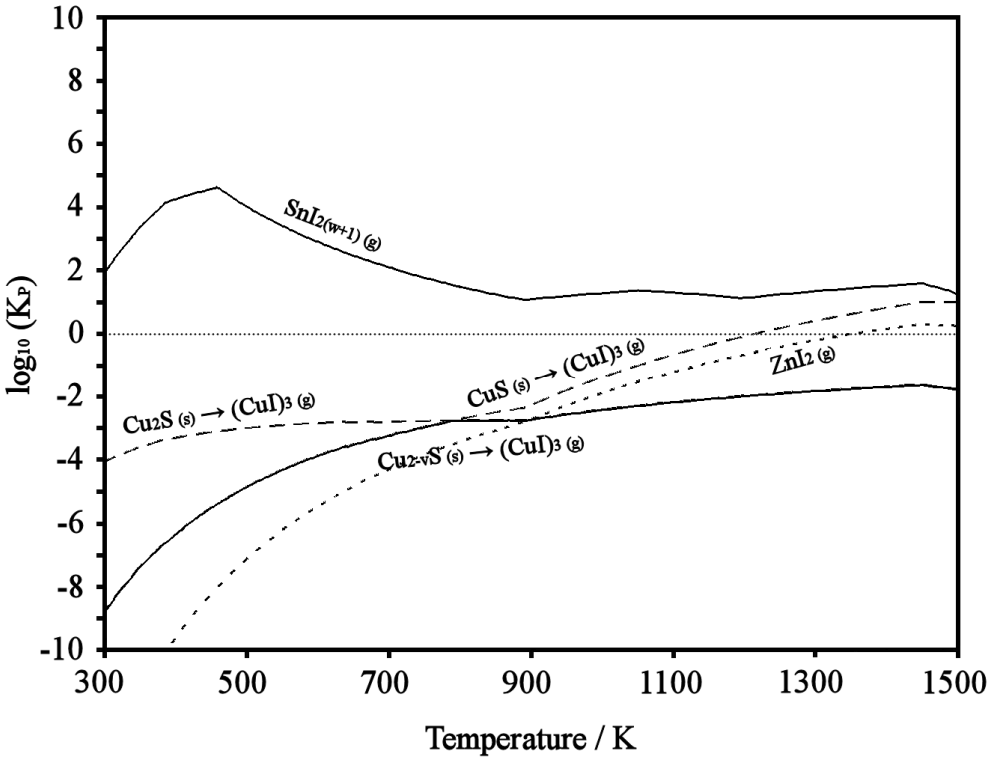

Fig. 5.4.4 Thermodynamic equilibrium constants for the formation of the iodide gaseous compounds of Cu, Zn and Sn from the corresponding most stable sulfides as a function of the temperature (from reactions 5.4.1, 5.4.4, 5.4.5, 5.4.9).

It must be highlighted that in the low temperature regime (500-700K) the equilibrium constants for the formation of the iodides of Cu, Zn and Sn from the corresponding sulfides span from 11 to 7 orders of magnitude difference, with the Sn being the easiest and Zn the most difficult to transport. The difference is reduced to only 4 orders of magnitude in the range 900-1100K, with Cu becoming the least transportable among the metals. From this thermochemical basis, Fig. 5.4.4 shows that the sulfides of Cu, Zn and Sn are likely to behave very differently with regard to transport with iodine. The risk of compositionally incongruent vapour transport of the unary iodides of Cu, Zn and Sn is highlighted.

5.5 Quaternary system: Cu-Sn-S-I

The Cu-Sn-S system has been recently re-investigated by Fiechter et al. [338]. Among the 17 known phases, an attempt was made to estimate the free energy of reaction between $Cu_2SnS_{3\,(s)}$ and iodine to form the Cu and Sn iodides as a function of the temperature (5.5.1).

Reac. 5.5.1 $Cu_2SnS_{3\,(s)} + 2(2+w)/x\ I_{x\,(g)} \rightarrow 2/3(CuI)_{3\,(g)} + SnI_{2(w+1)\,(g)} + 3/yS_{y\,(g)}$

The compound Cu_2SnS_3 (CTS) has been reported to melt congruently at 1129 K and to exist in the liquid form at least up to 1373 K [338], although subject to the risk of $SnS_{\,(g)}$ and $S_{y\,(g)}$ losses, as reported by Weber et al. [154]. As illustrated by the pseudo-binary join Cu_2S-SnS_2 reproduced in Fig. 5.5.1 from Olekseyuk et al. [133], Cu_2SnS_3 can be thought as the equimolar reaction product between the end members (reaction 5.5.2).

Reac. 5.5.2 $Cu_2S_{\,(s)} + SnS_{2\,(s)} \rightarrow Cu_2SnS_{3\,(s)}$

Unfortunately no experimental indication of the standard Gibbs free energy of formation of CTS from the elements has been reported in the literature. As a first approximation for the estimation of the free energy change of reaction 5.5.2 it would be possible to employ the "sulfide sum" procedure described by Craig et al. [339] and Vaughan et al. [340]. With their approach, complex sulfides are assumed to behave as if they consist of non-ideal mixtures of their simple end-members. According to this procedure, the enthalpy change of reaction 5.5.2 would be zero and the free energy change would be equal to the entropy gain of the reaction. However, Walsh [341] has estimated the enthalpy of formation of CTS from Cu_2S and SnS_2 from DFT studies as ~-70.4 $kJmol^{-1}$ (reaction 5.5.2), raising doubts on the applicability of the procedure reported by Craig et al. [339] and Vaughan et al. [340] to our system. Another DFT estimation is available from the work of Chen et al. [153], who computed the formation enthalpy of Cu_2SnS_3 from its total energy and its elemental standard states, similarly to the work done by Zhang et al. [115] on $CuInSe_2$. This has been reported to be -2.36 eV/f.u., which corresponds to ~ – 228 $kJmol^{-1}$.

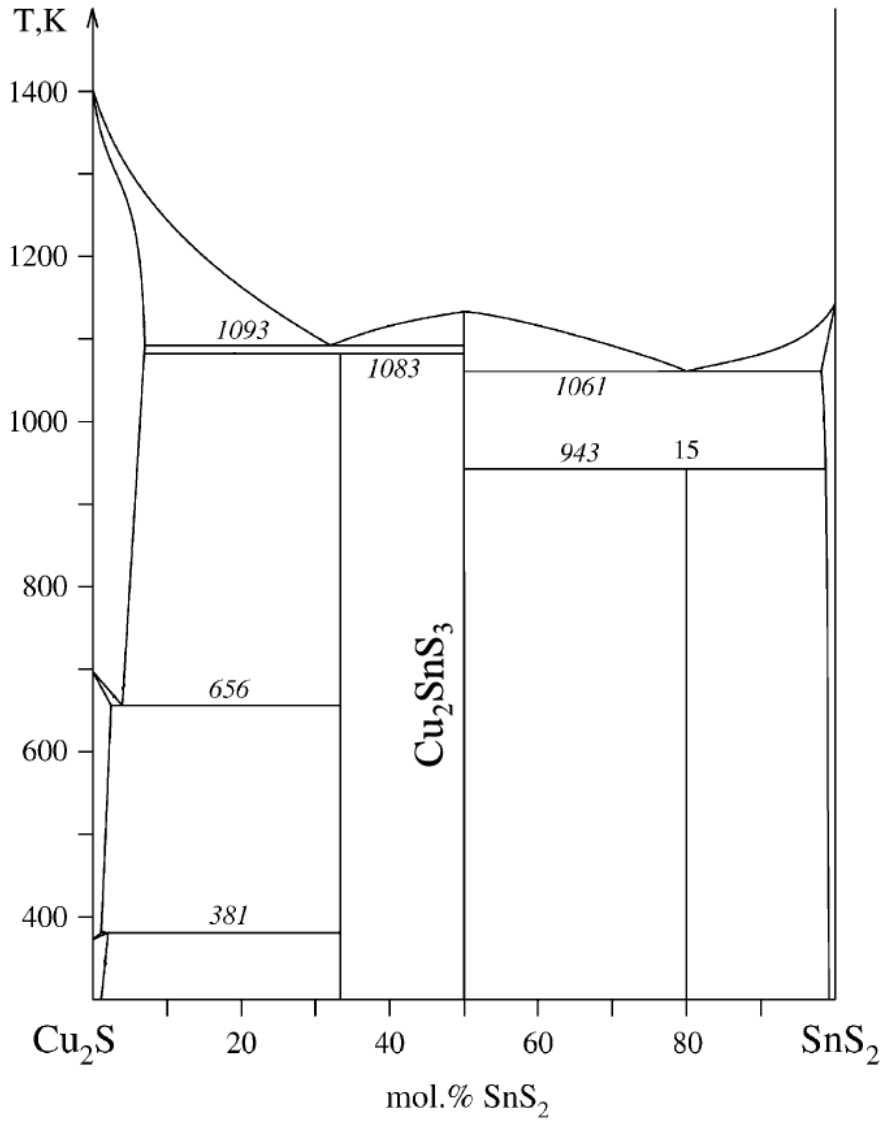

Fig. 5.5.1 Pseudo-binary phase diagram of the Cu_2S-SnS_2 system, as reported by Olekseyuk et al. [133].

In order to understand the chemical vapour transport phenomena in the present work, it is important to estimate the chemical potential of CTS as a function of temperature, i.e. the entropic term of $\mu°_{Cu2SnS3}$. DFT calculations of the chemical potentials of condensed phases are usually performed at T = 0 K, at which temperature μ approaches h. The reasons for performing calculations at this temperature have been explained by Qian et al. [342].

In the present work, estimation of the chemical potential of CTS and CZTS as a function of the temperature was performed in the following way. The principle of "sulfide sum" was applied to the chemical potential functions of the compounds involved in the reaction for which ΔH° is known by DFT work, with the addition of

the reported enthalpy change. This procedure is certainly an approximation. In order to minimise the error associated to it, the reactions considered for the data extraction are those involving the binary sulfides rather than elements plus sulfur, given the lower free energy change associated to the reaction between the binaries. Furthermore, the low temperature forms of the binary phases were considered for the computation, without taking into account their solid state transitions.

Following these considerations, Chen's results [153] on the elemental reaction were discarded and Walsh' [341] on the binary sulfides were used for the calculation of the chemical potential of CTS as a function of temperature. The procedure is summarised by Eqs. 5.5.1-5.5.3. The free energy change of reaction 5.5.2 is expressed by Eq. 5.5.1.

Eq. 5.5.1 $\Delta G^\circ = \mu^\circ_{Cu2SnS3} - (\mu^\circ_{Cu2S} + \mu^\circ_{SnS2})$

According to Qian et al. [342] the free energy change of reaction 5.5.2 computed by DFT is related to the chemical potentials of CTS, Cu_2S and SnS_2 through Eq. 5.5.2, which is formally correct only at T = 0 K.

Eq. 5.5.2 $h^\circ(0)_{Cu2SnS3} \sim \mu^\circ(0)_{Cu2SnS3} = \Delta G^\circ(0)+\mu^\circ(0)_{Cu2S}+\mu^\circ(0)_{SnS2}$

In the present investigation, Eq. 5.5.2 is assumed to be valid over the whole temperature range considered. In other words, it is assumed that the free energy change of reaction 5.5.2 is equal to the enthalpy change and that the enthalpy change does not vary with temperature. Following the estimation of the chemical potential of CTS, the computation of the free energy of reaction 5.5.1 was performed and the results are shown in section 5.6.

5.6 Pentenary system: Cu-Zn-Sn-S-I

Similarly to Cu_2SnS_3-I_2 the estimation of the free energy of reaction between $Cu_2ZnSnS_{4\,(s)}$ and iodine to form the unary iodides, as a function of the temperature was computed (5.6.1).

Reac. 5.6.1 $Cu_2ZnSnS_{4(s)}+2(3+w)/xI_{x(g)}\rightarrow 2/3(CuI)_{3(g)}+ZnI_{2(g)}+SnI_{2(w+1)\,(g)}+4/yS_{y(g)}$

The pseudo-binary phase diagram of the system Cu_2SnS_3-ZnS reported by Olekseyuk et al. [133] is shown in Fig. 5.6.1. According to their work, Cu_2ZnSnS_4 is formed by peritectic reaction at 1253 K between ZnS and a Zn-poor liquid phase.

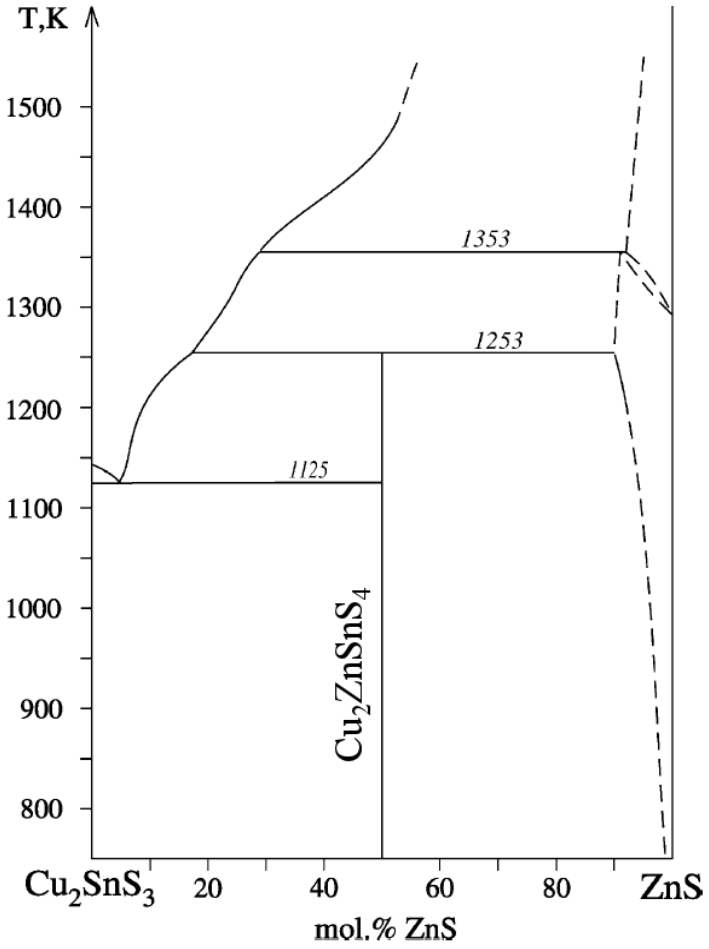

Fig. 5.6.1 Pseudo-binary phase diagram of the Cu_2SnS_3-ZnS system, as reported by Olekseyuk et al. [133].

As for Cu_2SnS_3, no experimental indication of the standard Gibbs free energy of formation of CZTS has been reported. According to the "sulfide sum" procedure

described by Craig et al. [339] and Vaughan et al. [340], the enthalpy change of reaction 5.6.2 is zero and the free energy change is equal to the entropy gain deriving from the non-ideal mixing of the binary sulfides.

Reac. 5.6.2 $Cu_2S_{(s)} + ZnS_{(s)} + SnS_{2(s)} \rightarrow Cu_2ZnSnS_{4(s)}$

Such an approximation is as good as the structures of the end-members are similar. In particular, the cation polyhedra of the binaries should resemble that of the complex sulfide [340]. The coordination polyhedra of the metals in the crystal structures of Cu_2S, ZnS and SnS_2 are quite dissimilar [343-346], ranging from two to six-fold. In fact, the Gibbs free energy of reaction 5.6.2, computed with DFT at T = 0 K by Chen et al [153] is -0.81 eV/f.u. ~ -78.15 $kJmol^{-1}$. A free energy gain for reaction 5.6.2 has been experimentally proven up to the peritectic temperature (1253 K) at which CZTS decomposes [133]. Therefore, it is possible that the free energy gain of reaction 5.6.2 decreases with increasing temperature, until it becomes positive at the peritectic temperature of CZTS.

Complementary information on the energy content of CZTS can be extracted from experimental investigations reported by Scragg et al. [281], who estimated the free energy change of reaction 5.6.2 as -22±6 $kJmol^{-1}$ at 550 °C from the measured pressure of $S_{2(g)}$ at the equilibrium with CZTS thin films. A less negative value of the free energy change of reaction 5.6.2 at higher temperature seems consistent with the fact that CZTS decomposes into ZnS and Zn-poor liquid at 1253 K.

In this work, similarly to the CTS case, the estimation of the chemical potential of CZTS was derived by summing the chemical potential functions of the binary sulfides on the left hand side of reaction 5.6.2 and the enthalpy change of reaction 5.6.2. However, as a value for the enthalpy change we employed a linear combination between the DFT-computed $\Delta H°$ by Chen et al [153] at 0 K and the experimentally derived $\Delta H°$ by Scragg et al at 550 °C. As per Cu_2SnS_3, the estimation is performed with the thermochemical functions of the low temperature forms of binary sulfides, excluding their solid state transitions from computation.

Zhai et al. [347] have estimated the enthalpy of reaction 5.6.3 from DFT studies at 0 K as + 0.1 eV/f.u., corresponding to ~+9.65 $kJmol^{-1}$ [347].

Reac. 5.6.3 $Cu_2ZnSnS_{4(s)} \rightarrow Cu_2SnS_{3(s)} + ZnS_{(s)}$

Zhai's estimation [347] is consistent with Walsh's [341] and Chen's [153] results and add little information to the definition of the chemical potential of CZTS.

Fig. 5.6.2 shows the estimated Gibbs free energy of reaction 5.6.2 as a function of the temperature, based on the estimation of the chemical potential of CZTS outlined above.

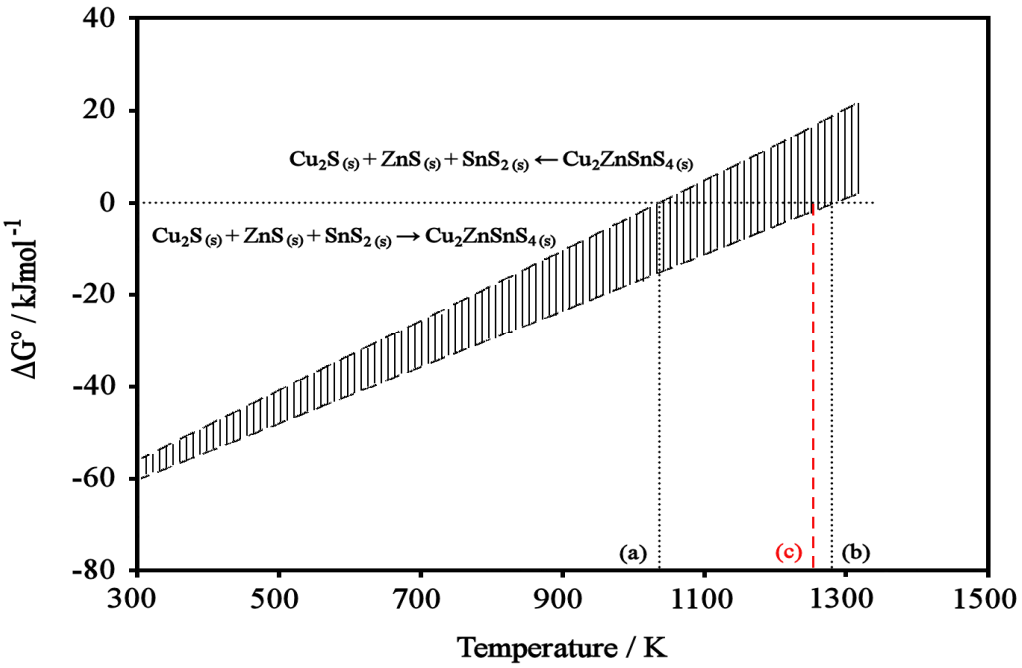

Fig. 5.6.2 Gibbs free energy of reaction 5.6.2, as obtained from estimation of the chemical potential of CZTS based on the linear extrapolation between the theoretical DFT calculations of Chen et al. at T = 0 K [153] and the experimental findings of Scragg et al. at T + 823 K [281]. Estimated decomposition temperature of CZTS into the solid binaries by consideration of the lower (a) and upper (b) error limits indicated by Scragg et al. [281] ($\Delta G° = -22 \pm 6$ kJmol^{-1}). The peritectic temperature of CZTS is represented by (c), as reported by Olekseyuk et al. [133].

From Fig. 5.6.2a-b, it is possible to extrapolate the temperature at which CZTS would decompose into the solid binary sulfides, considering the CZTS chemical potential extrapolated from Chen's [153] and Scragg's data [281]. In reality, it is known from Olekseyuk et al. (Fig. 5.6.1) [133] that CZTS decomposes at 1253 K (Fig. 5.6.2c) into solid $ZnS_{(s)}$ plus a liquid phase rich in Cu_2SnS_3. For the computation of Fig. 5.6.2 the thermochemical data of the low temperature solid binary sulfides were employed. Given the higher stability of the liquid phase forming at 1253 K (for which no thermochemical data is available) compared to the solid binary sulfides, an overestimation of the absolute free energy change of reaction 5.6.2 plotted in Fig. 5.6.2 is expected at high temperature. Nevertheless, the approximate estimation of the chemical potential of CZTS as a function of the

temperature obtained in this work is considered to be good enough to allow a coarse thermochemical prediction of reaction 5.6.1. The results of such a prediction are shown in Fig. 5.6.3, together with the computed free energies for the reactions corresponding to iodide formation from the binary sulfides (5.4.1-5.4.4-5.4.5-5.4.9) and Cu_2SnS_3 (5.5.1).

According to Fig. 5.6.3(a), the formation of gaseous iodides of Cu, Zn and Sn from solid CZTS (reaction 5.6.1) has a positive standard Gibbs free energy. Therefore, such a process is expected to be endoergonic up to about the peritectic temperature of CZTS (p_4: 1253 K). The direction of transport in the CVT reaction is given by the sign of the reaction enthalpy ΔH°, as inferred from Van't Hoff's equation (Eq. 5.1).

Eq. 5.1 $$\partial \ln[K_P(T)]/\partial T = \Delta H^\circ / RT^2$$

Fig. 5.6.3(b) shows that reaction 5.6.1 has a positive value of ΔH°, i.e. the reaction is endothermic. The system is expected to respond to a temperature increase with an increase of the thermodynamic equilibrium constant $K_P(T)$. Therefore, the direction of transport for the reverse reaction corresponding to the crystallization of CZTS from the unary iodides of Cu, Zn and Sn is from high to low temperatures.

The curve in Fig. 5.6.3(a) corresponding to CZTS (reaction 5.6.1) can be divided into three temperature regions with different slopes. Each slope variation is associated to the different species involved in the reaction and to their different entropic contributions. In particular, the change of the number of gaseous species as reaction 5.6.1 proceeds (Δn) is expressed by Eq. 5.6.1.

Eq. 5.6.1 $$\Delta n = (2/3 + 1 + 1 + 4/y) - 2\cdot(3+w)/x$$

Table 5.6.1 is a summary of the three different Δn of reaction 5.6.1 for the three temperature ranges characterised by discontinuity of the first derivative of ΔG° ($\partial \Delta G^\circ / \partial T = -\Delta S^\circ$), as shown in Fig. 5.6.3(a).

For reaction 5.6.1, the transition to a more positive change of the number of gaseous species with an increase of the temperature is consistent with the increase of the ΔS° of reaction, as observed in Fig. 5.6.3(a).

Table 5.6.1 Summary of the change of the number of gaseous species for reaction 5.6.1 for the different temperature ranges (ref. to Fig. 5.6.3a).

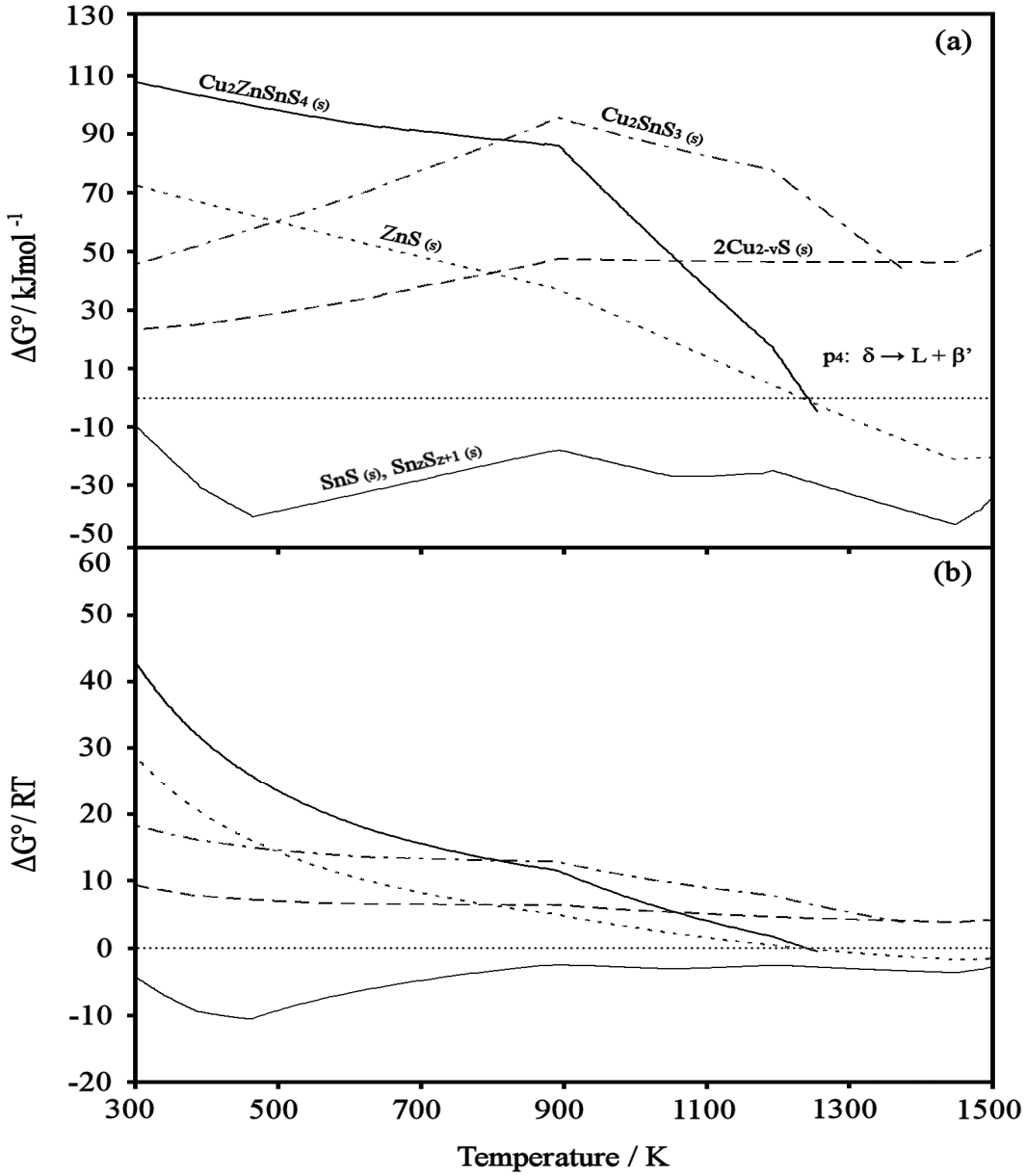

Fig. 5.6.3 (a) Standard Gibbs free energies for the formation of the iodide gaseous compounds of Cu, Zn and Sn from the corresponding sulfides and from Cu_2SnS_3 and Cu_2ZnSnS_4 as a function of the temperature. (b) Corresponding ΔG°/RT plots.

Reac. 5.6.1 $Cu_2ZnSnS_{4(s)}+2(3+w)/xI_{x(g)} \rightarrow 2/3(CuI)_{3(g)}+ZnI_{2(g)}+SnI_{2(w+1)\,(g)}+4/yS_{y(g)}$					
T range / K	**x**	**y**	**w**	**Reaction**	**Δn**
300<T<900	2	6<y<8	1	$Cu_2ZnSnS_{4\,(s)} + 4I_{2\,(g)} \rightarrow 2/3(CuI)_{3\,(g)} + ZnI_{2\,(g)} + SnI_{4\,(g)} + 4/yS_{y\,(g)}$	-5/6 < Δn < -4/6
900<T<1188	2	2	1	$Cu_2ZnSnS_{4\,(s)} + 4I_{2\,(g)} \rightarrow 2/3\,(CuI)_{3\,(g)} + ZnI_{2\,(g)} + SnI_{4\,(g)} + 2S_{2\,(g)}$	+2/3
1188<T<1253	2	2	0	$Cu_2ZnSnS_{4\,(s)} + 3I_{2\,(g)} \rightarrow 2/3\,(CuI)_{3\,(g)} + ZnI_{2\,(g)} + SnI_{2\,(g)} + 2S_{2\,(g)}$	+5/3

6. Chemical vapour transport growth of CZTS with I_2

As shown in Fig. 5.6.1, Olekseyuk et al. [133] have found that Cu_2ZnSnS_4 melts incongruently at 1253 K, crystallizing by the peritectic reaction p_4: L + β'(ZnS) → δ with a composition of the liquid phase far poor in ZnS. It is known that the formation of a phase-pure substance that crystallizes via a peritectic reaction may be difficult to achieve [348]. In such reactions a liquid needs to react with a solid and diffusion of material through the newly formed phase at the interface between the reactants is needed for the reaction to proceed. Therefore, the cooled system has the tendency to display phase segregation, especially if the cooling rate employed is high.

In the case of Cu_2ZnSnS_4, Shimada et al. have shown that its growth from the melt results in the presence of impurity phases such as Cu_2SnS_3, ZnS and SnS [349]. The solidification of a single-phase CZTS from the stoichiometric melt might be improved to some extent by the presence of a suitable seed or the action of a directional cooling, like in the Czochralski, the Bridgman-Stockbarger [350] or the gradient freezing techniques [351]. It is only very recently that Nagaoka et al. have shown the possibility of precipitating primary crystals of CZTS from molten hyper-eutectic solutions in the pseudo-binary system CZTS-Sn [352, 353].

Single crystals of the Cu_2FeSnS_4-Cu_2ZnSnS_4 pseudobinary series were synthesized by Bernardini et al. [64] for structural investigations using the salt-flux technique reported by Moh et al. [354]. This technique is based on the solvent properties of molten salts, where the reaction between the elements or precursors is carried out. A similar approach was also employed by Altosaar et al. [355] and Timmo et al. [356] who successfully crystallized $Cu_2Zn_{1-x}Cd_x$ $Sn(Se_{1-y}S_y)_4$ and $Cu_2ZnSnSe_{4-x}S_x$ powders from molten KI with the intent of fabricating mono-grain layer devices [357]. The difficulty of producing the sulfur end member in a pure form was highlighted, since the X-ray EDS analysis of the polished crystals pointed to the presence of the secondary phases alongside the dominating CZTS phase.

CZTS single crystals of reasonable dimensions were first produced by Nitsche et al. [316] with the chemical vapour transport (CVT) technique employing I_2 as the transporting agent; the crystals were reported to be black needles with dimensions of up to 20 mm x 0.2 mm x 0.2 mm. Compositional analysis was not reported, but structure refinement from XRD revealed that the compound is tetragonal with lattice parameters: $a = b = 5.427$ Å and $c = 10.848$ Å [358].

Among the techniques used for the growth of single crystals, the CVT has generally the advantage of employing lower operational temperatures and static configurations of the growing ampoule, the main drawbacks being the incorporation of the gaseous solvent species to some extent and the sensitivity of the technique to subtle variations of the growing conditions [318]. For example, CVT was successfully employed for the synthesis of single crystals of $CuInS_2$, for which crystallization from the melt is made difficult by the high temperature phase transitions [359].

It is known that for simple systems [360] crystallographic perfection in CVT growths is favoured under diffusion-limited transport rate, when nucleation density is minimized. However, due to the pentenary nature of our system, the formation of compositionally well defined sinks is subject to the risk of incongruent transport [324]. In fact, as discussed in section 5.4, the thermochemistries of the iodides of Cu, Zn and Sn are very different. Therefore the transport induced by the thermal gradient may be accompanied by preferential formation of the competing secondary phases of the Cu-Zn-Sn-S system, as it was shown for $CuInS_2$ [361].

In the present work single crystals of Cu_2ZnSnS_4 were grown within sealed quartz ampoules under two different I_2 loads. The effects of the temperature gradient on their habit, structure and composition were considered. Microscopic and nanoscopic uniformities of the crystals have been assessed with Scanning Electron Microscopy (SEM)/X-ray EDS and Transmission Electron Microscopy / Selected Area Electron Diffraction / Electron Energy Loss Spectroscopy (TEM/SAED/EELS), in order to ascertain whether the samples are suitable for more advanced structural and physical characterizations. These results are discussed in this chapter.

6.1 Experimental details of crystal growth

The equipment employed for the crystal growth experiments consists of a custom-made horizontal tubular furnace (Elite Thermal Systems Ltd.) with four independent controllers, each of which allows the configuration of individual setpoints and ramp rates. In the standard experimental configuration the system is intended to provide two zones of different temperatures, with as short a transition zone as possible between them. In order to ensure the most uniform temperature within each zone, the settings of the independent controllers were chosen after careful calibration with a test thermocouple placed along the tube inside a "dummy" quartz ampoule, thus emulating the desired experimental conditions as close as possible.

The experiments were run within sealed quartz ampoules of 23 mm internal diameter about 160 mm long. During the experiments the ampoule was touching the alumina work tube of 30 mm internal diameter that constitutes the walls of the furnace as shown in Fig. 6.1.1.

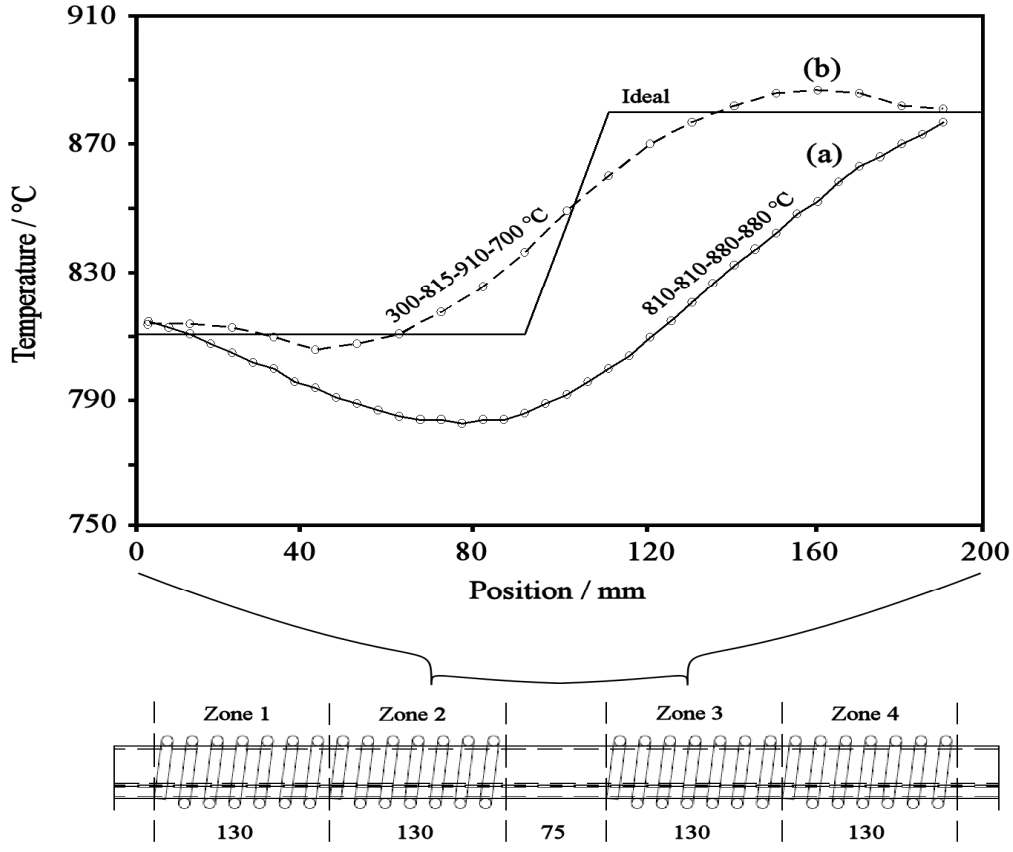

Fig. 6.1.1 Schematic representation of the four-zone furnace with the ideal (810-880 °C), and experimental temperature profiles obtained with typical settings (a,b).

In the present work, the optimization of the temperature profiles within the furnace required considerable efforts through adjustment of the four temperature settings and of the end plugs made of ceramic fibre.

Fig. 6.1.1 shows also the temperature profile along the ampoule, as measured with the thermocouple, at an unrefined (a) and a refined stage (b) of adjustment, compared to an "ideal" condition. In order to achieve a sharp temperature variation along the furnace, the unheated central part of the furnace required the controllers of zones 2 and 3 to operate at higher temperatures than expected from the ideal profile. As a consequence, in order to avoid overheating of the ends of the ampoule, zones 1 and 4 were operated at lower temperatures acting as radiation wells. The optimized profiles showed temperature uniformity on the order of ± 5 °C over 50-60 mm long plateaus. Thermal gradients are among the most crucial aspects for the crystal growth experiments.

The synthesis procedure started with the preparation of the precursor material by finely grinding together stoichiometric amounts of 5N purity Cu, Zn, Sn and an excess (1.5x) of sulfur in an agate mortar. The mixture was then transferred into an IR pellet press to form a green pellet (Fig. 6.1.2a). Similarly to Prabukanthan et al. [362], excess sulfur was employed with the intent of preventing any deviation from stoichiometry in the early stages of thermal treatment.

A quartz ampoule with a glass joint and a tight-seal valve was thoroughly washed with a 5% Decon 90 solution (Decon Laboratories Ltd.), rinsed with deionised water and left soaking overnight inside the fume hood in a 1:1 HNO_3:HCl solution, to allow dissolution of any impurities. The ampoule was then rinsed thoroughly with deionised water several times, connected to a Schlenk line under vacuum, and its external surfaces were heated with the oxidising flame of a Bunsen burner to ensure desorption of any gaseous components from the internal walls..

The pellet was then loaded into the ampoule connected to the Schlenk line, and several vacuum and inert gas (N_2, Ar or He) purge steps were performed up to the final background pressure of $5 \cdot 10^{-4}$ bar (Fig. 6.1.2b).

In some cases the green pellet was loaded into the ampoule together with the I_2 load, while in other cases an annealing pre-treatment on the green pellet was performed to form a sintered precursor to be used as source materials in the subsequent crystal growth experiment. This pre-treatment was run in the tubular furnace gradually heated up to 700°C and left for about 48 hours, similarly to Bernardini et al. [64] and Schorr et al. [68].

The ampoules containing the precursor material and the transporting agent were first subjected to a strong temperature gradient in order to allow the complete reaction of the precursor material with the I_2, as reported by Hönes et al. [73]. During this step, the material migrates towards the cold end of the ampoule where it forms a cluster homogenized on the atomic scale (Fig. 6.1.3a). Secondly, a reversed temperature gradient of appropriate magnitude was applied. The material migrates at the opposite end of the ampoule, where it should form single crystals (Fig. 6.1.3b).

The effects of temperature gradient and two different I_2 loads on the crystal habit and composition were explored. Table 6.1.1 summarizes the investigated growth parameters together with some results for each run.

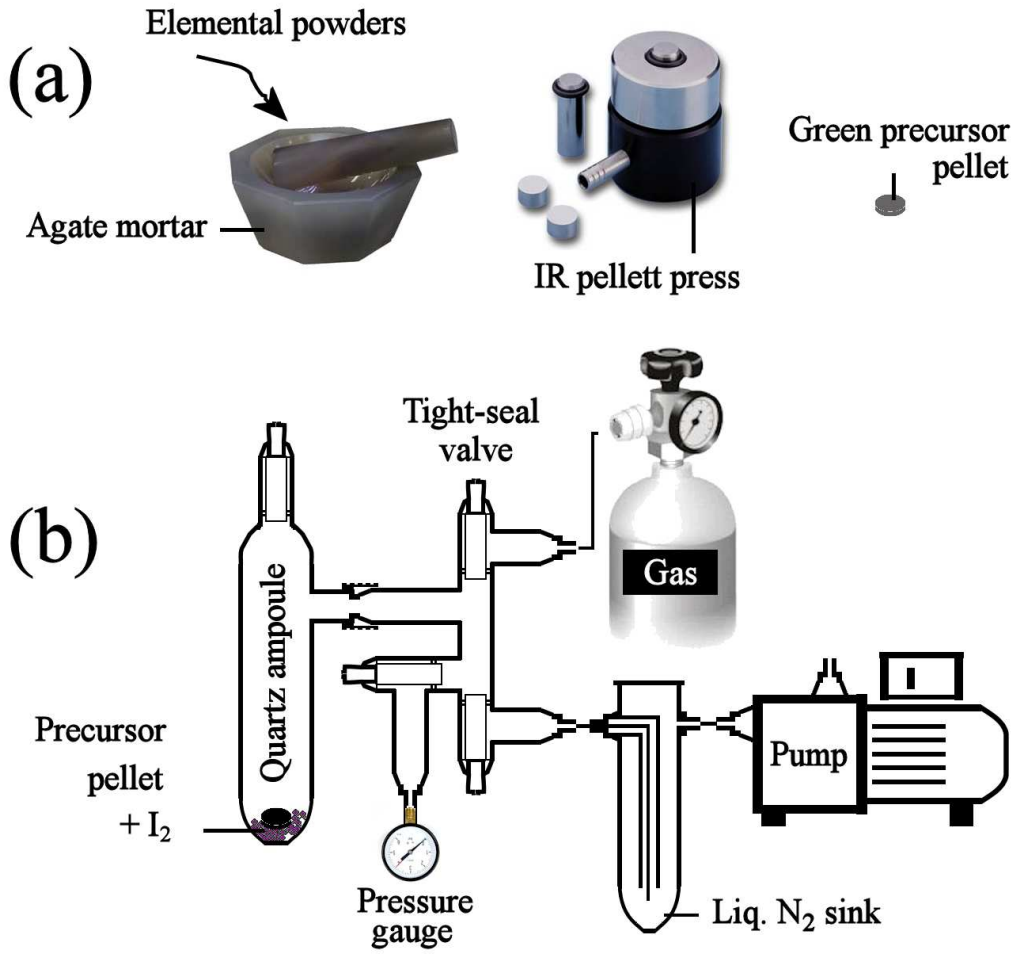

Fig. 6.1.2 Summary of the procedure employed for the crystal growth experiments. Mixing of the elemental precursors by grinding in agate mortar and formation of a green pellet with the aid of an IR pellet press (a). Loading of the precursor plus I_2 into the quartz ampoule attached to a Schlenk line to allow any suitable vacuum/gas purge cycles up to a final background pressure of $5 \cdot 10^{-4}$ bar.

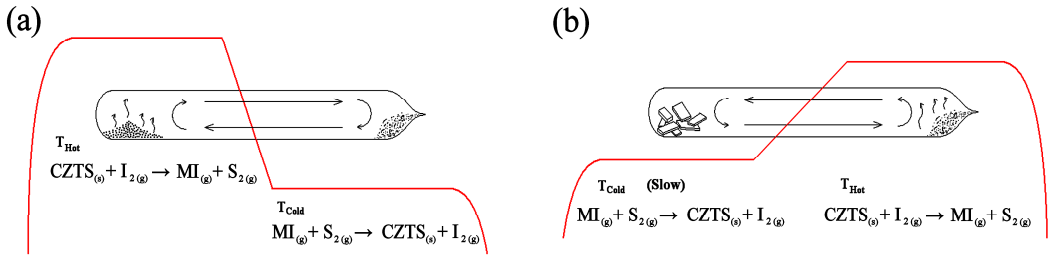

Fig. 6.1.3 Representation of the CVT process sequence with application of a strong temperature gradient for the formation of a homogeneous cluster (a), and actual crystal growth with application of a refined, reversed temperature gradient (b).

Test	Time/h	T_1 /°C	T_2 /°C	ΔT/°C	I_2 load /gcm^{-3}	Gas	Notes, habit and average size
1	168	880	810	70±5	$5\cdot10^{-3}$	N_2	(c) Edge-defined grains (2 mm); amorphous or microcristalline
2	48	880	810	70±5	$5\cdot10^{-3}$	N_2	(c) Edge-defined grains (1-2 mm); amorphous or microcristalline
3	48	850	810	40±5	$5\cdot10^{-3}$	N_2	(c) Edge-defined grains (2-3 mm); dendritic and elongated crystals (up to 10 mm); amorphous or microcristalline
4	24	880	750	130±5	$5\cdot10^{-3}$	N_2	(i) Dendritic crystals (1-2 mm)
5	72	840	840	0±5	$5\cdot10^{-3}$	N_2	Residues of test 3 employed. Lustrous wafer-thin (1-2mm)
6	96	820	750	70±5	$5\cdot10^{-3}$	N_2	(c) Amorphous or microcrystalline
7	72	820	760	60±5	$5\cdot10^{-3}$	N_2	(c) Amorphous or microcrystalline
8	48	820	770	50±5	$5\cdot10^{-3}$	N_2	(c) Amorphous or microcrystalline
9	72	880	750	130±5	$9\cdot10^{-4}$	N_2	(i) Thin needles (4 mm)
10	72	850	810	40±5	$9\cdot10^{-4}$	N_2	(i) Prisms (2 mm) formed at 840°C
11	72	870	820	30±5	$9\cdot10^{-4}$	N_2	(i) Microcrystalline mass
12	72	880	750	130±5	$9\cdot10^{-4}$	Ar	(i) Amorphous or microcrystalline
13	168	880	750	130±5	$5\cdot10^{-3}$	He	(c) Cluster of polycristals
14	24	790	740	50±5	$5\cdot10^{-3}$	He	(i) Cluster of polycristals

Table 6.1.1 Summary of the synthesis trials with parameters considered: duration, temperature of source and growth ends, temperature gradient, I_2 load, inert gas employed. Details on the completeness (c) or incompleteness (i) of the transport and on the resulting habit and average crystal size for each run are also included.

6.2 Compositional and structural characterization

The materials resulting from growth tests No. 3 and 9 were fully analyzed compositionally and morphologically either with an INCA XACT X-ray EDS system connected to a Jeol 6480LV SEM or with an INCA 300 Electron Probe Micro-Analysis (EPMA) connected to a Zeiss EVO 40 SEM (Carl Zeiss SMT Ltd., Cambridge). EDS was conducted using a 1nA probe at 25 keV, and all optimizations were performed against a pure cobalt standard used for further standardization of the collection conditions.

Sufficiently large samples were embedded in Taab Hard LV resin and polished up to a 0.1 μm alumina finish (Streuers) with a Metaserv rotary polishing machine for more accurate estimation of the bulk composition via SEM-X-ray EDS. The same samples were also loaded on a Reichert-Jung ultramicrotome for production of thin sections (< 90 nm). The blocks and ultramicrotome were cooled using liquid nitrogen to minimise local heating of the samples. The slices were analysed with a JEOL JEM1200EXII TEM for Selected Area Electron Diffraction (SAED) and further X-ray EDS analyses using an Oxford Instruments INCA Energy 350 system. Images were acquired using a Gatan Dual View Camera. Featured diffraction measurements were confirmed using a Jeol 2100F at 200 keV.

Other crystals were either Ar ion-milled in a Gatan precision ion-polishing system (PIPS) using a 3-5 kV beam and 6-8 degree gun angle, or crushed between mica foils and the fine resulting powder analysed at the TEM (JEOL 2100F FEG) for information on the compositional and structural homogeneity. Due to beam instability, the diffraction and elemental analyses were performed using a Gatan double tilt cryoholder cooled to 77 K and the current density was kept below 15 $pA \cdot cm^{-1}$. Analysis of the diffraction patterns was conducted using Gatan Digital Micrograph and Image J.

Determination of the lattice parameters of the single crystals was performed with a Bruker Nonius Kappa CCD diffractometer. Some samples were also analysed with a Gemini A Ultra (Oxford Instruments) in order to establish the crystal facets associated with the most convenient growth mechanisms under the different experimental conditions.

6.3 Results of Chemical Vapour Transport Experiments

6.3.1 Summary of experimental results

The thermochemistry of possible chemical vapour transport phenomena in the Cu-Zn-Sn-S-I system was analysed in chapter 5. It was proposed that the volatile components taking part to the CVT are the iodides of Cu, Zn and Sn, and elemental sulfur vapour. In such circumstances, the crystallization of Cu_2ZnSnS_4 may take place through reaction 6.3.1 (the reverse of reaction 5.6.1).

Reac. 6.3.1 $2/3(CuI)_{3(g)}+ZnI_{2(g)}+SnI_{2(w+1)\,(g)}+4/yS_{y(g)}\rightarrow Cu_2ZnSnS_{4(s)}+2(3+w)/xI_{x(g)}$

Such an overall reaction may well occur in a series of more complicated reaction steps. Nonetheless, under the conditions investigated, a net mass transport was observed from high to low temperature zones of the quartz ampoule, suggesting a negative enthalpy associated with reaction 6.3.1, consistent with the thermochemical computation reported in section 5.6.

Among the empirical growth conditions investigated and summarised in Table 6.1.1, the runs that resulted in the synthesis of single crystalline material of reasonable size (major axis > 2 mm) are experiments No. 9 and 3, on which the characterizations were focused (Figs. 6.3.2 and 6.3.3 respectively). These are reviewed in detail in Table 6.3.1, together with experiment No. 5, 12 and the examination of the transport residues of experiment No. 9, which deserved further attention. Fig. 6.3.1 shows the photographs of the materials obtained in the experiments listed in Table 6.3.1.

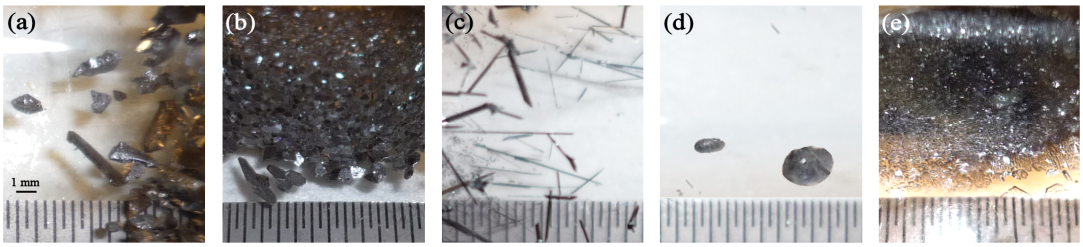

Fig. 6.3.1 Materials resulting from the growth tests as listed in Table 6.3.1. Experiment No. 3 (a), 5 (b), 9 at T_2 (c), 9 at T_1 (d) and 12 (e).

Test No.	**3 (growth) T_2**	**5 (isothermal)**	**9 (growth) T_2**	**9 (source) T_1**	**12 (growth) T_2**
Background gas	N_2	N_2	N_2	N_2	Ar
Ampoule i. d. / mm	23	23	23	23	23
Ampoule length / mm	160	160	160	160	160
Duration / days	48	72	72	72	72
T_1 /°C	850	840	-	880	880
T_2 /°C	810	840	750	-	750
ΔT /°C	40±5	0±5	130±5	130±5	130±5
I_2 load / gcm^{-3}	$5 \cdot 10^{-3}$	$5 \cdot 10^{-3}$	$9 \cdot 10^{-4}$	$9 \cdot 10^{-4}$	$9 \cdot 10^{-4}$
I_2 load / precursor load (molar ratio)	2.48	2.48	0.44	0.44	0.44
Grashof number	$4.8 \cdot 10^4$	0	$5.0 \cdot 10^3$	n/a	$5.0 \cdot 10^3$
Schmidt number	1.82	1.82	1.79	n/a	1.79
Rayleigh number	$8.7 \cdot 10^4$	0	$9.0 \cdot 10^3$	n/a	$9.0 \cdot 10^3$
Longitudinal diffusive share of transport [363]	0.19	∞	0.59	n/a	0.59
Source material employed	Green pellet	Result of experiment 3	Pre-treated pellet	Pre-treated pellet	Pre-treated pellet
Habit	Elongated crystals free from the ampoule's walls and edge-defined crystals	Wafer-thin lustrous crystals attached to the ampoule's walls	Thin needles free from the ampoule's walls	Hemispherical lump attached to the ampoule's walls	Amorphous or microcrystalline mass
Mean size / mm	2-3	1-2	4	3	< 0.5
Composition (SEM-EDS)	$Cu_{2.0\pm0.1}Zn_{1.0\pm0.1}Sn_{1.0\pm0.0}S_{4.0\pm0.1}$ $Cu_{2.2\pm0.0}Zn_{1.0\pm0.0}Sn_{2.4\pm0.1}S_{10.4\pm0.1}$ CuI, ZnS	n/a	$Cu_{1.9\pm0.1}Zn_{0.9\pm0.0}Sn_{1.0\pm0.0}S_{4.1\pm0.1}$ CuI	$Cu_{2.0\pm0.0}Sn_{1.0\pm0.0}S_{3.0\pm0.0}$(Zn traces) CuS CuI	n/a
Lattice parameters (XRD)	a = b = 5.421(1) Å c = 10.819(3) Å volume = 318 Å^3 α = β = γ = 90 ° c/(2a) = 0.998	n/a	a = b = 5.4290(2) Å c = 10.8340(4) Å volume = 319 Å^3 α = β = γ = 90 ° c/(2a) = 0.998	n/a	n/a
Lattice parameters (SAED)	a = b= 5.55 Å c = 10.52 Å volume = 324 Å^3 α = β = γ = 90 ° c/(2a) = 0.948 (at 77 K)	n/a	a = b = 5.67 Å c = 11.48 Å volume = 369 Å^3 α = β = γ = 90 ° c/(2a) = 1.012 (at 298 K)	n/a	n/a
Relevant figures	3a, 4a-i	3b	3c, 5a-c,h-i	3d, 5d-g	3e
Relevant literature of CZTS lattice parameters from different synthesis routes (XRD)	CVT single crystal: a=b= 5.427, c=10.848, volume= 319 Å^3				Schäfer et al. [358] (1974)
	CVT single crystal: a=b= 5.435, c=10.843, volume= 320 Å^3				Guen et al. [364] (1979)
	Salt flux single crystal: a=b= 5.434(1), c=10.856(1), volume= 320 Å^3				Bonazzi et al. [65] (2003)
	Powder sol. st. reaction: a=b= 5.428(2), c=10.864(4), volume= 320 Å^3				Schorr et al. [68] (2007)

Table 6.3.1 Summary of transport conditions for the most significant growth experiments (No. 3, 5, 9 and 12) and compositional/structural properties of the relevant materials obtained (n/a= not applicable/analysed). The CZTS lattice parameters from relevant XRD literature are also reported for comparison.

6.3.2 Experiment No. 9: growth with iodine load of $9 \cdot 10^{-4}$ gcm^{-3}

Fig. 6.3.2 shows collections of images for growth experiment No. 9. This test was run with a load of iodine corresponding to $9 \cdot 10^{-3}$ grams per cm^3 of the internal ampoule volume. A temperature gradient of 130 °C was employed in this experiment (T_1 = 880 °C, T_1 = 750 °C). Fig. 6.3.2a shows the visual appearance of the ampoule at the end of the growth test lasting 72 hours.

Despite the larger gradient and the longer duration of the experiment, the transport of material was incomplete. Needle-shaped crystals were formed at the cold end, as shown in Fig. 6.3.2b-c, while lumps of nutrient material were left at the source end of the ampoule (Fig. 6.3.1d). The needle-shaped crystals display very neat edges and elongated shape (1D predominance).

Similarly to growth test No. 3, traces of CuI crystals could be detected on the samples surface, although in smaller amount.

Fig. 6.3.2i is the SAED pattern of the ion-milled crystal on the [-110] zone axis. The lattice parameters obtained from SAED are reported in Table 6.3.1. The diffraction is consistent with previously reported tetragonal forms of CZTS. The Kikuchi lines were highly visible during tilting from one zone axis to another, revealing that the sample was thick enough to be unaffected by the electron beam in such conditions.

Figs. 6.3.2d-f are SEM-BSE micrographs of the hemispherical residue left at the source side of the quartz ampoule at the end of the transport experiment. It is possible to distinguish clearly four areas with different signal intensity. The black areas are voids and Fig. 6.3.2d shows that such porosity is concentrated in the inner part of the lump, with pores that extend radially towards the surface, delimiting grains with elongated shape. The EDS spectra of the three remaining areas are reported in Fig. 6.3.2g. The highly scattering brittle phase (white) has composition consistent with the formula CuI (with ~ 10 at. % O contaminations), the dominant grey phase has formula Cu_2SnS_3 (with residues of I < 1 at. %) and the low scattering phase (dark grey) is consistent with CuS (with Al and I contaminations < 2 at. %). The outer surface of the lump is surrounded by a 40 μm thick crust of CuI, which is also present in the bulk of the lump filling the spaces left by the dominant Cu_2SnS_3 phase. The CuS phase shows a high degree of porosity and is segregated over a band area in the middle of the dominant Cu_2SnS_3 phase between the voids in the centre of

the lump and the outer surface. A gradient of Zn concentration was found in the Cu_2SnS_3 phase from the inner to the outer part of the hemispheric lump, with a remarkable Zn concentration up to 6 at. % in the area between the CuI outer crust and the CuS-rich band, as shown in Fig. 6.3.2e.

Despite the low heating rate employed, the pre-treatment of the source material caused the Zn to be partially lost, owing probably to the large volume of the ampoule employed (same dimensions as for the crystal growth) [365]. Interestingly, under the growth conditions of experiment No. 9, in spite of the off-stoichiometry of the source material, the crystals grown at the cold end of the ampoule have composition consistent with the formula Cu_2ZnSnS_4, and no traces of the ternary Cu_2SnS_3 were found.

Fig. 6.3.2 Collection of images relative to the growing test No. 9 (cfr. Table 6.3.1, Figs. 6.3.1c-d). View of the quartz ampoule at the end of the experiment (a). SEM micrographs of typical needle shaped crystals (b-c). Cross sectional BSE micrographs of the hemispherical residue left at the hot end (d-f) with pronounced compositional contrast between the three phases present for which EDS spectrum with a 20 keV electron beam is reported (g). TEM bright field image of the edge of an ion-milled crystal (h) and its SAED pattern on the [-110] zone axis nominally at room temperature (i).

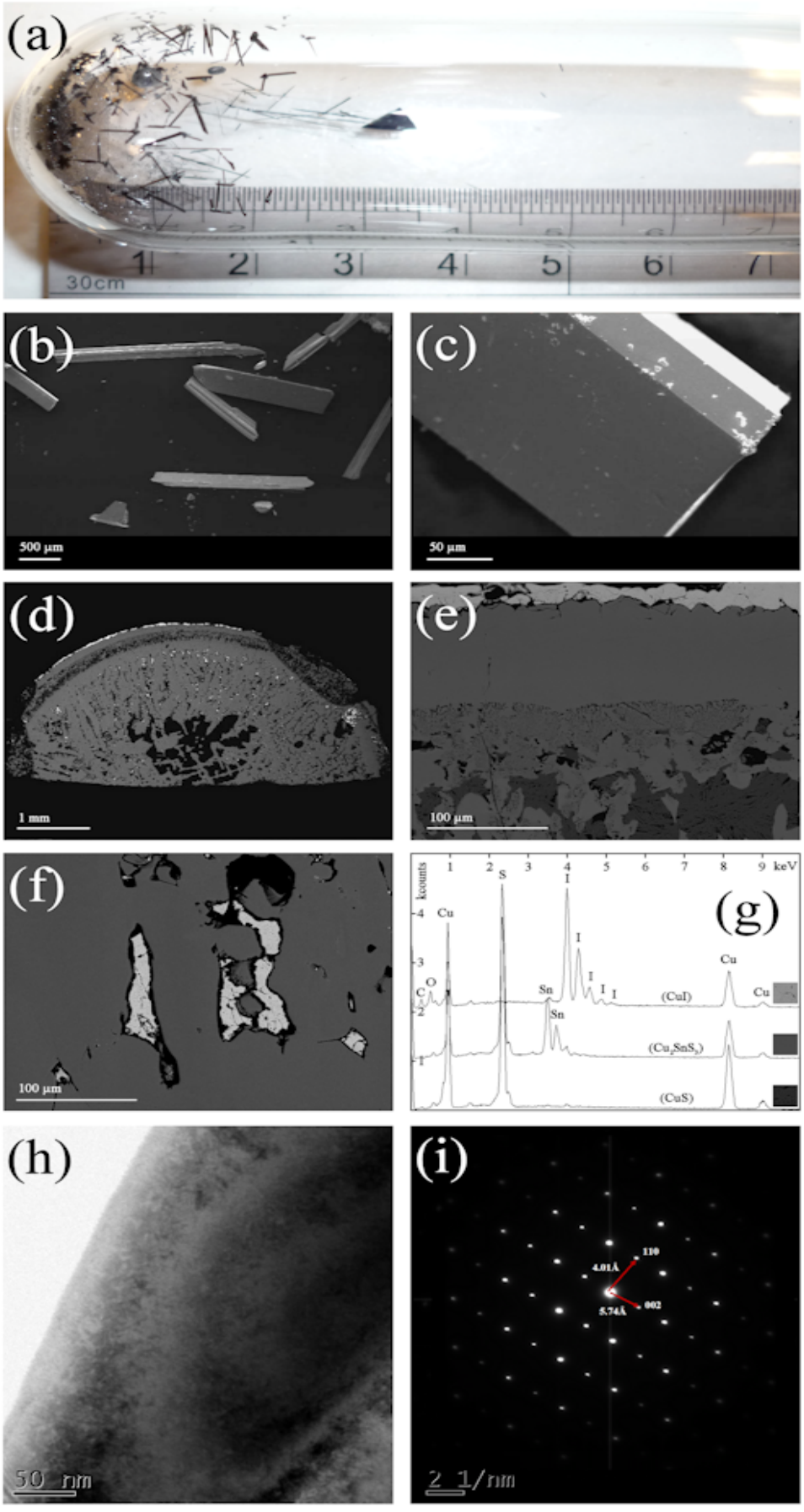
(a)
30cm
(b)
500 µm
(c)
50 µm
(d)
1 mm
(e)
100 µm
(f)
100 µm
(g)
keV
Cu
S
I
Sn
O
C
(CuI)
(Cu2SnS3)
(CuS)
(h)
50 nm
(i)
110
4.01Å
002
5.74Å
2 1/nm

6.3.3 Experiment No. 3: growth with iodine load of $5 \cdot 10^{-3}$ gcm^{-3}

Fig. 6.3.3 shows a collection of images for growth experiment No. 3. This test was run with a load of iodine corresponding to $5 \cdot 10^{-3}$ grams per cm^3 of the internal ampoule volume (more than 5 times the amount employed for test No. 3). A temperature gradient of 40 °C was employed in this experiment (T_1 = 850 °C, T_1 = 810 °C). Fig. 6.3.3a shows the visual appearance of the ampoule at the end of the 48 hours of treatment. Fig. 6.3.3b shows the morphology of a typical edge-defined grain crystal, a reasonably even 3D growth was obtained. Part of the crystal surface is depicted in Fig. 6.3.3c, where the compositional variation is highlighted by the EDS mapping of the emission lines of the relevant elements under a 20 keV electron beam ($K_{\alpha 1(Cu)}$, $K_{\alpha 1(Zn)}$, $L_{\alpha 1(Sn)}$, $K_{\alpha 1(S)}$, $L_{\alpha 1(I)}$). The resulting picture shows the presence of three phases: a substrate phase consistent with the composition Cu_2ZnSnS_4 (green), covered by crystals of ZnS (orange) and CuI (blue).

In order to get insights into the growth sequence, some of the crystals were embedded in hard resin and polished on random orientations as to examine the core morphology and composition. The cross sectional morphology of the crystals shows that the bulk structure is rather defective with abundant voids of size up to 20 μm (Fig. 6.3.3e).

The micro-scale compositional uniformity was assessed on the carbon-coated specimens via backscatter electron composition imaging and EDS point analyses at the SEM. Evidence of the high compositional uniformity is given by the BSE micrograph shown in Fig. 6.3.3g which was taken deliberately at very high contrast in order to enhance the compositional variation. The comparison with the secondary electron image in Fig. 6.3.3f shows contrast attributable to polishing artefacts rather than elemental inhomogeneity.

A CASINO V2.42 [366] simulation of the 20 keV electron beam trajectories in bulk Cu_2ZnSnS_4 was run in order to estimate the interaction volume that defines the spatial resolution of the point EDS analyses (Fig. 6.3.3d). The microprobe analyses performed this way on numerous points randomly distributed reveal a standard deviation lower than 1 at. % for each element present.

The nano-scale compositional uniformity was estimated via TEM-EDS on 90 nm thin slices of crystals cleaved from the embedded samples. Morphological analysis at the TEM shows the presence of domains with different contrast on the order of 20

nm; however, no appreciable compositional and structural differences were revealed either by EDS or SAED. TEM-EDS analyses performed at room temperature under beam currents higher than 25 $pAcm^{-1}$ revealed compositions that were consistently poorer of Sn and S in the ratio 1:2 compared to the SEM-EDS analyses. This is consistent with the evolution of $SnS_{(g)}$ and $S_{2(g)}$ from $Cu_2ZnSnS_{4(s)}$ in high vacuum [154] due to local heating by overexposure to the high energy electron beam (120 keV). Due to this unavoidable reaction, only the Cu:Zn compositional ratio can be considered as a reliable figure. Such ratio was found to be roughly 2:1. If the specimens were kept cool in a double-tilt filter at 77 K, no change in composition was observed even after prolonged beam exposure and the SAED interrogation revealed a consistent tetragonal structure throughout the samples (Fig. 6.3.3i). The lattice parameters as obtained from SAED are reported in Table 6.3.1.

Fig. 6.3.3 Collection of images relative to the growing test No. 3 (cfr. Table 6.3.1, Fig. 6.3.1a). View of the quartz ampoule at the end of experiment (a). SEM micrograph of a typical edge-defined crystal (b) and EDS compositional map of its surface (c) (blue: CuI; orange: ZnS; brown: Cu_2ZnSnS_4). CASINO V2.42 [366] simulation of interaction volume for 20 keV electrons with bulk Cu_2ZnSnS_4 (d). SEM micrograph of a polished crystal as seen from secondary electron (e-f) and BSE (g) detectors. TEM bright field micrograph of 90 nm thin slices of a crystal (h) with its SAED pattern at 77 K (i).

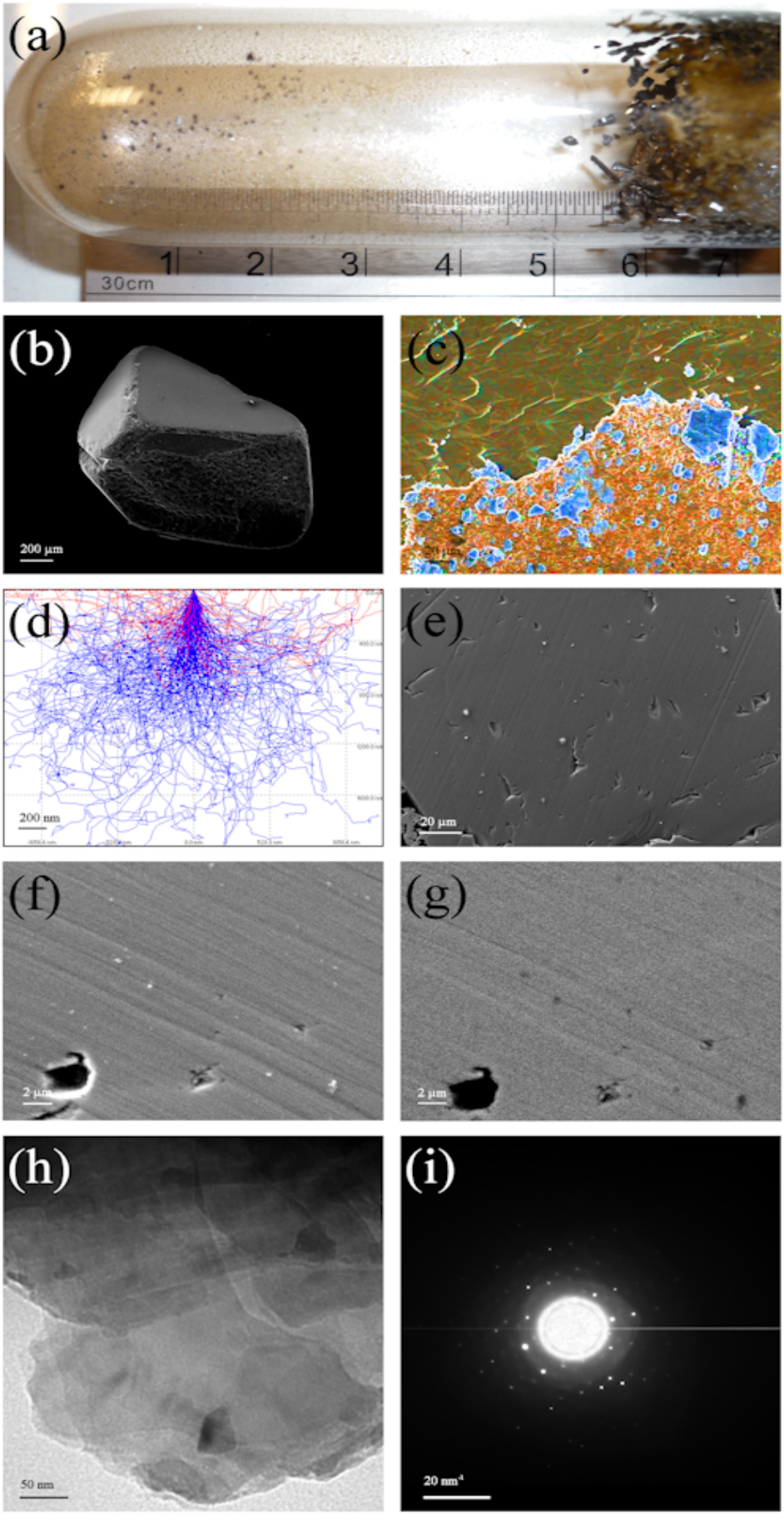
(a)
1
2
3
4
5
6
7
30cm
(b)
200 µm
(c)
(d)
200 nm
(e)
20 µm
(f)
2 µm
(g)
2 µm
(h)
50 nm
(i)
20 nm⁻¹

6.4 Discussion of preferential crystallization

In all experiments the crystallization of CZTS material (reaction 6.3.1) occurred at the position of the ampoule corresponding to the minimum of the longitudinal temperature profile for each run as assessed with the quartz dummy reactor. It was observed that even a well of just 5 °C was enough to induce preferential crystallization. Therefore, it was concluded that the enthalpy change associated to reaction 6.3.1 is negative, i.e. heat is released when Cu_2ZnSnS_4 crystallizes from the gaseous iodides of Cu, Zn and Sn under the experimental conditions tested. Furthermore, it was observed that the crystallization occurred preferentially on the walls of the ampoule for test No. 3 (Figs. 6.3.1a, 6.3.3a) and free from them if the iodine load was reduced, as for test No. 9 (Figs. 6.3.1c, 6.3.2a). Quenching of these two growth tests at regular time intervals followed by observation of the ampoules revealed two different means of transport. For test No. 3 a series of decomposition/crystallization steps took place throughout the length of the ampoule, while test No. 9 showed a direct transport from the hottest to the coldest end of the ampoule. From a rough estimation of the ampoule pressure for the two cases (~1.8 vs. ~0.32 bar for experiments No. 3 and 9 respectively, calculated based on PV=nRT with T=mean absolute temperature within the ampoule for each experiment), this behaviour is qualitatively consistent with the predictions of Zuo et al. [367] on the transition between a diffusion-dominated to a convection-dominated regime of mass transport in the system ZnS-I_2. The computed Grashof *Gr*. (Eq. 6.4.1), Schmidt *Sc*. (Eq. 6.4.2) and Rayleigh *Ra.* (Eq. 6.4.3) fluid numbers (Table 6.3.1) suggest that the longitudinal convective share of transport (that we name after Klosse et al. [363]) *Kl.* (Eq. 6.4.4) for test No. 3 is about three times higher than for test No. 9.

Eq. 6.4.1 $$Gr. = d^3 g\beta\rho^2\Delta T / \eta^2$$

Eq. 6.4.2 $$Sc. = \eta/(\rho D)$$

Eq. 6.4.3 $$Ra. = g\beta C_p(\Delta T)l^3 \big/ (10 \cdot \eta k)$$

Eq. 6.4.4 $$Kl. = 1/[a \cdot (Sc.Gr.)^{-2} + b]$$

where d and l are the ampoule diameter and length expressed in cm, g is the acceleration due to gravity ($9.81 \cdot 10^2$ cm·s^{-2} on the Earth's surface), β is the volumetric thermal expansion coefficient expressed in K^{-1}, ρ is the density expressed in g·cm^{-3}, ΔT is the temperature difference between source and growth ends of the ampoule expressed in K, η is the absolute viscosity (a.k.a. dynamic viscosity) expressed in g·cm^{-1}·s^{-1}, D is the diffusion coefficient expressed in cm^2·s^{-1}, C_p is the specific heat capacity expressed in J·kg^{-1}·K^{-1} and k is the thermal conductivity expressed in W·m^{-1}·K^{-1}. The dimensionless quantities a and b are functions of the ampoule aspect ratio l/d. The magnitudes of a and b can be obtained from the graph in Appendix 7 taken from Klosse et al. [363].

The *Kl*. number introduced by Klosse et al. [363] and computed by Eq.6.4.4 reflects the competitive behaviour between diffusion and thermal convection in CVT crystal growth experiments [363]. Eq. 6.4.4 can be divided in two terms: $a \cdot (Sc.Gr.)^{-2}$ and b. The first term is a measure of the diffusion contribution and the second term of the convection contribution to the overall mass transport in the CVT experiment.

In the present work, both experiments No. 3 and 9 show $a \cdot (Sc.Gr.)^{-2} << b$. Therefore, according to the analytical model of Klosse et al. [363], both experiments should be considered under convection-dominated regimes of mass transport. Furthermore, in the present study the Rayleigh numbers exceed $4 \cdot 10^3$, a value above which a strong deterioration of the crystal quality has been reported by Böttcher et al. [368] in CVT of the system ZnSe-I_2.

The fact that the crystals obtained from experiment No. 9 had very well defined morphology seems in contradiction with Klosse's suggestions [363] and Böttcher's findings [368]. However, this can be explained on the basis of the applicability range of Klosse's model [363]. As already pointed out in section 5 [360], with iodine concentrations below certain values, the transport rate is likely to be governed by the rate of heterogeneous reaction of source vaporisation, rather than by diffusion, regardless of the temperature gradient applied. We believe that this is most probably the case for test No. 9. Indeed, at the end of experiment No. 9, the mass transport from the hot to the cold end of the ampoule was incomplete. EDS microstructure analysis was performed on the residues of the source material (Figs. 6.3.1d and 6.3.2d-f) in order to gain information on the mechanism of CVT. The interpretation that can be drawn is as follows. Under the experimental conditions of experiment No. 9, at the source end (T_1 = 880 °C) the Zn poor CZTS precursor is mainly liquid (m.p.

Cu_2SnS_3 ~ 837 °C [369]). This allows the Zn atoms (limiting reagent) to diffuse easily through the droplet towards the surface where they are captured by the $I_{2\,(g)}$ to form $ZnI_{2\,(g)}$. The other metals also react with iodine and the formation of nearly stoichiometric CZTS at the cold end withdraws the mixture of gaseous iodides until there is enough Zn to be extracted from the source. The CuI formed by reaction of the CZTS precursor with I_2 is also present as a liquid phase at the test temperature (m.p. = 605 °C [369]). During cooling, the matrix of Cu_2SnS_3 at the source end crystallizes in elongated grains, the molten CuI remains trapped at the grain boundaries and the shrinkage due to its solidification causes this phase to be surrounded by voids. The Zn concentration gradient left in the source material is opposite to what it would be expected if Zn were to be selectively leached at the surface of the droplet. The heterogeneous reaction occurring at the interface between gaseous I_2 and condensed source material, should lead to a Zn-poor surface and a Zn-rich core. There appears to be no obvious explanations for such observation. No traces of ZnI_2 (b.p = 726 °C), SnI_4 (b.p = 353 °C) and SnI_2 (b.p = 717 °C) were found in the solid residue of the source material, as their boiling points are lower than the solidification temperature of Cu_2SnS_3. The fact that these iodides are not detected at the cold end too, is consistent with their lower thermodynamic stability compared to CuI, as resulting from the computation in chapter 5.

Comparison of the EDS analyses of the main (CZTS) sinks for experiments No. 3 and 9 reveal that the composition is nearly unaffected by the I_2 pressure within the ampoules (cfr. Table 2), although increased amounts of secondary phases were detected when the larger I_2 load was employed. Despite the lower iodine load and the Zn deficiency of the source material of test No. 9, no Cu_2SnS_3 was detected by EDS at the cold end of the ampoule. This suggests that, to a reasonable extent, the system shows the tendency to self-adjust the crystal growth as to produce the most stable phase (in this case Cu_2ZnSnS_4) so long as sufficient amounts of each component (e.g. Zn) are available at the source end. This self-regulatory behaviour occurs despite the fact that the reactions between the binary sulfides and iodine to form the unary iodides of Cu, Zn and Sn have very different thermodynamic equilibrium constants, as it is shown in Fig. 5.4.4.

With the intent to ascertain whether it is possible to enlarge the bigger crystals at the expenses of the smaller ones on the same principle of the Ostwald ripening [370], an isothermal treatment at 840 °C was conducted on the resulting mass of experiment No. 3 (test No. 5, cfr. Table 6.3.1). If the “ideal equilibrium” were to be reached, the

(few) well formed crystals should grow further until a single - nearly perfect - crystal is formed. The treatment was prolonged up to 72 hours and lead to the formation of highly lustrous wafer-thin edge-defined crystals with average size 1-2 mm, which adhered strongly to the ampoule's walls, as shown in Fig. 6.3.1b (2D predominance). During this experiment, relatively large crystals with pronounced development in the three dimensions (experiment No. 3, cfr. Fig. 6.3.1a) were slowly eroded and converted into crystals where the third dimension is strongly reduced (Fig. 6.3.1b). It is apparent that the dynamic decomposition/crystallization equilibrium that took place during test No. 5 resulted in the transport of mass towards the walls of the ampoule, rather than contributing to the growth of bulk crystals (free from the walls). This behaviour is opposite to that described by Szczerbakow et al. [371] in the self-selective vapour growth (SSVG) of bulk crystals. The key principle of the SSVG is shown in Fig. 6.4.1 [371].

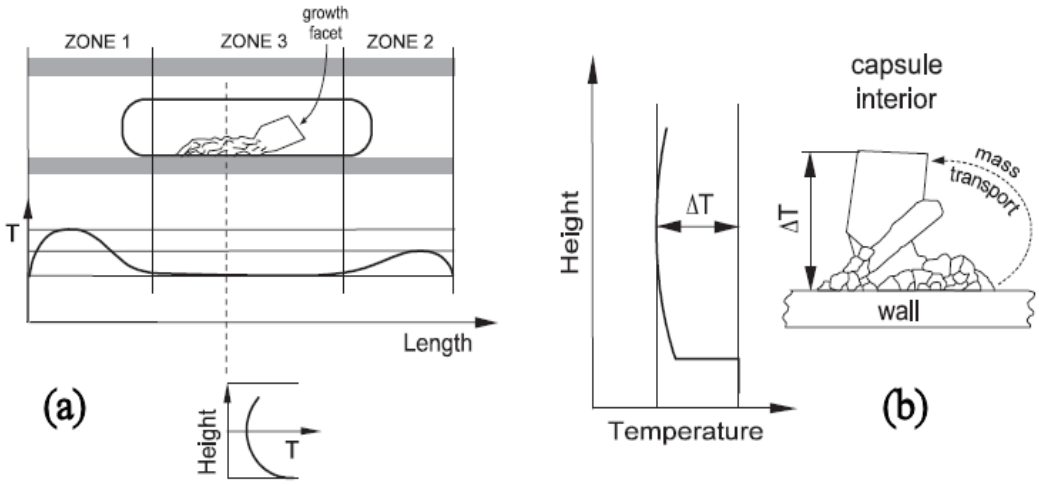

Fig. 6.4.1 Schematic representation of the principle governing the self-selective vapour growth of bulk crystals, modified from Szczerbakow et al. [371].

The SSVG experiment is a sealed tube technique suitable for materials with appreciable vapour pressure, where the source of polycrystalline material acts as the self-seed for further growth. The growth ampoule is statically inserted into a furnace where small but carefully adjusted temperature gradients are set (Fig. 6.4.1a). As shown in Fig. 6.4.1b, growth of single crystals with this technique is based on the active cooling by thermal radiation of the growth front respectively via application and natural occurrence of longitudinal and transversal temperature fields [372].

In the present work, the radial temperature profile is expected to be similar to the one shown in Fig. 6.4.1b, i.e. higher on the ampoule's walls (in direct contact with the heated furnace) and lower at the centre of the ampoule (away from the source of heat). Similarly to the condensation taking place in the SSVG that involves the latent heat of phase change, in the present work it is inferred that reaction 6.3.1 releases heat (this can be deduced from the observed direction of transport). In both cases this heat needs to be released and dissipated in the vicinity of the process for the crystallization to take place. Therefore, in both cases (SSVG and our CVT) the lower the temperature the higher is the thermodynamic driving force for crystallization. In CVT experiments with negative enthalpy of crystallization, a well formed crystal pointing towards the inner part of the ampoule (where the temperature is lower) should act as a good self-seed, as in the case of SSVG (Fig. 6.4.1a). Further growth should take place on its surface, until all the smaller, more defective crystals on the ampoule's wall are thoroughly consumed. However, SSVG and CVT differ in terms of the rate of mass transport. For experiment No. 3 (I_2 load of $5 \cdot 10^{-3}$ gcm^{-3}) the rate of transport was found to be considerably higher than in a typical SSVG experiment [371] ($\geq$ 0.17 gh^{-1} vs.0.02 mmh^{-1}). This is not surprising, since CVT is based on active mass transport ensured by the formation of volatile components, while in SSVG it depends solely on the (generally low) vapour pressure of the compound being grown [371].

Under isothermal conditions at high temperature (e.g. during experiment No. 5), a dynamic equilibrium is expected to take place, in which an equal number of moles of CZTS crystallize than they react to form the elemental iodides. The decomposition/crystallization rate under steady state conditions is ultimately dependent upon the concentration of free I_2 and S_2 in the system, as per reaction 6.4.1.

Reac. 6.4.1 $2/3(CuI)_{3(g)}+ZnI_{2(g)}+SnI_{2(w+1)\,(g)}+4/yS_{y(g)} \rightarrow Cu_2ZnSnS_{4(s)}+2(3+w)/xI_{x(g)}$

From the kinetic standpoint under steady state conditions, higher I_2 concentrations correspond to higher decomposition/crystallization rates of CZTS, meaning that more heat needs to be absorbed and released per time unit.

It is known that heat transfer by thermal conduction through the volume of growing crystals can lead to a reduction of the crystal growth rate as growth proceeds [371]. For example, conventional vapour growth methods like the Piper-Polich [373]

and the Markov-Davydov [374] are self-limiting in this sense, because the growth front is located at the hottest part of the crystal. Nevertheless, the inversion of the sign of the growth rate observed in experiment No. 5 (namely, crystal consumption) deserves some attention.

The transversal profile of thermal conductivity in our experimental setup is such that a more effective heat extraction can be attained by the ampoule's walls rather than by large crystals surrounded by the complex mixture of reacting gases (Fig. 6.4.2). It is reasonable to assume that under the conditions investigated in experiment No. 5, the position on the system's surface corresponding to the most effective path for heat extraction is the one showing preferential crystallization of CZTS. On the other hand, due to the lower I_2 pressure employed, experiment No. 9 is likely to display a lower decomposition/crystallization rate than experiments No. 3 and 5. A lower reaction rate at the steady-state equilibrium means that a reduced amount of heat needs to be exchanged per time unit. If the reaction rate at the steady state equilibrium is low enough for the heat to be effectively dissipated in the vicinity of the process, reaction 6.4.1 has the tendency to occur preferentially on the crystal's surface that remains cooler than the ampoule's walls. In such circumstances, crystal growth prevails on nucleation (experiment No. 9) or the bigger pre-existing crystals are stable against the action of I_2 and will further grow self-selectively at the expense of the smaller ones. If the opposite is true (under high rates of decomposition/crystallization), crystals free from the walls may have the tendency to be dissolved and a net mass transport may occur towards the ampoule's walls, where heat can be readily dissipated (experiment No. 5). These two different cases are shown schematically in Fig. 6.4.2, where the transversal profiles of temperature and thermal conductivity in the ampoule system are depicted.

Fig. 6.4.2 shows a schematic representation of the consequences of CVT under steady state equilibrium in longitudinally isothermal conditions (cfr. experiment No. 5, Table 6.3.1). The two scenarios with different directions of transport are depicted in proximity of the ampoule's walls respectively towards (a) and from (b) a well developed 3D crystal. The transversal profiles of temperature and thermal conductivity across the media in the closed ampoule are such that a more effective heat exchange is shown by the ampoule's walls in contact with the furnace's wall.

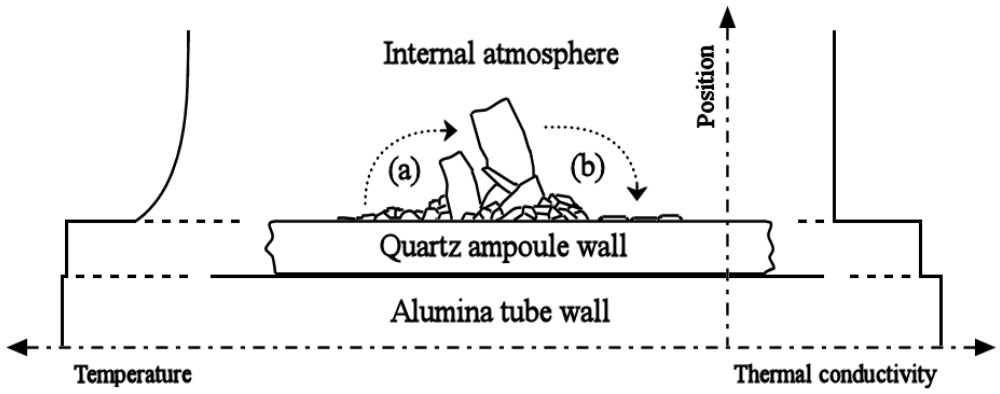

Fig. 6.4.2 Proposed chemical vapour transport scenarios under low (a) and high (b) rates of decomposition/crystallization during longitudinal isothermal treatment (a negative enthalpy change during crystallization is assumed, as in the present work). Transversal profiles of temperature and thermal conductivity (rough guides) of the experiment in proximity of the ampoule's and furnace's walls are superimposed.

As long as the rate of decomposition/crystallization is relatively small (under relatively low iodine and sulfur pressures) crystal growth occurs at the surface of bigger crystals at the expense of the smaller ones (Fig. 6.4.2a). If the decomposition/crystallization rate is comparatively higher (under higher iodine and sulfur partial pressures) the material is preferably transported towards the ampoule's walls, with the consumption of the 3D crystals and formation of 2D crystals that strongly adhere to the foreign surface (Fig. 6.4.2b).

The proposed explanation is consistent with the fact that bulk 3D CZTS crystals free from the walls were obtained during test No. 3 (Fig. 6.4.2a), despite the iodine and sulfur partial pressures employed were the same as for experiment No. 5 (where 2D crystal formation prevailed, as depicted by Fig. 6.4.2b). It is likely that the 3D crystals resulting by quenching of test No. 3 were formed before (or just after) the steady state equilibrium was reached, i.e. when part of the I_2 was sequestered (or just released) by the material to be transported from the higher temperature side. In such conditions (test No. 3), the effective I_2 pressure experienced by the material at the growth end is lower than it would be under steady state conditions (test No. 5). This translates into a lower decomposition/crystallization rate at the growth end during the early stages of chemical vapour transport (test No. 3), a conditions where the scenario in Fig. 6.4.2a is more favourable. Vice-versa, the very same ampoule left under prolonged isothermal conditions (test No. 5) allows the growing material to

experience the full iodine pressure, resulting in the opposite scenario being more favourable (Fig. 6.4.2b).

A 2D crystallization behaviour similar to the one observed for test No. 5 has been reported by Ciszek [375] for the synthesis of $CuInSe_2$ via I_2 vapour transport. During his experiments, typically lasting 120 hours, he failed to induce preferential crystallization using the cold finger seeding technique. On the contrary, the mass transport resulted in the formation of several morphologies, with the most favourable being in the form of (112) surface platelets. No explanation for the preferential crystallization of $CuInSe_2$ on the surface of the ampoule's walls rather than on the seed was provided by Ciszek [375]. The similarity between Ciszek's experiment and test No. 5 of the present investigation suggests that the proposed explanation (based on the high rate of decomposition/crystallization at the steady state equilibrium and on the most effective path for heat dissipation) could apply to both cases.

Similarly, it is explained why with lower I_2 loads (test No. 9, cfr. Table 6.3.1, Figs. 6.3.1c, 6.3.2a) the crystallization occurred preferentially free from the ampoule's walls rather than at their surface. Furthermore, test No. 12 (cfr. Table 6.3.1) was run under the same conditions of test No. 9 but using Ar instead of N_2 as the background gas. This choice lead to the formation of an amorphous or microcrystalline mass, as shown in Fig. 6.3.1e. This behaviour seems consistent with the lower thermal conductivity of the atmosphere inside the ampoule.

An investigation of the possible mechanisms followed by reaction 6.4.1 may help to understand further the different preferential crystallizations observed in Ciszek's and the present study (tests No. 3, 5, 9 and 12). Reaction 6.4.1 involves 4 and 2 reactant molecular species in the forward and reverse direction respectively. Reactions with molecularity higher than 2 are quite rare [376], therefore it is reasonable to suppose that the forward reaction may proceed via adsorption of one sulfur molecule or one unary iodide onto a solid surface (either an already formed crystal or the ampoule's walls), followed by collision respectively with either a unary iodide or a sulfur molecule, release of iodine and formation of a binary sulfide nucleus. The reaction can proceed via adsorption of iodide molecules of different type, resulting in the formation of different binary sulfide nuclei. Surface diffusion of such nuclei may be high enough to allow their ordered aggregation into a larger quaternary sulfide nucleus, a process that should be associated with a negative free energy change. In such a mechanism, the first step is the surface adsorption of unary iodides. Chemisorption is known to have a negative enthalpy change and a positive

entropy change [376], therefore colder surfaces are thermodynamically more convenient than hotter ones for this first step to take place. The considerations made earlier about the effective path for heat dissipation apply also to this reaction step. The second step in the proposed mechanism is the collision of a sulfur molecule with the adsorbed unary iodide (or vive versa). The result of an effective collision between these two molecules would be the release of a molecule of I_2 and the creation of a surface binary sulfide nucleus. According to the transition-state theory developed by Eyring [377], this second step requires the formation of an activated transition-state complex with enthalpy greater than the sum of the enthalpy of the reagents or the sum of the enthalpy of the products. Let us concentrate on the crystal growth once nucleation on a foreign surface (e.g. the ampoule's walls) has been already initiated (which is always necessary, unless a self-seeding technique is employed). Depending on the chemical nature of the adsorbent surface (e.g. number and kind of missing coordination) and on the local temperature, the transition-state complex may be more or less stabilised. Every family of crystallographic planes of the growing phase is characterised by a different sequence of atomic population with different surface unfilled bonds, and different thermal conductivities. From the thermodynamic point of view, breaking a bulk crystal to create two new surfaces requires some energy. The free energy change involved depends on the crystallographic direction of the surfaces being created. Therefore, it is clear that when the reverse process takes place (crystal growth) some crystallographic directions of growth are thermodynamically favoured over some others. Nevertheless, depending on the growth conditions during the CVT experiments and especially on the rate of decomposition/crystallization (dependent on the partial pressures of iodine and sulfur), prevalence of crystal facets other than the most thermodynamically stable may be possible.

In the present study, macroscopic indexing of the preferential crystallographic directions of growth for the CZTS samples CVT-grown under different I_2 pressures (experiments No. 3 and 9) was performed. Fig. 6.4.3 shows the results of the indexing analysis performed on a needle-shaped CZTS sample grown under low iodine pressure (experiment No. 9). The very well defined edges shown by this specimen made the assignment procedure straightforward. Unfortunately, this was not the case for the CZTS samples grown under higher I_2 pressure. Due to their less regular shape, assignment of the facets did not provide sensibly low Miller indexes (not shown).

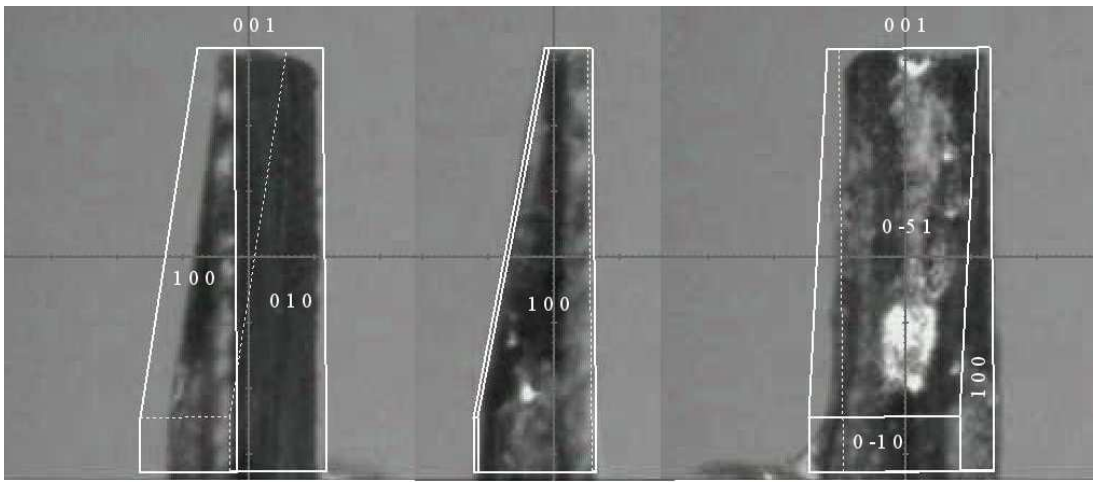

Fig. 6.4.3 Indexing analysis of the very top of a needle-shaped CZTS crystal CVT-grown under $9 \cdot 10^{-4}$ g·cm^{-3} I_2 (test No. 9).

Fig. 6.4.3 shows that the needle-shaped CZTS crystals obtained during experiment No. 9 grow along the (001) crystallographic direction, corresponding to the *c* axis of the *Kesterite* unit cell. Under the conditions investigated with test No. 9. the favoured CZTS facets are: (010), (100) and (0-51). Without a comparison with computational work it is difficult to know if these findings are consistent with a growth mechanism leading to the exposure of the most thermodynamically stable crystal surfaces, or if the crystal shape is the result of a kinetic trade-off.

7. Cu_2ZnSnS_4: *Kesterite* or *Stannite*?

In the present chapter, the results of a collection of analyses performed on the single crystals of CZTS obtained via the chemical vapour transport with I_2 are reported. A range of techniques has been employed to study the structural and electronic properties of the materials.

Section 7.1 presents the results of the powder and single crystal X-ray diffraction performed on CZTS samples CVT-grown under different pressures of iodine (experiments No. 3 and 9, see table 6.3.1). The result of the structural refinement for the assignment of the space group is also shown. Single crystal neutron diffraction analysis of a CZTS sample resulting from experiment No. 3 was also performed with the instrument VIVALDI (very intense vertical-axis Laue diffractometer) at the *Institut Laue-Langevin* in Grenoble (France) [378]. As for the X-ray diffraction analysis, the result of the structure refinement for the assignment of the space group is shown.

Section 7.2 presents the result of the Raman characterization of the CZTS crystals from experiments No. 3 and 9.

Section 7.3 presents the analyses of photoluminescence spectroscopy carried out to study the electronic properties of the CZTS materials synthesized by CVT.

7.1 X-ray and neutron scattering analyses of CZTS crystals

Table 7.1.1 summarises the structural characterizations with electron and X-ray diffraction of CZTS crystals grown via CVT under different loads of I_2.

Test No.	**3**	**9**
I_2 load / g·cm^{-3}	$5 \cdot 10^{-3}$	$9 \cdot 10^{-4}$
Lattice parameters obtained from SAED	$a = b = 5.55$ Å $c = 10.52$ Å volume = 324 Å^3 $\alpha = \beta = \gamma = 90$ ° $c/(2a) = 0.948$ (at 77 K)	$a = b = 5.67$ Å $c = 11.48$ Å volume = 369 Å^3 $\alpha = \beta = \gamma = 90$ ° $c/(2a) = 1.012$ (at 298 K)
Lattice parameters obtained from XRD	$a = b = 5.421(1)$ Å $c = 10.819(3)$ Å volume = 318 Å^3 $\alpha = \beta = \gamma = 90$ ° $c/(2a) = 0.998$ (at 298 K)	$a = b = 5.4290(2)$ Å $c = 10.8340(4)$ Å volume = 319 Å^3 $\alpha = \beta = \gamma = 90$ ° $c/(2a) = 0.998$ (at 298 K)
Space group (XRD)	I-4m2 (No. 119) R = 8.07%	
	I-42m (No. 121) R = 2.63%	I-42m (No. 121)
	I-4 (No. 82) R = 3.14%	
Literature values of CZTS lattice parameters from different synthesis routes (XRD)	$a=b= 5.427$ Å, $c=10.848$ Å, volume= 319 Å^3 CVT single crystal – Schäfer et al. [358] (1974)	
	$a=b= 5.435$ Å, $c=10.843$ Å, volume= 320 Å^3 CVT single crystal – Guen et al. [364] (1979)	
	$a=b= 5.434(1)$ Å, $c=10.856(1)$ Å, volume= 320 Å^3 Salt flux single crystal – Bonazzi et al. [65] (2003)	
	$a=b= 5.428(2)$ Å, $c=10.864(4)$ Å, volume= 320 Å^3 Powder, solid state reaction – Schorr et al. [68] (2007)	

Table 7.1.1 Summary of the SAED and XRD single crystal analyses for the determination of the unit cell parameters and of the space group of the CVT-grown CZTS samples obtained respectively with $5 \cdot 10^{-3}$ (experiment No. 3) and with $9 \cdot 10^{-4}$ g·cm^{-3} of I_2 (experiments No. 9). A review of the literature CZTS lattice parameters obtained by XRD is also given for comparison.

Table 7.1.1 shows that the crystals have tetragonal unit cells, consistently with the reported literature of CZTS. The differences between the lattice parameters estimated with X-ray diffraction and selected area electron diffraction (SAED) for both samples are significant, but it must be highlighted that the error uncertainty generally associated with the electron diffraction technique is larger than for XRD if aberrations of the TEM column are not taken into account [379].

The tetragonality factors $c/(2a)$ obtained from the X-ray diffraction analyses point to unit cells that are slightly compressed along the [001] crystallographic direction if compared to the literature values where this factor exceeds unity [68], but they are substantially in agreement with the more recently reported figure of 0.997 [69, 71]. The CZTS samples grown with a higher I_2 pressure (test No. 3) possess a smaller unit cell than those grown under lower I_2 pressure (test No. 9). Such a difference is only $1Å^3$, but the accuracy of the XRD measurement suggests that it is meaningful. Fig. 7.1.1 shows the experimental X-ray powder patterns of the two ground CZTS samples (tests No. 3 and 9). The results are compared to the calculated database X-ray powder pattern of CZTS reported by Bonazzi et al. [65]. The radiation employed for both experimental acquisitions and database pattern generation was CuK_α (λ = 1.5418 Å).

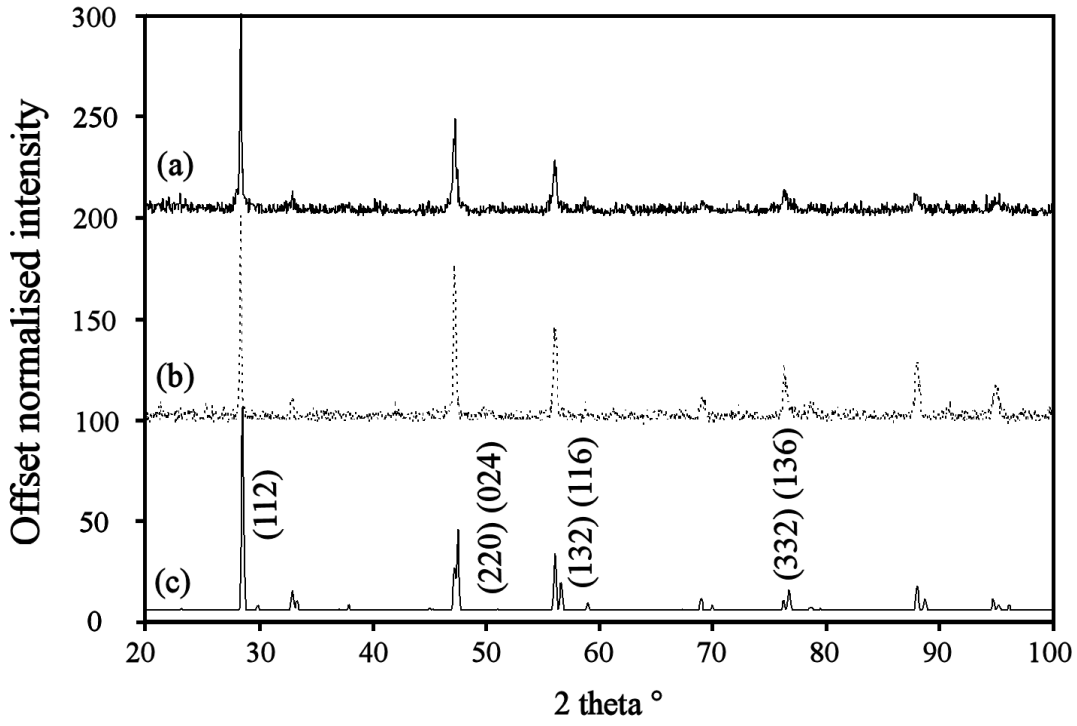

Fig. 7.1.1 Comparison between experimental X-ray powder patterns of ground CZTS crystals of experiments No. 9 (a) and 3 (b) with CZTS X-ray powder pattern calculated from the CZTS database structural data reported by Bonazzi et al. [65] (c). (CuK_α radiation was employed in both sets of data, λ = 1.5418 Å).

A close-up view of the major diffraction peaks from the XRD patterns in Fig. 7.1.1 is shown in Fig. 7.1.2, where the acquisition was performed with a higher 2θ resolution

and a longer collection time, with the intent to detect any structural differences between the crystals obtained with different I_2 loads (experiments No. 3 and 9).

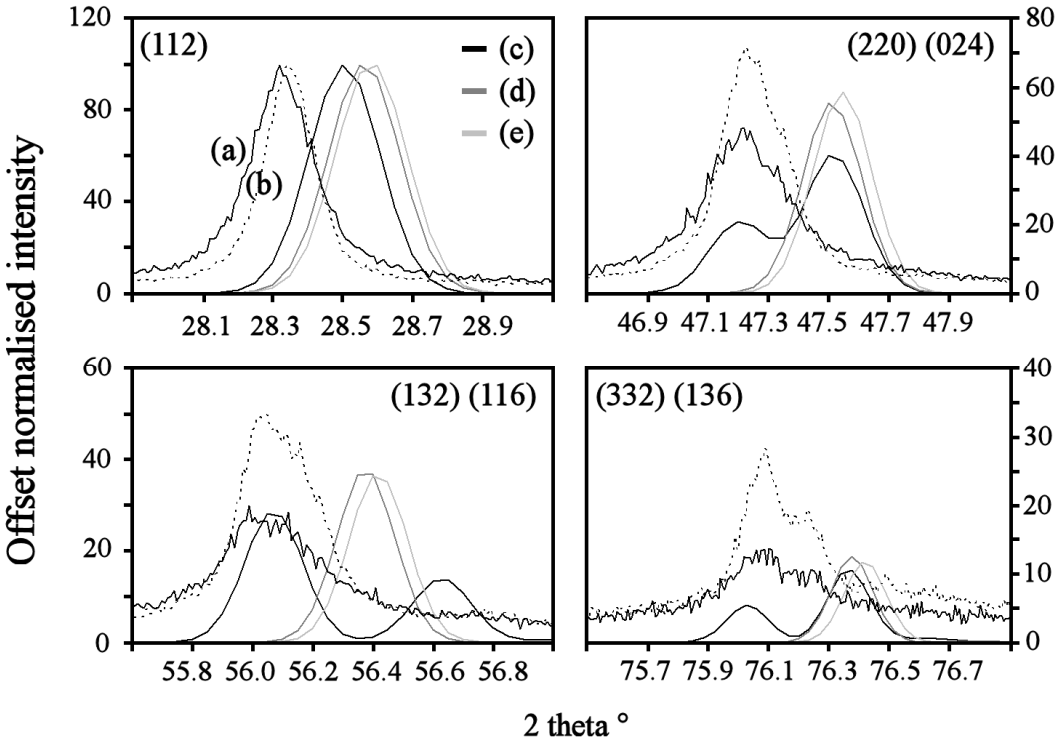

Fig. 7.1.2 Major peaks of the experimental X-ray powder patterns of the ground CZTS crystals of experiments No. 9 (a) and 3 (b) and of calculated X-ray powder patterns of CZTS [65] (c), Cu_2SnS_3 [380] (d) and ZnS [381] (e). The 2θ resolution and collection time employed were 0.01° and 30 s respectively. (The CuK_α, λ = 1.5418 Å radiation employed is consistent for all patterns).

Fig. 7.1.2 shows that the relative intensities of the diffraction peaks of the two crystals synthesized with different I_2 loads are different. The position of only the (112) peak of both samples is shifted towards lower 2θ compared to the database spectrum of CZTS by Bonazzi et al. [65]. Furthermore, in both samples the peaks (024) and (116) seem absent, and the relative intensity of the pair (332)(136) is opposite to what was reported by Bonazzi et al. [65].

I-42m (No. 121) is the space group that provides the best match of the X-ray diffraction data refinement from single crystal. This space group is the same expected for the *Stannite* unit cell represented in Fig. 1.B.2a. However, as reported in the introduction to part B, the virtually equal atomic form factors of Cu^+ and Zn^{2+} ions [307], make impossible to solve the Cu-Zn cation ordering in the structure of the CZTS samples solely by XRD. Therefore, as indicated by Schorr et al., neutron scattering is required to ultimately rule out the space group I-4 (No. 82) [67].

A single crystal neutron diffraction analysis was performed on one CZTS crystal grown under the conditions of experiment No. 3 (i.e. with I_2 load of $5 \cdot 10^{-3}$ g·cm^{-3}). The tool employed for this study is a unique instrument called VIVALDI (very intense vertical-axis Laue diffractometer) located at the *Institut Laue-Langevin* in Grenoble (France). VIVALDI allows large volumes of reciprocal lattice to be surveyed rapidly using an image-plate photographic Laue technique with a white neutron beam. The higher intensity offered by the use of a polychromatic radiation source allows detailed atomic structural information to be obtained from crystals of reduced size in a reasonable time. The CZTS sample analysed had a volume of roughly $4 \times 1 \times 0.5$ mm^3. Seven frames were acquired at different φ angles between the beam and the crystal (-15, 0, 15, 30, 45, 60, 75 °), and each frame required about 10 hours of acquisition for the low intensity spots to be detected appropriately. An example of neutron Laue pattern recorded with VIVALDI from the CZTS sample is shown in Fig. 7.1.3. Examination of the Laue patterns revealed that the crystal analysed was twinned (i.e. it was composed of two single crystals). However, this did not prevent the structure refinement, from which the space group I-4 was assigned, but with some Cu deficiency in the structure, leading to the formula $Cu_{1.8}Zn_{1.2}SnS_4$. This space group is different from the one obtained by refinement of the X-ray data, and describes the symmetry of the *Kesterite* unit cell represented in Fig. 1.B.2b.

Ichimura et al. [382] have computed by DFT the energetic stability of five possible CZTS structures with different cation ordering. All the proposed structures obey the constraint for which every S atom needs to be bonded to two Cu, one Zn and one Sn atoms. Ichimura et al. estimated that the energy difference per atom of the five structures is smaller than the thermal energy at room temperature. The X-ray and neutron powder diffraction patterns of these five structures have also been simulated, and shown to be slightly different for the structures [382].

Based on Ichimura's results and on the structural characterizations carried out in the present study, it cannot be excluded that the crystals synthesized via the CVT at temperatures ranging between 750 and 810 °C are composed of domains of the five possible CZTS structures, with stacking faults accommodating the domain boundaries.

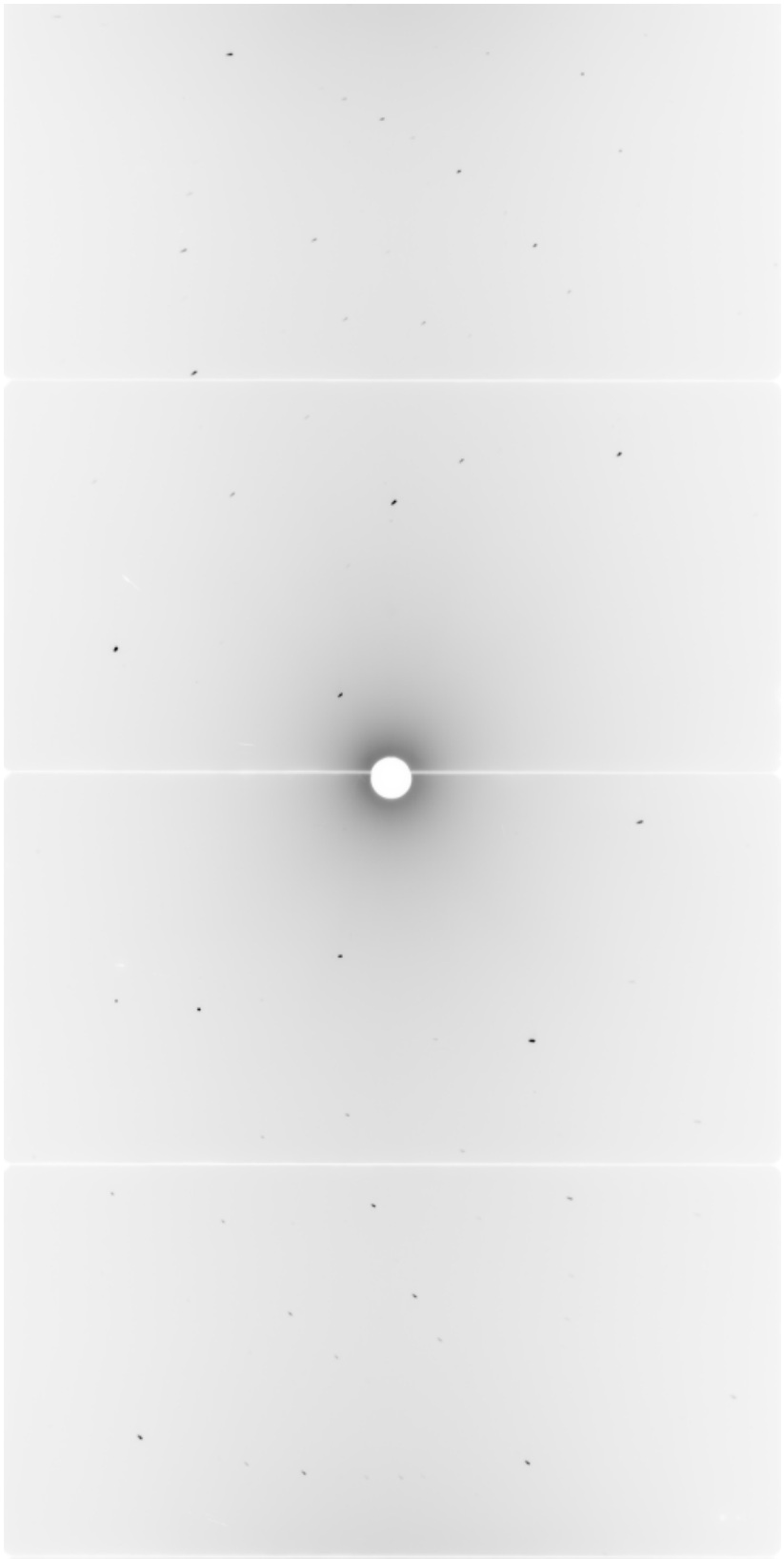

Fig. 7.1.3 Example of Laue pattern obtained by interaction of the polychromatic neutron beam (λ = 0.7-5.4 Å) and a CZTS crystal obtained from experiment No. 3 (CVT under I_2 load of $5 \cdot 10^{-3}$ g·cm^{-3}), as recorder by the VIVALDI instrument over an acquisition time of 9.7 hours.

7.2 Raman spectroscopy analysis of CZTS crystals

The crystals of CZTS formed by CVT with different I_2 loads were analyzed by Raman spectroscopy on a T64000 Jobin Yvon (Horiba Scientific) at the *Institut de Recerca en Energia de Catalunya* (IREC) located in Barceona (Spain).

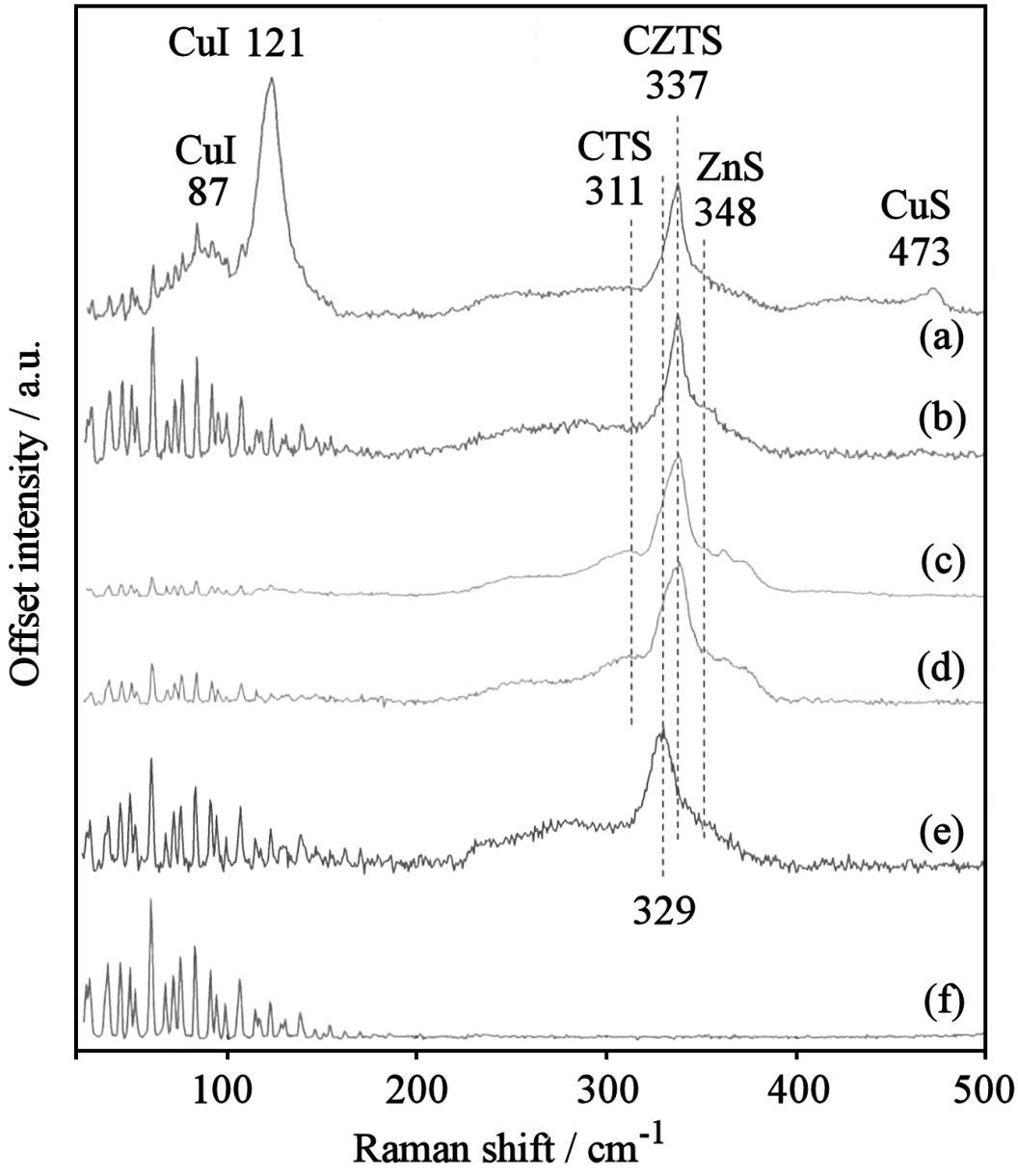

Fig. 7.2.1 Raman spectra of CZTS samples obtained via CVT experiments No. 3 ($5 \cdot 10^{-3}$ g·cm^{-3} I_2) (a-d) and 9 ($9 \cdot 10^{-4}$ g·cm^{-3} I_2) (e). Crystals from exp. No. 3 before (a,c) and after (b,d) mechanical removal of surface phases (see text). Ground CZTS crystals from exp. No. 9 (e) and air blank (f). The excitation wavelength employed was $\lambda = 514$ nm, the spot size was 5-10 μm and the integration time was 1.5 hours.

Raman measurements were carried out with an excitation wavelength of 514 nm, a spot size of 5-10 μm and an integration time of 1.5 hours. It should be pointed out that ZnS may not be visible in the Raman spectrum for this excitation wavelength, due to the absence of the resonance Raman effect (see Fig. 7.2.2). The results are shown in Fig. 7.2.1. Fig. 7.2.1a-d shows the Raman spectra performed on two different areas of a CZTS crystal obtained from experiment No. 3 (I_2 load = $5 \cdot 10^{-3}$ $g \cdot cm^{-3}$), where the peak at 337 cm^{-1} is attributed to CZTS [75, 314, 355]. Fig. 7.2.1a,c shows the spectra of the as-grown CZTS crystals from experiment No. 3, while spectra in Fig. 7.2.1b,d have been acquired after a mechanical treatment aimed at removing the secondary phases that were detected by EDS on the surface (section 6.3.3). Such a mechanical treatment was made by placing the samples in a closed rocking vessel containing high purity SiO_2 (1 μm size, Sigma Aldrich). This apparatus was assembled by modifying a system originally designed by Cummings et al. [383] for the electrodeposition of Cu films on Mo/$MoSe_2$ substrates. The vessel was rocked at a frequency of 100 Hz for 10 hours. Consistently with the EDS analyses (Fig. 6.3.3), Fig. 7.2.1a shows that the as-grown sample from experiment No. 3 contains secondary phases such as CuI (87 and 121 cm^{-1} [384]) and CuS (473 cm^{-1} [385-387]) that are absent on the mechanically treated ones (Fig. 7.2.1b,d). However, it was also found that the spectra of the mechanically treated crystals (experiment No. 3) show peak shoulders at 311 and 348 cm^{-1} that may be due to traces of Cu_3SnS_4 [388] and ZnS [389-391] respectively. Fig. 7.2.1e shows the spectrum of ground CZTS crystals from experiment No. 9 (I_2 load = $9 \cdot 10^{-4}$ $g \cdot cm^{-3}$), with a peak at 329 cm^{-1}. It is interesting to notice a red-shift of 8 cm^{-1} from the literature value of the corresponding peak of CZTS [75, 314, 355]. Such a shift may be attributed to the strain possibly induced in the material by the grinding procedure [392], although it could also arise from a different cation ordering.

As described by Fontané et al. [132], in order to enhance detection sensibility to the potential presence of ZnS, the Raman spectroscopy analyses can be performed with an excitation wavelength closer to the band-gap of ZnS, which is known to be around 3.8 eV [393]. Under such conditions, resonant excitation occurs leading to a sharp increase in the efficiency of the main vibrational mode of ZnS, and even traces of this phase are detected [394]. This analysis was performed on the crystals as taken from the ampoules after the CVT experiments No. 3 and 9 (rinsed only with acetone) and after the mechanical treatment aimed at removing the secondary phases from the

surface of the crystals of test No. 3. The results of the Raman spectroscopy analyses with UV excitation conditions (λ = 325 nm) are shown in Fig. 7.2.2.

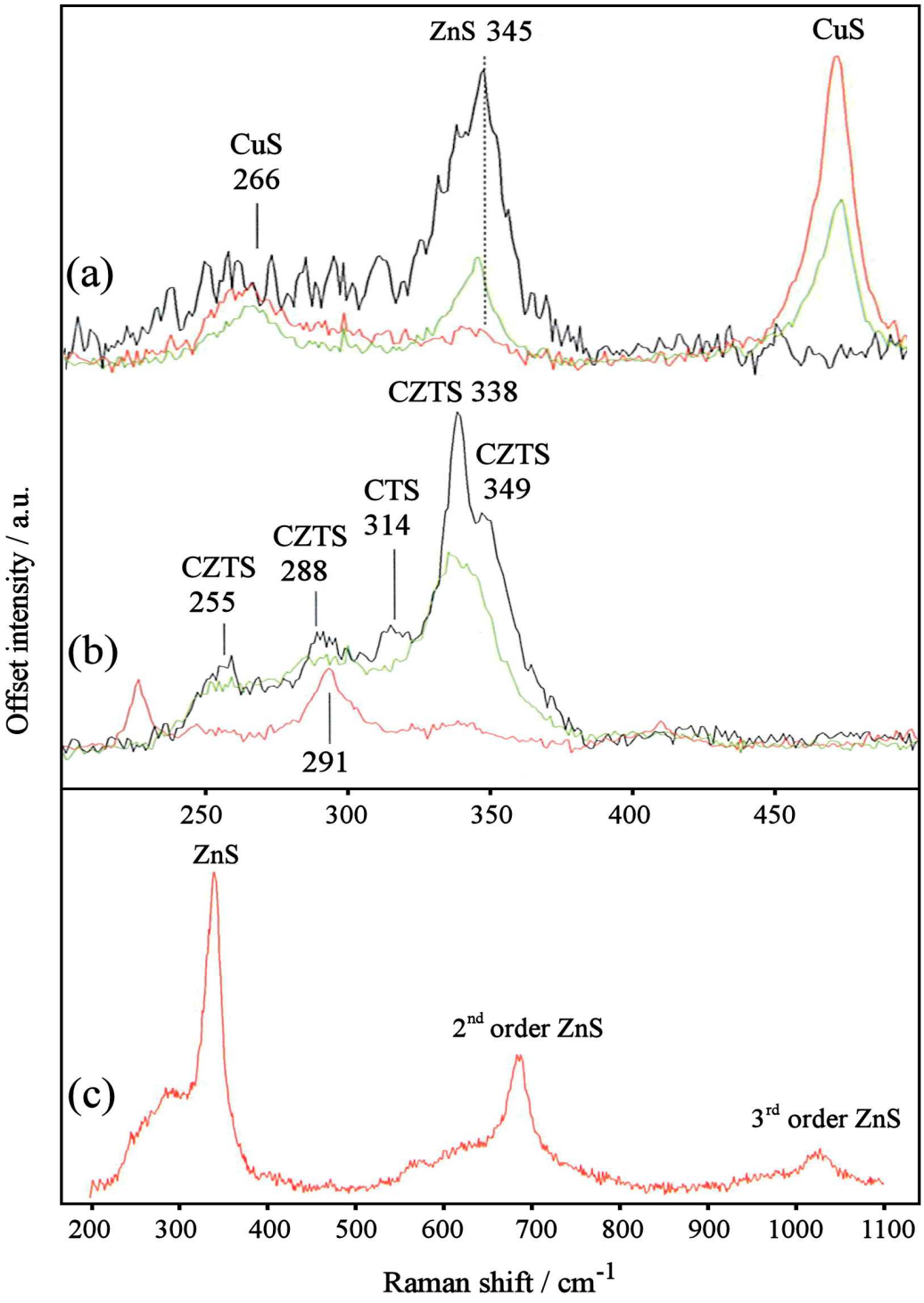

Fig. 7.2.2 Raman spectra of CZTS samples obtained via CVT experiments No. 3 ($5 \cdot 10^{-3}$ g·cm^{-4} I_2) (a-b) and 9 ($9 \cdot 10^{-4}$ g·cm^{-4} I_2) (c) under UV excitation conditions. Crystals from experiment No. 3 before (a) and after (b) mechanical removal of surface phases (see text) (analysis performed on three different points on the sample). Ground CZTS crystals from experiment No. 9 (c). The excitation wavelength was λ = 325 nm, the spot size was 5-10 μm and the integration time was 1.5 hours.

Figs. 7.2.2a-b show the Raman spectra of CZTS crystals from experiment No. 3, while Fig. 7.2.2c corresponds to the ground CZTS crystals from experiment No. 9.

The Raman analysis under UV excitation conditions (Fig. 7.2.2) confirms that the as-grown CZTS crystals from experiment No. 3 contain secondary phases: ZnS and CuS are clearly identified in Fig. 7.2.2a. The peak at 345 cm^{-1} attributed to ZnS is also detected on the Raman spectrum under UV excitation of the ground crystals from experiment No. 9 (Fig. 7.2.2c). For this sample, the second and third order bands of ZnS are also detected, giving a quite clear evidence of ZnS presence.

The presence of secondary phases on the surface of the as-grown crystals obtained from experiment No. 3 (Fig. 7.2.1a,c and Fig. 7.2.2a) is consistent with the EDS analyses and with the fact that the synthesis was carried out under a strong convective-dominated regime of transport (i.e. far from equilibrium).

Experiment No. 9 was run with a lower pressure of I_2 compared to experiment No. 3. The Raman spectrum shows that these crystals contain less secondary phases (Fig. 7.2.1e) than crystals from experiment No. 3 (Fig. 7.2.1a,c). However, the Raman analysis performed under resonant excitation conditions gives strong evidence that these crystals contain also ZnS (Fig. 7.2.2c). Interestingly, the main CZTS peak observed for the crystals synthesized with experiment No. 9 display a red-shift of 8 cm^{-1} compared to the literature value. It is not certain whether this shift is chemically meaningful or it is simply due to mechanical lattice strain.

For the crystals obtained from both experiments No. 3 and 9, the Raman peaks at 337 and 329 cm^{-1} attributed to CZTS have a comparatively larger width at half maximum than the corresponding of CZTS samples obtained by e.g. the salt flux method [355]. It may be that the synthetic route employed in the present work (based on the CVT with I_2) leads to crystals with a higher concentration of structural defects that could be responsible for the broadening of the Raman peak [151].

7.3 Photoluminescence spectroscopy analyses

The crystals of CZTS formed by CVT experiment No. 9 (I_2 load = $9 \cdot 10^{-4}$ g·cm^{-3}) were analyzed with photo-induced luminescence spectroscopy (PL), in order to study their electronic structure. The measurements were carried out at the *Université du Luxembourg* with a home-built micro PL spectroscopy system at T = 8 K using an excitation laser with wavelength λ = 514 nm and a spot size of 1 μm. Micro-resolved PL spectra were measured on one as-grown CZTS needle. A similar broad peak was recorded on three spots along the sample, with maxima at 1.35, 1.37 and 1.32 eV, as shown in Fig. 7.3.1a.

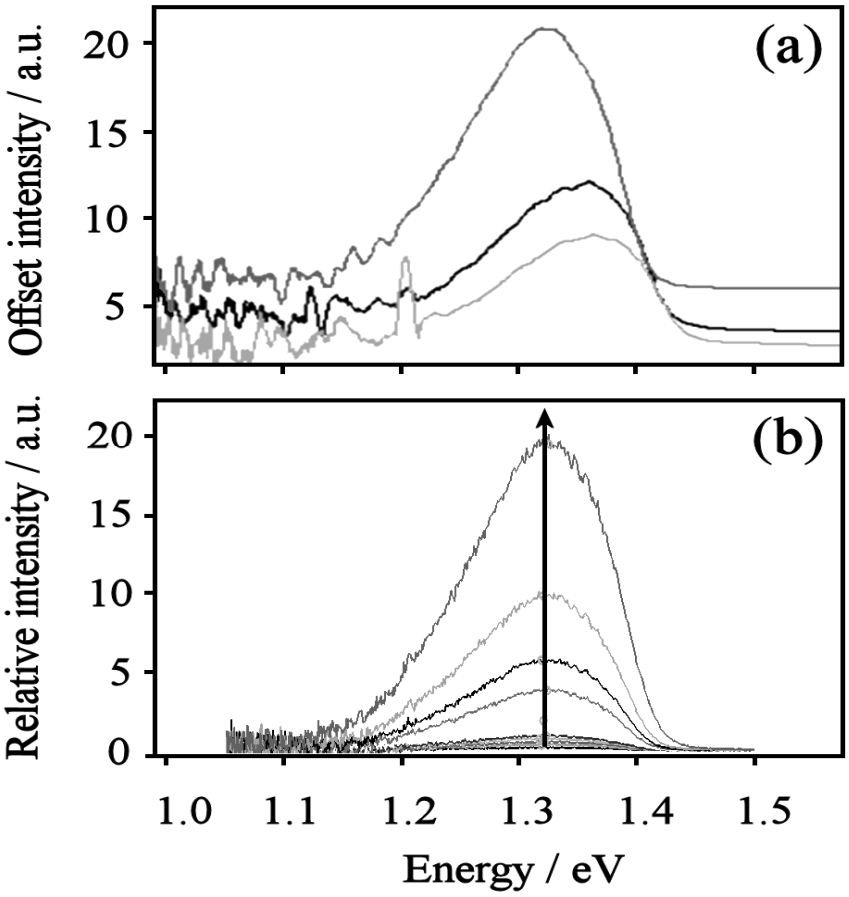

Fig. 7.3.1 Micro-resolved PL spectra of a CZTS crystal synthesized by CVT with an I_2 load of $9 \cdot 10^{-4}$ g·cm^{-3} (exp. No. 9) performed on three different points along the sample. The PL finger prints show maxima at 1.35, 1.37 and 1.32 eV (a). Intensity dependent PL measurements from 10 μW to 1 mW indicated by the arrow (b). All the analyses were performed at T = 8 K using an excitation wavelength of 514 nm (Ar ion laser) and a spot size of 1 μm.

The broad asymmetric shape and approximate energy of the emission peaks resemble closely the CZTS PL spectra reported by Altosaar et al. [355], Hönes et al. [73] and Tanaka et al. [72] on samples obtained via the salt flux method and the CVT with I_2. The shift of the position of the PL peaks recorded at different positions on the surface of the needle-shaped crystal suggests that the sample displays inhomogeneities of the electronic structure (Fig. 7.3.1a).

Intensity dependent micro-resolved photoluminescence measurements (Fig. 7.3.1b) were performed at T = 8 K on the same needle-shaped crystal (experiment No. 9). This analysis was performed with the aim of understanding the nature of the associated transition (excitonic or defect related), as described by Hönes et al. [73]. Fig. 7.3.1b shows the results of the intensity dependence of the broad PL emission peak of the needle-shaped CZTS crystal (exp. No. 9, I_2 load $9 \cdot 10^{-4}$ g·cm^{-3}) on the intensity of the excitation source. The power of the beam on the sample was varied between 10 μW to 1 mW, and the corresponding emission line response is indicated by the arrow in Fig. 7.3.1b. The peaks are centered at 1.32 eV and deviation from this value is less than 0.2 % with the beam power investigated (varied in a range of 2 orders of magnitude).

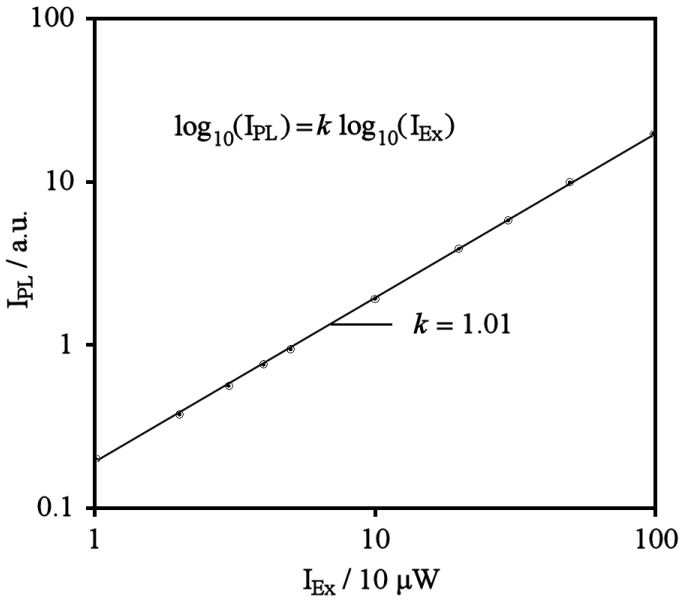

Fig. 7.3.2 Double-logarithmic plot of the CZTS (experiment No. 9) PL peak intensity dependence as a function of the intensity of the excitation source. From the slope of the line, a value of *k* of about 1 is estimated.

The intensity of the emission peak in a PL spectrum (I_{PL}) is related to the excitation intensity (I_{Ex}) by a power law expressed by Eq. 7.3.1 [395].

Eq. 7.3.1 $I_{PL} \alpha (I_{Ex})^K$

From the intensity dependence measurement, a value of the exponent *k* around 1 is estimated for the PL peak of the CZTS crystal obtained from experiment No. 9 (Fig. 7.3.2). A *k* value of approximately 1 could be due to either an excitonic or a defect related transition, and is not sufficient to discriminate between the two cases [73].

The interpretation of the broad asymmetric peak reported for CZTS samples in the region 1.3-1.4 eV is still debated in the literature. According to the DFT computation by Chen et al. [153] the peak might arise from a transition between the conduction band minimum and the energy level of the Cu/Zn antisite defects (that lie 0.12 eV above the valence band maximum).

Tanaka et al. [72] have reported a sharp dependence of the peak intensity with the sulfur deficiency on their CZTS crystals obtained by CVT with I_2, and have ascribed the PL broad peak to a donor-acceptor pair (DAP) recombination associated to the presence of sulfur vacancies. However, based on the DFT calculations of Chen et al. [153] (Fig. 1.B.4), such a transition should occur at ~0.65 eV.

For the CZTS samples produced by Altosaar et al. [355] with the salt flux technique, a blue-shift was observed with the intensity dependence of the PL peak. They proposed a band-to-tail recombination mechanism, since the blue-shift was believed to be too large to be associated with a DAP recombination. This band-to-tail transition occurs from the conduction band minimum to a broad tail of states located within the band-gap. Such tails are often found in *highly compensated* semiconductors, where there are comparable and high concentrations of donors and acceptors. In such conditions, most of the defects are charged, and a heterogeneous distribution of positive and negative charge densities is observed [396]. This uneven distribution of charges within the material brings about a spatially fluctuating electrostatic potential [397]. A similar phenomenon was previously reported for $CuIn_{0.5}Ga_{0.5}Se_2$ by Krustok et al. [398], who explained on such a basis the disappearance of the main excitonic transition at low temperature.

Concluding remarks for part B

The main objective of the work illustrated in part B of this thesis was the synthesis of high quality Cu_2ZnSnS_4 single crystals via the chemical vapour transport (CVT) in closed ampoules using iodine as the transporting agent.

In order to obtain preferential crystallization of single-phase CZTS material at the cold end of the ampoule, a meaningful pressure of the iodides of Cu, Zn and Sn must be ensured along the ampoule's length. In chapter 5 the thermochemistry of the Cu-Zn-Sn-S-I system was investigated from a computational perspective, with the intent to identify the temperature dependence of the free energy changes for the possible reactions involved. It was found that the formation of the volatile unary components $(CuI)_3$, ZnI_2 and $SnI_{2(w+1)}$ by the action of iodine on the corresponding sulfides is dependent on very different pressure of the components at equilibrium (Fig. 5.4.4). The CVT experiments (chapter 6) were performed after formation of a polycrystalline CZTS source by application of a strong temperature gradient. Nevertheless, the equilibria computed in Fig. 5.6.3 reveal the different thermodynamic tendency of the gaseous iodide species to form. The following sequence of volatility was deduced: $SnI_{2(w+1)} > (CuI)_3 > ZnI_2$ for $T < 900$ K and $SnI_{2(w+1)} > ZnI_2 > (CuI)_3$ for $T > 900$ K. The computation of the free energy changes for the reactions in the Cu-Zn-Sn-S-I system was based on the assumption that only the most stable reagents were present at each temperature. Deviations from the standard conditions (1bar I_2 and 1 bar S_2) were computed for the phase equilibria in the Cu-S and Sn-S systems. As expected from *Le Chatelier*'s principle, a shift towards higher temperatures for the reactions $CuS \rightleftharpoons Cu_2S$ and $SnS_2 \rightleftharpoons Sn_2S_3 \rightleftharpoons Sn_3S_4 \rightleftharpoons SnS$ with increasing sulfur pressure was obtained from the computation (Figs. 5.3.2-5.3.4). However, the analogous effect of iodine pressure would be needed in order to compute the best conditions for the desired phase formation. The ultimate ambition was to compute the effects of two temperatures (source and growth ends), and two pressures (I_2 and S_2) on the phase equilibria within the Cu-Zn-Sn-S-I system. This would correspond to a significant expansion of the approach done by Zavrazhnov et al. [399], who computed the phase equilibria of the Ga-Se-I system as functions of the two temperatures only. Unfortunately such a work would require a deep knowledge of computational science (besides knowledge of thermodynamic functions for all the phases involved) which prevented the study to be undertaken

within the time frame of this PhD. An estimation of the chemical potential of CZTS as a function of the temperature is proposed, based on a linear interpolation between published DFT-computed and experimental values at T = 0 K [153] and T = 823 K [281] respectively. Extrapolation of the proposed trend to higher temperatures provides an estimate of the decomposition temperature of CZTS into the binary sulfides that is consistent with the known peritectic decomposition temperature of CZTS [133], but with a ~ ± 100 °C range of uncertainty. Based on the estimated chemical potential of CZTS, a negative enthalpy change for the crystallization of CZTS from the iodides is proposed (Fig. 5.6.3). Figs. 5.6.2 and 5.6.3, as well as section 4.4 in part A of this thesis stress on the importance to identify reliable thermochemical functions for multinary sulfides.

Chapter 6 illustrates the experimental results of the synthesis of Cu_2ZnSnS_4 single crystals via the chemical vapour transport from the elements in the presence of I_2. From the direction of transport (from high to low temperatures), a negative enthalpy change for the crystallization reaction of CZTS from the iodides is estimated. This result is consistent with the computational work in Fig. 5.6.3. In agreement with simpler systems, it was found that an increase of the iodine load inside the ampoule has a strong effect on the transport mechanism, with a transition from a diffusion (reaction-limited) to a convection-dominated regime [368]. In turn, this was found to affect significantly the shape and quality of the crystals. Highly crystalline CZTS with needle-shape (1D predominance) was obtained with $9 \cdot 10^{-4}$ gcm^{-3} of I_2 (exp. No. 9), while more defective but larger crystals (3D predominance) were obtained with a nearly five-fold load (exp. No. 3). In the case with lower I_2 pressure a gradient of 130 °C was employed to speed up the process and achieve well formed crystals, while with higher I_2 pressure a gradient of 40 °C was necessary as larger gradients lead to the formation of polycrystalline material. There appears to be no meaningful effect of the iodine pressure employed on the composition of the CZTS samples. The samples showed high compositional uniformity at the SEM/EDS/BSE level. Nevertheless, it was found that the CZTS crystals obtained with higher I_2 load coexisted with surface binary phases such as ZnS and CuS (Figs. 7.2.1a and 7.2.2a). Interestingly, under a lower I_2 load (exp. No. 9) where the transport rate is limited by the heterogeneous reaction rate between source material and iodine, despite the very different thermodynamic equilibrium constants of the reactions between the binary sulfides and iodine to form the unary iodides of Cu, Zn and Sn (cfr. Fig. 5.4.4), the Cu-Zn-Sn-S-I system seems to be self-regulatory, i.e. there is a stronger tendency for the

crystallization of CZTS over the competing secondary phases compared to the case where the I_2 load was larger (exp. No 3), although some ZnS was detected by Raman under UV excitation conditions (Fig. 7.2.2c). In both experiments No. 3 and 9, CuI was detected as a secondary phase on the surface of the crystals. The strong driving force for crystallization of CuI expected from the computation (Fig. 5.4.2) is consistent with the obderved CuI segregation. CVT treatments in the absence of longitudinal temperature gradients were carried out with the aim of increasing the size of already formed crystals. Under the investigated conditions, the nucleation and growth of CZTS on the ampoule's walls (2D predominance) was found to be more convenient than the enlargement of pre-existing CZTS crystals pointing towards the interior of the ampoule. This behaviour is opposite to that described by Szczerbakow et al. [371] for the self-selective vapour growth of bulk crystals. In the present work, the thermal conductivity profile of the synthetic vessel and surrounding is thought to be the possible cause for this phenomenon. A more effective heat exchange is shown by the ampoule's walls in contact with the furnace's wall rather than by the atmosphere inside the ampoule. The decomposition/crystallization rate has a key role on the preferential crystallization under longitudinally isothermal conditions. At constant temperature, this rate is ultimately dependent upon the concentration of I_2 and S_2 in the system. Therefore, with higher I_2 loads the higher rate of heat exchange can be attained more effectively by the ampoule's walls and 2D crystallization is favoured. The opposite occurs with lower I_2 pressures, where 3D crystallization is comparatively more favourable. More studies are required in order to confirm or disregard the proposed explanation. This would help identifying the conditions for CZTS crystal enlargement/improvement under longitudinally isothermal CVT conditions. The influence of ampoules made of more insulating materials or, vice versa, the increase of the thermal conductivity of the atmosphere within the ampoule, might help making this process more favourable. An estimation of the temperature at which the crystallization reaction of CZTS becomes thermodynamically spontaneous would be beneficial for the design of such growth experiments. As pointed out earlier, thermochemical and computational investigations could give important information in this direction.

In chapter 7 the results of a collection of characterizations performed on the CZTS crystals produced in the present work is reported. Section 7.1 shows the X-ray and neutron diffraction analyses. XRD analysis shows that samples obtained under lower I_2 pressure (exp. No. 9) have slightly larger unit cells (Table 7.1.1), and the shape

and relative intensities of the X-ray reflections are different from those of the sample grown under higher I_2 pressure (exp. No. 3). Under both pressures, the CZTS crystal have slightly different XRD spectra compared to the database spectrum by Bonazzi et al. [65]. Refinement of the X-ray diffraction data suggests that I-42m is the space group that best matches the structure of the CZTS synthesized in the present work, while neutron data point to the space group I-4. Section 7.2 shows the Raman scattering analyses. An 8 cm^{-1} red-shift of the main CZTS mode is observed for the ground CZTS crystals synthesized with lower I_2 pressure (exp. No. 9), while the corresponding peak position for the sample obtained with higher I_2 pressure (exp. No. 3) is consistent with the values reported in the literature [75, 314, 355]. Section 7.3 shows the results of the photo-induced luminescence spectroscopy performed only on the CZTS samples from exp. No 9. A broad PL peak is detected at ~ 1.3 eV, consistent with previously reported spectra of CZTS obtained from a range of different synthetic routes [72, 73, 355, 400]. The nature of such an electronic transition is still debated, and no attempt to explain it was undertaken in the present work. However, a short discussion is given based on the current knowledge. If the transition is due to a band-to-tail recombination, as indicated by Altosaar et al. [355], a blue shift of the PL peak with increasing temperature may be expected, as it was reported for $CuIn_{0.5}Ga_{0.5}Se_2$ [398]. Tailing may be due to a heterogeneous distribution of charge densities within the semiconductor, causing the energetic levels of valence band maximum and conduction band minimum to fluctuate spatially [396, 397]. Kauk et al. [401] have shown that a change in the electronic properties of CZTSSe monograins after annealing in the presence of S_2 and/or SnS_2 is due to 'healing' of S- and/or Sn-deficient surfaces. The decrease of the broad PL peak intensity after sulfur annealing reported by Tanaka et al. [72] for CZTS crystals obtained by CVT, seems also associated to a sulfur-poor material. However, the direct relationship between the observed PL peak at ~ 1.3 eV and the sulfur vacancies in CZTS seems inconsistent with the energy difference between the level of the sulfur vacancies and the valence band maximum in CZTS. Based on the DFT calculations of Chen et al. [153] (Fig. 1.B.4), such a transition should occur at ~0.65 eV. [157]

Appendices

(1) Derivation of detailed balance efficiency limit

Sunlight is a spectrum of photons distributed over a wide range of energy (Fig. 1).

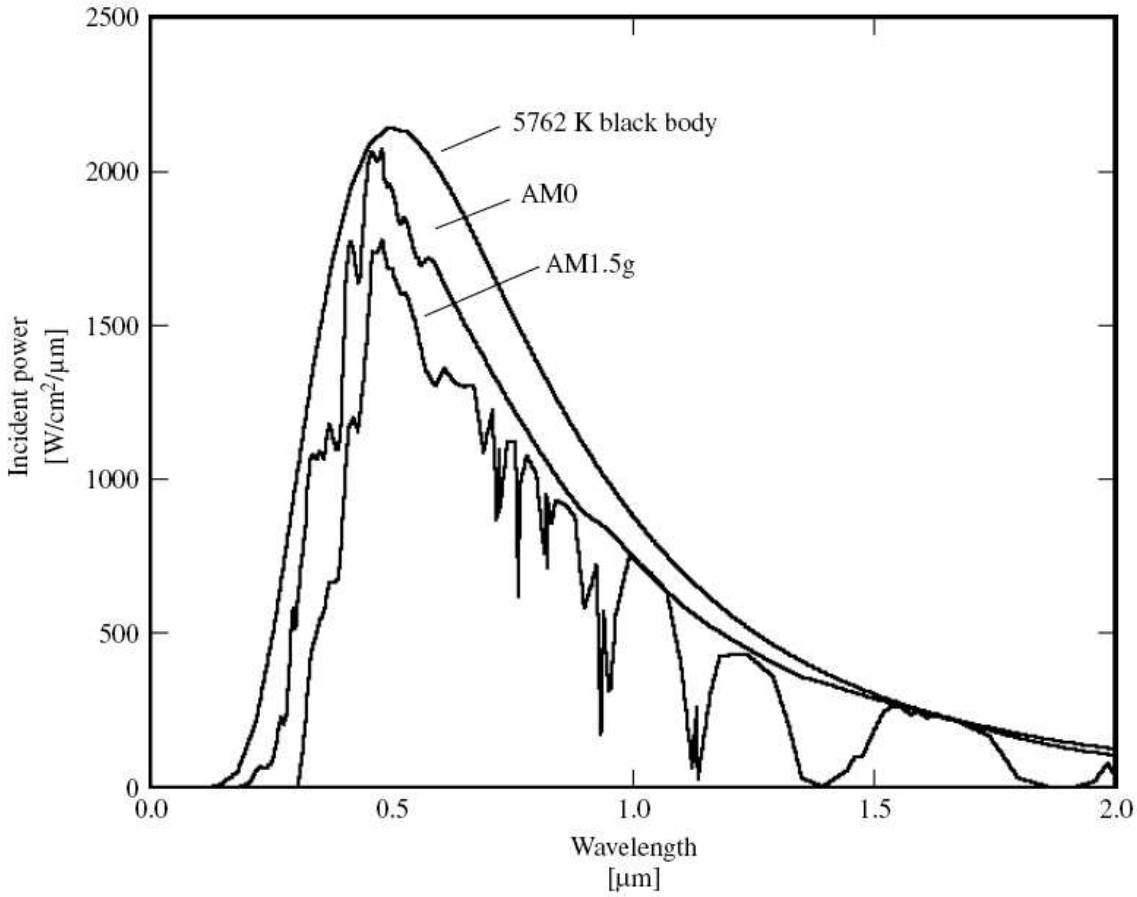

Fig. 1 AM0, AM1.5 solar spectra and 5762K black body radiation [402].

Except for some absorption phenomena, the Air Mass 0 (AM0), the extraterrestrial radiation of the Sun, is close to the black-body radiation of 5762K, from which an approximate value of the surface temperature of the Sun can be estimated. Emission of radiation from the Sun is roughly isotropic. However, given the great distance between the Earth and the Sun (approximately $\sim 1.5 \cdot 10^{11}$ m), the radiation reaching the Earth's surface can be approximated as composed of parallel streams of photons. The Air Mass is a measure of how absorption in the atmosphere affects the spectral features and intensity of the solar radiation reaching the Earth's surface. The Air Mass number is given by Air Mass = $1/\cos(\theta)$, where θ is the angle of incidence or zenith ($\theta = 0$ when the Sun is directly overhead). The Air Mass number is always

greater than or equal to one at the Earth's surface. The AM1.5 spectrum, corresponding to the solar irradiance taken on the Earth's surface after passing through the atmosphere 1.5 times, is the reference spectrum of the Sun for photovoltaic performance evaluations. The AM1.5 solar irradiance certified by the American Society for Testing and Materials (ASTM) can be freely downloaded here [33]. These data are plot in terms of number of incident photons per cm^2 as a function of the photon energy in Fig. 2.

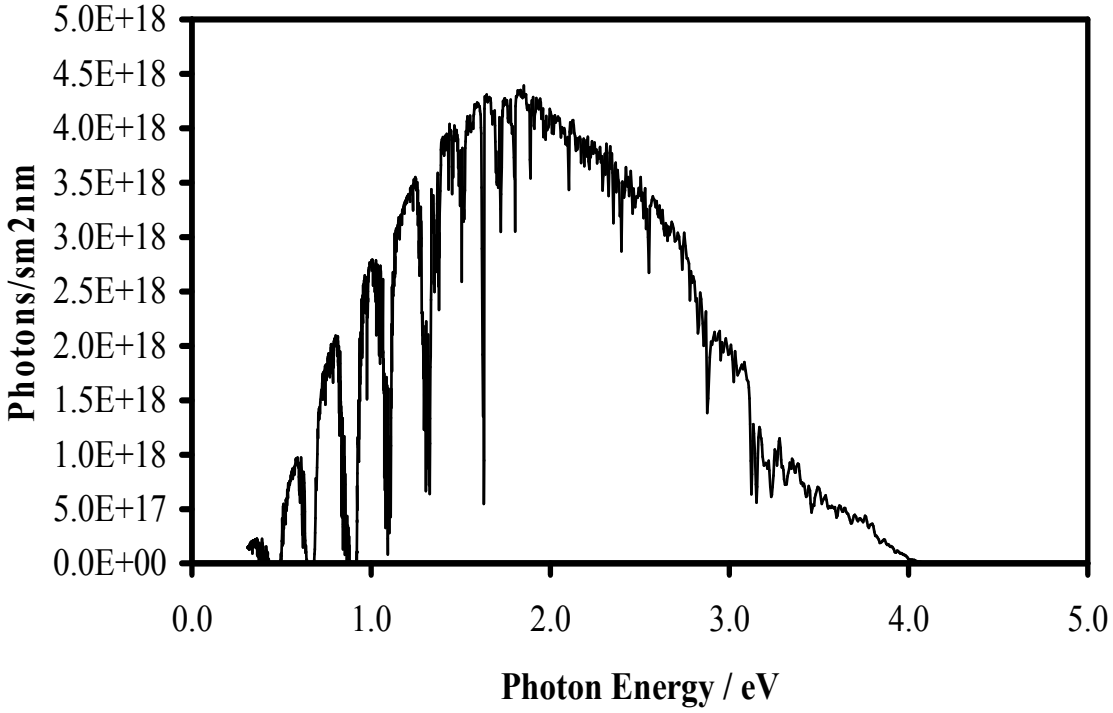

Fig. 2 AM1.5 spectrum showing the intensity of photons versus their energy

The efficiency limit of a single-junction photovoltaic device is due to several aspects. The most important was originally considered by Loferski [31] and Shockley and Queisser [32]. This aspect is based on the fact that in a semiconductor with *Eg* band-gap, electrons excited by photons with energy exceeding *Eg* are promptly thermalized to the energy *Eg*, while photons of energy lower than *Eg* are not able to generate electron-hole pairs. From the data in Fig. 2, and based on these considerations, it is possible to calculate a detailed balance limit of a solar cell with a single band-gap as a function of the band-gap energy (Fig. 3).

For each infinitesimal value of the spectrum photon energy, the following calculation is performed (Eq. 1).

Eq. 1 $$\eta(h\nu_1) = \frac{\left(\int_{h\nu_1}^{\infty} S(\nu)d\nu\right)\cdot h\nu_1}{\int_{0}^{\infty} S(\nu)\cdot h\nu d\nu}\cdot 100$$

where $\eta(h\nu_1)$ is the efficiency of a single band-gap solar cell with $h\nu_1$ as band-gap energy and S is the mathematical function describing the AM1.5 spectrum in terms of intensity of photons versus photon energy (Fig. 2). The term $\left(\int_{h\nu_1}^{\infty} S(\nu)d\nu\right)\cdot h\nu_1$ represents the output power of the device, $\int_{h\nu_1}^{\infty} S(\nu)d\nu$ is the total intensity of the absorbed photons, $\int_{0}^{\infty} S(\nu)\cdot h\nu d\nu$ is the power of the incident radiation.

Since the AM1.5 data available are a series of discrete values, the discrete version of Eq. 1 was employed for the computation (Eq. 2).

Eq. 2 $$\eta(h\nu_1) = \frac{\left(\sum_{i=h\nu_1}^{i=\infty} s_i\right)\cdot h\nu_1}{\sum_{i=0}^{i=\infty} s_i\cdot h\nu_i}\cdot 100$$

where s_i is the value of the intensity of the photon with energy $h\nu_i$.

Fig. 3 shows the results of the computation. The maximum of the graph corresponds to a ~51% efficiency, and is predicted for a band-gap energy of ~1.1eV. Such a plot is an overestimation of the real efficiency limit of a single-junction solar cell, because only the thermalization losses are taken into account. If also recombination and other losses are considered in the computation, the resulting graph is lower in efficiency. Fig. 4 shows the detailed balance efficiency limit that takes into account these phenomena, taken from Würfel [29].

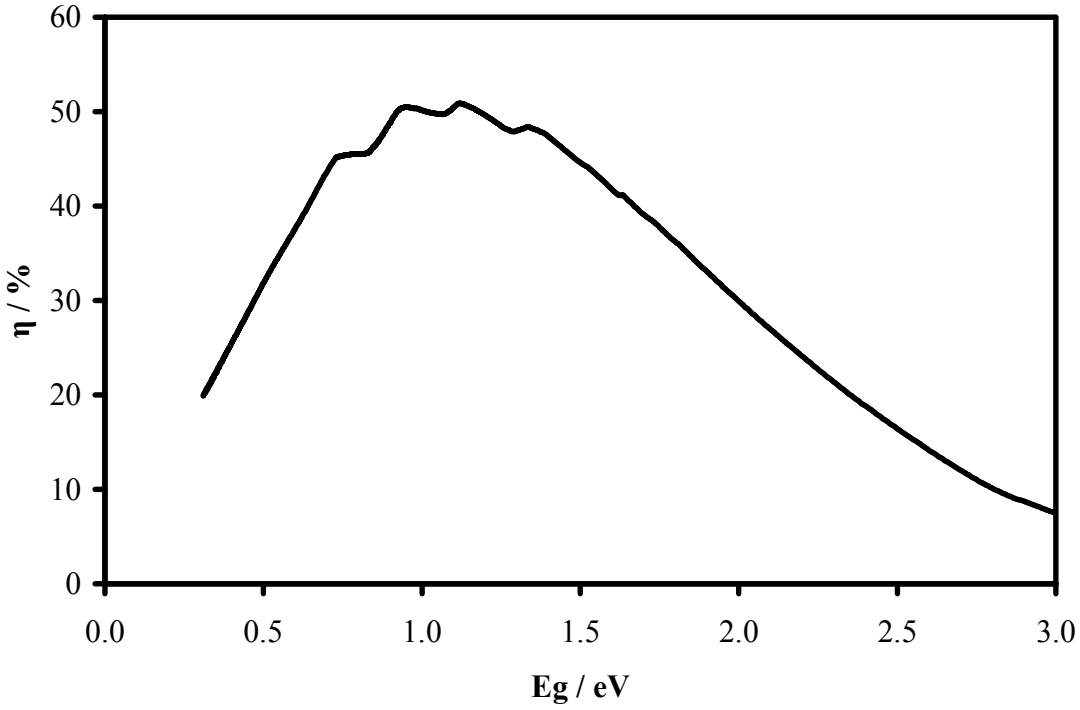

Fig. 3 Calculated detailed balance efficiency limit of a single band-gap photovoltaic device as a function of the value of its band-gap energy, based only on the thermalization losses.

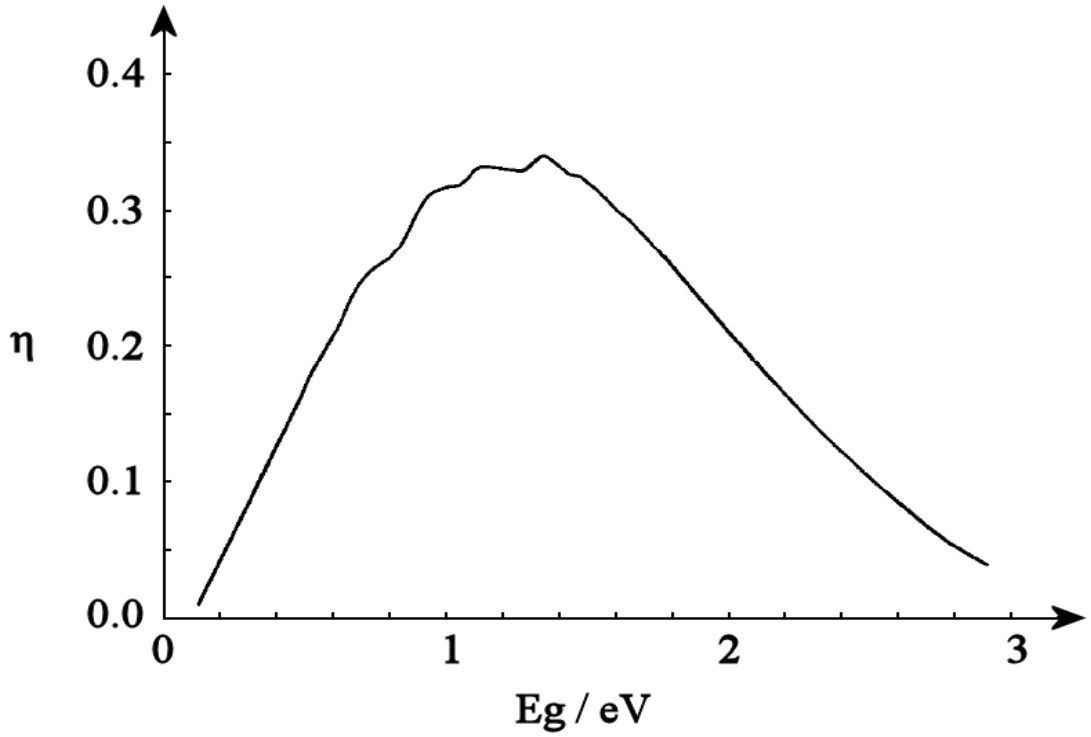

Fig. 4 Detailed balance efficiency limit of a single band-gap photovoltaic device as a function of the value of its band-gap energy, as reported by Würfel [29].

(2) Diagrams of I-42m and I-4 space groups

International Tables for Crystallography (2006). Vol. A, Space group 121, pp. 426–427.

$I\bar{4}2m$ D_{2d}^{11} $\bar{4}2m$ Tetragonal

No. 121 $I\bar{4}2m$ Patterson symmetry $I4/mmm$

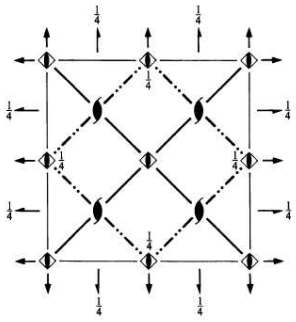

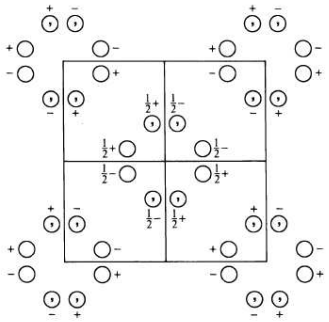

Origin at $\bar{4}2m$

Asymmetric unit $0 \le x \le \frac{1}{2}$; $0 \le y \le \frac{1}{2}$; $0 \le z \le \frac{1}{2}$; $x \le y$

Symmetry operations

For $(0,0,0)+$ set

(1) 1 (2) 2 $0,0,z$ (3) $\bar{4}^+$ $0,0,z$; $0,0,0$ (4) $\bar{4}^-$ $0,0,z$; $0,0,0$
(5) 2 $0,y,0$ (6) 2 $x,0,0$ (7) m $x,\bar{x},z$ (8) m x,x,z

For $(\frac{1}{2},\frac{1}{2},\frac{1}{2})+$ set

(1) $t(\frac{1}{2},\frac{1}{2},\frac{1}{2})$ (2) $2(0,0,\frac{1}{2})$ $\frac{1}{4},\frac{1}{4},z$ (3) $\bar{4}^+$ $\frac{1}{2},0,z$; $\frac{1}{2},0,\frac{1}{4}$ (4) $\bar{4}^-$ $0,\frac{1}{2},z$; $0,\frac{1}{2},\frac{1}{4}$
(5) $2(0,\frac{1}{2},0)$ $\frac{1}{4},y,\frac{1}{4}$ (6) $2(\frac{1}{2},0,0)$ $x,\frac{1}{4},\frac{1}{4}$ (7) c $x+\frac{1}{2},\bar{x},z$ (8) $n(\frac{1}{2},\frac{1}{2},\frac{1}{2})$ x,x,z

$I\bar{4}$ S_4^2 $\bar{4}$ Tetragonal

No. 82 $I\bar{4}$ Patterson symmetry $I4/m$

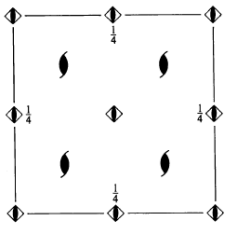

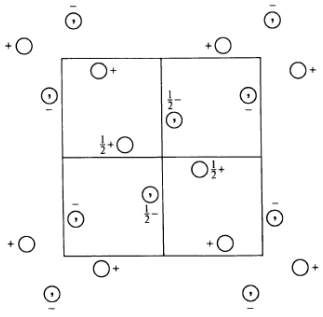

Origin at $\bar{4}$

Asymmetric unit $0 \le x \le \frac{1}{2}$; $0 \le y \le \frac{1}{2}$; $0 \le z \le \frac{1}{2}$

Symmetry operations

For $(0,0,0)+$ set

(1) 1 (2) 2 $0,0,z$ (3) $\bar{4}^+$ $0,0,z$; $0,0,0$ (4) $\bar{4}^-$ $0,0,z$; $0,0,0$

For $(\frac{1}{2},\frac{1}{2},\frac{1}{2})+$ set

(1) $t(\frac{1}{2},\frac{1}{2},\frac{1}{2})$ (2) $2(0,0,\frac{1}{2})$ $\frac{1}{4},\frac{1}{4},z$ (3) $\bar{4}^+$ $\frac{1}{2},0,z$; $\frac{1}{2},0,\frac{1}{4}$ (4) $\bar{4}^-$ $0,\frac{1}{2},z$; $0,\frac{1}{2},\frac{1}{4}$

Generators selected (1); $t(1,0,0)$; $t(0,1,0)$; $t(0,0,1)$; $t(\frac{1}{2},\frac{1}{2},\frac{1}{2})$; (2); (3); (5)

Positions

Multiplicity, Wyckoff letter, Site symmetry			Coordinates $(0,0,0)+$	$(\frac{1}{2},\frac{1}{2},\frac{1}{2})+$			Reflection conditions
							General:
16	j	1	(1) x,y,z (5) $\bar{x},y,\bar{z}$	(2) $\bar{x},\bar{y},z$ (6) $x,\bar{y},\bar{z}$	(3) $y,\bar{x},\bar{z}$ (7) $\bar{y},\bar{x},z$	(4) $\bar{y},x,\bar{z}$ (8) y,x,z	hkl : $h+k+l=2n$ $hk0$: $h+k=2n$ $0kl$: $k+l=2n$ hhl : $l=2n$ $00l$: $l=2n$ $h00$: $h=2n$
							Special: as above, plus
8	i	. . m	x,x,z	$\bar{x},\bar{x},z$	$x,\bar{x},\bar{z}$	$\bar{x},x,\bar{z}$	no extra conditions
8	h	2 . .	$0,\frac{1}{2},z$	$\frac{1}{2},0,\bar{z}$	$0,\frac{1}{2},\bar{z}$	$\frac{1}{2},0,z$	hkl : $l=2n$
8	g	. 2 .	$x,0,\frac{1}{2}$	$\bar{x},0,\frac{1}{2}$	$0,\bar{x},\frac{1}{2}$	$0,x,\frac{1}{2}$	no extra conditions
8	f	. 2 .	$x,0,0$	$\bar{x},0,0$	$0,\bar{x},0$	$0,x,0$	no extra conditions
4	e	2 . mm	$0,0,z$	$0,0,\bar{z}$			no extra conditions
4	d	$\bar{4}$ . .	$0,\frac{1}{2},\frac{1}{4}$	$0,\frac{1}{2},\frac{3}{4}$			hkl : $l=2n$
4	c	2 2 2 .	$0,\frac{1}{2},0$	$\frac{1}{2},0,0$			hkl : $l=2n$
2	b	$\bar{4}$ 2 m	$0,0,\frac{1}{2}$				no extra conditions
2	a	$\bar{4}$ 2 m	$0,0,0$				no extra conditions

Symmetry of special projections

Along [001] $p4mm$
$\mathbf{a}' = \frac{1}{2}(\mathbf{a}-\mathbf{b})$ $\mathbf{b}' = \frac{1}{2}(\mathbf{a}+\mathbf{b})$
Origin at $0,0,z$

Along [100] $c2mm$
$\mathbf{a}' = \mathbf{b}$ $\mathbf{b}' = \mathbf{c}$
Origin at $x,0,0$

Along [110] $p1m1$
$\mathbf{a}' = \frac{1}{2}(-\mathbf{a}+\mathbf{b})$ $\mathbf{b}' = \frac{1}{2}\mathbf{c}$
Origin at $x,x,0$

Maximal non-isomorphic subgroups

I [2] $I\bar{4}11$ ($I\bar{4}$, 82) (1; 2; 3; 4)+
[2] $I21m$ ($Fmm2$, 42) (1; 2; 7; 8)+
[2] $I221$ ($I222$, 23) (1; 2; 5; 6)+

IIa [2] $P\bar{4}2_1c$ (114) 1; 2; 3; 4; (5; 6; 7; 8) + $(\frac{1}{2},\frac{1}{2},\frac{1}{2})$
[2] $P\bar{4}2_1m$ (113) 1; 2; 7; 8; (3; 4; 5; 6) + $(\frac{1}{2},\frac{1}{2},\frac{1}{2})$
[2] $P\bar{4}2c$ (112) 1; 2; 5; 6; (3; 4; 7; 8) + $(\frac{1}{2},\frac{1}{2},\frac{1}{2})$
[2] $P\bar{4}2m$ (111) 1; 2; 3; 4; 5; 6; 7; 8

IIb none

Maximal isomorphic subgroups of lowest index

IIc [3] $I\bar{4}2m$ ($\mathbf{c}' = 3\mathbf{c}$) (121); [9] $I\bar{4}2m$ ($\mathbf{a}' = 3\mathbf{a}, \mathbf{b}' = 3\mathbf{b}$) (121)

Minimal non-isomorphic supergroups

I [2] $I4/mmm$ (139); [2] $I4/mcm$ (140); [3] $I\bar{4}3m$ (217)

II [2] $C\bar{4}2m$ ($\mathbf{c}' = \frac{1}{2}\mathbf{c}$) ($P\bar{4}m2$, 115)

Generators selected (1); $t(1,0,0)$; $t(0,1,0)$; $t(0,0,1)$; $t(\frac{1}{2},\frac{1}{2},\frac{1}{2})$; (2); (3)

Positions

Multiplicity, Wyckoff letter, Site symmetry			Coordinates				Reflection conditions
			$(0,0,0)+$	$(\frac{1}{2},\frac{1}{2},\frac{1}{2})+$			General:
8	g	1	(1) x,y,z	(2) $\bar{x},\bar{y},z$	(3) $y,\bar{x},\bar{z}$	(4) $\bar{y},x,\bar{z}$	hkl : $h+k+l=2n$ $hk0$: $h+k=2n$ $0kl$: $k+l=2n$ hhl : $l=2n$ $00l$: $l=2n$ $h00$: $h=2n$
							Special: no extra conditions
4	f	2 . .	$0,\frac{1}{2},z$	$\frac{1}{2},0,\bar{z}$			
4	e	2 . .	$0,0,z$	$0,0,\bar{z}$			
2	d	$\bar{4}$ . .	$0,\frac{1}{2},\frac{3}{4}$				
2	c	$\bar{4}$ . .	$0,\frac{1}{2},\frac{1}{4}$				
2	b	$\bar{4}$ . .	$0,0,\frac{1}{2}$				
2	a	$\bar{4}$ . .	$0,0,0$				

Symmetry of special projections

Along [001] $p4$
$\mathbf{a}' = \frac{1}{2}(\mathbf{a}-\mathbf{b})$ $\mathbf{b}' = \frac{1}{2}(\mathbf{a}+\mathbf{b})$
Origin at $0,0,z$

Along [100] $c1m1$
$\mathbf{a}' = \mathbf{b}$ $\mathbf{b}' = \mathbf{c}$
Origin at $x,0,0$

Along [110] $p1m1$
$\mathbf{a}' = \frac{1}{2}(-\mathbf{a}+\mathbf{b})$ $\mathbf{b}' = \frac{1}{2}\mathbf{c}$
Origin at $x,x,0$

Maximal non-isomorphic subgroups

I [2] $I2$ $(C2, 5)$ (1; 2)+
IIa [2] $P\bar{4}$ (81) 1; 2; 3; 4
[2] $P\bar{4}$ (81) 1; 2; (3; 4) + $(\frac{1}{2},\frac{1}{2},\frac{1}{2})$
IIb none

Maximal isomorphic subgroups of lowest index

IIc [3] $I\bar{4}$ ($\mathbf{c}' = 3\mathbf{c}$) (82); [5] $I\bar{4}$ ($\mathbf{a}' = \mathbf{a}+2\mathbf{b}, \mathbf{b}' = -2\mathbf{a}+\mathbf{b}$ or $\mathbf{a}' = \mathbf{a}-2\mathbf{b}, \mathbf{b}' = 2\mathbf{a}+\mathbf{b}$) (82)

Minimal non-isomorphic supergroups

I [2] $I4/m$ (87); [2] $I4_1/a$ (88); [2] $I\bar{4}m2$ (119); [2] $I\bar{4}c2$ (120); [2] $I\bar{4}2m$ (121); [2] $I\bar{4}2d$ (122)
II [2] $C\bar{4}$ ($\mathbf{c}' = \frac{1}{2}\mathbf{c}$) ($P\bar{4}$, 81)

Symmetry tables of space groups I-42m (No. 121) and I-4 (No. 82) [308].

(3) Thermochemical functions

Interpolating thermochemical functions (Eqs. 1-5) and values of the coefficients for the 46 compounds of the Cu-Zn-Sn-S-I system (Table 1) employed in the computational work reported in chapter 5.

Eq. 1 $t = 10^{-3} \cdot T/K$

Eq. 2 $c° = a + b \cdot t + c \cdot t^{-2} + d \cdot t^{2}$ Heat capacity / $Jmol^{-1}K^{-1}$

Eq. 3 $h° = 10^{3} \cdot (H^{+} + a \cdot t + b/2 \cdot t^{2} - c \cdot t^{-1} + d/3 \cdot t^{3})$ Enthalpy / $Jmol^{-1}$

Eq. 4 $s° = S^{+} + a \cdot \ln(10^{3}\, t) + b \cdot t - c/2 \cdot t^{-2} + d/2 \cdot t^{2}$ Entropy / $Jmol^{-1}K^{-1}$

Eq. 5 $\mu° = 10^{3} \cdot [H^{+} - S^{+} \cdot t - a \cdot t \cdot [\ln(10^{3} \cdot t) - 1] - b/2 \cdot t^{2} - c/2 \cdot t^{-1} - d/6 \cdot t^{3}]$ Gibbs free energy / $Jmol^{-1}$

Formula	**ΔT / K**	**a**	**b**	**c**	**d**	**H^{+}**	**S^{+}**
CuS (s)	298-774	44.35	11.046			-67.432	-189.458
CuS (g)	298-2000	37.271	0.075	-0.192		308.733	39.044
Cu_2S (s1)	298-376	52.844	78.743			-98.751	-203.643
Cu_2S (s2)	376-717	112.048	-30.752			-109.423	-503.288
Cu_2S (s3)	717-1402	84.642				-96.477	-343.472
Cu_2S (l)	1402-2000	89.119				-93.13	-369.046
CuI (s1)	298-642	62.634	-6.443	-0.577		-88.357	-261.597
CuI (s2)	642-680	58.576				-79.067	-227.717
CuI (s3)	680-868	59.413				-76.414	-228.437
CuI (l)	868-1675	64.852				-71.513	-254.153
CuI (g)	298-2000	37.405	0.502	-0.1		130.745	41.868
$(CuI)_3$ (g)	298-2000	133.177	-0.084	-0.36		-57.646	-296.253
ZnS (Sph.)	298-1293	49.246	5.272	-0.485		-221.561	-227.145
ZnS (Wur.)	1293-2000	49.455	4.435	-0.135		-207.746	-217.224
ZnS (g)	298-2000	37.279	0.071	-0.268		190.071	23.595
ZnI_2 (s)	298-719	85.144	11.461	-1.255		-238.259	-334.094
ZnI_2 (l)	719-999	121.336				-240.744	-536.514
ZnI_2 (g)	298-2000	58.158				-80.694	-3.128
SnS_2 (s)	298-1138	64.894	17.573			-173.682	-287.533
Sn_2S_3 (s)	298-1033	107.027	43.932			-297.455	-458.462

Sn_3S_4 (s)	298-983	150.959	62.342			-418.063	-635.18
SnS (s1)	298-875	35.69	31.296	-0.377		-121.242	-137.808
SnS (s2)	875-1153	40.92	15.648	-0.377		-118.728	-158.534
SnS (l)	1153-1477	74.894				-115.91	-352.616
SnS (g)	298-2000	36.945	0.335	-0.23		97.206	30.473
SnI_4 (g)	298-418	140.93	3.908	-0.9		-256.083	-535.133
SnI_4 (l)	418-626	167.762				-245.559	-646.826
SnI_4 (g)	298-2000	108.194	-0.159	-0.251	-2.636	-151.054	-171.307
SnI_2 (s)	298-593	70.291	29.288			-171	-241.026
SnI_2 (l)	593-990	94.558				-161.413	-346.859
SnI_2 (g)	298-2000	61.923		-0.46		-20.885	-12.205
S_8 R	298-368	14.795	24.075	0.071		-5.242	-59.014
S_8 M	368-388	17.552	19.606			-5.746	-72.831
S_8 (l)	388-717	45.032	-16.636			-11.957	-218.137
S_8 (g)	298-2000	180.318	1.7424	-2.243		36.884	-610.195
S_7 (g)	298-2000	155.122	2.448	-2.034		58.332	-488.315
S_6 (g)	298-2000	132.131	0.502	-1.841		54.138	-409.232
S_5 (g)	298-2000	106.935	1.059	-1.577		72.179	-309.859
S_4 (g)	298-2000	79.881	3.276	-1.18		117.88	-153.143
S_3 (g)	298-2000	53.781	4.531	-0.649		120.459	-41.868
S_2 (g)	298-2000	35.062	2.582	-0.293		117.049	25.98
S (g)	298-2000	24.234	-4.109	0.059	1.343	270.119	31.249
I_2 (s)	298-387	30.125	81.63			-12.61	-79.842
I_2 (l)	298-458	82.006				-10.927	-316.949
I_2 (g)	298-2000	37.254	0.778	-0.05		50.881	47.387
I (g)	298-2000	20.393	0.402	0.029		100.776	64.637

Table 1 Coefficients of the chemical species investigated in the present study as per Eqs 1-4 (data taken from Knacke et al. [259]).

(4) Cu-S phase equilibria

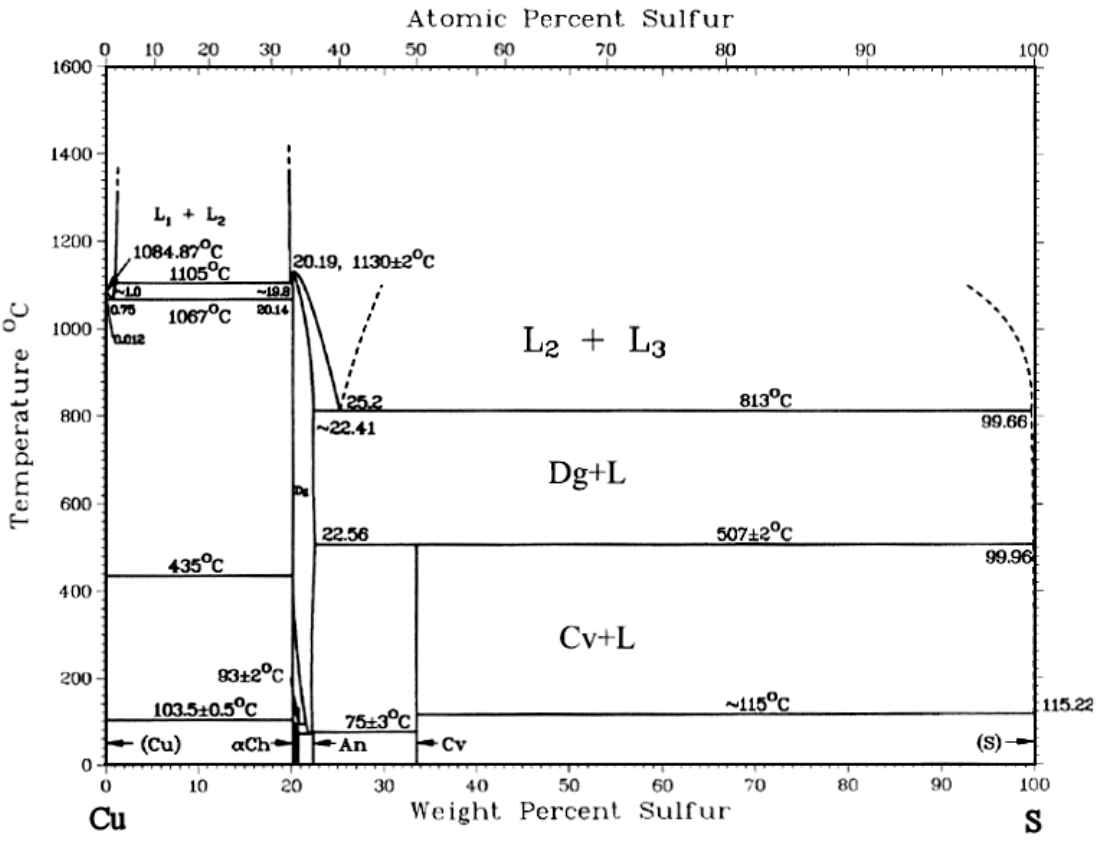

Fig. 5 Cu-S binary phase diagram as reported by Massalski et al. [176].

(5) Sn-S phase equilibria

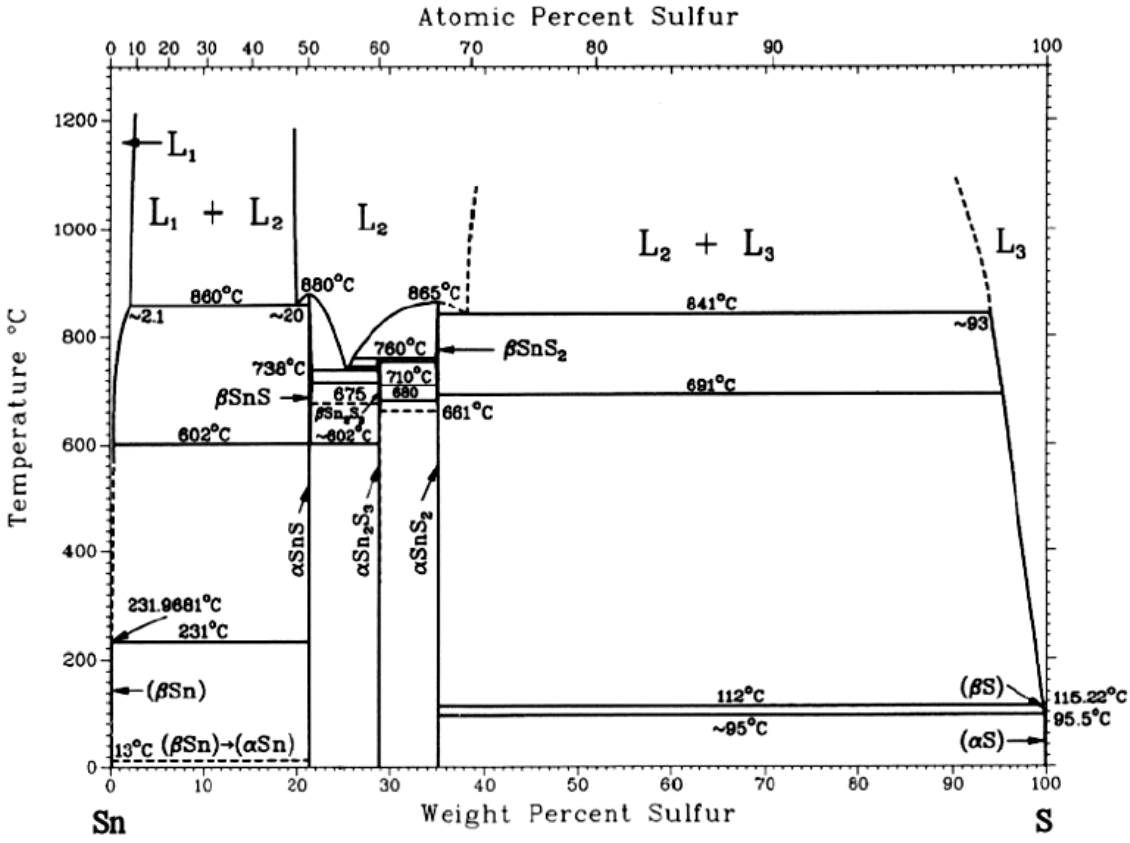

Fig. 6 Sn-S binary phase diagram as reported by Massalski et al. [176].

(6) Zn-S phase equilibria

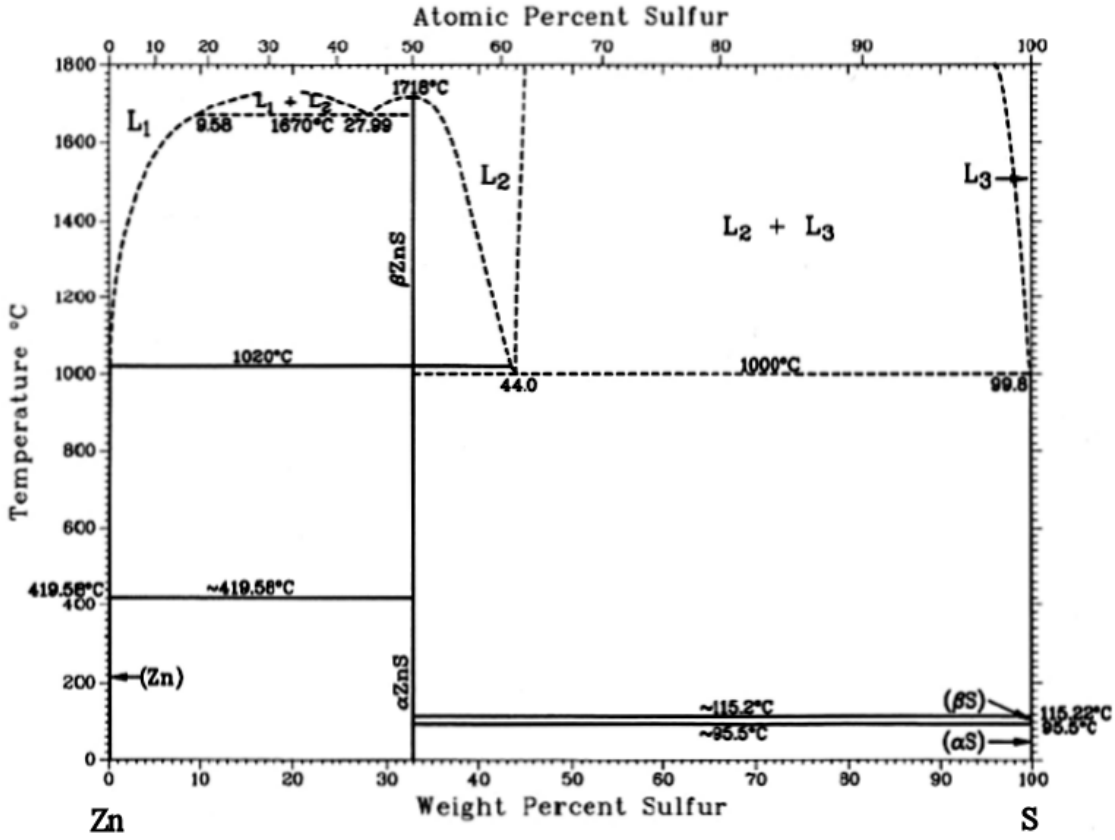

Fig. 7 Zn-S binary phase diagram as reported by Massalski et al. [176].

(7) Convective share of transport

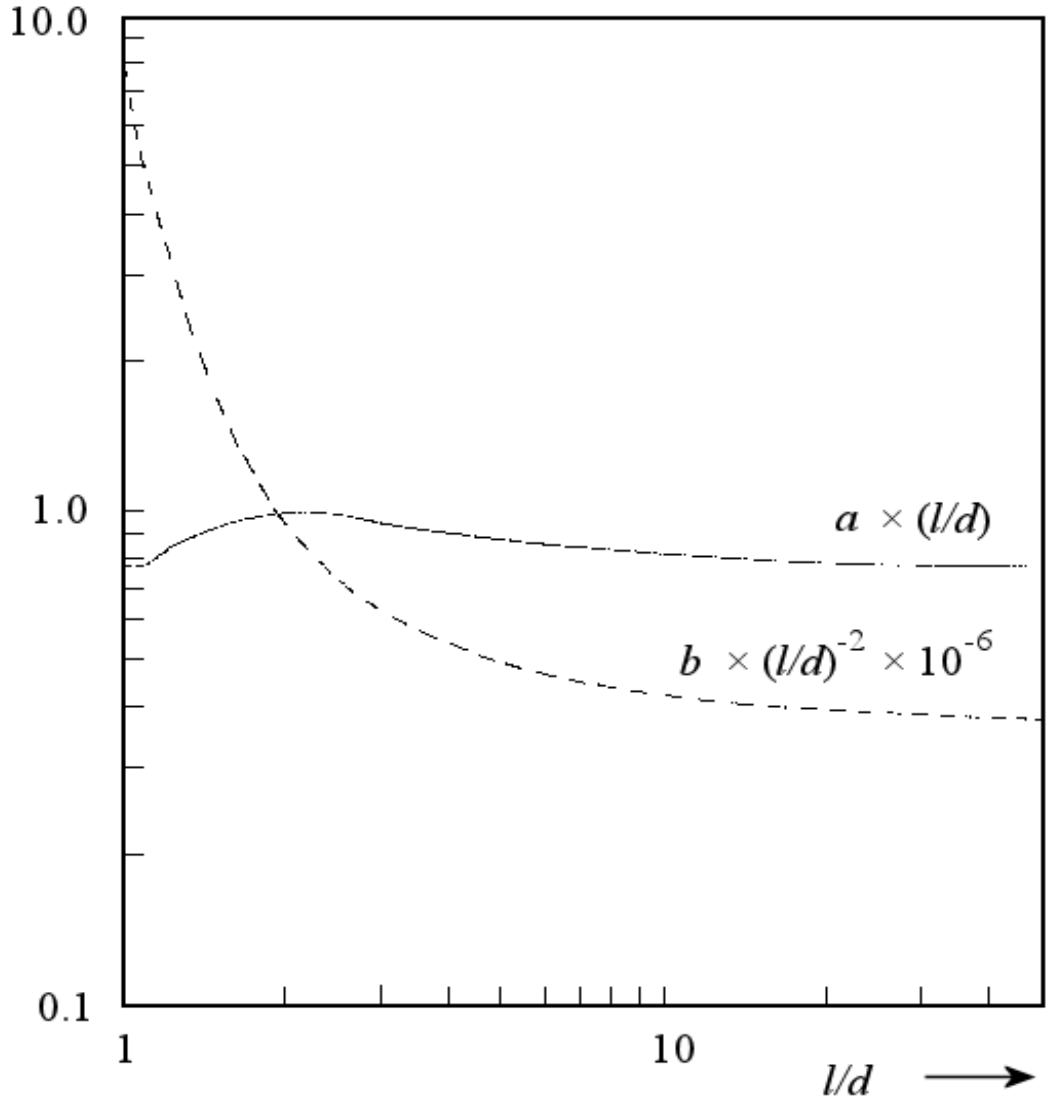

Fig. 8 Graph for the determination of the dimensionless quantities *a* and *b* as functions of the ampoule aspect ratio (*l/d*) employed for the computation of the longitudinal convective share of transport *Kl.* (Eq. 6.4.3), modified from Klosse et al. [363].

Eq. 6.4.3 $Kl. = 1/[a \cdot (Sc.Gr.)^{-2} + b]$

where *Sc.* is the Schmidt fluid number, *Gr.* is the Grashof fluid number.

Bibliographic references

[1] K. Mariolacos, *Neues Jahrbuch fur Mineralogie, Monatshefte* (1998) 164-170.
[2] R.H. Davies, A.T. Dinsdale, J.A. Gisby, J.A.J. Robinson, S.M. Martin, *Calphad* 26 (2002) 229-271.
[3] A.T. Dinsdale, A. Watson, A. Kroupa, J. Vrestal, A. Zemanova, J. Vizdal, *Lead-Free Solders Volume 1*. COST office, 2008.
[4] K. Momma, F. Izumi, *Journal of Applied Crystallography* 41 (2008) 653-658.
[5] O.E.C.D., *Economic Outlook 90 Projection*. December 2011 ed.; Organization for Economic Co-Operation and Development, 2011.
[6] I.M.F., *World economic outlook*. International Monetary Fund, Washington, 2011.
[7] D.O.E., *International Energy Outlook*. U.S. Energy Information Administration, Washington, 2011.
[8] J. Schindler, W. Zittel, *Crude Oil – The Supply Outlook*. Energy Watch Group / Ludwig-Boelkow-Foundation, Berlin, 2008.
[9] W. Zittel, J. Schindler, *Coal: Resources and Future Production*. Energy Watch Group / Ludwig-Boelkow-Foundation, Ottobrunn, 2007.
[10] M.K. Hubbert, *Drilling and Production Practice* (1956).
[11] A.-E. Becquerel, *Compte Rendu des Seances de l'Academie des Sciences* 9 (1839) 561-567.
[12] A. Jäger-Waldau, *PV Status Report 2011*. European Commission, DG Joint Research Centre, Institute for Energy, Renewable Energy Unit, Ispra (VA), Italia, 2011.
[13] J.L. Sawin, E. Martinot, *Renewables 2011 Global Status Report*. REN21 Secretariat and Deutsche Gesellschaft für Internationale Zusammenarbeit (GIZ) GmbH, Paris, 2011.
[14] T.A. Huld, M. Šúri, E.D. Dunlop, M. Albuisson, L. Wald, 20th European Photovoltaic Solar Energy Conference and Exhibition, Barcelona, Spain, 2005.
[15] Desertec Foundation, http://www.desertec.org/, Retrieved on 15-1-2012.
[16] N.S. Lewis, *ChemSusChem* 2 (2009) 383-386.
[17] N.S. Lewis, *Basic research needs for solar energy utilization, report of the basic energy sciences workshop on solar energy utilization*. U.S. Department of Energy, Washington, 2005.
[18] L.L. Kazmerski, *Journal of Electron Spectroscopy and Related Phenomena* 150 (2006) 105-135.
[19] A. Luque, S. Hegedus, John Wiley & Sons Ltd., Chichester,
West Sussex PO19 8SQ, England, 2003.
[20] M.d. Wild-Scholten, *Energy payback times of PV modules and systems* (2009).
[21] N. Pearsall, *Strategic Research Agenda for Photovoltaic Solar Energy Technology*. European Photovoltaic Technology Platform, Luxembourg, 2011.
[22] H.S. Ullal, B.v. Roedern, 22nd European Photovoltaic Solar Energy Conference (PVSEC) and Exhibition, Milano, 2007.
[23] J.F. Carlin, U.S. Geological Survey, Reston, Virginia, 2011, pp. 198.
[24] *British Geological Survey - Risk list* 2011.
[25] C. Wadia, A.P. Alivisatos, D.M. Kammen, *Environmental Science & Technology* 43 (2009) 2072-2077.

[26] B.A. Andersson, *Progress in Photovoltaics: Research and Applications* 8 (2000) 61-76.
[27] L.M. Peter, *Philosophical Transactions of the Royal Society A: Mathematical, Physical and Engineering Sciences* 369 (2011) 1840-1856.
[28] C. Kittel, *Introduction to solid state physics*. 1971.
[29] P. Würfel, *Physics of Solar Cells - From Principles to New Concepts*. Wiley-VCH Verlag GmbH & Co. KGaA, Weinheim, 2005.
[30] R.H. Bube, *Photoelectronic properties of semiconductors*. Cambridge University Press, 1992.
[31] J.J. Loferski, *Journal of Applied Physics* 27 (1956) 777-784.
[32] W. Shockley, H.J. Queisser, *Journal of Applied Physics* 32 (1961) 510-519.
[33] L.L. Kazmerski, *National Renewable Energy Laboratory (NREL), Golden, CO* http://www.nrel.gov/pv/ - Retrieved 07-04-2012 (2012).
[34] S. Trasatti, *Pure and Applied Chemistry* 58 (1986) 955-966.
[35] R. Krishnan, Encyclopedia of Electrochemistry, Wiley-VCH Verlag GmbH & Co. KGaA, 2007.
[36] L.M. Peter, in: J.M. Feliu-Martinez, V.C. Paya, (Eds.), Electrochemistry, Encyclopedia of Life Support Systems, Oxford, 2010.
[37] W.W. Gärtner, *Physical Review* 116 (1959) 84-87.
[38] L.M. Peter, P.J. Dale, J.J. Scragg, G. Zoppi, I. Forbes, *Physica Status Solidi (b)* 245 (2008) 1772-1778.
[39] J.J. Scragg, P.J. Dale, L.M. Peter, *Electrochemistry Communications* 10 (2008) 639-642.
[40] R.A. Smith, *Semiconductors*. 2nd ed.; Cambridge Univeristy Press, London, 1978.
[41] D. Colombara, L.M. Peter, K. Hutchings, K.D. Rogers, S. Schäfer, J.T.R. Dufton, M.S. Islam, *Thin Solid Films* 520 (2012) 5165-5171.
[42] M.A. Green, K. Emery, Y. Hishikawa, W. Warta, E.D. Dunlop, *Progress in Photovoltaics: Research and Applications* 20 (2012) 12-20.
[43] G.B. Haxel, J.B. Hedrick, G.J. Orris, *USGS Fact Sheet 087-02* (2002).
[44] B.R. Pamplin, *Nature* 188 (1960) 136-137.
[45] B.R. Pamplin, *Prog. Cryst. Growth Charact* 3 (1981) 179.
[46] H. Wang, *International Journal of Photoenergy* 2011, 10 pages (2011) Article ID 801292.
[47] K. Ito, T. Nakazawa, *Japanese Journal of Applied Physics* 27 (1988) 2094-2097.
[48] N. Nakayama, K. Ito, *Applied Surface Science* 92 (1996) 171-175.
[49] H. Katagiri, N. Sasaguchi, S. Hando, S. Hoshino, J. Ohashi, T. Yokota, *Solar Energy Materials and Solar Cells* 49 (1997) 407-414.
[50] T.M. Friedlmeier, N. Wieser, T. Walter, H. Dittrich, H.W. Schock, *Proceedings of the 14th European Conference of Photovoltaic Science and Engineering and Exhibition* (1997) 1242.
[51] H. Katagiri, K. Jimbo, S. Yamada, T. Kamimura, W.S. Maw, T. Fukano, T. Ito, T. Motohiro, *Applied Physics Express* 1 (2008) 041201.
[52] B.-A. Schubert, B. Marsen, S. Cinque, T. Unold, R. Klenk, S. Schorr, H.-W. Schock, *Progress in Photovoltaics: Research and Applications* Short communications (2010).
[53] K. Wang, O. Gunawan, T. Todorov, B. Shin, S.J. Chey, N.A. Bojarczuk, D. Mitzi, S. Guha, *Applied Physics Letters* 97 (2010) 143508-3.
[54] T.K. Todorov, K.B. Reuter, D.B. Mitzi, *Advanced Materials* 9999 (2010) NA.

[55] J.J. Scragg, D.M. Berg, P.J. Dale, *Journal of Electroanalytical Chemistry* 646 (2010) 52-59.
[56] A. Ennaoui, M. Lux-Steiner, A. Weber, D. Abou-Ras, I. Kötschau, H.W. Schock, R. Schurr, A. Hölzing, S. Jost, R. Hock, T. Voß, J. Schulze, A. Kirbs, *Thin Solid Films* 517 (2009) 2511-2514.
[57] Q. Guo, G.M. Ford, W.-C. Yang, B.C. Walker, E.A. Stach, H.W. Hillhouse, R. Agrawal, *Journal of the American Chemical Society* (2010) null-null.
[58] D.A.R. Barkhouse, O. Gunawan, T. Gokmen, T.K. Todorov, D.B. Mitzi, *Progress in Photovoltaics: Research and Applications* 20 (2012) 6-11.
[59] G. Springer, *Canadian Mineralogist* 11 (1972) 535-541.
[60] S.R. Hall, S.A. Kissin, J.M. Stewart, *Acta Crystallographica Section A* 31 (1975) S67.
[61] S.R. Hall, J.T. Szymanski, J.M. Stewart, *Canadian Mineralogist* 16 (1978).
[62] S.A. Kissin, D.R. Owens, *Canadian Mineralogist* 17 (1979) 125-135.
[63] S.A. Kissin, *Canadian Mineralogist* 27 (1989) 689-697.
[64] G.P. Bernardini, P. Bonazzi, M. Corazza, F. Corsini, G. Mazzetti, L. Poggi, G. Tanelli, *European Journal of Minerals* 2 (1990) 219-225.
[65] P. Bonazzi, L. Bindi, G.P. Bernardino, S. Menchetti, *Canadian Mineralogist* 41 (2003).
[66] S. Schorr, H.-J. Hoebler, M. Tovar, Berlin neutron scattering center (BENSC), Berlin, 2006.
[67] S. Schorr, *Thin Solid Films* 515 (2007).
[68] S. Schorr, H.-J. Hoebler, M. Tovar, *European Journal of Minerals* 19 (2007).
[69] S. Schorr, G. Gonzalez-Aviles, *Phys. Status Solidi A* 206 (2009).
[70] S. Schorr, M. Tovar, H.-J. Hoebler, H.-W. Schock, *Thin Solid Films* 517 (2009) 2508-2510.
[71] S. Schorr, *Solar Energy Materials and Solar Cells* 95 (2011) 1482-1488.
[72] K. Tanaka, Y. Miyamoto, H. Uchiki, K. Nakazawa, H. Araki, *physica status solidi (a)* 203 (2006) 2891-2896.
[73] K. Hönes, E. Zscherpel, J. Scragg, S. Siebentritt, *Physica B: Condensed Matter* 404 (2009) 4949-4952.
[74] M. Grossberg, J. Krustok, K. Timmo, M. Altosaar, *Thin Solid Films* 517 (2009) 2489-2492.
[75] M. Himmrich, H. Haeuseler, *Spectrochimica Acta Part A: Molecular Spectroscopy* 47 (1991) 933-942.
[76] K. Muska, M. Kauk, M. Altosaar, M. Pilvet, M. Grossberg, O. Volobujeva, *Energy Procedia* (2011).
[77] Y. Moëlo, E. Makovicky, N.N. Mozgova, J.L. Jambor, N. Cook, A. Pring, W. Paar, E.H. Nickel, S. Graeser, S. Karup-Møller, T. Balic-□ unic, W.G. Mumme, F. Vurro, D. Topa, *European Journal of Mineralogy* 20 (2008) 7-62.
[78] P. Villars, A. Prince, H. Okamoto, *Handbook of Ternary Alloys Phase Diagrams*. ASM International, 1995.
[79] E.W. Nuffield, *Economic Geology* 42 (1947) 147-160.
[80] W.N. Jan C. Portheine, *Zeitschrift für Kristallographie* 141 (1975) S 387-402.
[81] A.N. Wachtel, A., *Journal of Electronic Materials* 9 (1980) 281-297.
[82] L.I. Soliman, A.M.A.E. Soad, H.A. Zayed, S.A.E. Ghfar, *Fizika A* 11 (2003) 139-152.
[83] Y. Rodríguez-Lazcano, M.T.S. Nair, P.K. Nair, *Journal of Crystal Growth* 223 (2001) 399-406.

[84] P.K. Nair, L. Huang, M.T.S. Nair, H. Hu, E.A. Meyers, R.A. Zingaro, *Journal of Materials Research* 12 (1997) 651-656.
[85] J.J.M. Binsma, H.A. van der Linden, *Thin Solid Films* 97 (1982) 237-243.
[86] B.M. Basol, *IEEE Transactions on electron devices* 37 (1990) 418.
[87] S.P. Grindle, C.W. Smith, S.D. Mittleman, *Applied Physics Letters* 35 (1979) 24-26.
[88] G. Hodes, D. Cahen, *Solar Cells* 16 (1986) 245-254.
[89] S. Ikegami, *Solar Cells* 23 (1988) 89-105.
[90] P. Cowache, D. Lincot, J. Vedel, *Journal of The Electrochemical Society* 136 (1989) 1646-1650.
[91] D. Cunningham, M. Rubcich, D. Skinner, *Progress in Photovoltaics: Research and Applications* 10 (2002) 159-168.
[92] D. Lincot, J.F. Guillemoles, S. Taunier, D. Guimard, J. Sicx-Kurdi, A. Chaumont, O. Roussel, O. Ramdani, C. Hubert, J.P. Fauvarque, N. Bodereau, L. Parissi, P. Panheleux, P. Fanouillere, N. Naghavi, P.P. Grand, M. Benfarah, P. Mogensen, O. Kerrec, *Solar Energy* 77 (2004) 725-737.
[93] B. Basol, *NREL/SR-520-48590* (2009).
[94] M. Powalla, B. Dimmler, K.-H. Groß, 20th European Photovoltaic Solar Energy Conference, Barcelona, Spain, 2005.
[95] P. Jackson, D. Hariskos, E. Lotter, S. Paetel, R. Wuerz, R. Menner, W. Wischmann, M. Powalla, *Progress in Photovoltaics: Research and Applications* 19 (2011) 894-897.
[96] I. Repins, M.A. Contreras, B. Egaas, C. DeHart, J. Scharf, C.L. Perkins, B. To, R. Noufi, *Progress in Photovoltaics: Research and Applications* 16 (2008) 235-239.
[97] R. Gay, M. Dietrich, C. Frederic, C. Jensen, K. Knapp, D. Willett, Proceedings of the 12th European Photovoltaic Solar Energy Conference, pp. 935–938, 1994., Amsterdam, The Netherlands, 1994, pp. 935-938.
[98] U.P. Singh, S.P. Patra, *International Journal of Photoenergy* 2010 (2010).
[99] K. Kushiya, M. Tachiyuki, T. Kase, I. Sugiyama, Y. Nagoya, D. Okumura, M. Sato, O. Yamase, H. Takeshita, *Solar Energy Materials and Solar Cells* 49 (1997) 277-283.
[100] Y. Goushi, H. Hakuma, K. Tabuchi, S. Kijima, K. Kushiya, *Solar Energy Materials and Solar Cells* 93 (2009) 1318-1320.
[101] T. Dalibor, S. Jost, H. Vogt, A. Heiß, S. Visbeck, T. Happ, J. Palm, A. Avellán, T. Niesen, F. Karg, *Proceedings of EU PVSEC - Hamburg* (2011).
[102] R. Klenk, T. Walter, H.W. Schock, D. Cahen, *Advanced Materials* 5 (1993) 114-119.
[103] J.R. Tuttle, M. Contreras, M.H. Bode, D. Niles, D.S. Albin, R. Matson, A.M. Gabor, A. Tennant, A. Duda, R. Noufi, *Journal of Applied Physics* 77 (1995) 153-161.
[104] T. Wada, N. Kohara, T. Negami, M. Nishitani, *Journal of Materials Research* 12 (1997) 1456-1462.
[105] S. Nishiwaki, S. Siebentritt, M. Giersig, M.C. Lux-Steiner, *Journal of Applied Physics* 94 (2003) 6864-6870.
[106] C. Calderón, P. Bartolo-Pérez, J. Clavijo, J.S. Oyola, G. Gordillo, *Solar Energy Materials and Solar Cells* 94 (2010) 17-21.
[107] T. Tanaka, A. Yoshida, D. Saiki, K. Saito, Q. Guo, M. Nishio, T. Yamaguchi, *Thin Solid Films* 518 (2010) S29-S33.
[108] Y. Hamakawa, Springer Series in Photonics, Springer, 2004.
[109] L. Gutay, D. Regesch, J.K. Larsen, Y. Aida, V. Depredurand, S. Siebentritt, *Applied Physics Letters* 99 (2011) 151912.

[110] J.K. Larsen, L. Gutay, S. Siebentritt, *Applied Physics Letters* 98 (2011) 201910.
[111] T. Haalboom, T. Gödecke, F. Ernst, M. Rühle, R. Herberholz, H.W. Schock, C. Beilharz, K.W. Benz, Proceedings of the 11th Conference on Ternary and Multinary Compounds, Institute of Physics, Salford, 1998, pp. 249-252.
[112] S. Niki, P.J. Fons, A. Yamada, Y. Lacroix, H. Shibata, H. Oyanagi, M. Nishitani, T. Negami, T. Wada, *Applied Physics Letters* 74 (1999) 1630-1632.
[113] J. Kessler, J. Sicx-Kurdi, N. Naghavi, J.-F. Guillemoles, D. Lincot, O. Kerrec, M. Lamirand, L. Legras, P.Mogensen, *Proceedings of the 20th European Photovoltaic Solar Energy Conference, Barcelona, Spain* (2005) 1704-1708.
[114] H. Katagiri, *Materials Research Society Symposium Proceedings* 1165 (2009) M04-01.
[115] S.B. Zhang, S.-H. Wei, A. Zunger, H. Katayama-Yoshida, *Physical Review B* 57 (1998) 9642.
[116] S.-H. Wei, S.B. Zhang, *Journal of Physics and Chemistry of Solids* 66 (2005) 1994-1999.
[117] H.-W. Schock, R. Noufi, *Progress in Photovoltaics: Research and Applications* 8 (2000) 151-160.
[118] S. Chen, X.G. Gong, A. Walsh, S.-H. Wei, *Applied Physics Letters* 96 (2010) 021902-3.
[119] F. Biccari, C. Malerba, P. Mangiapane, A. Mittiga, E. Salza, M. Valentini, G. Arabito, L. Mannarino, ENEA
Ministero dello Sviluppo Economico, 2010.
[120] C. Persson, *Applied Physics Letters* 93 (2008) 072106.
[121] C. Persson, *Journal of Applied Physics* 107 (2010) 053710-8.
[122] U. Rau, K. Taretto, S. Siebentritt, *Applied Physics A: Materials Science & Processing* 96 (2009) 221-234.
[123] J.-F. Guillemoles, L. Kronik, D. Cahen, U. Rau, A. Jasenek, H.-W. Schock, *The Journal of Physical Chemistry B* 104 (2000) 4849-4862.
[124] S.-H. Wei, S.B. Zhang, A. Zunger, *Journal of Applied Physics* 85 (1999) 7214-7218.
[125] H.C. Hsieh, *Journal of Applied Physics* 53 (1982) 1727-1733.
[126] J.F. Guillemoles, *Thin Solid Films* 361-362 (2000) 338-345.
[127] P.J. Dale, K. Hoenes, J. Scragg, S. Siebentritt, Photovoltaic Specialists Conference (PVSC), 2009 34th IEEE, 2009, pp. 002080-002085.
[128] A. Gobeaut, L. Laffont, J.M. Tarascon, L. Parissi, O. Kerrec, *Thin Solid Films* 517 (2009) 4436-4442.
[129] J.J. Scragg, P.J. Dale, L.M. Peter, *Thin Solid Films* 517 (2009) 2481-2484.
[130] J.J. Scragg, Chemistry PhD thesis, University of Bath, Bath, 2010.
[131] H. Flammersberger, Engineering Sciences MSc thesis, Uppsala, 2010.
[132] X. Fontané, L. Calvo-Barrio, V. Izquierdo-Roca, E. Saucedo, A. Perez-Rodriguez, J.R. Morante, D.M. Berg, P.J. Dale, S. Siebentritt, *Applied Physics Letters* 98 (2011) 181905-3.
[133] I.D. Olekseyuk, I.V. Dudchak, L.V. Piskach, *Journal of Alloys and Compounds* 368 (2004) 135-143.
[134] A. Nagoya, R. Asahi, R. Wahl, G. Kresse, *Physical Review B* 81 (2010) 113202.
[135] H. Araki, M. Aya, K. Yuki, S. Tatsuhiro, J. Kazuo, M.W. Shwe, K. Hironori, Y. Makoto, O. Koichiro, T. Akiko, *Thin Solid Films* 517 (2008) 1457-1460.
[136] J.B. Li, V. Chawla, B.M. Clemens, *Advanced Materials* (2012) n/a-n/a.
[137] S. Ahmed, K.B. Reuter, O. Gunawan, L. Guo, L.T. Romankiw, H. Deligianni, *Advanced Energy Materials* 2 (2011) 253-259.

[138] R.N. Bhattacharya, W. Batchelor, H. Wiesner, F. Hasoon, J.E. Granata, K. Ramanathan, J. Alleman, J. Keane, A. Mason, R.J. Matson, R.N. Noufi, *Journal of the Electrochemical Society* 145 (1998) 3435-3440.
[139] R.N. Bhattacharya, J.F. Hiltner, W. Batchelor, M.A. Contreras, R.N. Noufi, J.R. Sites, *Thin Solid Films* 361–362 (2000) 396-399.
[140] H. Tung-Po, C. Chia-Chih, W. Chung-Shin, C. Jen-Chuan, G. Jhe-Wei, C. Wei-Chien, Photovoltaic Specialists Conference (PVSC), 2009 34th IEEE, 2009, pp. 000052-000054.
[141] A. Virtuani, E. Lotter, M. Powalla, U. Rau, J.H. Werner, M. Acciarri, *Journal of Applied Physics* 99 (2006) 014906.
[142] P.A. Fernandes, P.M.P. Salomé, A.F. da Cunha, B.-A. Schubert, *Thin Solid Films* 519 (2011) 7382–7385.
[143] A. Redinger, D.M. Berg, P.J. Dale, S. Siebentritt, *Journal of the American Chemical Society* 133 (2011) 3320-3323.
[144] T.A.M. Friedlmeier, Universität Stuttgart, Stuttgart, 2001.
[145] J. Nelson, Imperial College Press, London, 2003.
[146] D. Colombara, L.M. Peter, K.D. Rogers, J.D. Painter, S. Roncallo, *Thin Solid Films* 519 (2011) 7438-7443.
[147] N.J. Gerein, J.A. Haber, *Chemistry of Materials* 18 (2006) 6289-6296.
[148] N.J. Gerein, J.A. Haber, Photovoltaic Energy Conversion, Conference Record of the 2006 IEEE 4th World Conference on, 2006, pp. 564-566.
[149] V. Izquierdo-Roca, A. Perez-Rodriguez, J.R. Morante, J. Alvarez-Garcia, L. Calvo-Barrio, V. Bermudez, P.P. Grand, L. Parissi, C. Broussillon, O. Kerrec, *Journal of Apllied Physics* 103 (2008) 123109.
[150] J. Alvarez-García, E. Rudigier, N. Rega, B. Barcones, R. Scheer, A. Pérez-Rodríguez, A. Romano-Rodríguez, J.R. Morante, *Thin Solid Films* 431–432 (2003) 122-125.
[151] V. Izquierdo-Roca, A. Pérez-Rodríguez, L. Calvo-Barrio, J. Álvarez-García, J.R. Morante, V. Bermudez, O. Ramdani, J. Kurdi, P.P. Grand, L. Parissi, O. Kerrec, *Thin Solid Films* 516 (2008) 7021-7025.
[152] L.E. Oikkonen, M.G. Ganchenkova, A.P. Seitsonen, R.M. Nieminen, *Journal of Physics: Condensed Matter* 23 (2011) 422202.
[153] S. Chen, J.-H. Yang, X.G. Gong, A. Walsh, S.-H. Wei, *Physical Review B* 81 (2010) 245204.
[154] A. Weber, R. Mainz, H.W. Schock, *Journal of Applied Physics* 107 (2010) 013516-6.
[155] N.J. Gerein, J.A. Haber, Photovoltaic Specialists Conference, 2005. Conference Record of the Thirty-first IEEE, 2005, pp. 159-162.
[156] J.J. Scragg, P.J. Dale, D. Colombara, L.M. Peter, *ChemPhysChem* Accepted (2012).
[157] D. Colombara, L.M. Peter, K.D. Rogers, K. Hutchings, *Journal of Solid State Chemistry* 186 (2012) 36-46.
[158] U. Gösele, K.N. Tu, *Journal of Applied Physics* 53 (1982) 3252-3260.
[159] T.J. Konno, K. Wakoh, K. Shoji, K. Sumiyama, K. Suzuki, *Journal of Physics: Condensed Matter* 10 (1998) 5619.
[160] J. Zhou, G.-Q. Bian, Q.-Y. Zhu, Y. Zhang, C.-Y. Li, J. Dai, *Journal of Solid State Chemistry* 182 (2009) 259-264.
[161] A. Rabhi, M. Kanzari, B. Rezig, *Materials Letters* 62 (2008) 3576-3578.
[162] A. Kyono, M. Kimata, *American Mineralogist* 90 (2005) 162-165.
[163] S. Perniu, A. Duta, J. Schoonman, *IEEE* (2006).
[164] B.R. Nag, *Infrared Physics & Technology* 36 (1995) 831-835.

[165] D. Tang, J. Yang, F. Liu, Y. Lai, M. Jia, J. Li, Y. Liu, *Electrochemical and Solid-State Letters* 15 (2012) D11-D13.
[166] S. Manolache, A. Duta, L. Isac, M. Nanu, A. Goossens, J. Schoonman, *Thin Solid Films* 515 (2007) 5957-5960.
[167] M. Kanzari, A. Rabhi, B. Rezig, *Thin Solid Films* 517 (2009) 2477-2480.
[168] Y. Rodriguez-Lazcano, M.T.S. Nair, P.K. Nair, *Journal of The Electrochemical Society* 152 (2005) G635-G638.
[169] G. Zoppi, N. Beattie, J. Major, R. Miles, I. Forbes, *Journal of Materials Science* 46 (2011) 4913-4921.
[170] W.B. Pearson, *Zeitschrift für Kristallographie* 171 (1985) 23-39.
[171] O. Teppo, P. Taskinen, *Scandinavian Journal of Metallurgy* 20 (1991) 174-182.
[172] H. Okamoto, *Journal of Phase Equilibria* 16 (1995) 472-472.
[173] X. Liu, C. Wang, I. Ohnuma, R. Kainuma, K. Ishida, *Journal of Phase Equilibria* 21 (2000) 432-442.
[174] D. Manasijevic, D. Minic, D. Zivkovic, D. Rajnovic, *Intermetallics* 16 (2008) 107-112.
[175] W. Gierlotka, D. Jendrzejczyk-Handzlik, *Journal of Alloys and Compounds* 484 (2009) 172-176.
[176] T.B. Massalski, *Binary Alloy Phase Diagrams*. 2nd ed.; ASM International, 1990.
[177] T. Watanabe, *Materials Science and Engineering: A* 179–180, Part 1 (1994) 193-197.
[178] P.L. Cavallotti, L. Nobili, A. Vicenzo, *Electrochimica Acta* 50 (2005) 4557-4565.
[179] O. Younes, L. Zhu, Y. Rosenberg, Y. Shacham-Diamand, E. Gileadi, *Langmuir* 17 (2001) 8270-8275.
[180] F.A. Kröger, *Journal of The Electrochemical Society* 125 (1978) 2028-2034.
[181] D. Lincot, *Thin Solid Films* 487 (2005) 40– 48.
[182] A. Brenner, *Electrodeposition of Alloys - Principles and Practice*. Academic Press, New York
London, 1963.
[183] E. Raub, *Zeitschrift für Erzbergbau und Metallhuttenwessen* 5 (1952) 155-160.
[184] L.L. Barbosa, M.R.H. de Almeida, R.M. Carlos, M. Yonashiro, G.M. Oliveira, I.A. Carlos, *Surface and Coatings Technology* 192 (2005) 145-153.
[185] M. Pourbaix, *Atlas of Electrochemical Equilibria in Aqueous Solutions*. Cebelcor, Bruxelles, 1974.
[186] R. Hansen, Chemical Engineering, Newark College of Engineering, 1952.
[187] F.-y. Liu, Y. LÜ, Z.-a. Zhang, Y.-q. Lai, J. Li, Y.-x. Liu, *Transactions of Nonferrous Metals Society of China* 18 (2008) 884-889.
[188] N.N. Greenwood, A. Earnshaw, *Chemistry of the Elements*. Pergamon Press.
[189] C.Y. Cummings, G. Zoppi, I. Forbes, P.J. Dale, J.J. Scragg, L.M. Peter, G. Kociok-Köhn, F. Marken, *Journal of Electroanalytical Chemistry* 645 (2010) 16-21.
[190] S. Kashida, K. Yamamoto, *Journal of Physics: Condensed Matter* 3 (1991) 6559.
[191] G. Will, E. Hinze, A.R.M. Abdelrahman, *European Journal of Mineralogy* 14 (2002) 591-598.
[192] R.A. Wibowo, W.S. Kim, B. Munir, K.H. Kim, *Advanced Materials Research* 29-30 (2007) 79-82.
[193] M. Bär, B.-A. Schubert, B. Marsen, S. Krause, S. Pookpanratana, T. Unold, L. Weinhardt, C. Heske, H.-W. Schock, *Applied Physics Letters* 99 (2011) 152111.

[194] F.J. Bryant, A.K. Hariri, S. Salkalachen, C.G. Scott, *J. Phys. D: Appl. Phys.* 16 (1983) 1755-1760.
[195] J.R. Lambert, *Reviews of Infectious Diseases* 13 (1991) S691-S695.
[196] S. Amore, E. Ricci, G. Borzone, R. Novakovic, *Materials Science and Engineering: A* 495 (2008) 108-112.
[197] B. Brunetti, D. Gozzi, M. Iervolino, V. Piacente, G. Zanicchi, N. Parodi, G. Borzone, *Calphad* 30 (2006) 431-442.
[198] R. Novakovic, D. Giuranno, E. Ricci, S. Delsante, D. Li, G. Borzone, *Surface Science* 605 (2011) 248-255.
[199] A. Sabbar, A. Zrineh, J.P. Dubès, M. Gambino, J.P. Bros, G. Borzone, *Thermochimica Acta* 395 (2002) 47-58.
[200] M.F. Razmara, C.M.B. Henderson, R.A.D. Pattrick, *Mineralogical Magazine* (1997) 79-88.
[201] S. Pawar, A. Pawar, P. Bhosale, *Bulletin of Materials Science* 8 (1986) 423-426.
[202] P.S. Sonawane, P.A. Wani, L.A. Patil, T. Seth, *Materials Chemistry and Physics* 84 (2004) 221-227.
[203] J.T.R. Dufton, A. Walsh, P.M. Panchmatia, L.M. Peter, D. Colombara, M.S. Islam, *Physical Chemistry Chemical Physics* 14 (2012) 7229-7233.
[204] V. Kocman, E.W. Nuffield, *Acta Crystallographica* B29 (1973) 2528.
[205] E. Makovicky, *Journal of Solid State Chemistry* 49 (1983) 85-92.
[206] T.T. Chow, W. He, J. Ji, A.L.S. Chan, *Solar Energy* 81 (2007) 123-130.
[207] F. Mesa, A. Dussan, G. Gordillo, *physica status solidi (c)* 7 (2010) 917-920.
[208] N.J. Gerein, J.A. Haber, *Chemistry of Materials* 18 (2006) 6297-6302.
[209] V. Estrella, M.T.S. Nair, P.K. Nair, *J Semiconductor Science and Technology* 2 (2003) 190-194.
[210] K. Siemer, J. Klaer, I. Luck, J. Bruns, R. Klenk, D. Bräunig, *Solar Energy Materials and Solar Cells* 67 (2001) 159-166.
[211] D.-Y. Peng, J. Zhao, *The Journal of Chemical Thermodynamics* 33 (2001) 1121-1131.
[212] L. Chen, J. Huang, C.-L. Yang, *Environmental Progress* 20 (2001) 175-181.
[213] C.L. Liao, C.W. Chu, K.Z. Fung, I.C. Leu, *Journal of Alloys and Compounds* 441 (2007) L1-L6.
[214] F. Jia, C. Yu, K. Deng, L. Zhang, *The Journal of Physical Chemistry C* 111 (2007) 8424-8431.
[215] X. Lu, E. Bischoff, R. Spolenak, T.J. Balk, *Scripta Materialia* 56 (2007) 557-560.
[216] X. Lu, T.J. Balk, R. Spolenak, E. Arzt, *Thin Solid Films* 515 (2007) 7122-7126.
[217] L. Ribeaucourt, G. Savidand, D. Lincot, E. Chassaing, *Electrochimica Acta* 56 (2011) 6628-6637.
[218] A. Sugaki, H. Shima, Technology reports, Technology report of Yamaguchi University, 1972, pp. 45-70.
[219] M. Yan, M. Scaronob, D.E. Luzzi, V. Vitek, G.J. Ackland, M. Methfessel, C.O. Rodriguez, *Physical Review B* 47 (1993) 5571.
[220] M. Zribi, M. Kanzari, B. Rezig, *Materials Letters* 60 (2006) 98-103.
[221] F. Mesa, G. Gordillo, T. Dittrich, K. Ellmer, R. Baier, S. Sadewasser, *Applied Physics Letters* 96 (2010) 082113-082113-3.
[222] W.N. Shafarman, L. Stolt, in: A. Luque, S. Hegedus, (Eds.), Cu(InGa)Se_2 Solar Cells, John Wiley and Sons, Chichester, West Sussex PO19 8SQ, England, 2003.

[223] B. Shin, O. Gunawan, Y. Zhu, N.A. Bojarczuk, S.J. Chey, S. Guha, *Progress in Photovoltaics: Research and Applications* (2011) n/a-n/a.
[224] B.J. Stanbery, *Critical Reviews in Solid State & Materials Science* 27 (2002) 73.
[225] A.M. Gabor, J.R. Tuttle, D.S. Albin, M.A. Contreras, R. Noufi, A.M. Hermann, *Applied Physics Letters* 65 (1994) 198-200.
[226] T. Todorov, D.B. Mitzi, *ChemInform* 41 (2010) no-no.
[227] C. von Klopmann, J. Djordjevic, E. Rudigier, R. Scheer, *Journal of Crystal Growth* 289 (2006) 121-133.
[228] N.B. Pilling, R.E. Bedworth, *Journal of the Institute of Metals* 29 (1923) 529-591.
[229] H.S. Ulal, B. von Roedern, *Solid State Technology* 51 (2008) 52-54.
[230] N.G. Dhere, *Solar Energy Materials and Solar Cells* 91 (2007) 1376-1382.
[231] H. Katagiri, K. Jimbo, W.S. Maw, K. Oishi, M. Yamazaki, H. Araki, A. Takeuchi, *Thin Solid Films* 517 (2009) 2455-2460.
[232] T.L. Chu, S.S. Chu, S.C. Lin, J. Yue, *Journal of The Electrochemical Society* 131 (1984) 2182-2185.
[233] H. Araki, Y. Kubo, A. Mikaduki, K. Jimbo, W.S. Maw, H. Katagiri, M. Yamazaki, K. Oishi, A. Takeuchi, *Solar Energy Materials and Solar Cells* 93 (2009) 996-999.
[234] B.H. Ryu, S.P. Yoon, J. Han, S.W. Nam, T.H. Lim, S.A. Hong, K.B. Kim, *Electrochimica Acta* 50 (2004) 189-198.
[235] E. Antolini, *Solid State Ionics* 170 (2004) 159-171.
[236] K.N. Lee, in: R. Dennis, (Ed.), The gas turbine handbook, U.S. Department of Energy - National Energy Technology Laboratory, Morgantown - West Virginia, 2006.
[237] C. von Klopmann, J. Djordjevic, R. Scheer, *Journal of Crystal Growth* 289 (2006) 113-120.
[238] R. Schurr, A. Hölzing, S. Jost, R. Hock, T. Voβ, J. Schulze, A. Kirbs, A. Ennaoui, M. Lux-Steiner, A. Weber, I. Kötschau, H.W. Schock, *Thin Solid Films* 517 (2009) 2465-2468.
[239] E. Rudigier, J. Djordjevic, C. von Klopmann, B. Barcones, A. Pérez-Rodríguez, R. Scheer, *Journal of Physics and Chemistry of Solids* 66 (2005) 1954-1960.
[240] C. Broussillou, M. Andrieux, M. Herbst-Ghysel, M. Jeandin, J.S. Jaime-Ferrer, S. Bodnar, E. Morin, *Solar Energy Materials and Solar Cells* 95, Supplement 1 (2011) S13-S17.
[241] V.F. Ross, *Economic Geology* 49 (1954) 734-752.
[242] G. Tammann, *Zeitschrift für anorganische und allgemeine Chemie* 111 (1920) 78.
[243] H. Schmalzried, *Angewandte Chemie International Edition in English* 2 (1963) 251-254.
[244] J.-C. Zhao, M.R. Notis, *Materials Science and Engineering: R: Reports* 15 (1995) 135-207.
[245] C. Kinoshita, T. Eguchi, *Acta Metallurgica* 20 (1972) 45-52.
[246] D.L. Beke, Z. Erdélyi, *Physical Review B* 73 (2006) 035426.
[247] F.H. Lu, P. Franke, C.S. Nichols, R. Dieckmann, *Journal of Applied Physics* 76 (1994) 848-857.
[248] F.-H. Lu, *Computational Materials Science* 14 (1999) 48-55.
[249] S. Mrowec, K. Przybylski, *High Temperature Materials and Processes* 6 (1984) 1-79.

[250] V. Kupčík, L. Veselá-Nováková, *Mineralogy and Petrology* 14 (1970) 55-59.
[251] L.F. Lundegaard, E. Makovicky, T. Boffa-Ballaran, T. Balic-Zunic, *Physics and Chemistry of Minerals* 32 (2005) 578-584.
[252] L.F. Lundegaard, R. Miletich, T. Balic-Zunic, E. Makovicky, *Physics and Chemistry of Minerals* 30 (2003) 463-468.
[253] L.H. Ahrens, *Geochimica et Cosmochimica Acta* 2 (1952) 155-169.
[254] R. Shannon, *Acta Crystallographica Section A* 32 (1976) 751-767.
[255] D. Chakrabarti, D. Laughlin, *Journal of Phase Equilibria* 5 (1984) 148-155.
[256] M. Takagi, *Journal of the Physical Society of Japan* 9 (1954) 359-363.
[257] J. Sun, S.L. Simon, *Thermochimica Acta* 463 (2007) 32-40.
[258] Q.S. Mei, K. Lu, *Progress in Materials Science* 52 (2007) 1175-1262.
[259] O. Knacke, O. Kubaschewski, *Thermochemical Properties of Inorganic Substances*. 2nd ed.; Springer-Verlag, Verlag Stahleisen Berlin, New York, Düsseldorf, 1991.
[260] H. Rau, T.R.N. Kutty, J.R.F. Guedes De Carvalho, *The Journal of Chemical Thermodynamics* 5 (1973) 833-844.
[261] L.P. Hammett, *Journal of the American Chemical Society* 59 (1937) 96-103.
[262] D.A. Sverjensky, *Nature* 358 (1992) 310-313.
[263] D.A. Sverjensky, P.A. Molling, *Nature* 356 (1992) 231-234.
[264] S. Chaisitsak, A. Yamada, M. Kongai, *Japanese Journal of Applied Physics* 41 (2002) 507-513.
[265] M.A. Contreras, I. Repins, W.K. Metzger, M. Romero, D. Abou-Ras, *physica status solidi (a)* 206 (2009) 1042-1048.
[266] J.-F. Nowak, M. Lambertin, J.-C. Colson, *Corrosion Science* 17 (1977) 603-613.
[267] J. Furer, M. Lambertin, J.-C. Colson, *Corrosion Science* 17 (1977) 625-632.
[268] S. Sanchez, S. Cassaignon, J. Vedel, H.G. Meier, *Electrochimica Acta* 41 (1996) 1331-1339.
[269] S. Cassaignon, T. Pauporté, J. Guillemoles, J. Vedel, *Ionics* 4 (1998) 364-371.
[270] A. Etienne, *Journal of The Electrochemical Society* 117 (1970) 870-874.
[271] N.R. de Tacconi, K. Rajeshwar, R.O. Lezna, *The Journal of Physical Chemistry* 100 (1996) 18234-18239.
[272] A. Brückman, *Corrosion Science* 7 (1967) 51-59.
[273] L.M. Peter, *Journal of Electroanalytical Chemistry and Interfacial Electrochemistry* 98 (1979) 49-58.
[274] D. Kieven, A. Grimm, I. Lauermann, T. Rissom, R. Klenk, *Applied Physics Letters* 96 (2010) 262101.
[275] Z. Grubać, M. Metikos-Hukovic, *Journal of Electroanalytical Chemistry* 565 (2004) 85-94.
[276] S.P. Sharma, *Journal of The Electrochemical Society* 127 (1980) 21-26.
[277] J. Oudar, J. Bénard, *Acta Metallurgica* 7 (1959) 295-296.
[278] V.A. Phillips, *Journal of Applied Physics* 33 (1962) 712-717.
[279] T.E. Graedel, J.P. Franey, G.J. Gualtieri, G.W. Kammlott, D.L. Malm, *Corrosion Science* 25 (1985) 1163-1180.
[280] J.M. Saleh, C. Kemball, M.W. Roberts, *Transactions of the Faraday Society* 57 (1961).
[281] J.J. Scragg, T. Ericson, T. Kubart, M. Edoff, C. Platzer-Björkman, *Chemistry of Materials* 23 (2011) 4625-4633.
[282] G. Matei, Y. Takasaki, K. Itagaki, K. Koike, *Journal of the Mining and Materials Processing Institute of Japan* 116 (2000) 515-519.

[283] V. Piacente, V.D. Gianfreda, G. Bardi, *The Journal of Chemical Thermodynamics* 15 (1983) 7-14.
[284] V. Piacente, P. Scardala, D. Ferro, *Journal of Alloys and Compounds* 178 (1992) 101-115.
[285] B.K. Veselovskii, *Zhurnal Prikladnoi Khimii* 15 (1942) 422.
[286] G.G. Gospodinov, A.S. Pashinkin, Z. Boncheva-Mladenova, A.V. Novoselova, *Izvestiya Akademii Nauk SSSR - Neorganicheskie Materialy* 6 (1970) 1242.
[287] G.P. Ustyugov, E.N. Vigdorovich, B.M. Kuadzhe, I.A. Timoshin, *Izvestiya Akademii Nauk SSSR - Neorganicheskie Materialy* 5 (1969) 589.
[288] A.A. Ryazantsev, A.S. Pashinkin, A.V. Novoselova, *Vestnik Moskovskogo Universiteta Khimii* 23 (1968) 95.
[289] S. Jones, *Advances in extractive metallurgy* Int. Symp. IMM (1977).
[290] J. Yang, Y.-C. Liu, H.-M. Lin, C.-C. Chen, *Advanced Materials* 16 (2004) 713-716.
[291] A.K. Fischer, *Journal of Chemical Physics* 45 (1966) 375-377.
[292] Y. Hua, Y. Yang, F. Zhu, *Journal of Materials Science and Technology* 19 (2003) 4.
[293] A. Sugaki, H. Shima, A. Kitakaze, Technology reports, Technology reports of Yamaguchi University, 1973, pp. 169-181.
[294] P.C. Chaubal, M. Nagamori, *Metallurgical and Materials Transactions B* 19 B (1988) 547-556.
[295] K.T. Ramakrishna Reddy, I. Forbes, R.W. Miles, *Applied Surface Science* 169-170 (2001) 387-391.
[296] A. Joswig, M. Gossla, H. Metzner, U. Reislöhner, T. Hahn, W. Witthuhn, *Thin Solid Films* 515 (2007) 5921-5924.
[297] N.F. Spycher, M.H. Reed, *Economic Geology* 84 (1989) 328-359.
[298] V.P. Zakaznova-Iakovleva, A.A. Migdisov, V.P. Zakaznova-Iakovlevaa, O.M. Suleimenov, A.E. Williams-Jones, Y.V. Alekhin, *Geochimica et Cosmochimica Acta* 65 (2001) 289-298.
[299] A.V. Steblevskii, V.V. Zharov, A.S. Alikhanyan, V.I. Gorgoraki, A.S. Pashinkin, *Russian Journal of Inorganic Chemistry* 34 (1989) 891-894.
[300] J.P. King, Y. Asmeron, *Tribology Transactions* (1981) 497-504.
[301] D. Ozimina, *Tribology Letters* 13 (2002) 111-117.
[302] A.V. Steblevskii, V.V. Zharov, A.S. Alikhanyan, A.S. Pashinkin, V.I. Gorgoraki, *Russian Journal of Inorganic Chemistry* 34 (1989) 1821-1826.
[303] D.B. Mitzi, M. Yuan, W. Liu, A.J. Kellock, S.J. Chey, L. Gignac, A.G. Schrott, *Thin Solid Films* 517 (2009) 2158-2162.
[304] S. Merdes, R. Mainz, J. Klaer, A. Meeder, H. Rodriguez-Alvarez, H.W. Schock, M.C. Lux-Steiner, R. Klenk, *Solar Energy Materials and Solar Cells* 95 (2011) 864-869.
[305] K. Maeda, K. Tanaka, Y. Fukui, H. Uchiki, *Solar Energy Materials and Solar Cells* 95 (2011) 2855-2860.
[306] R.T. Downs, The RRUFF Project: an integrated study of the chemistry, crystallography, Raman and infrared spectroscopy of minerals. 19th General Meeting of the International Mineralogical Association, Kobe, Japan, 2006.
[307] P.J. Brown, A.G. Fox, E.N. Maslen, M.A. O'Keefe, B.T.M. Willis, in: E. Prince, (Ed.), International tables for crystallography, International Union of Crystallography, 2006, pp. 554-595.
[308] in: T. Hahn, (Ed.), International Tables for Crystallography - Volume A, Space-group symmetry International Union of Crystallography, 2006.

[309] J. Paier, R. Asahi, A. Nagoya, G. Kresse, *Physical Review B* 79 (2009) 115126.
[310] S. Chen, X.G. Gong, A. Walsh, S.-H. Wei, *Physical Review B* 79 (2009) 165211.
[311] S. Chen, X.G. Gong, A. Walsh, S.-H. Wei, *Applied Physics Letters* 94 (2009) 041903-041903-3.
[312] E.M. Kartzmark, *Journal of Chemical Education* 57 (1980) 125.
[313] D.B. Mitzi, O. Gunawan, T.K. Todorov, K. Wang, S. Guha, *Solar Energy Materials and Solar Cells* 95 (2011) 1421-1436.
[314] P.A. Fernandes, P.M.P. Salomé, A.F. da Cunha, *Thin Solid Films* 517 (2009) 2519-2523.
[315] P.A. Fernandes, P.M.P. Salomé, A.F. da Cunha, *Journal of Alloys and Compounds* 509 (2011) 7600-7606.
[316] R. Nitsche, D.F. Sargent, P. Wild, *Journal of Crystal Growth* 1 (1966).
[317] H. Schäfer, *Chemical Transport Reactions*. Academic Press Inc., 1964.
[318] M.M. Faktor, I. Garrett, *Growth of crystals from the vapour*. Chapman and Hall, Ltd., London, 1976.
[319] G. Mandel, *The Journal of Chemical Physics* 37 (1962) 1177-1180.
[320] R. Nitsche, *Journal of Physics and Chemistry of Solids* 17 (1960) 163-165.
[321] C. Paorici, L. Zanotti, G. Zuccalli, *Journal of Crystal Growth* 43 (1978) 705-710.
[322] O. Senthil Kumar, S. Soundeswaran, R. Dhanasekaran, *Crystal Growth & Design* 2 (2002) 585-589.
[323] H. Schäfer, H. Plautz, C. Balarew, J. Bazelkov, *Zeitschrift für anorganische und allgemeine Chemie* 440 (1978) 130-136.
[324] I. Jandl, K.W. Richter, H. Ipser, *Solid State Sciences* 13 (2011) 1108-1114.
[325] M. Lenz, R. Gruehn, *Chemical Reviews* 97 (1997) 2967-2994.
[326] F.J. Zeleznik, S. Gordon, *Industrial & Engineering Chemistry* 60 (1968) 27-57.
[327] P. Vonka, J. Leitner, *Calphad* 19 (1995) 25-36.
[328] B.I. Noläng, M.W. Richardson, *Journal of Crystal Growth* 34 (1976) 198-204.
[329] B.I. Noläng, M.W. Richardson, *Journal of Crystal Growth* 34 (1976) 205-214.
[330] J.H.E. Jeffes, *Journal of Crystal Growth* 3-4 (1968) 13-32.
[331] P. Björnbom, *Industrial & Engineering Chemistry Fundamentals* 20 (1981) 161-164.
[332] R.W. Missen, W.R. Smith, *Journal of Chemical Education* 67 (1990) 876.
[333] M.R. Samuels, *Industrial & Engineering Chemistry Fundamentals* 10 (1971) 643-644.
[334] W.B. White, S.M. Johnson, G.B. Dantzig, *Chemical Equilibrium in Complex Mixtures*. AIP, 1958.
[335] W.R. Smith, R.W. Missen, *Journal of Chemical and Engineering and Education* 13 (1979) 26-32.
[336] W.R. Smith, R.W. Missen, *Chemical Reaction Equilibrium Analysis: Theory and Algorithms*. John Wiley & Sons, 1982.
[337] S.C. Althoen, R. McLaughlin, *The American Mathematical Monthly* 94 (1987) 130-142.
[338] S. Fiechter, M. Martinez, G. Schmidt, W. Henrion, Y. Tomm, *Journal of Physics and Chemistry of Solids* 64 (2003) 1859-1862.
[339] J.R. Craig, P.B. Barton, *Economic Geology* 68 (1973) 493-506.

[340] D.J. Vaughan, J.R. Craig, *Mineral chemistry of metal sulfides*. Cambridge University Press, Cambridge, 1978.
[341] A. Walsh, *Personal communication* (2011).
[342] G.-X. Qian, R.M. Martin, D.J. Chadi, *Physical Review B* 38 (1988) 7649.
[343] P. Lukashev, W.R.L. Lambrecht, T. Kotani, M. van Schilfgaarde, *Physical Review B* 76 (2007) 195202.
[344] G. Dubrovskii, *Physics of the Solid State* 40 (1998) 1557-1562.
[345] M.J. Buerger, B.J. Wuensch, *Science* 141 (1963) 276-277.
[346] C.-Y. Yeh, Z.W. Lu, S. Froyen, A. Zunger, *Physical Review B* 46 (1992) 10086.
[347] Y.-T. Zhai, S. Chen, J.-H. Yang, H.-J. Xiang, X.-G. Gong, A. Walsh, J. Kang, S.-H. Wei, *Physical Review B* 84 (2011) 075213.
[348] H.W. Kerr, J. Cisse, G.F. Bolling, *Acta Metallurgica* 22 (1974) 677-686.
[349] T. Shimada, K. Oishi, K. Jimbo, H. Katagiri, H. Araki, O. Yoshida, M. Yamazaki, S. Kobayashi, N. Tsuboi, IEICE Technical report, 2005.
[350] M. Lachab, A.A. Attia, C. Llinarès, *Journal of Crystal Growth* 280 (2005) 474-482.
[351] H. Matsushita, T. Ichikawa, A. Katsui, *Journal of Materials Science* 40 (2005) 2003-2005.
[352] A. Nagaoka, K. Yoshino, H. Taniguchi, T. Taniyama, H. Miyake, *Journal of Crystal Growth* (2012).
[353] A. Nagaoka, K. Yoshino, H. Taniguchi, T. Taniyama, H. Miyake, *Japanese Journal of Applied Physics* 50 (2011) 128001.
[354] G.H. Moh, L.A. Taylor, *Neues Jahrbuch für Mineralogie - Monatshefte* (1971) 450-459.
[355] M. Altosaar, J. Raudoja, K. Timmo, M. Danilson, M. Grossberg, J. Krustok, E. Mellikov, *Physica Status Solidi (a)* 205 (2008) 167-170.
[356] K. Timmo, M. Altosaar, J. Raudoja, K. Muska, M. Pilvet, M. Kauk, T. Varema, M. Danilson, O. Volobujeva, E. Mellikov, *Solar Energy Materials and Solar Cells* 94 (2010) 1889-1892.
[357] M. Altosaar, A. Jagomägi, M. Kauk, M. Krunks, J. Krustok, E. Mellikov, J. Raudoja, T. Varema, *Thin Solid Films* 431-432 (2003) 466-469.
[358] W. Schäfer, R. Nitsche, *Materials Research Bulletin* 9 (1974).
[359] J.J.M. Binsma, L.J. Giling, J. Bloem, *Journal of Crystal Growth* 50 (1980) 429-436.
[360] K. Böttcher, H. Hartmann, *Journal of Crystal Growth* 146 (1995) 53-58.
[361] H. Goslowsky, S. Fiechter, R. Könenkamp, H.J. Lewerenz, *Solar Energy Materials* 13 (1986) 221-232.
[362] P. Prabukanthan, R. Dhanasekaran, *Crystal Research and Technology* 43 (2008) 1292-1296.
[363] K. Klosse, P. Ullersma, *Journal of Crystal Growth* 18 (1973) 167-174.
[364] L. Guen, W.S. Glaunsinger, A. Wold, *Materials Research Bulletin* 14 (1979) 463-467.
[365] A. Klimova, V. Ananichev, M. Arif, L. Blinov, *Glass Physics and Chemistry* 31 (2005) 760-762.
[366] D. Drouin, A.R. Couture, D. Joly, X. Tastet, V. Aimez, R. Gauvin, *Scanning* 29 (2007) 92-101.
[367] R. Zuo, W. Wang, *Journal of Crystal Growth* 236 (2002) 695-710.
[368] K. Böttcher, H. Hartmann, R. Röstel, *Journal of Crystal Growth* 159 (1996) 161-166.
[369] L.I. Berger, B.R. Pamplin, *Properties of semiconductors - Handbook of Chemistry and Physics*. 89th ed.; CRC/Taylor and Francis, Boca Raton, 2009.

[370] F.W. Ostwald, *Lehrbuch der Allgemeinen Chemie*. Engelmann, Leipzig, 1896.
[371] A. Szczerbakow, K. Durose, *Progress in Crystal Growth and Characterization of Materials* 51 (2005) 28.
[372] A. Szczerbakow, *Journal of Crystal Growth* 257 (2003) 31-41.
[373] W.W. Piper, S.J. Polich, *Journal of Applied Physics* 32 (1961) 1278-1279.
[374] E.V. Markov, A.A. Davydov, *Izvestiya Akademii Nauk SSSR - Neorganicheskie Materialy* 7 (1971) 575.
[375] T.F. Ciszek, *Journal of Crystal Growth* 70 (1984) 405-410.
[376] P. Atkins, J.d. Paula, *Physical Chemistry*. 8th ed.; Oxford University Press, Oxford, 2006.
[377] H. Eyring, *The Journal of Chemical Physics* 3 (1935) 107-115.
[378] C. Wilkinson, J.A. Cowan, D.A.A. Myles, F. Cipriani, G.J. McIntyre, *Neutron News* 13 (2002) 37-41.
[379] E. Mugnaioli, G. Capitani, F. Nieto, M. Mellini, *American Mineralogist* 94 (2009) 793-800.
[380] X. Chen, H. Wada, A. Sato, M. Mieno, *Journal of Solid State Chemistry* 139 (1998) 144-151.
[381] M. Rabadanov, *Kristallografiya* 40 (1995) 21-27.
[382] M. Ichimura, Y. Nakashima, *Japanese Journal of Applied Physics* 48 (2009).
[383] C.Y. Cummings, P.E. Frith, G. Zoppi, I. Forbes, K.D. Rogers, D.W. Lane, F. Marken, *Thin Solid Films* 519 (2011) 7458–7463.
[384] O. Brafman, M. Cardona, Z. Vardeny, *Physical Review B* 15 (1977) 1081-1086.
[385] M. Ishii, K. Shibata, H. Nozaki, *Journal of Solid State Chemistry* 105 (1993) 504-511.
[386] C.G. Munce, G.K. Parker, S.A. Holt, G.A. Hope, *Colloids and Surfaces A: Physicochemical and Engineering Aspects* 295 (2007) 152-158.
[387] B. Minceva-Sukarova, M. Najdoski, I. Grozdanov, C.J. Chunnilall, *Journal of Molecular Structure* 410–411 (1997) 267-270.
[388] P.A. Fernandes, P.M.P. Salomé, A.F.d. Cunha, *Journal of Physics D: Applied Physics* 43 (2010) 215403.
[389] J. Serrano, A. Cantarero, M. Cardona, N. Garro, R. Lauck, R.E. Tallman, T.M. Ritter, B.A. Weinstein, *Physical Review B* 69 (2004) 014301.
[390] W.G. Nilsen, *Physical Review* 182 (1969) 838-850.
[391] O. Brafman, S.S. Mitra, *Physical Review* 171 (1968) 931-934.
[392] T.M.G. Mohiuddin, A. Lombardo, R.R. Nair, A. Bonetti, G. Savini, R. Jalil, N. Bonini, D.M. Basko, C. Galiotis, N. Marzari, K.S. Novoselov, A.K. Geim, A.C. Ferrari, *Physical Review B* 79 (2009) 205433.
[393] J.F. Scott, T.C. Damen, W.T. Silfvast, R.C.C. Leite, L.E. Cheesman, *Optics Communications* 1 (1970) 397-399.
[394] Y.-M. Yu, S. Nam, B. O, K.-S. Lee, Y.D. Choi, M.-Y. Yoon, P.Y. Yu, *Materials Chemistry and Physics* 78 (2003) 149-153.
[395] T. Schmidt, K. Lischka, W. Zulehner, *Physical Review B* 45 (1992) 8989-8994.
[396] S. Siebentritt, U. Rau, in: R. Hull, R.M. Osgood, J. Parisi, H. Warlimont, (Eds.), Springer Series in Materials Science, Springer, 2005.
[397] W.Z. Shen, S.C. Shen, Y. Chang, W.G. Tang, L.S. Yip, W.W. Lam, I. Shih, *Infrared Physics & Technology* 37 (1996) 509-512.
[398] J. Krustok, H. Collan, M. Yakushev, K. Hjelt, *Physica Scripta* 1999 (1999) 179.

[399] A.Y. Zavrazhnov, I.D. Zartsyn, D.N. Turchen, A.V. Naumov, V.P. Zlomanov, *Inorganic Materials* 40 (2004) S101-S127.
[400] D.M. Berg, Physique PhD thesis, Université du Luxembourg, Luxembourg, 2011.
[401] M. Kauk, K. Muska, M. Altosaar, J. Raudoja, M. Pilvet, T. Varema, K.Timmo, O. Volobujeva, *Energy Procedia* 10 (2011) 197-202.
[402] J.L. Gray, in: A. Luque, S. Hegedus, (Eds.), Handbook of Photovoltaic Science and Engineering, John Wiley & Sons, 2003.